

Membrane Electrode Assembly Development in High-Temperature Proton Exchange Membrane Fuel Cells

A thesis submitted to The University of Manchester for the degree of

Doctor of Philosophy

in the Faculty of Science and Engineering



2022

Zunmin Guo

School of Engineering, Department of Chemical Engineering

Table of contents

Table of contents	2
List of figures	9
List of tables.....	15
Abbreviations.....	18
Nomenclature.....	21
Abstract.....	22
Declaration.....	23
Copyright Statement	24
Acknowledgement	25
Chapter 1: Introduction.....	26
1.1 Background.....	26
1.2 Motivation.....	28
1.3 Aims and objectives.....	28
1.4 Outline of thesis	29
Chapter 2: Background	31
2.1 Introduction.....	31
2.2 Fuel cell concepts.....	31
2.2.1 History of fuel cells.....	31
2.2.2 Working principles of fuel cells.....	33
2.2.3 Efficiency	34
2.3 Analysis of fuel cell performance	35
2.3.1 Open circuit voltage.....	35
2.3.2 Polarization curve	36

Table of contents

2.3.3	Linear sweep voltammetry	39
2.3.4	Electrochemical impedance spectroscopy.....	41
2.3.5	Durability	43
2.4	Fuel cell components	44
2.4.1	Bipolar plates	45
2.4.2	Gas diffusion layer	47
2.4.3	Catalyst layer	49
2.4.4	Proton exchange membranes	51
2.5	Limitations of HT-PEMs	54
2.5.1	Phosphoric acid leaching	54
2.5.2	Oxidative degradation	56
2.5.3	Mechanical degradation	57
2.6	Conclusion to this chapter	59
Chapter 3: Literature review		60
3.1	Introduction.....	60
3.2	Alleviating phosphoric acid leaching.....	60
3.2.1	Adding encapsulating structure in the membrane	61
3.2.2	Introducing strong interactions between polymers and PA	68
3.3	Alleviating membrane oxidative degradation	73
3.3.1	Crosslinking	73
3.3.2	Synthesis of polymer with branched structure	79
3.3.3	Introducing electron-withdrawing group or stable polymers	81
3.3.4	Inorganic additives with high oxidative stability	86
3.4	Improving membrane mechanical strength.....	89
3.4.1	Crosslinking	89
3.4.2	Blending with a stable polymer	98

Table of contents

3.4.3	Incorporating inorganic materials	100
3.4.4	Modifying membrane with designed structure	105
3.5	Durability of acid-based membranes	107
3.5.1	Crosslinking	109
3.5.2	Incorporating proton-conductive additives	111
3.5.3	Modifying membrane with designed structure	114
3.6	Conclusion to this chapter	117
Chapter 4: Experimental work and characterization techniques		120
4.1	Introduction	120
4.2	Preparation of clay-based materials	120
4.2.1	Why choose clay-based materials (vermiculite and muscovite)?	120
4.2.2	Preparation of silica nanosheets	121
4.2.3	Preparation of functionalized silica nanosheets	122
4.3	Preparation of membrane electrode assembly	123
4.3.1	Preparation of membranes	124
4.3.2	Preparation of microporous layer	127
4.3.3	Preparation of catalyst layer	129
4.3.4	Hot-pressing	130
4.4	Fuel cell testing	131
4.4.1	Polarization curve	134
4.4.2	Linear sweep voltammetry	134
4.4.3	Electrochemical impedance spectroscopy	135
4.4.4	Durability test	136
4.5	Characterization techniques	137
4.5.1	Thermogravimetric Analysis	137
4.5.2	Fourier-transform infrared spectroscopy	138

Table of contents

4.5.3	X-ray diffraction	139
4.5.4	X-ray photoelectron spectroscopy	140
4.5.5	Universal testing machine (mechanical testing)	141
4.5.6	Brunauer-Emmett-Teller (BET) Surface area	142
4.5.7	Scanning electron microscopy	143
4.5.8	Transmission electron microscopy.....	144
4.6	Conclusion to this chapter.....	146
Chapter 5: Performance of standard polyethersulfone-polyvinylpyrrolidone membranes		147
5.1	Introduction.....	147
5.2	Membrane preparation	148
5.2.1	PES/PVP-7020-Indirect	148
5.2.2	PES/PVP-7020-Direct.....	148
5.2.3	PES/PVP-6020-Indirect	149
5.2.4	PES/PVP360-Indirect.....	149
5.3	Membrane characterization.....	149
5.3.1	Fourier-transform infrared spectroscopy analysis.....	149
5.3.2	Thermogravimetric analysis.....	150
5.3.3	Mechanical properties	150
5.3.4	Acid doping and swelling	152
5.4	Fuel cell performance.....	153
5.4.1	Polarization curve	153
5.4.2	Durability	153
5.4.3	Hydrogen crossover	154
5.4.4	Electrochemical impedance spectroscopy and proton conductivity	156
5.5	Conclusion to this chapter.....	156

Chapter 6: Performance of polyethersulfone-polyvinylpyrrolidone/silica nanosheets composite membranes	158
6.1 Introduction.....	158
6.2 Characterization of SN, E-SN and S-SN.....	158
6.2.1 Elemental analysis.....	158
6.2.2 Morphology and textural property analysis	160
6.2.3 X-ray diffraction analysis.....	162
6.2.4 Fourier-transform infrared spectroscopy analysis.....	163
6.2.5 X-ray photoelectron spectroscopy analysis.....	164
6.3 Characterization of composite membranes	166
6.3.1 Morphology analysis.....	166
6.3.2 Thermogravimetric analysis.....	166
6.3.3 Mechanical properties	167
6.3.4 Acid doping and swelling	169
6.3.5 Fourier-transform infrared spectroscopy analysis.....	170
6.3.6 Proton conductivity	170
6.4 Evaluation of the composite membranes in a HT-PEMFC.....	172
6.4.1 Polarization curve	172
6.4.2 Durability	174
6.4.3 Electrochemical impedance spectroscopy.....	176
6.5 Conclusion to this chapter.....	179
Chapter 7: Performance of polyethersulfone-polyvinylpyrrolidone/muscovite composite membranes	180
7.1 Introduction.....	180
7.2 Characterizations of muscovite.....	180
7.2.1 Morphology analysis.....	180

Table of contents

7.2.2	X-ray diffraction analysis.....	181
7.2.3	Fourier-transform infrared spectroscopy.....	182
7.2.4	X-ray photoelectron spectroscopy analysis.....	183
7.2.5	Thermogravimetric analysis.....	184
7.2.6	Textural property analysis.....	185
7.3	Characterization of composite membranes	185
7.3.1	Morphology analysis.....	185
7.3.2	Fourier-transform infrared spectroscopy analysis.....	186
7.3.3	Acid doping and swelling	188
7.3.4	Mechanical properties	189
7.4	Evaluation of the composite membranes in a HT-PEMFC.....	191
7.4.1	Polarization curve	191
7.4.2	Durability	191
7.4.3	Electrochemical impedance spectroscopy.....	192
7.5	Conclusion to this chapter.....	193
Chapter 8: Investigation of acid retention ability in polybenzimidazole/muscovite composite membranes		195
8.1	Introduction.....	195
8.2	Characterization of composite membranes	196
8.2.1	Morphology analysis.....	196
8.2.2	Fourier-transform infrared spectroscopy analysis.....	198
8.2.3	Mechanical properties	202
8.2.4	Thermogravimetric analysis.....	203
8.2.5	Acid doping level and dimensional property	204
8.2.6	Proton conductivity	205
8.3	Performance of the composite membranes in a HT-PEMFC.....	205

Table of contents

8.3.1	Polarization curve	205
8.3.2	Accelerated stress test	207
8.3.3	Hydrogen crossover	209
8.3.4	Electrochemical characterizations of the membranes	210
8.3.5	Phosphorus distribution of the composite membranes after durability test	212
8.3.6	Investigation of interactions between muscovite and phosphoric acid	213
8.4	Conclusion to this chapter	215
Chapter 9: Conclusion and future prospect		216
9.1	Summary	216
9.1.1	Optimization of the preparation procedures of PES-PVP membrane	216
9.1.2	Improvement of SN and muscovite incorporated PES-PVP membranes	216
9.1.3	Investigation of acid retention ability of clay added HT-PEMs	216
9.2	Conclusion	217
9.3	Future prospects	217
9.3.1	Molecular modelling	217
9.3.2	Filler functionalization	217
9.3.3	Filler alignment in membranes	218
9.3.4	Filler functionalized polymer	218
9.3.5	Selection of clay-based filler using machine learning	218
9.3.6	In-situ analysis for inorganic-organic membranes	218
References		219
Appendix A: Publications		244
Appendix B: Conferences		246

List of figures

Fig. 1.1. Scheme of power supply through fuel cell technology (4).....	26
Fig. 2.1. (a) The electrolysis of water, and (b) simple schematic of the hydrogen fuel cell (3). ..	31
Fig. 2.2. Hydrogen fuel cell working mechanism.....	33
Fig. 2.3. Comparison of efficiency limit between PEMFC at standard pressure and the Carnot limit with a 50 °C exhaust temperature (3).....	34
Fig. 2.4. Polarization curve of a single PEMFC (3).....	36
Fig. 2.5. Tafel plots of slow and fast reactions (3).....	37
Fig. 2.6. Measurements of hydrogen crossover current by LSV at different scan rates (48).....	41
Fig. 2.7. (a) Nyquist plot for a MEA using PA doped PBI without muscovite at 0.6 A and 150 °C, and (b) equivalent circuit used to fit the Nyquist plots (R_0 and L_1 are the membrane resistance and inductance of the cell, respectively; R_1 and CPE_1 are the anode charge transfer resistance and a constant phase element at high frequency, respectively; R_2 is the sum of cathode charge transfer resistance and mass transfer resistance, while CPE_2 is a constant phase element at low frequency) (46).....	43
Fig. 2.8. Diagram of the cell configuration of a PEMFC.....	44
Fig. 2.9. Schematic representation of conventional methods: (a) CCS, (b) CCM, and (c) decal-transfer (57).....	45
Fig. 2.10. Flow field designs used in the PEMFC (60).....	46
Fig. 2.11. Conceptual diagrams of the conventional GDE with MPL (a) and the GDE eliminated MPL (b) (61).....	47
Fig. 2.12. SEM images of GDL; surface and edge views of (a) and (d) woven fibres in carbon cloth (Ballard 1071HCB), (b) and (e) straight stretched fibres in carbon paper (Toray H-060), (c) and (f) felt/spaghetti fibres in carbon paper (Freudenberg C2) (63).	48
Fig. 2.13. The cubic lattice (isotropic) (A), hex lattice (anisotropic) (B) and carbon paper (C) of MPL (64).....	48
Fig. 2.14. Energy diagram for an exothermic reaction with and without using catalyst.....	49
Fig. 2.15. Schematic representation of catalyst layer.....	50
Fig. 2.16. Schematic representation of a non-uniformly dispersed catalyst layer (74).....	51

Fig. 2.17. Conductivity mechanism in (a) Nafion and (b) PBI in which (1) stands for acid-water proton transfer, (2) stands for acid-N-H sites proton transfer, and (3) stands for acid-acid proton transfer (79).....	53
Fig. 2.18. Methods for testing PA leaching, oxidative degradation and mechanical degradation of membranes.	56
Fig. 3.1. Overview of the topic covered in this chapter.	60
Fig. 3.2. (a) Schematic of PA doped three-layered membrane. (b) Cell voltage and acid collection from the exhaust gases at 200 mA cm ⁻² and 180 °C (17).....	65
Fig. 3.3. Percentage weight loss of membranes (a) at 80 °C/40% RH and (b) at 220 °C/0% RH (89).....	71
Fig. 3.4. Crosslinked membranes using p-xylylene dichloride or p-xylene dibromide as the crosslinker. Synthetic route of (a) crosslinked PBI (157). (b) Crosslinked poly(arylene ether sulfone) (158). (c) Crosslinked PPO (159). (d) crosslinked SPEEK-Im (160).	76
Fig. 3.5. (a) Fenton test results of F ₆ PBI, F ₆ PBI with 5 wt% R ₁ , R ₂ or R ₃ , mPBI, and Nafion 115 membranes at 80 °C, and (b) structure of F ₆ PBI with R ₁ , R ₂ or R ₃ . The inserted images are the appearance of membrane samples after 133 h Fenton test (164).	77
Fig. 3.6. (a) Synthesis route and (b) Fenton test results of PBI-B ₃ -x (174). (c) Synthesis route and (d) Fenton test results of branched OPBI using different branching agents (175).	80
Fig. 3.7. (a) Scheme of branched pPBI block F ₆ -PBI copolymer and branched F ₆ -PBI block pPBI copolymer, and (b) Fenton results of PBI membranes (176).	81
Fig. 3.8. (a) Synthesis of PBI membranes with the addition of electron-withdrawing groups in Eaton's reagent, and (b) Fenton results of fluorine-containing PBI membrane (P1-P5) (181)...	84
Fig. 3.9. (a) Fenton results and (b) proton transferring pathway in the PBIOH-ILS membranes (193).....	89
Fig. 3.10. (a) Structure of QOPBI, (b) mechanical properties of dry membranes and (c) PA-doped membranes (142).	97
Fig. 3.11. (a) Traditional proton transferring pathway in a main chain structure and (b) side chain structure (248).....	106
Fig. 3.12. A summary of approaches with excellent lifetime in HT-PEMFCs.	108
Fig. 3.13. Performance comparison of the reported applications based on the durability of HT-PEMFCs where brown, blue and green bars stand for the applications utilizing crosslinking,	

incorporating proton-conductive additives, and modifying membrane structures, respectively.	108
Fig. 4.1 Schematic representation of clay structure.	121
Fig. 4.2 Photographs of raw vermiculite (left) and SN (right).	122
Fig. 4.3. Schematics of a membrane electrode assembly (MEA).	123
Fig. 4.4. Scheme and steps involved in MEA fabrication.	123
Fig. 4.5. ADL of pure PES-PVP membrane as a function of doping time.	126
Fig. 4.6. Schematic representation of the preparation of PA doped composite membrane.	127
Fig. 4.7. ADL of pure PBI membrane as a function of doping time.	127
Fig. 4.8. Procedure for preparation of microporous ink.	129
Fig. 4.9. The muffle furnace and GDL sintered temperature profile.	129
Fig. 4.10. Schematic of hot-pressing process and a prepared MEA.	131
Fig. 4.11. HT-PEMFC testing station.	132
Fig. 4.12. (a) A HT-PEMFC setup and (b) a schematic of graphite bipolar plate with serpentine flow channels.	132
Fig. 4.13. Typical fuel cell polarization curve in a HT-PEMFC at 150°C.	134
Fig. 4.14. (a) Hydrogen crossover data at different cell temperatures (51), and (b) hydrogen crossover current densities of PA/PBI/xMus membranes after accelerated stress test.	135
Fig. 4.15. An example of EIS curve and fitted curve with fitted impedance data using Randles circuit model in the Gamry software (Gamry Echem Analyst).	136
Fig. 4.16. Schematic representation of TGA (320).	137
Fig. 4.17. Schematic representation of FTIR (321)	138
Fig. 4.18. Instruments for powder XRD with fixed goniometer (1), and with fixed X-ray source (2) (323).	139
Fig. 4.19. Schematic representation of the XPS instrumentation (324).	140
Fig. 4.20. Schematic representation of the tensile test instrument (325).	141
Fig. 4.21. Schematic representation of BET surface area analyser (vacuum (VAC), calibration (CAL), adsorbate (ADS), pressure gauge (P), V1-V7 valves) (326).	142

Fig. 4.22. Physical observation of Micromeritics ASAP 2020 (327).	143
Fig. 4.23. Schematic representation of the core components of a SEM (328).....	144
Fig. 4.24. Schematic representation of the key components of a TEM (328).....	145
Fig. 5.1. Membrane casting methods: (a) direct-mixing preparation, and (b) indirect-mixing preparation.	148
Fig. 5.2. FTIR spectra of PA-doped PES-PVP blended membranes.	149
Fig. 5.3. TGA curves of PES-PVP blended membranes.....	150
Fig. 5.4. Stress-strain curve of membranes (a) before and (b) after PA doping.	151
Fig. 5.5. Polarization curves of all fresh PES-PVP membranes at 150 °C without humidification.	153
Fig. 5.6. (a) Durability test and (b) decay rate of PA doped PES-PVP membranes at 0.60 V and 150 °C during 1200 min durability test.....	154
Fig. 5.7. Hydrogen crossover current density of different membranes (a) before and (b) after 1200 min durability test.	155
Fig. 6.1 Schematic for the preparation of SN, E-SN and S-SN.	159
Fig. 6.2. (a) HAADF-STEM image of SN and (b-d) corresponding EDS elemental maps for Si, O, and Mg, respectively.	160
Fig. 6.3. Typical SEM images of (a) vermiculite, (b) SN, (c) E-SN and (d) S-SN.....	161
Fig. 6.4. Histograms of lateral flake size of (a) vermiculite, (b) SN, (c) E-SN, and (d) S-SN.	161
Fig. 6.5. HAADF STEM images (a) and HRTEM images (b) of vermiculite and SN, respectively. The insets in (a) and (b) are the corresponding FFT images.....	162
Fig. 6.6. XRD patterns for vermiculite, SN, E-SN and S-SN.	163
Fig. 6.7. FTIR spectra for vermiculite, SN, E-SN and S-SN.	164
Fig. 6.8. (a) XPS spectra of vermiculite, SN and S-SN. High-resolution XPS near (c) O 1s for SN and S-SN, and (d) S 2p for S-SN.	165
Fig. 6.9. Cross-sectional SEM images of (a) P/0SN, (b) P/0.25SN, (c) P/0.50SN, (d) P/0.75SN, (e) P/0.25E-SN, and (f) P/0.25S-SN membranes.....	166
Fig. 6.10. TGA curves of SN, E-SN, S-SN and P/xSN composite membranes.....	167

Fig. 6.11. Stress-strain curves of (a) undoped and (b) PA doped P/xSN, P/0.25E-SN and P/0.25S-SN membranes.	168
Fig. 6.12. FTIR spectra of PA doped P/xSN, P/0.25E-SN and P/0.25S-SN membranes.	170
Fig. 6.13. Proton conductivity of PA doped P/xSN, P/0.25E-SN and P/0.25S-SN membranes at different temperatures.	171
Fig. 6.14. Cell performances of P/xSN/PA, P/0.25E-SN/PA and P/0.25S-SN/PA membranes at 150 °C.	172
Fig. 6.15. Proton conductivity and power density of P/xSN/PA with different loadings of SN at 150 °C.	173
Fig. 6.16. (a) durability test and (b) decay rate of PA doped PES-PVP/SN composite membranes at 0.60 V and 150 °C during 1200 min durability test.....	176
Fig. 6.17. EIS Nyquist plots of (a) P/0SN/PA, (b) P/0.25SN/PA, (c) P/0.50SN/PA, (d) P/0.75SN/PA, (e) P/0.25E-SN/PA, and (f) P/0.25S-SN/PA.	178
Fig. 7.1. (a) SEM image, and (b) histogram of flake size of raw as-received muscovite.	181
Fig. 7.2. XRD curve (K-kaolinite, M-muscovite) of muscovite.	182
Fig. 7.3. FTIR spectra of muscovite.....	182
Fig. 7.4. (a) XPS survey spectrum and (b) XPS O 1s spectrum of muscovite.....	184
Fig. 7.5. TGA curve of muscovite.	185
Fig. 7.6. Cross-sectional SEM images of (a) P/0Mus, (b) P/0.25Mus, (c) P/0.50Mus, and (d) P/0.75Mus membranes.....	186
Fig. 7.7. FTIR spectra of undoped PES-PVP membrane in (a) 3100-500 cm ⁻¹ and (b) 500-400 cm ⁻¹ , and (c) PA doped PES-PVP/Mus membranes (4000-400 cm ⁻¹).	187
Fig. 7.8. Stress-strain curves of (a) undoped and (b) PA doped PES-PVP/Mus membranes. .	190
Fig. 7.9. Polarization curves of fresh muscovite incorporated PES-PVP membranes.....	191
Fig. 7.10. (a) durability test and (b) decay rate of PA doped PES-PVP/muscovite composite membranes at 0.60 V and 150 °C during 1200 min durability test.	192
Fig. 7.11. EIS Nyquist plots of PA doped PES-PVP/muscovite composite membranes measured at 0.6 A and 150 °C without humidification.	193

Fig. 8.1. Physical observation of (a) PBI membrane, (b) PBI/0.5Mus, (c) PBI/1Mus, and (d) PBI/2Mus.	197
Fig. 8.2. Surface SEM images of (a) PBI/0Mus, (b) PBI/0.5Mus, (c) PBI/1Mus, and (d) PBI/2Mus.	197
Fig. 8.3. Cross-sectional SEM images of (a) PBI/0Mus, (b) PBI/0.5Mus, (c) PBI/1Mus, and (d) PBI/2Mus.	198
Fig. 8.4. (a) Surface morphology, and elemental distribution mappings of (b) C, (c) N, (d) O, (e) Al, and (f) Si in the PBI/1Mus composite membrane.	198
Fig. 8.5. FTIR spectra of (a) undoped PBI/0Mus and PBI/1Mus membranes (inset: a comparison of PBI/0Mus and PBI/1Mus from 1000 to 400 cm^{-1}) and (b) PA doped PBI/0Mus and PBI/1Mus membranes (inset: a comparison of PBI/1Mus and PA/PBI/1Mus from 1700 to 1400 cm^{-1}). .	200
Fig. 8.6. Stress-strain curves of (a) undoped and (b) PA doped PBI/xMus membranes.	203
Fig. 8.7. TGA curves of PBI/xMus membranes.	204
Fig. 8.8. Proton conductivity of PA/PBI/xMus at 140-170 $^{\circ}\text{C}$	205
Fig. 8.9. Polarization curves of muscovite incorporated PBI membranes at 0 h.	206
Fig. 8.10. (a) Durability test under AST conditions, (b) polarization curves after 70 h AST, and (c) decay rate at 0, 0.6, and 1.0 A cm^{-2} of PA/PBI/xMus membranes at 150 $^{\circ}\text{C}$ without humidification.	208
Fig. 8.11. Hydrogen crossover current densities of (a) PA/PBI/xMus membranes before AST and (b) PA/PBI/xMus membranes after AST.	210
Fig. 8.12. EIS comparisons of (a) PA/PBI/0Mus, (b) PA/PBI/0.5Mus, (c) PA/PBI/1Mus, and (d) PA/PBI/2Mus before and after AST.	211
Fig. 8.13. Phosphorus distribution of the cross-sectional MEAs with (a) PA/PBI/0Mus, (b) PA/PBI/0.5Mus, (c) PA/PBI/1Mus, and (d) PA/PBI/2Mus after 70 h AST.	213
Fig. 8.14. (a) TGA curves of muscovite and P-muscovite. XPS O 1s spectra of (b) P-muscovite.	214

List of tables

Table 2.1. Important milestone in the field of fuel cells	32
Table 2.2. Common circuit elements used in equivalent circuit models.....	42
Table 3.1. Recent advances to add encapsulating structure to alleviate the PA leaching	61
Table 3.2. Recent advances to introduce strong interactions to alleviate the PA leaching	68
Table 3.3. Applications of acid-based PEMs with enhanced oxidative stability via crosslinking	73
Table 3.4. Applications of HT-PEMs with enhanced oxidative stability via introducing electron-withdrawing groups	82
Table 3.5. Applications of HT-PEMs with enhanced oxidative stability via adding additives ..	86
Table 3.6. Crosslinking for mechanical reinforcement of HT-PEMs	90
Table 3.7. Polymer blending applications for mechanical reinforcement.....	98
Table 3.8. Inorganic additives for the mechanical reinforcement.....	100
Table 3.9. Summary of durability data for selected membranes via crosslinking.	109
Table 3.10. Summary of durability data for selected membranes via incorporating proton-conductive additives.....	112
Table 3.11. Summary of durability data for selected membranes via modifying membrane structures.	115
Table 4.1. Comparison of different membrane materials in hydrogen fuel cells.....	124
Table 4.2. Calculation of parameters in microporous layer.	128
Table 4.3. Calculation of parameters in catalyst layer.	130
Table 5.1. Configurations of each prepared membrane.	147
Table 5.2. Summary of mechanical properties of blend membranes before and after PA doping.	152
Table 5.3. Summary of acid uptake, ADL and swelling properties of prepared membranes. ..	152

List of tables

Table 5.4. Summary of ohmic resistance (R_0), anode charge transfer resistance (R_1), and cathode charge transfer resistance (R_2) before and after durability test, and the proton conductivity of fresh MEAs.	156
Table 5.5. Summary of the impacts of different membrane preparation methods.	157
Table 6.1. Elemental composition of vermiculite and SN determined from STEM EDS mapping results.	159
Table 6.2. Textural properties of vermiculite and SN.	162
Table 6.3. Summary of mechanical properties of composite membranes before and after PA doping at ambient temperature and humidity.	168
Table 6.4. Acid uptake, ADL, area and volume swelling of the PA doped composite membranes.	169
Table 6.5. OCV values of composite membranes before and after durability test at 150 °C. ..	173
Table 6.6. Performance comparison of PA doped organic-inorganic HT-PEMs without humidification.	174
Table 6.7. Summary of ohmic resistance (R_0), anode charge transfer resistance (R_1), and cathode charge transfer resistance (R_2) before and after durability test obtained from equivalent circuits.	178
Table 7.1. Full FTIR assignment of muscovite.	183
Table 7.2. The main chemical compositions and formula of muscovite.	184
Table 7.3. Textural properties of muscovite.	185
Table 7.4. Full FTIR assignment of undoped and acid doped PES-PVP/Mus membranes.	188
Table 7.5. Summary of acid uptake, ADL and swelling properties of PES-PVP/Mus membranes.	189
Table 7.6. Summary of mechanical properties of PES-PVP/Mus composite membranes before and after PA doping at ambient temperature and humidity.	190
Table 7.7. Summary of ohmic resistance (R_0), anode charge transfer resistance (R_1), cathode charge transfer resistance (R_2), and proton conductivity of fresh MEAs obtained from equivalent circuits.	193
Table 7.8. Performance comparison between silica nanosheets and muscovite in HT-PEMs. ..	194

List of tables

Table 8.1. Full FTIR assignment of PBI/xMus and PA/PBI/xMus.	200
Table 8.2. Summary of mechanical properties of membranes before and after PA doping at ambient temperature and humidity.	202
Table 8.3. Properties of the PA doped PBI composite membranes with different muscovite loadings.	204
Table 8.4. Performance comparison of PA doped PBI-based composite membrane without humidification.	206
Table 8.5. Summary of ohmic resistance (R_0), anode charge transfer resistance (R_1), and the sum of cathode charge transfer resistance and mass transfer resistance (R_2) before and after durability test obtained from equivalent circuits.	212

Abbreviations

ABPBI	Poly(2,5-benzimidazole)
ADL	Acid doping level
AFC	Alkaline fuel cell
APIIm	1-(3-aminopropyl)imidazole
APTES	(3-Aminopropyl)triethoxysilane
AST	Accelerated stress test
BET	Brunauer-Emmett-Teller
BrPAEK	Bromomethylated poly (aryl ether ketone)
CL	Catalyst layer
CMPSf	Chloromethylated polysulfone
CMPSU	Chloromethylated polysulfone
cPIL	Cross-linkable polymeric ionic liquid
CPE	Constant phase element
DMAc	Dimethylacetamide
DMF	N,N-dimethylformamide
EDS	Energy-Dispersive X-ray Spectroscopy
EIS	Electrochemical impedance spectroscopy
EPA	Ethyl phosphoric acid
E-SN	Exfoliated silica nanosheets
EGO	Electrochemically exfoliated graphene oxide
FTIR	Fourier transform infrared spectroscopy
F6-PBI	Fluorine-containing PBI
GDL	Gas diffusion layer
GO	Graphene oxide

Abbreviations

HT-PEM	High-temperature proton exchange membrane
HT-PEMFC	High-temperature proton exchange membrane fuel cell
ICTES	3-isocyanatopropyl)triethoxysilane
IPA	Isopropanol
KH550	3-aminopropyltriethoxysilane
KH560	3-Glycidyloxypropyl)trimethoxysilane
LSV	Linear sweep voltammetry
LT-PEMFC	Low-temperature proton exchange membrane fuel cell
MPL	Microporous layer
MEA	Membrane electrode assembly
MPTES	(3-mercaptopropyl)trimethoxysilane
Mus	muscovite
mPBI	poly[2,2'-m-(phenylene)-5,5'-bibenzimidazole]
NR	Not reported
OCV	Open circuit voltage
PA	Phosphoric acid
PAFC	Phosphoric acid fuel cell
PAAm-g-CS	Polyacrylamide-graft-chitosan
PAME	Poly(azomethine-ether)
PBI	Polybenzimidazole
PES	Polyethersulfone
PEM	Proton exchange membrane
PEEK	Poly(ether ketone sulfone)s
PEK-c	Polyetherketone-cardo
PPO	Poly(2,6-dimethyl-1,4-phenylene oxide)

Abbreviations

PSU	Polysulfone
PyPBI	Poly[2,2'-(2,6-pyridine)-5,5'-bibenzimidazole]
PVDF	Poly(vinylidene fluoride)
PVDF-HFP	Poly(vinylidene fluoride-co-hexafluoropropylene)
PVP	Polyvinylpyrrolidone
PTFE	Polytetrafluoroethylene
PVPA	Poly(vinylphosphonic acid)
qPVBzCl ⁺	Quaternized poly (vinyl benzyl chloride)
QA	Quaternary ammonium
SN	Silica nanosheets
S-SN	Sulfonated silica nanosheets
SEM	Scanning electron microscope
SOFC	Solid oxide fuel cell
SO ₂ PBI	Poly(aryl sulfone benzimidazole)
TEM	Transmission electron microscopy
TGA	Thermogravimetric Analysis
TMBP	4,4'-diglycidyl (3,3',5,5'-tetramethyl biphenyl)
XRD	X-ray diffraction analysis
XPS	X-ray photoelectron spectroscopy
1,4-PDI	1,4-phenylene diisocyanate
2D	two-dimensional

Nomenclature

ξ	fuel cell efficiency
ΔG	Gibbs free energy
ΔH	energy content of the fuel
E	standard electric potential
F	Faraday constant
E_0	reversible cell voltage
E_a	standard potential for the oxidation of hydrogen
E_c	standard reduction potentials
T	temperature
P	partial pressure of reactants and products
I	Current
$J_{H_2}^{A \rightarrow C}$	hydrogen permeation rate
K_{H_2}	hydrogen permeability coefficient
$P_{H_2}^A$	hydrogen partial pressure at the anode side
W_{wet}	membrane weight after acid doping at room temperature
W_{dry}	membrane weight before acid doping at room temperature
σ	proton conductivity
L	membrane thickness
A	membrane active area

Abstract

High-temperature proton exchange membrane fuel cells (HT-PEMFCs) are studied worldwide as efficient energy conversion devices. Great efforts have been made in the area of designing and developing phosphoric acid (PA)-based high-temperature proton exchange membranes (HT-PEMs). However, the current HT-PEMs suffer limited proton conductivity, acid leaching, along with chemical and mechanical degradations. This thesis focuses on the incorporation of inorganic clay-based fillers (silica nanosheets and muscovite) into HT-PEMs in order to improve proton conductivity, reduce acid leaching and alleviate membrane degradation.

The first experimental work of this thesis is based on the optimization of polyethersulfone-polyvinylpyrrolidone (PES-PVP) membrane preparation procedures. It was found that the membranes prepared using high-molecular-weight polymers and indirect mixing method exhibited better mechanical properties and durability than the membrane prepared using low-molecular-weight polymer or direct mixing method. The possible reason is that the membrane prepared using high-molecular-weight polymer or the indirect-mixing method has a dense and homogenous structure and therefore has a longer lifetime.

Later, silica nanosheets (SN), functionalized and exfoliated SN, and as-received muscovite were introduced into PES-PVP membranes and tested at 150 °C without humidification. The surface functional groups (hydroxyl or sulfone groups) and the layered structures of clay-based fillers appear to facilitate the proton conductivity and protect the membrane from radical attack to get improved power density and durability.

To better understand how the clay-based fillers work in HT-PEMFCs and alleviate the acid leaching in HT-PEMs, polybenzimidazole (PBI) membranes which have better durability and longer lifetime than PES-PVP membranes were used as HT-PEMs in this work. In addition, since muscovite has similar properties with SN in terms of the improvement of membrane properties and cell performance, the as-received muscovite which is a lot cheaper and has simpler preparation procedure than SN was chosen as the inorganic filler and added into PBI membranes to investigate the acid leaching issue. Accelerated stress test was employed to accelerate acid leaching and facilitate the evaluation of acid leaching issue in HT-PEMs. Due to the muscovite-PA and muscovite-PBI crosslinks confirmed by energy dispersive X-ray spectroscopy, thermogravimetric analysis, and X-ray photoelectron spectroscopy, the inorganic-organic composite membranes showed improved performance, alleviated acid leaching and better durability.

Declaration

I declare that no portion of the work referred to in the thesis has been submitted in support of an application for another degree or qualification of this or any other university or other institute of learning.

Zunmin Guo

May, 2022

Copyright Statement

- i. The author of this thesis (including any appendices and/or schedules to this thesis) owns certain copyright or related rights in it (the “Copyright”) and s/he has given The University of Manchester certain rights to use such Copyright, including for administrative purposes.
- ii. Copies of this thesis, either in full or in extracts and whether in hard or electronic copy, may be made only in accordance with the Copyright, Designs and Patents Act 1988 (as amended) and regulations issued under it or, where appropriate, in accordance with licensing agreements which the University has from time to time.
- iii. This page must form part of any such copies made. The ownership of certain Copyright, patents, designs, trademarks and other intellectual property (the “Intellectual Property”) and any reproductions of copyright works in the thesis, for example graphs and tables (“Reproductions”), which may be described in this thesis, may not be owned by the author and may be owned by third parties. Such Intellectual Property and Reproductions cannot and must not be made available for use without the prior written permission of the owner(s) of the relevant Intellectual Property and/or Reproductions.
- iv. Further information on the conditions under which disclosure, publication and commercialisation of this thesis, the Copyright and any Intellectual Property and/or Reproductions described in it may take place is available in the University IP Policy (see <http://documents.manchester.ac.uk/DocuInfo.aspx?DocID=487>), in any relevant Thesis restriction declarations deposited in the University Library, The University Library’s regulations (see <http://www.manchester.ac.uk/library/aboutus/regulations>) and in The University’s policy on Presentation of Thesis.

Acknowledgement

When I was a child, to be a doctor will be one of greatest and successful people in my mind. Now, I almost achieve the goal and make the dream come true. PhD is not a complete of life but a start of new point. From my perspective, the PhD research is not like a tutorial during your undergraduate study but you need walk or run by yourself under the supervision of your supervisor.

Regardless of how many days and nights you spent by yourself, how aloneness you were when you walked from lab to the small accommodation especially in the evening, how desperate when you failed in one of your PhD projects, or how difficult when you tried to find a position, all will deserve when you start to find some small expected results and get accepted emails from the ideal journals.

In terms of who I want to thank for the PhD, the first person is my supervisor, Prof. Stuart M. Holmes. After I completed my master degree in 2017 from his group, I worked for two years in a pharmaceutical company, China. Finally, I decided to proceed my PhD before Stuart gave me an opportunity to come back to Manchester. Also, he is always helpful, patient and kind to guide me and support everything he can do. Discussions with him are always indicating me some ideas in the research. If you need collaborations, he is always happy to help to contact others. The most important point is he always has a quick reply when you need helps no matter paper revisions or meeting enquiries. I will appreciate him all the time and thank him to help me take the most important step in my life.

I also need to thank my family members. There will not exist any achievements without their supports. Every time I feel sad and disappointed, it is their support and encouragement to help me pass through the darkness. Their love gives me endless passions and forces to complete this work and carry on.

I would like to thank my colleagues, Dr. Maria Perez-Page, Dr. Madhumita Sahoo, Dr. Jianuo Chen, Dr. Zhaoqi Ji, Dr. Rana Hassan-Naji, Dr. Wenji Yang, and PhD student Ziyu Zhao, Mengxi Li, Zeyu Zhou, Elliot Craddock and Xiaochen Yang for their help, great support and lovely events.

Chapter 1: Introduction

1.1 Background

The increasing concern over the availability of the world's fossil fuels and the detrimental influence on the environment associated with the consumption of fossil fuels have motivated the research for alternative green energy technologies (1). However, due to the intermittence of most renewable energy source, it remains challenges in energy generation and maintenance to ensure the stability of power network (2). Great efforts have been made to explore alternative approaches, such as converting energy from one form (electricity) to a storable form (hydrogen) via electrolysis. Subsequently, the stored energy can be converted back to electricity when needed as shown in Fig. 1.1 (3, 4). Fuel Cells are one of the most promising energy-conversion devices that convert the chemical energy by electrochemical reactions into electricity. As fuel cells can continuously generate electricity with high efficiency and near-zero pollution emission, they represent a promising substitute to traditional electrical sources and heat generators, and can be employed in a wide range of applications from micro power sources to multiple-megawatts power stations.

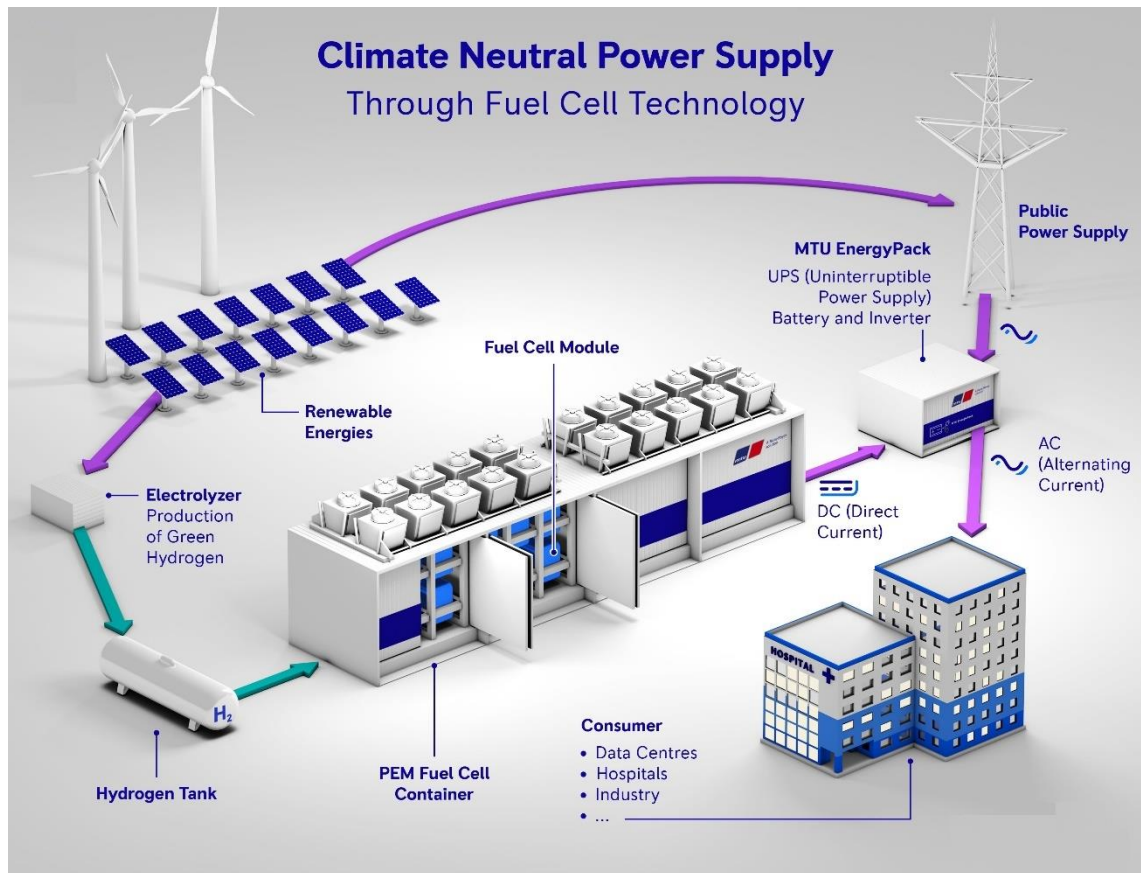


Fig. 1.1. Scheme of power supply through fuel cell technology (4).

The fuel cell is composed of two electrodes (anode and cathode), where the reactions take place, and an electrolyte, which allows the ion transfer from anode to cathode. Fuel cells can be categorized by the electrolyte type (5), such as the alkaline fuel cell (AFC), phosphoric acid fuel cell (PAFC), molten carbonate fuel cell (MCFC), proton exchange membrane fuel cell (PEMFC), anion exchange membrane fuel cell (AEMFC) and solid oxide fuel cell (SOFC). The electrolytes of AFC, PAFC and MCFC are alkaline aqueous solution, phosphoric acid and molten-carbonate, respectively, which are corrosive and limit their competitiveness and viability (6). Therefore, PEMFC, AEMFC and SOFC are considered to be the most suitable energy-conversion technologies. Since PEMFC has potential advantages such as portable applications and high efficiency, PEMFC is regarded as one of the most promising clean energy technologies (7). According to the operating temperature, PEMFCs can be divided into low-temperature PEMFCs working at 30-100 °C (LT-PEMFCs) and high-temperature PEMFCs working at 100-200 °C (HT-PEMFCs). As the core constituent in PEMFCs, proton exchange membranes (PEMs) are responsible for the transfer of protons from anode to cathode, separating the reactants, and insulating electrons to avoid short circuit. This solid proton exchange membrane has several advantages over the traditional liquid electrolyte, such as being compact, easy handling, easy assembling and sealing, and excellent resistance to gas crossover (8). LT-PEMFCs usually use polymeric materials (perfluorosulfonic acid-based membranes such as Nafion) as the electrolyte. The advantages, such as high conductivity, good chemical and mechanical stability, fast start-up, high efficiency and power density, make LT-PEMFCs one of the most mature technologies for the development of hydrogen fuel cell vehicles which were commercialized in 2013 by Hyundai (9), in 2015 by Toyota (10), and in 2016 by Honda (11).

Compared with LT-PEMFC, HT-PEMFC attracts a great attention for several reasons: (i) carbon monoxide tolerance: when the concentration of carbon monoxide is more than 10 ppm, it will be absorbed by the platinum catalyst and result in catalyst poisoning (12). As the CO adsorption onto the Pt surface has high negative entropy, low temperature will facilitate CO adsorption (13). The fuel cells operating at high temperature will then have higher CO tolerance. (ii) Electrode kinetics: higher operating temperature results in faster electrode reactions at the cathodes (oxygen reduction). (iii) Water management: since LT-PEMFCs operating at below 100 °C need the humidified gas as the fuel supply, fuel cell flooding is more probably to occur and reduce fuel cell performance. However, humidifier is not necessary for HT-PEMFCs due to the different membrane type, such as phosphoric acid-based HT-PEMFCs, which utilize phosphoric acid as proton conductor (14). This can result in less balance of plant and complex system control in the fuel cell systems. (iv) Heat management: unlike LT-PEMFCs which need a cooling system to remove excess heat produced during operations, the residual heat in HT-PEMFCs can be utilized.

1.2 Motivation

Since high-temperature proton exchange membranes (HT-PEMs) usually face the acid leaching issues and poor mechanical and chemical stabilities at high temperature, the performance and durability of HT-PEMs are recognized as the primary limitations before the commercialization of this technology. Many efforts have been tried to address these problems, such as crosslinking (15), modifying the polymer or membrane structure (16, 17), and incorporating inorganic materials (18). Organic-inorganic composite membranes have been regarded as one of the most promising approaches due to their stable mechanical and chemical properties and low cost. For instance, hygroscopic inorganic oxides (SiO_2 , TiO_2 , and ZrO_2) (19-21), perovskite structure materials (22, 23), metal sulfophenyl phosphate (24, 25) or carbonaceous materials (26) have been incorporated into HT-PEMs to get improved performance or durability. Particularly, the incorporation of clay minerals into membranes has attracted interest because of their hygroscopicity, high surface area and low cost (27). Clay-based materials such as laponite (28), montmorillonite (29-31), and sepiolite (32, 33) were explored as the membrane additives in HT-PEMFC applications. The hygroscopic and barrier properties of clay may offer enhanced performance achieved by increased proton pathway and reduced hydrogen crossover, respectively.

In this project, for the first time, silica nanosheets (derived from natural vermiculite) and muscovite are chosen as the membrane fillers to be incorporated into HT-PEMs, and the corresponding fuel cell performances are tested. In addition, as few studies focus on the durability degradation and deactivation mechanisms of the organic-inorganic composite membrane-based HT-PEMFCs, there is a lack of substantial work to show mechanisms related to the cell degradation. Therefore, the deactivation mechanisms are investigated by several in-situ and ex-situ techniques. The acid distribution and the effects of the interactions between inorganic fillers and polymer on the HT-PEM properties are studied to explore deactivation mechanisms and acid retention ability of composite membranes.

1.3 Aims and objectives

The aim of this research is to optimise the performance of HT-PEMFC by improving the proton conductivity, acid retention ability and the durability of HT-PEMs.

The objectives in this research are shown as below:

- Determine the most suitable PES-PVP membranes prepared using different mixing methods and different-molecular-weight polymers which can give the best power density and durability.
- Prepare silica nanosheets and the functionalized forms using silane coupling agents or liquid exfoliation method, incorporate these inorganic materials into the membranes to

optimize the loading of silica nanosheet in terms of proton conductivity and durability, and investigate the effects of silica nanosheets on the chemical and physical properties of HT-PEMs.

- Introduce another clay material, muscovite, into HT-PEMs, explore cell performance and the best loading of muscovite in membranes, and gain insights into acid leaching and the deactivation mechanisms of HT-PEMFC.

1.4 Outline of thesis

This thesis is comprised of eight further chapters which will present findings in the following order:

Chapter 2: introduces the general concepts of fuel cells, fuel cell efficiency, types of fuel cells, different parts of fuel cells, and challenges of high-temperature proton exchange membranes (HT-PEMs).

Chapter 3: illustrates a review of the literature on recent applications of HT-PEMs, and current approaches to tackle membrane degradation problems (acid leaching, chemical and mechanical degradation).

Chapter 4: concentrates on the methodology of how to prepare clay-based materials and MEAs for fuel cells (microporous layer, catalyst layer and membrane). The fuel cell working station and electrochemical techniques (polarization curve, linear sweep voltammetry, electrochemical impedance spectroscopy, and durability test) are introduced in this chapter to characterize the electrochemical properties of fuel cells. Moreover, this chapter also explains the sample characterization techniques including Thermogravimetric Analysis, Fourier-transform infrared spectroscopy, universal testing machine (mechanical testing), X-ray diffraction, X-ray photoelectron spectroscopy, BET Surface area, scanning electron microscopy, and transmission electron microscopy.

Chapter 5: displays the results of the standard polyethersulfone-polyvinylpyrrolidone (PES-PVP) membrane with optimal preparation method and polymer molecular weight.

Chapter 6: presents the results of PES-PVP/silica nanosheets composite membranes. The results related to the characterizations of silica nanosheets and composite membranes are reported. Later the cell performance and corresponding discussions on the reasons why the improvements were observed in the organic-inorganic composite membranes are described.

Chapter 7: introduces the incorporation of muscovite into PES-PVP membranes and explores the effect of muscovite onto the cell performance and durability. The characterizations of muscovite and the related inorganic-organic composite membranes are included. In addition, the

comparison of silica nanosheets and muscovite working as inorganic fillers in HT-PEMs is also discussed.

Chapter 8: shows the results of polybenzimidazole (PBI)/muscovite membranes to validate the enhancement of muscovite in HT-PEMs and understand the degradation mechanisms (especially acid leaching) in a long time. The results of PBI/muscovite membranes including the analyses of composite membranes and cell performance are presented in this chapter.

Chapter 9: summarizes and concludes the work completed during the study and future prospects.

Chapter 2: Background

2.1 Introduction

In this chapter, detailed information is presented regarding the understanding of fuel cell fundamentals. Fuel cell concepts including background, working principle, and electrochemical theory will be introduced. Analysis of fuel cell performance, in terms of activation loss, ohmic loss and mass transfer loss, will subsequently be added. This chapter will also introduce fuel cell components (bipolar plates, electrodes and membranes), and discuss the limitations and challenges of high-temperature proton exchange membranes.

2.2 Fuel cell concepts

2.2.1 History of fuel cells

The history and development of the fuel cell date back to almost 200 years ago when Sir William Grove, recognized as the father of fuel cell, started the research in 1839 (34). Benefiting from the water electrolysis process discovered in 1800 by Sir Anthony Carlisle and William Nicholson who showed water can be decomposed into hydrogen and oxygen using electricity as shown in Fig. 2.1a, Grove conceptualized and designed this possible reverse reaction to generate electricity by consuming oxygen and hydrogen (3). By immersing two platinum electrodes in a dilute acid electrolyte and placing the other side into the oxygen and hydrogen tubes, a constant current was produced between the electrodes as shown in Fig. 2.1b.

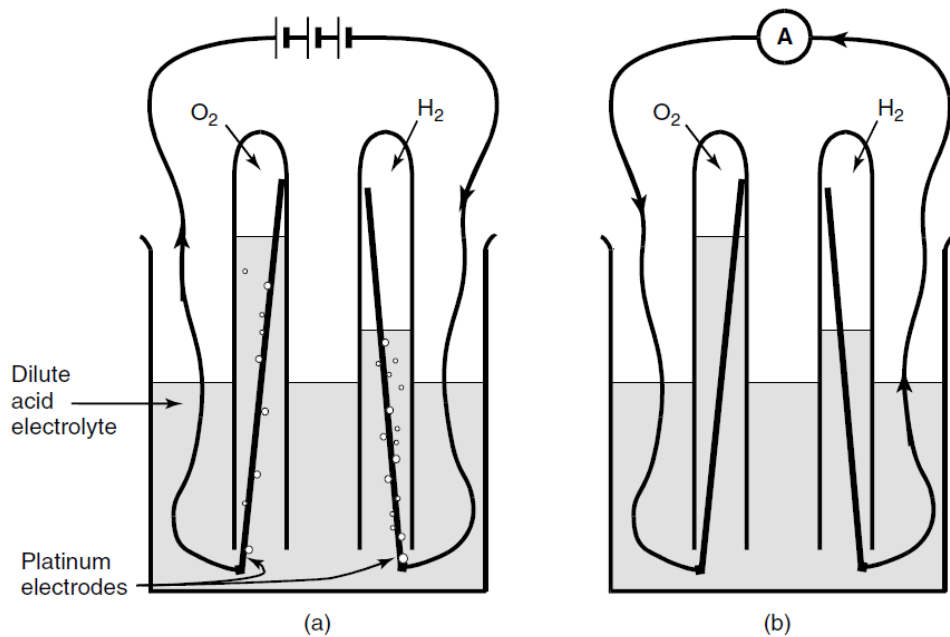


Fig. 2.1. (a) The electrolysis of water, and (b) simple schematic of the hydrogen fuel cell (3).

In the 20th century, fuel cell technology was further developed by Francis Thomas Bacon from

developing the first practical fuel cell which can directly convert hydrogen and air into electricity through electrochemical process in 1932 to construct a 5-kW alkaline fuel cell (AFC) in 1959. His work attracted attention from NASA in the 1960s as a part of the Apollo spacecraft. Later, as the pioneers to introduce commercialized proton exchange membrane fuel cells (PEMFCs), General Electric (GE) and DuPont used polystyrene sulphate and perfluorosulfonic acid (Nafion) as ion-exchange membranes in PEMFCs. Further research continued into the 21st century where fuel cells have been developed in multiple sectors such as transportation, stationary and portable applications. Table 2.1 highlights the main milestones for the history of fuel cells (35, 36).

Table 2.1. Important milestone in the field of fuel cells

Years	Important milestones in the field of fuel cells
1839	Grove demonstrated the hydrogen fuel cell
1889	Ludwig Mond and Carl Langer developed porous and 3D shaped electrodes
1893	Friedrich Wilhelm Ostwald explained the basic electrochemistry and the different parts of fuel cells
1896	William W. Jacques built the first fuel cell stacks
1921	Emil Baur developed first molten carbonate fuel cell
1933-1959	Thomas Francis Bacon developed AFC
1950	Teflon was first applied in acid electrolyte and platinum electrodes
1955-1958	Thomas Grubb and Leonard Niedrach developed PEMFC at GE
1958-1961	G.H.J. Broers and J.A.A. Ketelaar firstly developed molten salts as electrolyte
1960	NASA used AFC in Apollo space program
1961	G.V. Elmore and H.A. Tanner introduced and developed phosphoric acid fuel cell
1962-1966	The PEMFC developed by GE was used in NASA's space program
1968	DuPont firstly introduced Nafion membrane
1992	Jet Propulsion Laboratory developed methanol fuel cells
1990s	Extensive research focused on PEMFC

2000s Commercialized fuel cell vehicles in 2013 by Hyundai (9), in 2015 by Toyota (10), and in 2016 by Honda (11)

2.2.2 Working principles of fuel cells

The fuel cell is a device capable of converting chemical energy of fuel to electricity, and it has become a promising alternative power source for stationary, portable, and vehicular applications due to the quiet operation process, quick start-up and load response, efficient energy conversion, and low exhaust emission. Usually, in a hydrogen fuel cell, hydrogen and oxygen are supplied to anode and cathode, respectively. As shown in Fig. 2.2, a single fuel cell contains flow fields for gas flow and a membrane electrode assembly (two electrodes and a membrane in the middle) where electrochemical reactions will happen at the interface of fuel gas, catalyst and electrolyte. The protons which are produced from the oxidation of hydrogen will pass through the electrolyte to cathode as shown in equation 2.1, while the corresponding electrons which are rejected by the high-electrical-resistance membrane will flow through the external circuit to produce electricity. In the cathode side, the protons will react with oxygen to produce water through the efficient four-electron transfer process (equation 2.2a). Sometimes when there are some incomplete reduction reactions, oxygen reduction in acidic media may have a two-electron transfer to produce peroxide species as an intermediate, followed by further reduction to water (equation 2.2b) (37). Equation 2.3 shows the entire reaction of PEMFC. In other words, the reactions will automatically happen on the catalyst surface to produce water if there are no membrane as a separator. In a fuel cell, the reaction still happens but the external circuit and electrolyte separate the full reaction into two half parts, where the electrons will be utilized to generate electricity through external circuit and the protons will pass through the electrolyte.

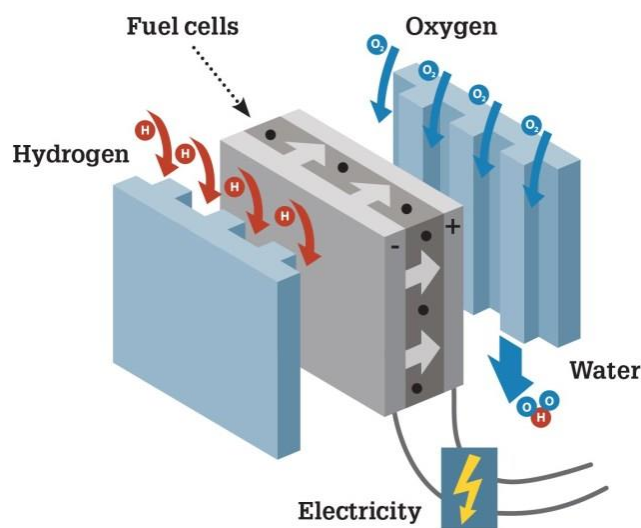
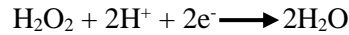


Fig. 2.2. Hydrogen fuel cell working mechanism.





2.2.3 Efficiency

Fuel cell efficiency is usually compared with the Carnot efficiency of traditional combustion engines. Due to the irreversible issues such as the existence of the internal forces and flows and the heat energy of the reactant gas which has exhaust temperature and cannot be recycled (38), the Carnot efficiency is the maximum efficiency of a heat engine. However, fuel cells which can directly convert chemical energy to electricity are not limited by the Carnot cycle. The maximum fuel cell efficiency (ξ) is the same as thermodynamic efficiency of energy conversion, which is a ratio between Gibbs free energy (ΔG) and the energy content of the fuel (ΔH) as shown in equation 2.4.

$$\xi = \Delta G / \Delta H \quad (2.4)$$

The thermodynamic efficiencies of the Carnot cycles with different exhaust temperatures are compared to the theoretical efficiencies of H_2/O_2 fuel cell in Fig. 2.3 (3). When the temperature rises over 100 °C, the energy generated from the fuel gas will transfer to water due to water evaporation and lower entropy state of the gas product. This is reflected by the molar enthalpies of liquid and vapor water, which is -286 kJ/mol for liquid form and -242 kJ/mol for gas form at 298.15 K and 1 bar as shown in equation 2.5 and 2.6.

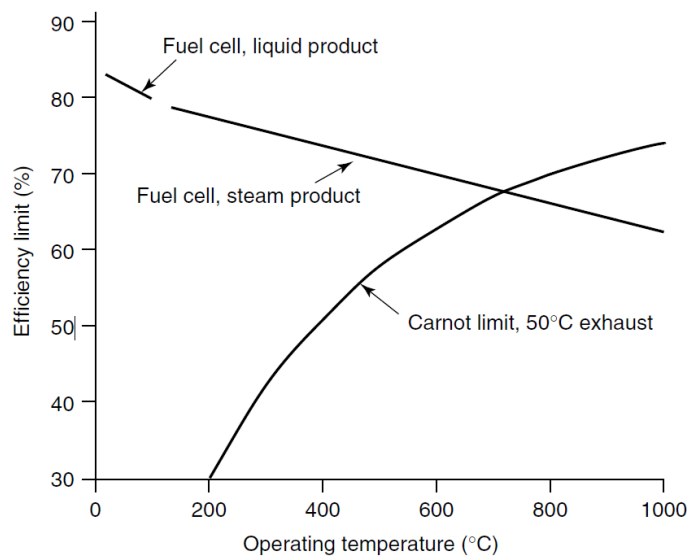
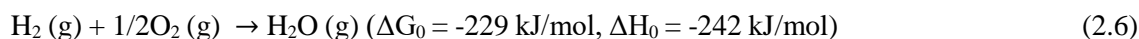
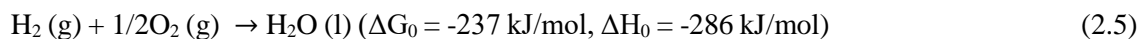


Fig. 2.3. Comparison of efficiency limit between PEMFC at standard pressure and the Carnot limit with a 50 °C exhaust temperature (3).



Hence, the vaporization (or condensation) of water needs to be taken into consideration to calculate the efficiency of the hydrogen based electrochemical energy conversion technologies. The overall efficiency of a fuel cell usually depends on operating temperature and the evolved heat which can be recovered. For instance, if fuel cells can combine heat and power units, the waste heat utilization are generally beneficial to the enhancement of fuel cell efficiency.

2.3 Analysis of fuel cell performance

2.3.1 Open circuit voltage

In the fuel cell process, the Gibbs free energy is related to standard electric potential (E) as shown in equation 2.7 where n is the number of electrons involved in the reaction (two electrons), and F stands for the Faraday constant ($96500 \text{ C g}^{-1} \text{ mol}^{-1}$). Taking the product as the water steam as an example, according to the standard Gibbs free energy change ($\Delta G_0 = -237 \text{ kJ/mol}$ in equation 2.5), the reversible cell voltage (E_0) of the overall H_2/O_2 fuel cell reaction can be calculated as 1.23 V which gives the maximum potential in a fuel cell running under the standard conditions of 1 bar and 298K.

$$\Delta G_0 = -nFE_0 \quad (2.7)$$

From an electrochemical viewpoint, this standard potential can also be calculated from the potential differences of individual electrode reactions as shown in equation 2.8 where E_c and E_a are standard electric potential of cathode and anode reactions, respectively (39). Because the electrochemical dissociation of hydrogen is almost reversible on a platinized platinum electrode, the standard potential for the oxidation of hydrogen (E_a) and the reduction of protons on platinum is taken as 0.00 V by definition at all temperatures. As described in equation 2.7, E_c (1.23 V) is calculated by the relationship between Gibbs free energy change and electric potential for the corresponding cathode reactions under standard conditions. Therefore, the standard electric potential is calculated as 1.23 V according to equation 2.8.

$$E = E_c - E_a \quad (2.8)$$

This situation changes in practical conditions as a fuel cell is operated at different temperature, pressure or reactant activity other than standard conditions. The theoretical reversible voltage at actual temperature and pressure conditions can be calculated from standard potential using the Nernst equation (equation 2.9) where R stands for universal gas constant ($8.314 \text{ J/mol}\cdot\text{K}$), T is temperature (K), and P stand for partial pressure of reactants and products (3). From equation 2.9, it is evident that temperature and reactant concentration have direct impacts on cell voltage.

$$E = E_0 + \frac{RT}{nF} \ln (P_{H_2}P_{O_2}/P_{H_2O}) \quad (2.9)$$

2.3.2 Polarization curve

A fuel cell performance can be represented by a polarization curve where the cell potential is plotted as a function of cell current density as shown in Fig. 2.4. Theoretically, the open circuit voltage (OCV) of a single fuel cell can reach to 1.23 V according to equation 2.6 and 2.7 if the reaction happened in a fuel cell is a spontaneous process. However, the OCV in a practical cell is usually up to 1.0 V and gradually drops down with the increase of current density. This may be explained by the fuel crossover through the electrolyte which can cause a mixed electrode potential, internal current through the membrane, or the cathode mixed potential on the catalyst surface produced by a reaction between the platinum and O_2 (3, 39, 40).

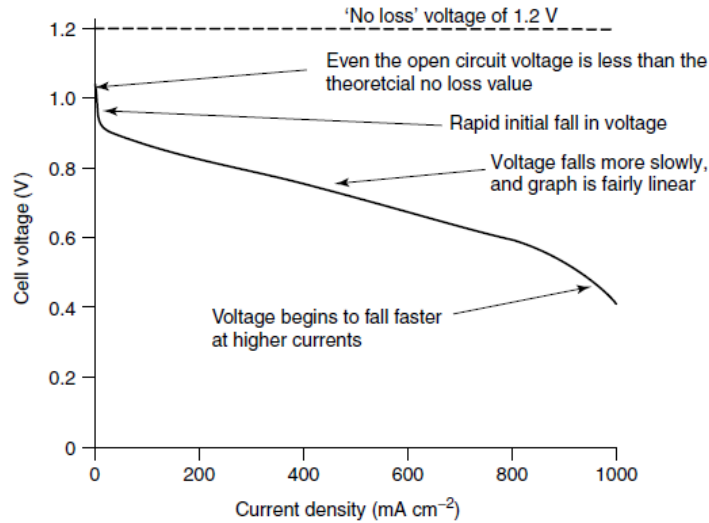


Fig. 2.4. Polarization curve of a single PEMFC (3).

In the polarization curve, the cell voltage decreases with the increase of current density during the operation of a fuel cell. This is usually caused by irreversible losses (named as polarization losses) including activation loss, ohmic loss, mass transfer loss and fuel crossover. The voltage loss is initially caused by the activation loss when the current density is low, then the ohmic loss dominates the following region. Afterwards, in the high-current-density region of the polarization curve where the reaction rate becomes fast, the fuel (oxygen or hydrogen) might not be sufficient in the catalyst sides to result in mass transfer loss. The voltage can be expressed as equation 2.10:

$$V_o = V_{ocv} - V_{act} - V_{ohm} - V_{mass} - V_{cross} \quad (2.10)$$

where V_o , V_{ocv} , V_{act} , V_{ohm} , V_{mass} and V_{cross} stand for cell voltage, OCV, voltage for activation loss, voltage for ohmic loss, voltage for mass transfer loss and voltage for fuel crossover, respectively.

2.3.2.1 Activation loss

In the initial part of polarization curve, the activation loss is caused by activating electrochemical reactions (hydrogen oxidation and oxygen reduction) and kinetics transferring electrons at the surface of the electro-catalyst layers, especially at the cathode oxygen reduction reaction. The activation loss can be obtained by plotting the logarithm of the current density against the overpotential in a Tafel plot according to equation 2.11 and 2.12 where A stands for the Tafel slope, and i_0 is the exchange current density which is the current density when the activation loss begins to move from zero as shown in Fig. 2.5 (3). The α is the charge transfer coefficient which is the percentage of the applied electrical energy in the electrochemical reaction. R , T and F are ideal gas constant (8.314 J/mol·K), absolute temperature (K) and Faraday's constant (96485 C/mol), respectively.

$$V_{\text{act}} = A \ln(i/i_0) \quad (2.11)$$

$$A = \frac{RT}{2\alpha F} \quad (2.12)$$

Because α in the fast reaction is larger than the slow reaction in the same fuel cell, the best-fit line intercept at X-axis (i_0) of fast reaction is bigger than that of slow reaction and the slope of the fast reaction is smaller than that of the slow reaction as shown in Fig. 2.5. Therefore, enhancing the electrochemical rate including increasing cell temperature, fuel flow rate and concentration, or improving the catalyst utilization (such as using the catalysts with effective surface area) can lead to larger exchange current density and further lower activation loss (3). One interesting point is that the increased temperature can increase the value of Tafel slope and activation loss according to equation 2.12, however, the increased exchange current density caused by the temperature can bring more effects on the reduction of activation loss.

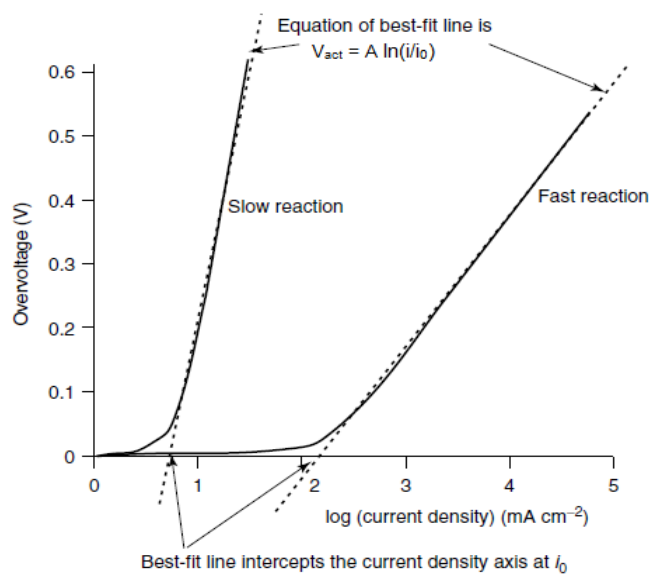


Fig. 2.5. Tafel plots of slow and fast reactions (3).

2.3.2.2 Ohmic loss

Ohmic loss (V_{ohm}) comprises the resistance of transferring ions through the electrolyte, and the resistance of conducting electrons through the fuel cell components (electrodes, bipolar plates and current collectors) or interconnections (contact resistances). As ohmic loss is related to the natural resistance of materials, the voltage drop is almost linear with the increase of current density in the region of ohmic loss as shown in Fig. 2.4. The ohmic resistance can be expressed by Ohm's law in equation 2.13 where V_{ohm} , I and R are the voltage, current and the electrical resistance per area, respectively:

$$V_{\text{ohm}} = IR \quad (2.13)$$

As the materials used in fuel cells are usually of high-electronic conductivity, the electronic resistance can be neglected in comparison with the membrane resistance so that the ohmic resistance is usually regarded as membrane resistance. The use of highly electrically conductive electrodes, employing thin or highly proton conductive membranes, and improving the designs of interconnections can be the solutions to reduce the voltage drop due to ohmic losses. However, the approach using thinner membrane should be carefully considered as the thinner membrane may result in lower mechanical strength and fuel crossover.

2.3.2.3 Mass transfer loss

Mass transport loss (V_{mass}) is the voltage loss due to the insufficient fuel at the active catalyst sites, where the low concentration of reactant has a significant effect on the final region of the polarization curve as shown in Fig. 2.4. Because the fuel is consumed at the catalyst layer, the concentration and pressure of fuel near catalyst surface are lower than the bulk flow, which may lead to the shortage of fuel to the catalyst to get mass transfer loss. Reducing mass transport loss is a significant factor in improving the performance especially in the high-current-density region. The potential loss caused by mass transfer (V_{mass}) can be expressed by equation 2.14 where P_1 is the pressure when the current density is zero and P_2 is the pressure at any current density. F , R and T are Faraday's constant (96485 C/mol), ideal gas constant (8.314 J/mol·K), absolute temperature (K), respectively (3):

$$V_{\text{mass}} = \frac{RT}{2F} \ln\left(\frac{P_2}{P_1}\right) \quad (2.14)$$

The mass transport loss is usually related to the properties of catalyst layer (including Pt/C catalyst, ionomer and pores). The Pt/C catalyst affords the reaction sites and electron transfer; the ionomers can act as binders, and facilitate ions transport and water management; and the pores (usually mesopores (41)) in the catalyst layer benefit for mass transport to ensure the contact of reactant molecules/ions with active sites. Therefore, the catalyst and ionomer should have optimal distributions to get proper porosity and gas permeability. Several approaches were reported to

reduce mass transfer losses via the modification of electrode structure, such as using an additional solvent to control the polarity, applying a pore-forming agent, optimizing the ionomer content, and introducing 3D nanostructure (carbon nanotubes, carbon nanofibers, layer-by-layer assemblies and inverse opal structures) for catalyst supports (42).

2.3.2.4 Fuel crossover

The reactant permeation from one side to another is called as fuel crossover, which has three negative effects on fuel cell performance: fuel efficiency reduction, cathode potential depression, and peroxide radical formation (43). Specifically, the fuel crossover can result in the hydrogen loss at anode side and the oxidation of permeated hydrogen at cathode side, leading to mixed potential to get reduced OCV. The permeated hydrogen will react with oxygen directly to produce free radicals or H_2O_2 to attack catalyst and membrane to accelerate catalyst and membrane degradations.

Hydrogen crossover can be described by Fick's law as shown in equation 2.15 where $J_{H_2}^{A \rightarrow C}$ is the hydrogen permeation rate, K_{H_2} is the hydrogen permeability coefficient, $P_{H_2}^A$ is the hydrogen partial pressure at the anode side and L is the membrane thickness:

$$J_{H_2}^{A \rightarrow C} = K_{H_2} \times \frac{P_{H_2}^A}{L} \quad (2.15)$$

The hydrogen concentration gradient across the membrane is the driving force for the hydrogen to pass from anode to cathode, illustrating that the increase in the partial pressure of hydrogen on the anode side will increase the hydrogen permeation rate (44). Therefore, the partial pressure gradient of hydrogen is considered as the local variation of hydrogen crossover. Also, hydrogen crossover rate has a close relationship with gas humidity, temperature, membrane thickness and clamping pressure (45). Several methods focusing on the membrane modification have been developed to reduce fuel crossover in HT-PEMFCs, such as fabricating dense membranes, constructing highly proton conductive membranes but with less acid uptake to get reduced volume swelling, preparing the composite membrane to increase the fuel pathway through the membranes (46), or adding a barrier layer such as single layer graphene (47) or other multiple layers onto the membrane surface (17).

2.3.3 Linear sweep voltammetry

The membrane aids proton conduction and serves as an electron insulator between anode and the cathode. Meanwhile, the membrane should ideally be impermeable to gases but it is unavoidable that some gases can move through the membrane and reach the other side. When oxygen and hydrogen permeate through the membrane to react with each other, the fuel gas cannot be efficiently utilized and the formation of radicals can cause cell performance deterioration. Therefore, the measurement of hydrogen crossover is vital important for the fundamental

understanding and practical mitigation of membrane failure and fuel cell degradation (17). Numerous techniques have been developed to measure hydrogen crossover of PEMs such as using volumetric method, gas chromatography, cyclic voltammetry, mass spectrometry or linear sweep voltammetry (LSV) (48).

LSV is the most commonly, simplest and the most efficient technique to measure hydrogen crossover. In this technique, hydrogen and nitrogen are supplied to anode and cathode, respectively, whilst the scan potential usually ranges from 0 up to 0.8 V because higher scan voltages will lead to Pt oxidation (49). The LSV experimental procedure involves controlling the potential of the fuel cell cathode (working electrode) and monitoring any electrochemical activity that occurs in the form of a current. Since nitrogen is the only substance introduced into the cathode side, any current generated in the given potential range is solely attributed to the electrochemical oxidation of hydrogen that crosses through the membrane from the anode to cathode. The hydrogen crossover current typically increases with the scan potential and rapidly reaches a limiting value when the potential grows to around 300 mV (50). At this value all permeated hydrogen is instantaneously oxidized due to the high overpotential applied. Based on the limiting current, the hydrogen flux can be calculated using Faraday's law (49). However, LSV suffers from some weaknesses which affects the accuracy of measurements. For example, the scan rate is limited to 5 mV/s or lower because higher scan rates give rise to larger inconsistent measurement curves as shown in Fig. 2.6 (red and green solid LSV curves) where the deviations exist in 4 mV/s or 2 mV/s scan rates (48). In addition, as the short-circuit resistance (some electrons can pass through the membrane to generate short-circuit current and short-circuit resistance) of the membrane has some impacts on the current response in LSV curve, the current response at about 0.4 V is usually regarded as the final measurement of hydrogen crossover current as shown in Fig. 2.6 red dashed line. The crossover test shows the synthetic effect of hydrogen crossover and the electrical short. The level of hydrogen diffusion is given by the flat portion of the curve and the level of electrical short is calculated from the sloping linear relationship between the applied voltage and the measured current, specifically the measured current between 0.3 V and 0.8 V (51). Therefore, after considering the impact of short-circuit resistance, the measured actual value of hydrogen crossover current (blue dashed line) is smaller than the original red dashed line in Fig. 2.6.

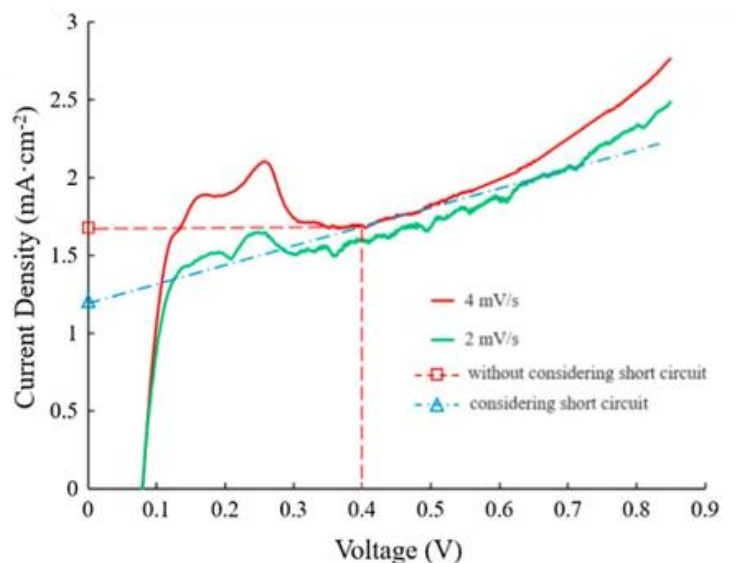


Fig. 2.6. Measurements of hydrogen crossover current by LSV at different scan rates (48).

In this work, LSV was tested by the Gamry 5000E potentiostat when the hydrogen and nitrogen were fed to anode and cathode at the flow rate of 100 mL/min, respectively. The cathode works as the working electrode at 1 mV/s from 0 to 0.7 V against anode.

2.3.4 Electrochemical impedance spectroscopy

Electrochemical reactions in HT-PEMFCs consist of electron transfer at electrode surface. These reactions mainly relate to electrolyte resistance, adsorption of electroactive species, charge transfer at electrode surface, and mass transfer from the bulk solution to the electrode surface. The whole reaction process can be considered as an electric circuit, including resistance, capacitors, or constant phase elements combined in parallel or in series.

Electrochemical impedance spectroscopy (EIS) is an effective technique to extract each component in an electric circuit using a potentiostat to apply AC impedance in electrochemical systems. In this technique, a small AC amplitude perturbation is added to a constant direct current signal with a changing frequency. By scanning the frequency, the impedance change can be recorded and each component value can be obtained.

The equivalent circuit should represent the electrochemical system and give the best possible match between the model's impedance and the measured impedance of the system. The most popular electric circuit for a simple electrochemical reaction is the Randles circuit model, which includes electrolyte resistance, charge-transfer resistance at the electrode/electrolyte interface, double-layer capacitance, and mass transfer resistance. A lot of powerful numerical analysis software such as Zview or Gamry Echem Analyst can be employed to fit the EIS spectra and give the best values for equivalent circuit parameters. Some common equivalent circuit elements for an electrochemical system are listed in Table 2.2 (52).

Table 2.2. Common circuit elements used in equivalent circuit models

Equivalent element	Name	Parameters	Units
R	Resistance	R	Ω
C	Capacitance	C	$F=s/\Omega$
L	Inductance	L	$H=\Omega \text{ s}$
W	Infinite Warburg	σ	$\Omega/(s)^{1/2}$
BW	Finite Warburg (Bounded Warburg)	σ R_0	$\Omega/(s)^{1/2}$ Ω
CPE	Constant phase element (CPE)	q n	s^n/Ω 1
BCPE	Bounded CPE	q n R_0	s^n/Ω 1 Ω

As shown in Fig. 2.7, an example of Nyquist plot of HT-PEMFC and the equivalent circuit of the MEA are presented. As the Nyquist plot is not the circuit presenting an ideal capacitor (53), CPE was used in this case. At high frequencies, the imaginary impedance (at 10000 Hz) is around 0.22 $\text{ohm}\cdot\text{cm}^2$ which equals to the electrolyte resistance R_m , while the resistance at low frequency (0.1 Hz) is the sum of R_m and charge transfer resistance R_{ct} . However, the analysis of the impedance data can still be troublesome, because specialized electrochemical processes such as Warburg diffusion or adsorption might contribute to the impedance to further complicate the situation.

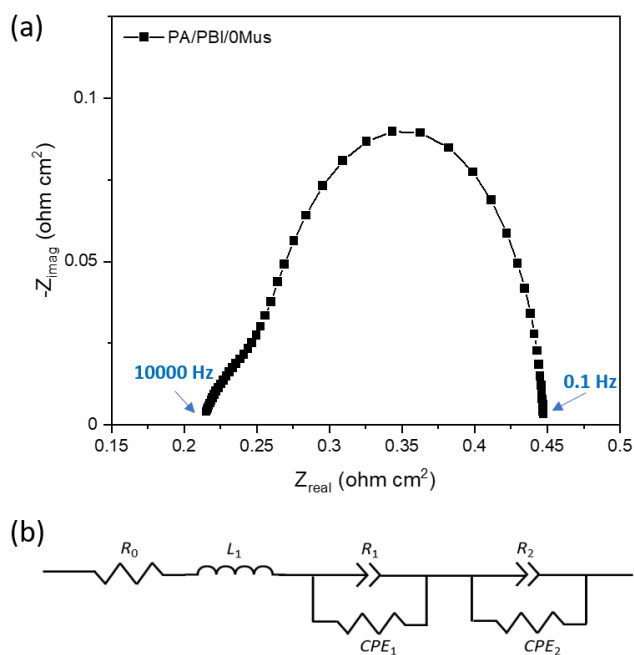


Fig. 2.7. (a) Nyquist plot for a MEA using PA doped PBI without muscovite at 0.6 A and 150 °C, and (b) equivalent circuit used to fit the Nyquist plots (R_0 and L_1 are the membrane resistance and inductance of the cell, respectively; R_1 and CPE_1 are the anode charge transfer resistance and a constant phase element at high frequency, respectively; R_2 is the sum of cathode charge transfer resistance and mass transfer resistance, while CPE_2 is a constant phase element at low frequency) (46).

2.3.5 Durability

Durability is the ability of a PEMFC or stack to resist permanent change in performance over time. Degradation does not lead to catastrophic failure but simply to a decrease in performance that is not recoverable or reversible due to some aging problems such as loss of electrochemical surface area, carbon corrosion, phosphoric acid loss, or membrane degradation. Several methods have been developed to measure fuel cell durability, including operating fuel cell in steady-state (constant voltage or current) or accelerated conditions.

Steady-state tests can be used to examine degradation rate and degradation mechanisms of components under steady-state conditions. Measurements of polarization curves, membrane resistance, hydrogen crossover, and electrochemical surface area can be performed in situ periodically during the durability test to measure performance changes as a function of time. Although the steady-state durability test is straightforward, this technique is inconvenient for large-scale applications as it is time-consuming and expensive.

Accelerated stress test (AST) is an accelerated experimental technique for PEMFCs to simulate the actual driving cycles or to accelerate the degradation. Compared with the long-term operation at constant load, AST is running the fuel cell at a periodical change of load which represents higher stress for PEMFCs and induces performance losses in less time. For the actual PEMFC operation in vehicular applications, fuel cells may be subject to frequent start-up-shutdown cycles, dynamic load responses, idling, accelerating, fuel rich or starvation conditions, or cold start (54), hence, AST is more suitable to estimate the cell performance for the development of actual PEMFCs. Besides the assessment of accelerated degradation in shorter time, another advantage of AST is to obtain knowledge about the influences of test conditions on ageing mechanisms by provoking degradation in a controlled way. For instance, running a HT-PEMFC at high current densities (the fuel cell is operated 16 minutes at 1.0 A cm^{-2} , 4 minutes at 0.6 A cm^{-2} and every 6 h 10 minutes at 0.0 A cm^{-2}) can cause strong electrolyte leaching to test the phosphoric acid retention ability of HT-PEMs in a short time (55). Also, Potential cycling (the fuel cell is cycled between 0.5 V and 0.9 V with 3 min dwelling time for each voltage) was reported to evaluate the stability of platinum and carbon support material of the electrode in HT-PEMFCs (56).

In this work, both steady-state test and AST will be used to evaluate the performance of HT-PEMFCs. The steady-state test will be employed to evaluate the decay rate of the PES-PVP composite membranes in chapter 5-7, while the AST will be applied to explore the phosphoric acid retention in PBI membranes which will be introduced in chapter 8.

2.4 Fuel cell components

The core component of a PEMFC is the membrane electrode assembly (MEA) which contains a proton exchange membrane in the middle sandwiched by anode and cathode. The electrode consists of catalyst layer and gas diffusion layer as shown in Fig. 2.8. As a key component in PEMFC, the PEM is a semi-permeable membrane that separates the reactant gases and transports protons. The bipolar plates are combined on both sides of the MEA with the reactants (hydrogen and oxygen) supplied to the anode and cathode sides, respectively. In this section, each component of fuel cells including bipolar plates, gas diffusion layer, catalyst layer and proton exchange membrane will be introduced.

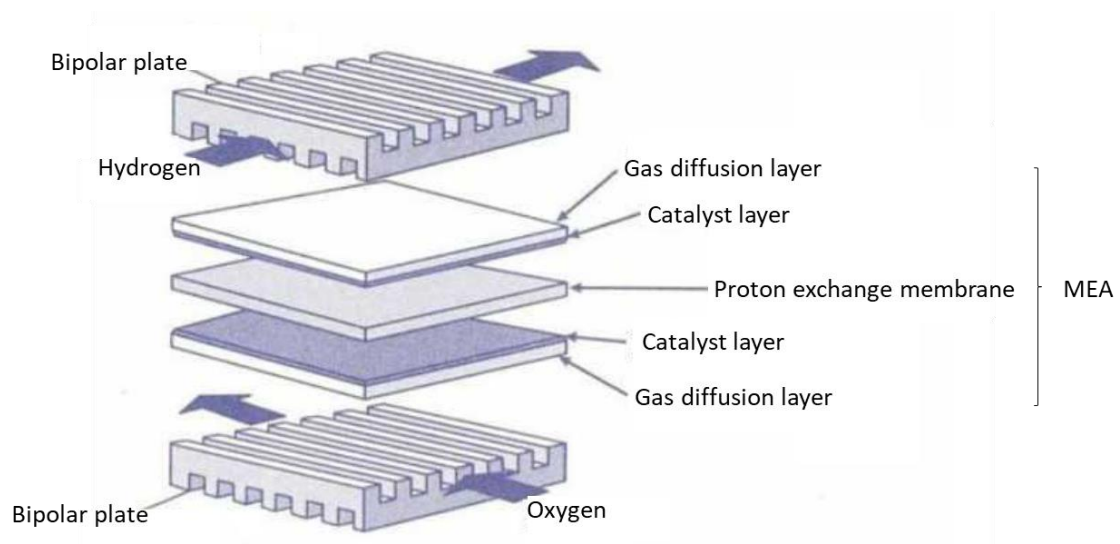


Fig. 2.8. Diagram of the cell configuration of a PEMFC

In terms of the preparation of MEA, three different methods (catalyst-coated substrate (CCS), catalyst-coated membrane (CCM), and decal-transfer methods) are categorized depending on the substrate used, as shown in Fig. 2.9 (57). CCS is to deposit the catalyst layer onto the substrate of gas diffusion layer. This method is simple and suitable for mass production, however, it may lead to poor contact between PEM and the catalyst layer. Another method is CCM which directly sprays the catalyst layer onto the membrane to get improved interface contact between PEM and the catalyst layer. However, the hydration/dehydration of PEM may cause membrane creep and further lead to the damage to catalyst layer in the CCM method to get a poor durability. Another

method is to prepare a catalyst layer on a Teflon sheet and transfer it onto the PEM using hot-pressing, which is known as the decal-transfer method.

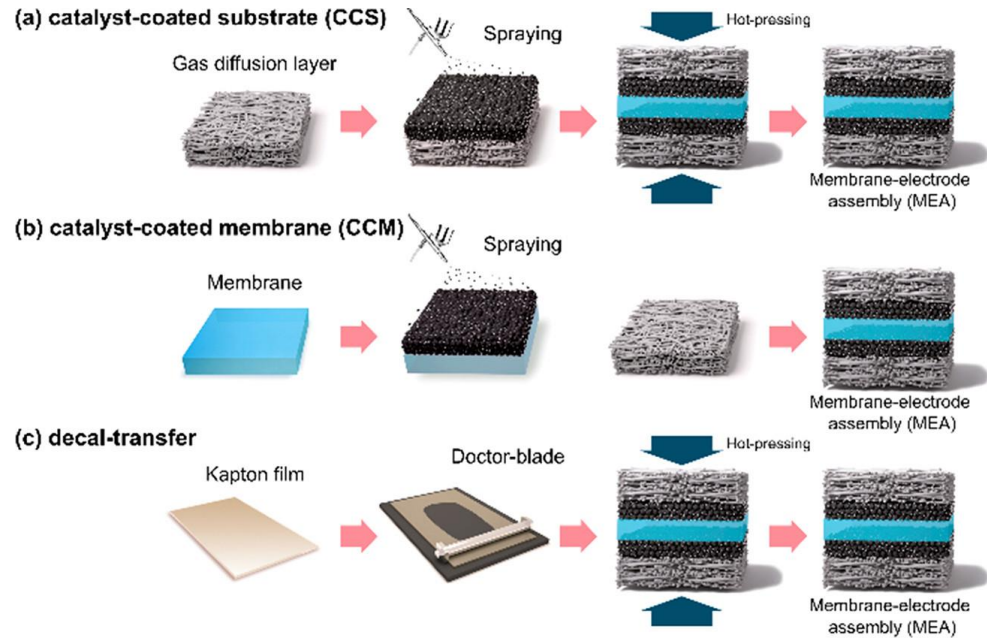


Fig. 2.9. Schematic representation of conventional methods: (a) CCS, (b) CCM, and (c) decal-transfer (57).

2.4.1 Bipolar plates

As a critical element of PEMFC, bipolar plates perform series of functions such as conveying electrons to the external circuit, providing mechanical support for membrane electrode assembly and the whole fuel cell stack (a number of fuel cells stacked together using bipolar plates where anode is on one side and the cathode is on the other as shown in Fig. 2.8), transporting reaction gases to anode and cathode, and removing products and heat from the cell. According to the type of base material, bipolar plates are mainly divided into graphite bipolar plates, metallic bipolar plates and composite bipolar plates (58). Graphite plates have been utilized for bipolar plates due to their high thermal and electrical conductivity, low density and good chemical resistance. Graphite is suitable to the stationary applications which need longevity other than compactness. However, for the portable or transportation applications where the compactness and sufficient mechanical strength are required, the brittle and porous graphite bipolar plates are volume-consuming and permeable which cannot provide enough mechanical support. Besides, the manufacturing process of graphite bipolar plates is time-consuming and expensive, limiting its mass production. Therefore, alternative materials such as carbon-polymer composites and metals have been paid attention.

Carbon-polymer composites are made of resin matrices with conductive fillers (carbon black, carbon fibre and carbon nanotubes). The composite bipolar plates can provide better mechanical

stability and impermeable properties than graphite bipolar plates. However, the balance between conductivity and mechanical strength still limits the further commercialization. Another approach is the metal bipolar plate which usually contains stainless steel, titanium, nickel, aluminium, copper or their alloys. The physical and chemical properties, and manufacturability of the metal bipolar plates benefit their widely uses in global automotive fuel cell industry. The drawback of metal plates is their low corrosion resistance to acid, which can be overcome by protective coatings, such as conductive polymer films, metal nitride/carbide films and noble metal films (59). In this work, as the durability test is needed and the compactness is not the priority, the graphite bipolar plate is chosen in the whole experiments.

Another important design is the flow field which is cut into the bipolar plate to create pathways for reactants and products. The flow field design is highly related to cathode water flooding and overall performance. In PEMFCs, according to the flow channel designs, dimensions, shape and size of the rib/channel, and effective area of the flow channel, there are the common used flow fields such as single straight, parallel, serpentine, interdigitated, pin, spiral, cylindrical, radial, natural inspired, square tubular and fractal flow field designs as shown in Fig. 2.10 (60). The most common used serpentine and interdigitated flow fields perform better in water removal and uniform water distribution, but high pressure drop and uneven reactants distribution may increase mass transfer resistance. For other designs such as parallel and pin type, dead areas are easily formed due to insufficient or uneven water discharging. Recently, the 3D flow field has been a hot topic because it promotes uniform water distribution in the membrane to prevent water flooding. Future research needs more explorations to reduce the costs of the manufacturing and design (59).

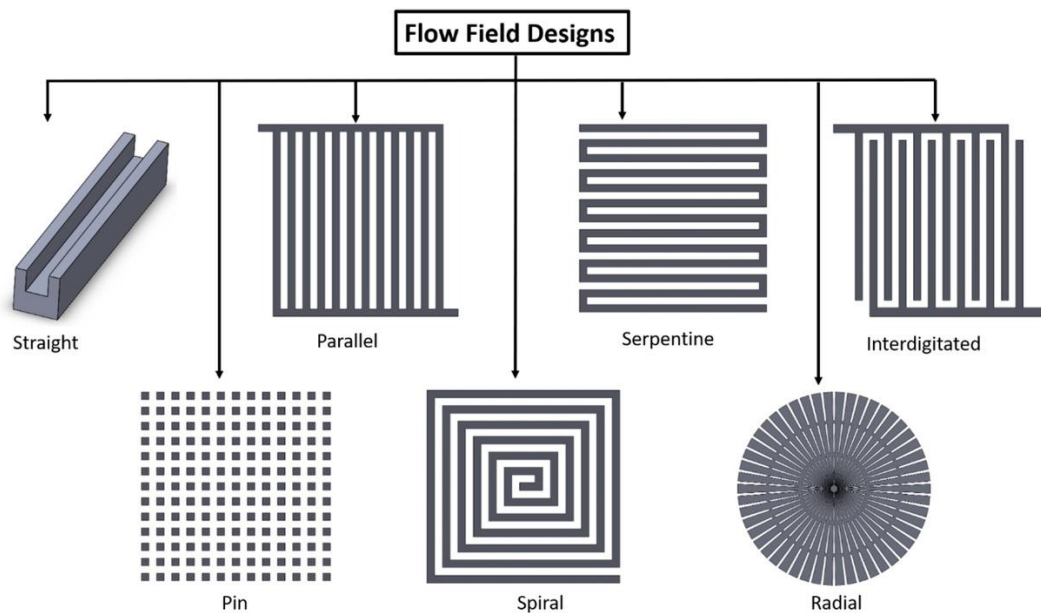


Fig. 2.10. Flow field designs used in the PEMFC (60).

2.4.2 Gas diffusion layer

As one of the crucial components in PEMFCs, the gas diffusion layer (GDL) is designed to distribute the reactants efficiently, drive the products (water) away from catalyst layer to prevent electrode flooding, and allow electron transport. Traditional GDL contains a microporous layer (MPL) and a macroporous substrate (such as carbon paper or carbon cloth). A recent application reported the GDL without using MPL in HT-PEMFCs works better than the conventional GDL as shown in Fig. 2.11 (61). Due to the existence of water vapor at high temperature and the use of high catalyst loading, the MPL is not essential in HT-PEMFCs. Also, as the catalysts are mainly deposited onto the stems and junctions of the carbon paper, the elimination of the MPL can result in a 3D interlaced micropore/macropore composite structure in the catalyst layer, facilitating gas transport and catalyst utilization to get an improved cell performance. In our work, the objective does not focus on the modification of GDL, therefore, the traditional GDL as shown in Fig. 2.11a will be employed.

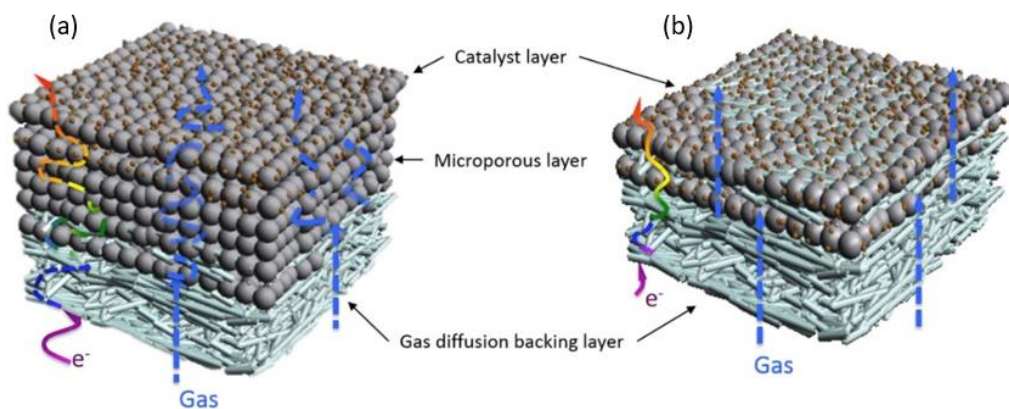


Fig. 2.11. Conceptual diagrams of the conventional GDE with MPL (a) and the GDE eliminated MPL (b) (61).

The MPL is a mixture of carbon black and polytetrafluoroethylene (PTFE) where the PTFE acts as binder and hydrophobic agent to get a good water management. The macroporous substrate is usually made from the carbon fibres and then treated with a hydrophobic agent such as PTFE, polyvinylidene fluoride, and fluorinated ethylene propylene to provide hydrophobicity. Various ways, dipping, spraying, and brushing, have been used to coating hydrophobic agents into the MPL. A representing hydrophobic treatment is dipping the MPL into a suspension which contains hydrophobic polymers, followed by drying and heating above 350 °C to remove surfactants and uniformly distribute the hydrophobic polymers (62). The amount of hydrophobic agent throughout the MPL is controlled by dipping time and concentration of the suspension. Until now, three commercialized carbon paper or cloth are the commonly used MPL in PEMFCs as shown in Fig. 2.12.

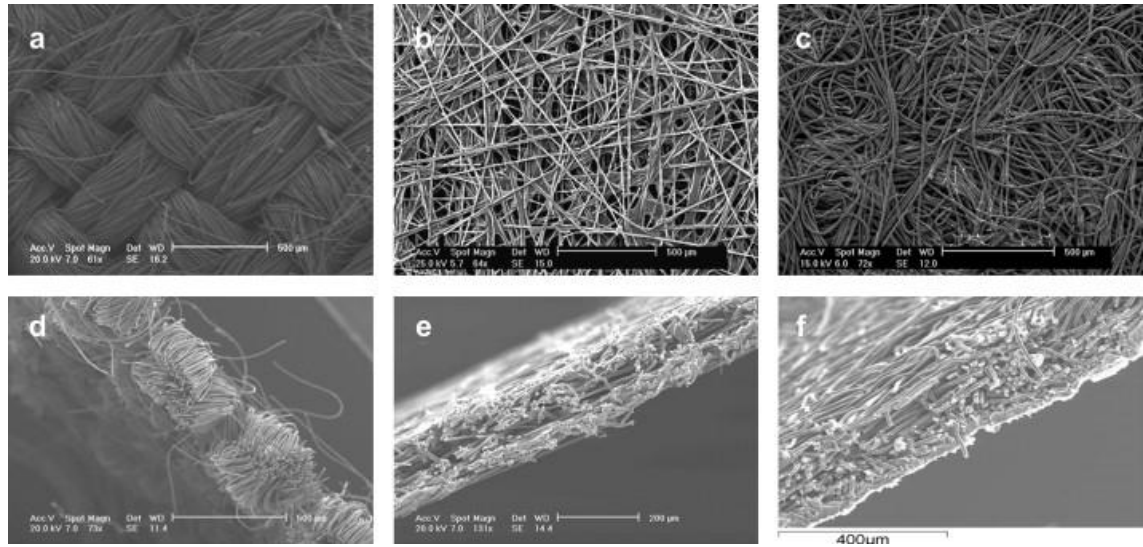


Fig. 2.12. SEM images of GDL; surface and edge views of (a) and (d) woven fibres in carbon cloth (Ballard 1071HCB), (b) and (e) straight stretched fibres in carbon paper (Toray H-060), (c) and (f) felt/spaghetti fibres in carbon paper (Freudenberg C2) (63).

Conventional MPL materials are comprised of carbon paper or cloth with random structure which can be considered to be an uncontrolled management of both electron and fluid transport either to or from the catalyst layer. This uncontrolled transport can result in heterogeneous reaction rates under the rib and channel regions and ultimately causes a decrease in potential performance due to the flooding in the GDL. This will occupy pores for oxygen diffusion or resistance to electron flow. Recent work was developed by Niblett et al. (64) who designed two ordered microstructures (Fig. 2.13a and b) and simulated the pore-scale single phase flow in the void space and electron transport in the solid space in structured and unstructured MPL. A more homogeneous transfer of both electrons and fluids was observed in the MPL with ordered structure, allowing for higher current densities being able to be reached at the same voltage used in a conventional MPL (Fig. 2.13c). Future work needs to focus on the design of ordered MPLs or GDLs to optimize the reactant and product pathways, and reduce electronic resistance.

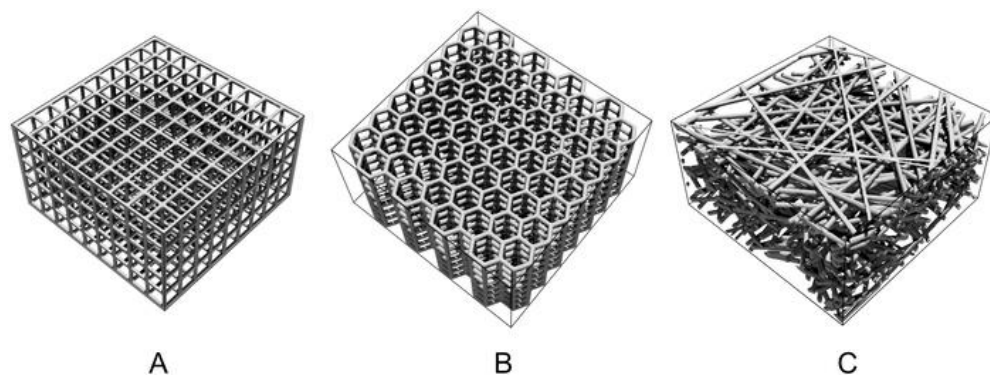


Fig. 2.13. The cubic lattice (isotropic) (A), hex lattice (anisotropic) (B) and carbon paper (C) of MPL (64).

2.4.3 Catalyst layer

2.4.3.1 Catalyst

Before introducing the recent advances in catalysts, the basic information about how the catalyst works will be firstly explained. As shown in Fig. 2.14, at the preliminary stage, the reactants are stable without any chemical reactions. After a certain amount of activation energy is applied (such as changing temperature or pressure), the reaction will proceed using the catalyst. However, if there are no catalyst, the required activation energy will be larger than the reaction using the catalyst.

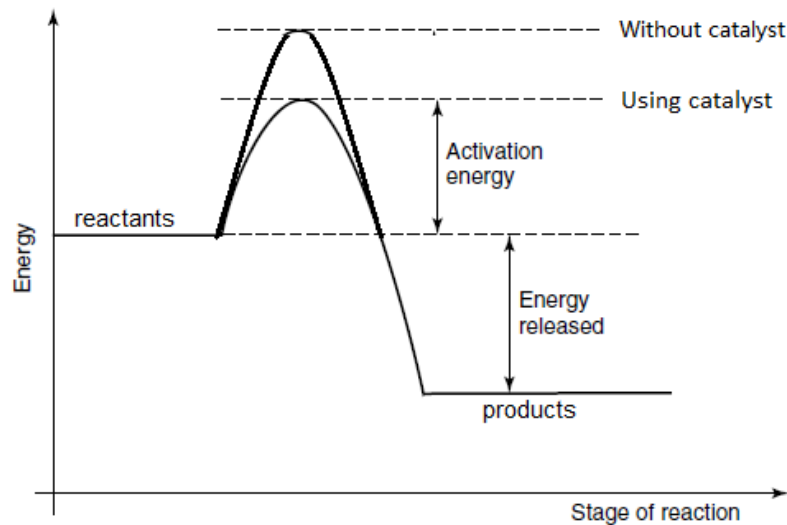


Fig. 2.14. Energy diagram for an exothermic reaction with and without using catalyst

As illustrated in Fig. 2.15 which shows an example of cathode electrode, the conventional catalyst is a porous media with heterogeneous structure and multiple constituents, consisting of catalyst support, platinum particles, ionomer and void space, while the proton conducting media are perfluorosulfonic acid ionomer (such as Nafion or Aquivion) in LT-PEMFCs or phosphoric acid in HT-PEMFCs. Multiple transport processes simultaneously occur in the catalyst layer, including oxygen transport in the void space and oxygen dissolution in the ionomer, proton migration in the ionomer, fuel and electron conduction in the connected carbon support, and the reactions at the triple-phase boundary. However, the fuel cell catalyst usually faces two major challenges (high cost and catalyst degradation), limiting the large-scale deployment of fuel cells.

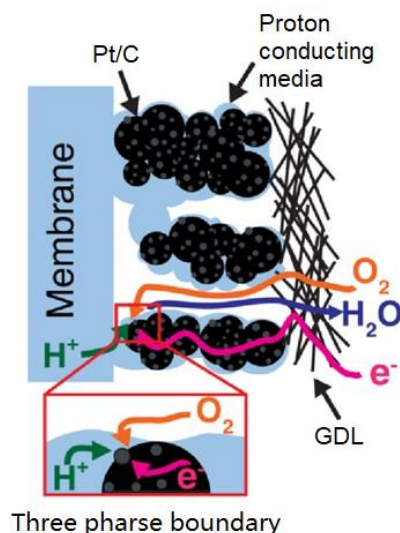


Fig. 2.15. Schematic representation of catalyst layer.

In terms of reducing the cost of catalysts, several approaches have been employed such as decreasing the usage of platinum group metals (PGM) by alloying Pt with a first-row transition metal (such as PtNi and PtCo (65, 66)), and developing PGM-free catalysts to completely replace platinum with earth-abundant materials (M-N-C, M stands for Fe, Co, Mn or other transition metals, N is nitrogen and C is carbon element (67)). Incorporating first-row transition metals with a smaller atomic radius in the Pt-based alloy brings beneficial strain and alloy effects, which can weaken O_2 /intermediates adsorption and thus improve intrinsic oxygen reduction reaction activity. For the PGM-free M-N-C catalyst, the nitrogen coordinated single metal sites which are atomically dispersed throughout the carbon can catalyse the oxygen reduction reaction using a small amount of catalysts. Another benefit of M-N-C is that Pt will be more stable with strengthened metal-support interactions (66).

In terms of catalyst degradation, Pt dissolution and carbon corrosion have been revealed as the primary degradation mechanisms. They can initiate secondary degradation processes such as Ostwald ripening, particle migration, agglomeration and particle detachment (68). All those mechanisms lead to a decrease in the electrochemically active surface area, which typically results in a lower electrode activity and power losses in PEMFCs. Several approaches have been applied to overcome this drawback and enrich the stability and activity of electrocatalysts, including replacing the carbon-based support materials using CNT, graphene, carbon nanofiber, high surface area carbon, and electronic conductive metal oxide support (metal-organic frameworks, carbon/metal oxide composite supports, or sub-oxide support) (69, 70). Due to their resistance to carbon corrosion and more available and stable sites for Pt anchoring, these novel catalyst supports can alleviate the deactivation of Pt catalyst to get stable catalyst performance.

2.4.3.2 Catalyst binder

In HT-PEMFCs, phosphoric acid from the membrane acts as a proton conductor and is an essential component of the triple-phase boundary in HT-PEMFCs. If the amount of phosphoric acid is insufficient in the catalyst layer, the performance of the fuel cell is lowered due to reduced triple-phase boundary formation. Conversely, if there is excess phosphoric acids in the catalyst layer, Pt particles will be covered by phosphoric acid, thereby blocking their pores and obstructing gas transportation. Herein, both the distribution of phosphoric acid and the formed structural and pore network must be uniform within the catalyst layer to ensure the high efficiency of the triple-phase boundary. To improve the distribution of phosphoric acid and the formation of the structural network in the catalyst layer, polymeric binders can be added. Different from LT-PEMFCs which usually use Nafion as catalyst binder to act as proton conducting media to conduct protons, catalyst binders in HT-PEMFCs include hydrophobic (PTFE and PVDF) or hydrophilic polymeric binders (polybenzimidazole and polyvinylpyrrolidone) (71-73). It was found the hydrophilic binder in HT-PEMFCs can easily result in phosphoric acid flooding, low gas permeability and further interrupt the catalyst reactions (71), while the hydrophobic polymeric binder can interact with catalysts and provide hydrophobic regions within the catalyst layer through which the reactant gas can access the catalyst sites. The binder controls the triple-phase boundary between electrolyte (phosphoric acid), catalyst and reactant gases.

Among the various hydrophobic binders reported to date, PTFE is widely used in HT-PEMFCs due to its high chemical and thermal stability, and the hydrophobicity. Recent work investigated the PTFE dispersion (74) and the optimal weight ratio between PTFE and carbon (73) in the catalyst layer. As shown in Fig. 2.16, the uneven distribution of PTFE in catalyst layer can lead to reduced triple-phase boundary and cell performance, illustrating that the homogeneous dispersion and optimal amount of PTFE in catalyst layer is vital important.

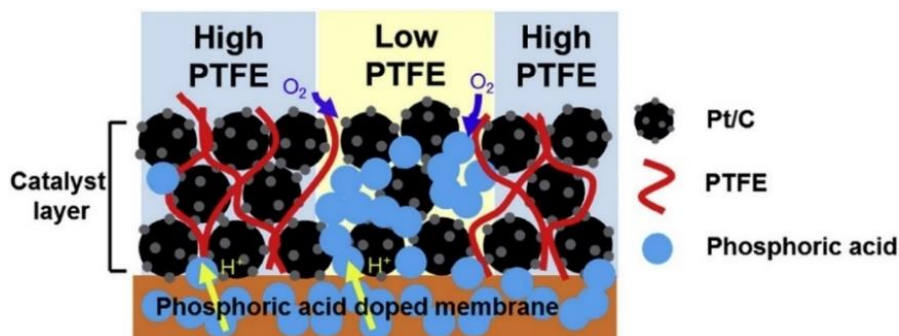


Fig. 2.16. Schematic representation of a non-uniformly dispersed catalyst layer (74).

2.4.4 Proton exchange membranes

According to the operating temperature of PEMFCs, there are two types of PEMFCs, low-temperature PEMFCs (LT-PEMFCs) running at the temperature less than 100 °C, and high-

temperature PEMFCs (HT-PEMFCs) running at 100-200 °C. The hydrocarbon or perfluorosulfonic acid proton exchange membranes (Nafion) are usually used as electrolyte membranes in LT-PEMFCs. Proton transfer in low-temperature proton exchange membranes (LT-PEMs) usually follows two mechanisms (vehicle and Grotthuss mechanism) as shown in Fig. 2.17a (75). As the membrane has hydrophobic Teflon backbones and free volume within the polymeric chains, proton transfer through the solid perfluorinated membrane mainly follows the vehicle mechanism where the protons are solvated by water molecules to form H_3O^+ and diffuse through the membrane under hydrated conditions (76). The second faster mechanism (Grotthuss mechanism) in perfluorinated membranes is the proton hopping from one hydrolysed ionic site ($\text{SO}_3^- \text{H}_3\text{O}^+$) to another across the membrane. In the hydrated low-temperature proton exchange membranes, this Grotthuss mechanism has less contribution to the proton conductivity than the vehicle mechanism (77). Nafion has high conductivity, excellent chemical stability, mechanical strength and flexibility, and long-term durability. However, it functions only in a highly hydrated state and its glass transition temperature is limited up to 125 °C (78), therefore, it is limited to operation at temperatures up to around 80 °C under ambient pressure. As such, a humidifier is needed to humidify the gas in LT-PEMFCs. Meanwhile, several challenges such as low CO tolerance and water management limit the further commercialization of LT-PEMs (79).

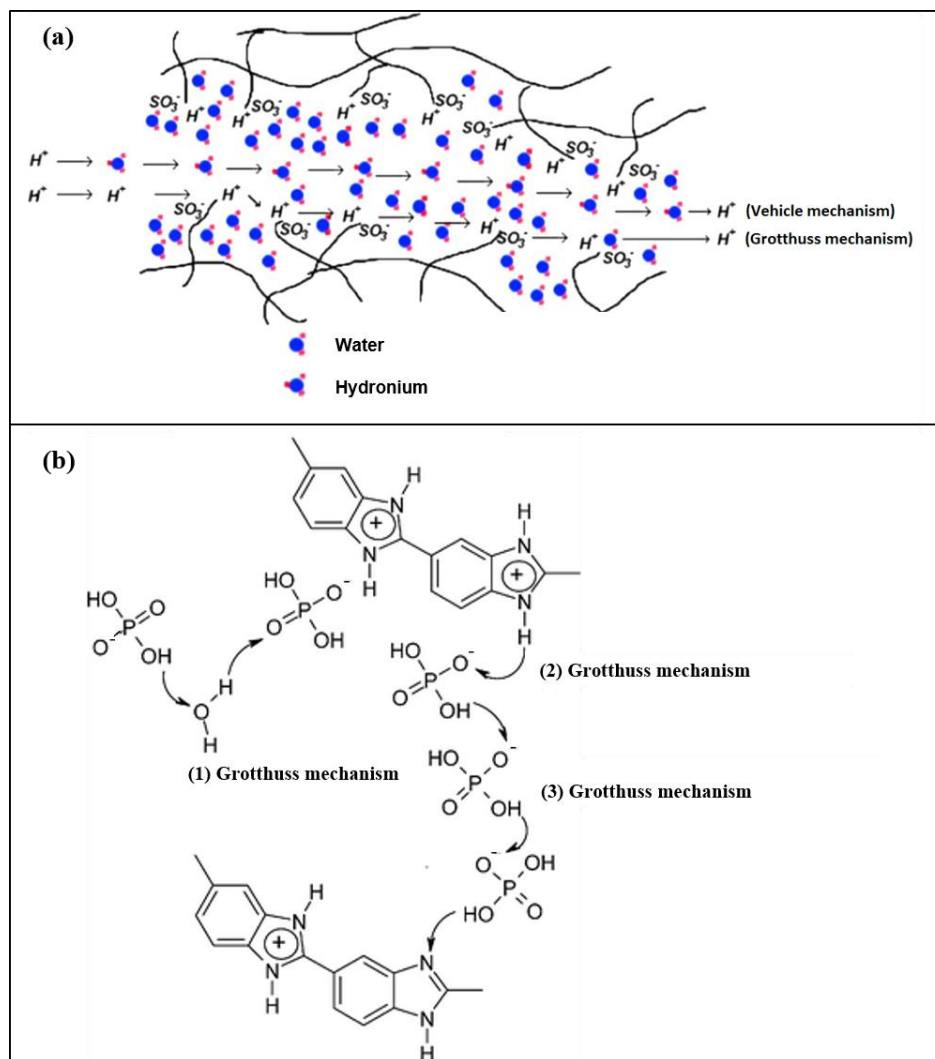
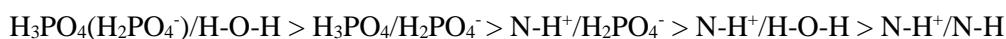


Fig. 2.17. Conductivity mechanism in (a) Nafion and (b) PBI in which (1) stands for acid-water proton transfer, (2) stands for acid-N-H sites proton transfer, and (3) stands for acid-acid proton transfer (79).

PEMFC operating at high temperatures has in recent years been recognized as a promising solution to meet these technical challenges. Treating membrane with low-volatility acids is one method to increase the working temperature of PEMs. Membranes doped with different acids result in enhanced proton conductivities. For instance, Xing et al. (80) discovered that the proton conductivity order in different acids doped polybenzimidazole (PBI) membranes is as follows: $H_2SO_4 > H_3PO_4 > HClO_4 > HNO_3 > HCl$. Although H_2SO_4 has highest proton conducting capability, H_2SO_4 -based PBI membrane depends on the relative humidity (RH) and needs at least 50% RH to achieve the maximum conductivity (81). Therefore, phosphoric acid is chosen as one of the favourable options in HT-PEMFCs that can operate without humidification and dependence on the RH of the system. In the case of HT-PEMFC in this study, the phosphoric acid doped polyethersulfone-polyvinylpyrrolidone (PES-PVP) or polybenzimidazole (PBI) will be used as an electrolyte membrane.

Unlike the proton transfer mechanism in LT-PEMs (more vehicle and less Grotthuss proton transfer), the PA molecules form extensive hydrogen bonding networks offering the rapid Grotthuss mechanism for proton conduction through the proton exchange membranes (HT-PEMs) via the rearrangement of hydrogen bonds between PA molecules (Fig. 2.17b) (14, 82). As HT-PEM is running at 100-200 °C, few water molecules will diffuse through the membranes limiting the vehicle mechanism. This Grotthuss mechanism, which mainly depends on PA molecules without the participation of water molecules, allows the PA doped membranes to work at high temperature. However, the relative humidity might increase the membrane proton conductivity because a faster proton transfer will be observed when the H₂O molecules are involved through Grotthuss mechanism. The proton transfer in PA-doped PBI membrane happens between two molecules (acid-water, acid-acid, or acid-N-H sites) and their proton transferring rate was reported as the following (83):



Therefore, at low acid doping level (ADL), proton transfer mainly happens between the N-H sites and PA anions (N-H⁺/H₂PO₄⁻) due to the high protonation levels of the N-H sites and lack of free acids. At high ADL, the free acids will conduct protons in the way of H₃PO₄/H₂PO₄⁻, while the proton transfer in membrane with a certain RH condition will be in the form of H₃PO₄(H₂PO₄⁻)/H-O-H.

2.5 Limitations of HT-PEMs

Although PA doped membrane offers several benefits compared with LT-PEMFCs, some drawbacks still limit its further commercialization in fuel cell market. The introduction of PA into the membrane improves proton conductivity but at the sacrifice of mechanical strength. In addition, the acid leaching cannot be avoided especially when the polymer chains can undergo oxidative degradation after a long operation time. The weakened interactions between PA molecules and polymer chains will further accelerate the acid loss and degradation of HT-PEMs. Therefore, three main limitations of HT-PEMs, acid leaching, membrane oxidative degradation, and mechanical degradation, will be discussed.

2.5.1 Phosphoric acid leaching

Even though PA molecules are bound with the polymer chains via hydrogen bonds, acid loss will inevitably occur in an operating HT-PEMFC (83). This will not only have lower acid doping level and proton conductivity, but the membrane with severe acid loss will also lead to the degradation and corrosion of fuel cell components and further deteriorate cell performance and shorten cell lifetime (17, 84, 85).

Acid loss mechanisms have been studied and developed for many years. Initially, the acid absorbance mechanism was proposed by Mori et al. (86) in the 1980s: the acid loss occurs because the electrodes can retain PA molecules. Later, Li et al. (87) reported another acid leaching mechanism. They found that the free PA can be washed out of membranes by the produced water. In 2006, Yu et al. (88) discovered that the PA loss from the cathode side at 190 °C was 10 times higher than at 80 °C and 160 °C. Then the steam distillation mechanism was proposed that PA molecules leach out of membrane with water vapor. Very recently, it was reported that PA leaching out of the membrane is caused by the presence of water (89) as the interactions between PA molecules and produced water is stronger than the interactions between PA molecules and basic sites of the polymer chains. Lee et al. (90) further reported that PA loss was due to the polymer's inability to hold water and PA molecules because the membrane polymers have insufficient attractions to water and PA when it's beyond a certain ADL. For instance, the strong interactions between PA molecules and biphosphate-ammonium ion pair in the polymer are able to attract more PA molecules so that PA loss will be reduced even in the presence of water (90). Therefore, enhancing interactions between PA molecules and basic sites in polymer chains provides a better pathway for acid retention in HT-PEMFCs. In addition, Eberhardt et al. (91) reported PA loss is caused by the electrochemical pumping during the operation of fuel cells. PA saturation in the anode gas diffusion layer and flow field facilitates the formation of PA droplets and then result in PA loss. To conclude, PA leaching out of the membranes happens in four ways (16, 91): (i) PA can be pressed out of the membrane during the hot-pressing process when fabricating membrane-electrode assembly (MEA). (ii) High temperature (above 140 °C) leads to the PA evaporation. (iii) The unbound PA molecules leach out of membranes because PA can be extracted by the water. (iv) The electrochemical pumping of hydrogen phosphate ions migrates free PA moving from cathode to anode.

Currently, three major methods have been developed to detect the acid leaching out of the PA doped membranes as shown in Fig. 2.18. The common used one is to hang the PA doped membrane over boiling water or put the membrane under a certain humidity and temperature, and then record the weight loss of the leached acid (89, 92). Another approach is to collect the acid from the exhaust gases and analyse the amount using inductively coupled plasma-optical emission spectroscopy (17, 93). The third one is based on acid-base titration to measure the acid inside the MEA before and after test (94). Other techniques such as energy dispersive X-ray spectroscopy (95), electron probe micro-analysis (96), micro-computed tomography (55) and X-ray tomographic microscopy (97) were also developed to get the acid distribution in MEAs. Since only ex-situ methods have been used to determine the acid retention of membranes, some in-situ methods such as analysing a running HT-PEMFC at a synchrotron source to measure the acid loss may be needed to explore in the future.

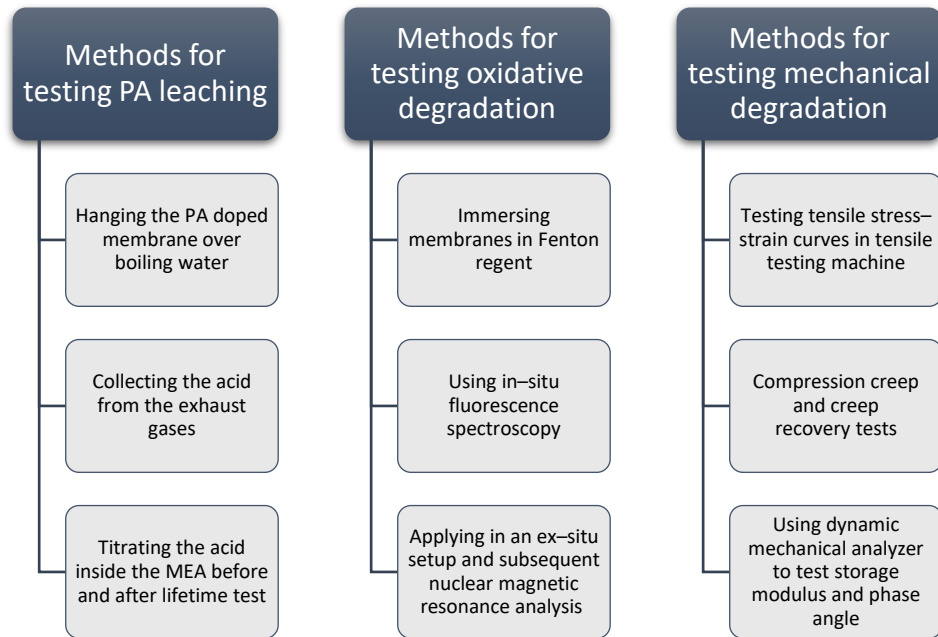


Fig. 2.18. Methods for testing PA leaching, oxidative degradation and mechanical degradation of membranes.

2.5.2 Oxidative degradation

Fuel crossover will result in chemical reactions on the surface of platinum catalyst to produce hydrogen peroxide (H_2O_2) as proposed by Araya et al. (98):



Originating from decomposition of H_2O_2 , radicals (HO and HO_2) can attack C-H bonds in the polymer chains or H-containing terminal groups, thus leading to membrane oxidative degradation (99). In addition, some metal ions (such as Fe^{2+} and Cu^{2+}) which come from the corrosion of end plates or metal bipolar plates will catalyse the radicals and affect the membrane oxidative stability, as shown in following equations (100):



The produced HO and HO₂ radicals can attack the branching points of the polymers, the ether links, or the α -carbon of aromatic groups, thus leading to the opening of imidazole rings or scissions of the macromolecular chains in the HT-PEMs (101). The further formation of membrane thinning or pinholes might cause the failure of fuel cells.

Membrane oxidative degradation can be measured by several in-situ or ex-situ methods as shown in Fig. 2.18 (102-106). Fenton test is the most common ex-situ method to evaluate the oxidative degradation of membranes. The membrane oxidative stability is evaluated by the membrane mass loss before and after being immersed in Fenton reagent (usually containing 3% H₂O₂ and 4 ppm Fe²⁺) where the HO and HO₂ radicals are produced from the decomposition of H₂O₂ catalysed by Fe²⁺. Although the conditions in Fenton reagent do not mimic the situation in fuel cell operation and the membrane can become rigid in a short time at a high degradation rate in the Fenton reagent, the Fenton test is regarded as a facile test to evaluate the chemical stability of PEMs. The membranes that perform well in the Fenton test usually have better oxidative stability during in-situ operating fuel cells.

2.5.3 Mechanical degradation

The intermolecular interactions in the membrane generate the mechanical properties. In PA doped PEMs, the attractive forces between polymer chains and PA molecules include dipole-dipole interaction (hydrogen bonding), induction forces, and dispersion or London forces (a type of van der Waals forces between atoms and molecules), providing the mechanical strength (107-109). As the membrane thickness of LT-PEMFC is large (usually 50-200 μ m), the mechanical degradation of PEMs is not the most critical problem for fuel cell performance (110, 111). Thinner membranes (normally less than 50 μ m) have been developed in HT-PEMFCs to reduce the membrane resistance and improve the proton conductivity. In addition, PA molecules result in volume swelling and increase the spaces between the polymer chains to get weakened intermolecular forces (108), leading to a decreased mechanical strength. Therefore, mechanical degradation in HT-PEMFC is more severe than in LT-PEMFC.

2.5.3.1 Mechanical stability

Many forms including membrane perforations, tears, cracks and pinholes can reflect mechanical stability (101). Perforations or tears usually occur during the fabrication of the membranes as foreign impurities might be introduced and result in uneven pressure in the membranes. In addition, the non-uniform pressure on the membrane during the cell running might lead to membrane defects such as pinholes and cracks, thus resulting in reactant crossover and mixed potential on the electrodes (43). Undesirable exothermic reactions will further generate extra hot spots which might cause the deterioration of mechanical properties such as the softening or melting of the PEM (112). The decrease of membrane mechanical strength will in return

accelerate the fuel crossover and speed up the formation of defects which will lead to further mechanical degradation in a destructive cycle. Also, the different reactant pressures or uneven installing pressures may stretch the membranes (113). Especially at the points where the reactions happen, the formation of defective gasket sealing or hot spots can cause mechanical failure (114).

Three characteristics, tensile strength, Young's modulus, and elongation at break, are usually used to represent membrane mechanical properties. The common method is using the tensile testing machine to measure the mechanical properties (Fig. 2.18). Then the related tensile stress-strain curves will be obtained. In addition, using dynamic mechanical analyser to test the membrane creeping behaviour (115) and mechanical properties with temperatures is another approach to evaluate membrane mechanical properties. Although the conditions in fuel cells cannot be fully repeated, these methods can be an indication for the evaluation of membrane mechanical properties.

2.5.3.2 Dimensional stability

The HT-PEMs usually need to be immersed in phosphoric acid (PA) to get sufficient proton conductivity. This acid doped membrane shows a lowering of the mechanical strength because the acid uptake leads to dimensional changes of the membrane (also named as swelling). The polymer backbone is separated and the intermolecular hydrogen bonding is weakened in acid doped HT-PEMs due to membrane swelling. In addition, membrane swelling can facilitate the access of the peroxide radicals to the macromolecular chains to cause membrane chemical degradation. Phosphoric acid is thus a strong plasticizer and the acid uptake has to be balanced so that the membrane remains sufficiently strong for processing and MEA fabrication. The volume swelling can be calculated according to the equation below,

$$\text{Swelling (\%)} = (V_{\text{doped}} - V_{\text{undoped}})/V_{\text{undoped}} \quad (2.24)$$

where V_{undoped} and V_{doped} are the volume of the undoped and doped membrane, respectively. The volume of the undoped and doped membrane can be calculated from the dimensional changes of the membrane. The dimensional changes of a membrane can be divided into the area, thickness and volume. The area and thickness swelling of the membranes can also be calculated by comparing area and thickness differences before and after PA doping, respectively.

The dimensional stability is also an indicator to justify the membrane property. The membrane acid uptake is related to the amount of acid uptake in membranes and the acids benefit for the proton transfer through membranes. However, if the acid uptake is too much to get a greater membrane swelling, the HT-PEMs will get more radicals attack to the polymer backbones, suffer poor mechanical strength, and face limited durability. The acids are also prone to leach from the membrane to bring some further issues such as acid flooding in the catalyst layer (causing mass transfer resistance), erosions to the carbon support (leading to catalyst losses and increased charge

transfer resistance), and membrane thinning induced by reduced acids (resulting in deteriorated mechanical strength of membranes and durability). Therefore, proper membrane swelling must be controlled in HT-PEMs

2.6 Conclusion to this chapter

In summary, this chapter has introduced the basics of fuel cells, from the history of fuel cells to the electrochemical fundamentals. The structure and function of fuel cell components, bipolar plates, gas diffusion layer, catalyst layer and proton exchange membranes, have also been discussed. Furthermore, the comparison of two kinds of PEMs (LT-PEMs and HT-PEMs) has been further performed: HT-PEMs have been paid more attention than LT-PEMs since HT-PEMs have easier heat and water management and higher carbon monoxide tolerance. Later, current limitations of HT-PEMs (acid leaching, oxidative and mechanical degradation) have been discussed. After the background study on the introduction of fuel cells and HT-PEMs, recent approaches how to tackle these challenges of HT-PEMs will be concluded in the next chapter.

Chapter 3: Literature review

3.1 Introduction

Three major degradation problems of HT-PEMs (acid leaching, chemical and mechanical degradation) have a great impact on the durability of the HT-PEMFCs. As shown in Fig. 3.1, different approaches for the alleviation of HT-PEM degradation problems will be discussed in the following sections. In the part of alleviating phosphoric acid leaching, to prepare trapping sites for the PA molecules or to increase interactions between polymer chains and PA molecules have been discussed. To tackle the oxidative degradation of HT-PEMs, several approaches will be introduced, namely, synthesizing polymer with crosslinked or branched structures to protect polymer backbone from radical attacking, and introducing anti-oxidative groups or inorganic materials into the membranes to alleviate oxidative degradation. In addition, similar strategies such as crosslinking and adding inorganic materials were found to effectively enhance the membrane mechanical strength. Other approaches, blending with another stable polymer and modifying the membrane structures, will also be reviewed in the section of improving membrane mechanical strength.

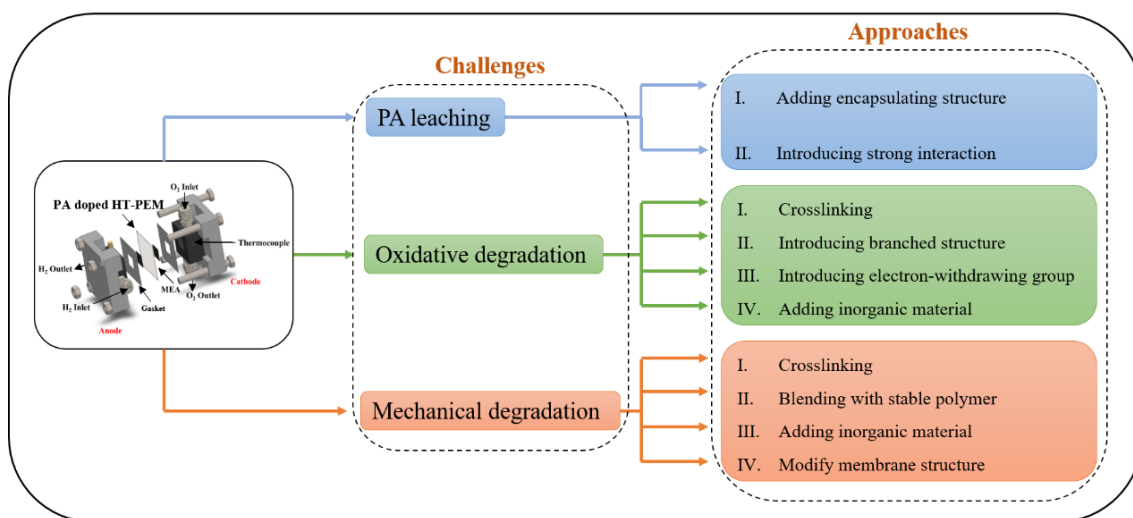


Fig. 3.1. Overview of the topic covered in this chapter.

3.2 Alleviating phosphoric acid leaching

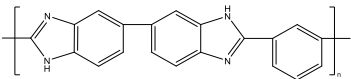
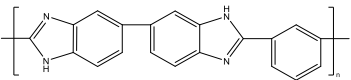
In HT-PEMFCs, PA molecules behave as the proton conductors and connections between electrolyte and electrodes. The unbound PA is distributed throughout the whole MEA in the initial-activation operating stage, while the bound PA will stay in the membrane matrix which connects with the membrane materials to act as the bridge for proton transfer. However, during the operation, the membrane polymers are always being attacked by the radicals produced by fuel crossover (explained in section 2.5.2) and incomplete two-electrode oxygen reduction reactions

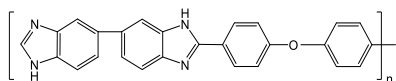
at cathode (see equation 2.2b) (14), which render the macromolecules of polymers unstable and lead to the scissions of polymer chains. Since the chain scission generates terminal groups and small molecules that will be further oxidised by an endpoint oxidation (116), the PA molecules which are interacted with polymer chains will leach out of the membrane. This will lead to the increased membrane resistance for electrochemical reactions, reduce the proton conductivity and mechanical stability, and degrade the membrane durability (117). Recent strategies to reduce PA leaching will be described, and namely: adding an encapsulating structure in the membrane, and introducing strong interactions (such as hydrogen or chemical bonds) between membrane materials and PA molecules. We focus here on the acid retention properties of membranes, and other properties will be reviewed in the later sections.

3.2.1 Adding encapsulating structure in the membrane

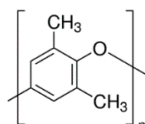
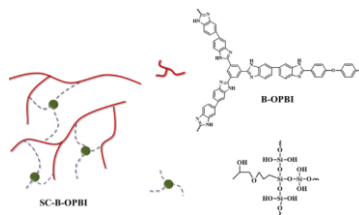
To efficiently reduce PA leaching, many studies have been focused on the introduction of encapsulating structures into the membrane. Table 3.1 displays a summary of reported work about different solutions for PA leaching problems. We will consider here three approaches: (i) preparing multilayer membrane (17, 118). (ii) Crosslinking, through adding crosslinker or conducting other reactions to connect the polymers into a whole continuous network to increase the difficulties of PA permeating through the membrane (16, 94, 119) or trap PA in their networks (120-123). (iii) Incorporating acidic surfactant (124), hygroscopic porous or layered inorganic materials (18, 19, 32, 33, 92, 125-136), which can provide trapping sites or hydrogen bonding for polymer chains to encapsulate PA molecules in the membrane to some extent.

Table 3.1. Recent advances to add encapsulating structure to alleviate the PA leaching

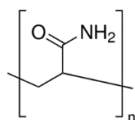
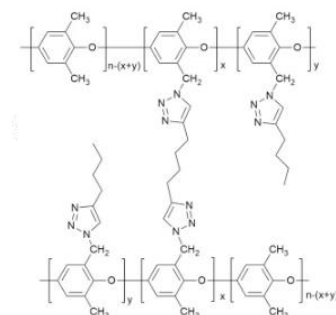
Polymer	Modification	PA retention ability	Ref.
	Multilayer	73 ng/(cm ² ·h) acid loss rate collected from exhaust	(17)
PTFE/GMP/PTFE	Multilayer	21 wt% loss after 1 h operation	(118)
	Crosslinked by thermal curing	91-118 μmol/cm ²	(94)



Branched structure crosslinked by KH560 81.1 wt% remaining at 80 °C and 40% RH after 45 h (16)



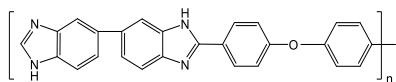
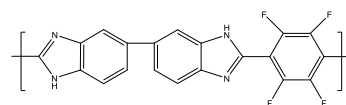
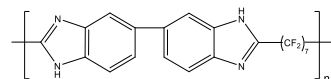
After alkyne-azide cycloaddition, crosslinked by 1,7-octadiyne More than 70% retention in 80 °C and 50% RH for 1 h (119)



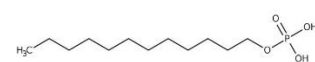
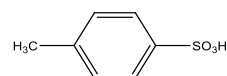
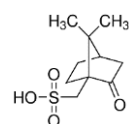
Semi-interpenetrating polymer network Almost no loss under 2.1 × 10⁴ Pa with 100% RH at 80 °C (120-122)

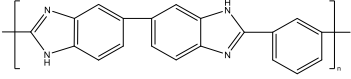
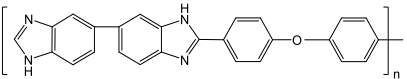
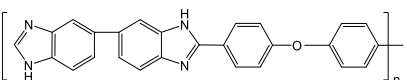
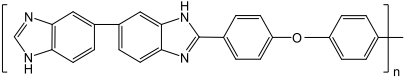
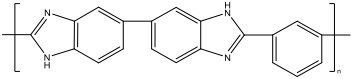
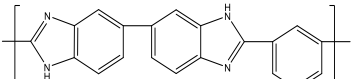
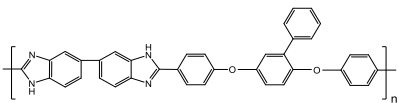
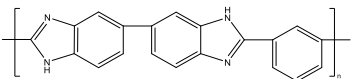
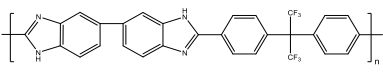
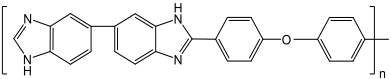
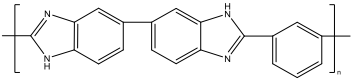
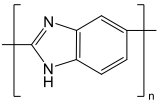
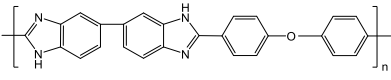
NR

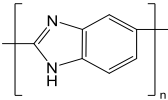
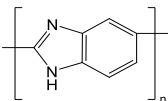
Introducing fluorine into the polymer Less than 45 wt.% loss under vapor condition at 100 °C for 7 h (123)



Adding three different surfactants like molecules Less than 54 wt% loss under vapor condition at 100 °C for 3 h (124)



	Adding perovskite structure BaZrO ₃ nanoparticles	Around 10 wt% remaining in hot water for 2 h	(125)
	Adding TiP ₂ O ₇ ,	More than 29.7 wt% remaining under hot vapor for 5 h	(126)
	Adding TiO ₂ , SiO ₂ , or ZrP	Less than 81.5 wt% loss over hot water for 5 h	(19)
	Adding TiOSO ₄	No obvious loss under water at 80 °C for 2 h	(127)
	Adding TiO ₂	0.6 wt% loss from the exhaust for over 1200 h	(128)
	Adding SiO ₂	Less than 40 wt% loss under water vapor for 7 h	(129)
	Crosslinking and adding SiO ₂	36 wt% loss in water vapor for 6 h	(130)
	Adding PWA-meso-silica	NR	(18)
	Adding zwitterion-coated silica nanoparticle	More than 80 wt% remaining in distilled water for 2 h	(131)
	Adding ionic liquid modified silica	Less than 70 wt% over boiling water for 5 h	(92)
	Adding SiO ₂ and pre-heat-treating MEA	NR ^a	(132, 133)
	Adding graphene oxide	7.8 wt% loss at 80 °C and 95% RH after 48 h	(134)
	Adding clay surfactant modified by CTAB, CPyB and CImiB	Less than 60 wt% loss over boiling water for 3 h	(135)

	Adding sulfonated sepiolite particles	33.3 wt% loss over boiling water for 5 h	(33)
	Incorporating one-dimensional silicon nanorods made from sepiolite	Less than 33 wt% loss over boiling water for 5 h	(32)
PES-PVP	Adding silica nanosheets made from vermiculite	NR	(136)

^aNR = not reported.

One of the strategies to alleviate PA leaching is to prepare multilayer membranes. Lu et al. (118) reported the preparation of three-layered membrane by incorporating a microporous glass fibre (GMF) with nano-porous polytetrafluoroethylene (PTFE) film on each side to provide mechanical support and reduce acid leaching out of the MEA. The comparison of PA leaching between layered membrane and pure GMF membrane was performed by a weighing method. After one-hour test, the layered membrane has only 21 wt% PA loss, which is much less than that of pure GMF membrane (73 wt%). By coating PTFE membranes onto either side of the GMF, the multilayer membrane significantly reduced PA loss. A similar multilayer application was studied by Kannan et al. (17). The layered PBI membrane contained a middle layer with a higher acid content and was sandwiched by two PBI layers as shown in Fig. 3.2a. The middle layer was prepared via direct casting from phosphoric acid to act as an acid reservoir. The PA loss during fuel cell operation was assessed by collecting PA from the exhaust gas. Although the acid collection rates for three-layered and standard membrane are similar, the central layer of the three-layered membrane has higher acid content and allows more acid to loss. Therefore, comparing to the voltage decay of standard single PBI membrane (11-14 $\mu\text{V/h}$ at 180 °C), this three-layered membrane showed a low voltage decay rate (2.3-4.1 $\mu\text{V/h}$ at 180 °C) and outstanding stability (10000 h) as shown in Fig. 3.2b, where L and X stand for linear and crosslinked PBI membranes, respectively, and 1 or 3 are the number of layers.

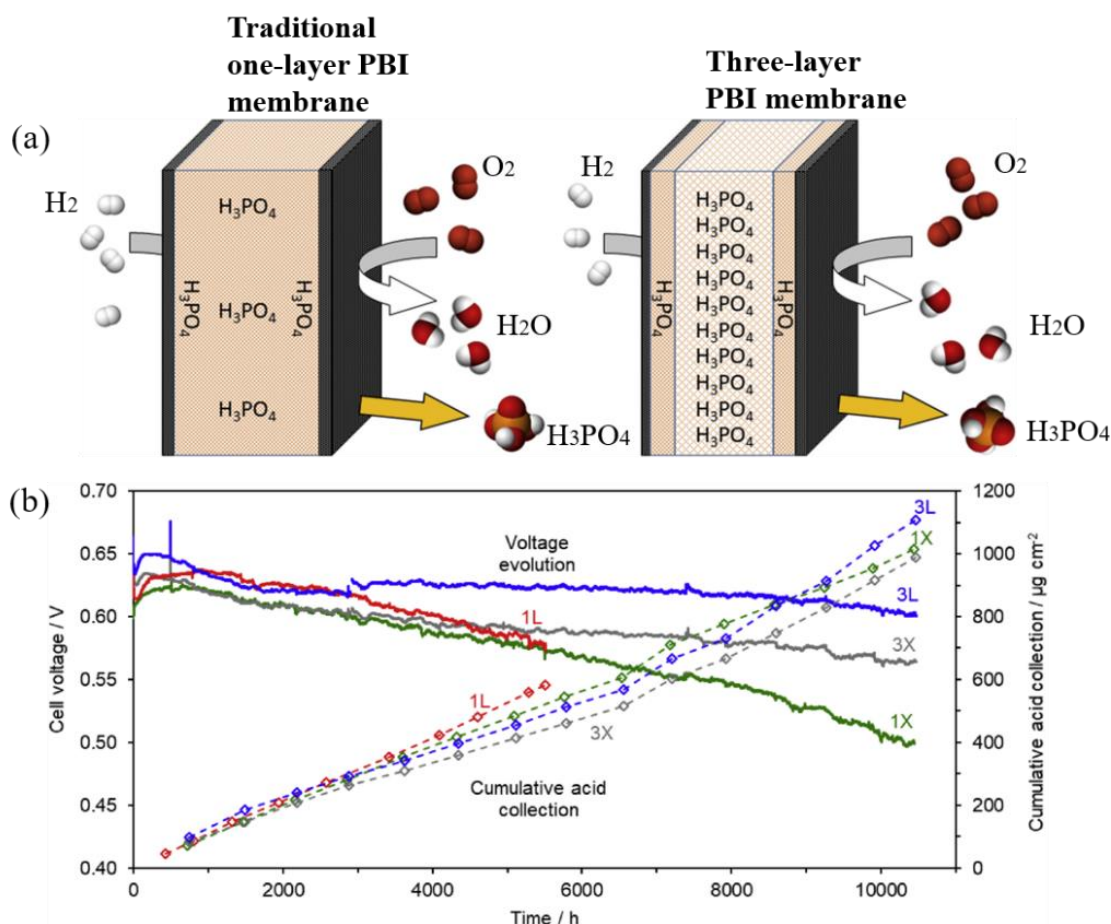


Fig. 3.2. (a) Schematic of PA doped three-layered membrane. (b) Cell voltage and acid collection from the exhaust gases at 200 mA cm^{-2} and 180°C (17).

Sondergaard et al. (94) synthesized thermally crosslinked PBI membranes with the lowest voltage degradation rate ($1.4 \mu\text{V/h}$ within 13000 h), comparing with a pure PBI membrane ($4.6 \mu\text{V/h}$). The acid loss was evaluated using acid-base titration to determine the acid content of the MEAs. The result shows that the thermally treated crosslinked membrane has a lower average acid loss comparing to that of the linear membrane.

Hu et al. (16) recently developed silane-crosslinked branched PBI membrane with improved proton conductivity and acid retention. The acid doped membranes were placed at 80°C and 40% relative humidity (RH), and the mass loss was recorded along the time. After 45 h, the percentage of PA retained in pure poly[2,2'-(p-oxydiphenylene)-5,5'-benzimidazole] (OPBI), branched OPBI, branched OPBI with 5 wt% silane crosslinker ((3-Glycidyloxypropyl)trimethoxysilane, KH560), and branched OPBI with 10 wt% KH560 crosslinker was 66.3%, 69.7%, 76.5%, and 81.1%, respectively. It showed the PA retention ability was improved after branching and silane-crosslinking. This can be explained that the encapsulation of PA molecules inside the branched and silane-crosslinked networks benefits the improvement of acid retention of membranes (16). Similarly, by reacting with 1,7-octadiyne, triazole-containing crosslinked poly(2,6-dimethyl-1,4-

phenylene oxide) (PPO) membrane showed enhanced PA retention ability. The acid retention ability was tested by exposing the membrane to water vapor at 80 °C and 50% RH for 1 h (119). As it becomes difficult for water molecules to penetrate the membrane with crosslinked dense structure, the PA retention ability increases with the degree of crosslinking.

An alternative approach to reduce PA leaching involves polyacrylamide (PAM), which is a stable and highly hygroscopic hydrogel. The acid retention test showed PA molecules are efficiently caged inside the three-dimensional (3D) PAM (120). Due to the 3D framework which can mitigate PA loss, PAM and its derivative hydrogels were applied in several acid-doped HT-PEM applications as shown below: Tang et al. (120, 121) prepared two kinds of semi-interpenetrating polymer network (semi-IPN) hydrogels. One is the PA-imbibed PAM/PAM interpenetrating (IPN) hydrogel (120). Another application is the PAM/poly(vinyl alcohol) semi-IPN in which poly(vinyl alcohol) plays the role to afford mechanical strength (121). By titrating the sample to determine the PA loss of MEAs at 80 °C under 2.1×10^4 Pa with 100% RH, PA content remains unchanged, showing PA molecules are efficiently caged inside the IPN structure without loss. Additionally, Tang et al. (122) also used the microporous PAM hydrogel as a matrix. After PA content was determined by titration with 0.1 M NaOH solution, the unchanged PA content before and after running shows that microporous PAM hydrogel membrane has excellent PA retention ability.

Another PA trapping example is the novel fluorine-containing PBI membranes prepared by Pu et al. (123). Poly(2,2'-(tetrafluoro-p-phenylene)-5,5'-bibenzimidazole) (4F-PBI) and poly(2,2'-tetradecafluoroheptylene-5,5'-bibenzimidazole) (14F-PBI) were synthesized with enhanced processability and chemical stability. In the PA leaching test, acid-doped poly(2,2'-heptylene-5,5'-bibenzimidazole) (Hepta-PBI) which is the reference membrane, 4F-PBI, and 14F-PBI were placed under vapor condition at 100 °C for several hours, and the mass change of membrane was measured. It showed that PA loss in Hepta-PBI is faster than in 4F-PBI and 14F-PBI. This can be explained that the fluorine in 4F-PBI and 14F-PBI weakened the intermolecular forces among their polymer chains, facilitating more free volume to trap PA molecules. It was also found that acid leaching decreases with increasing fluorine content.

Sana et al. (124) reported the preparation of OPBI membrane with addition of three different surfactants, mono-n-dodecyl phosphate (MDP), p-toluenesulfonic acid (PTSA) and camphorsulfonic acid (CSA). Acid leaching tests showed the PA weight loss ratio of OPBI, OPBI/20 wt% MDP membranes, OPBI/20 wt% CSA, and OPBI/20 wt% PTSA were 64%, 54%, 33% and 27%, respectively. The improved acid retention can be explained that the phosphate groups in MDP and sulphonic groups in PTSA and CSA foster the formation of hydrogen bonding

with PA molecules, and the crystallinity and porous morphology of composite membranes can absorb and retain the PA molecules.

Some inorganic additives such as titanium oxide (128, 137, 138) and titanium pyrophosphate (TiP_2O_7) (126), zirconium phosphate (ZrP) (19) and titanium oxysulfate (TiOSO_4) (127) were reported to reduce PA leaching and facilitate proton transfer. For instance, Ooi et al. (126) synthesized TiP_2O_7 by treating TiO_2 with H_3PO_4 and incorporated it into PBI membrane. The acid retention ability of the TiP_2O_7 added PBI membrane was tested using hot water vapor acid leaching method. Due to the strong hygroscopicity of the inorganic materials, the amount of retained acid was improved from 12.8% in pure PBI membrane to 31.2%, 29.7% and 36.32% in PBI with 1 wt% TiP_2O_7 (PBI-1 TiP_2O_7), PBI-2 TiP_2O_7 and PBI-2 TiO_2 , respectively. Additionally, PBI-2 TiP_2O_7 has a higher proton conductivity (2.69 mS/cm) than that of PBI-2 TiO_2 (2.03 mS/cm) at 160 °C under 8 mol ADL, suggesting that the phosphate groups of TiP_2O_7 promote the proton migration across the membrane.

Being inorganic materials with high hygroscopicity, perovskite-structure BaZrO_3 nanoparticles (125), and silicon oxide (19, 129, 130) can effectively trap phosphoric acid and reduce acid leaching. For example, Hooshyari et al. (125) reported that the intermolecular hydrogen bonding between PA molecules and the oxygen sites in BaZrO_3 improved the PA retention. The PA retention was tested by washing the nanocomposite membranes with hot water for 2 h and the weight changes were measured. In addition, the introduction of silica particles which were modified by phosphotungstic acid (18), imidazole groups (139), zwitterion (131), or ionic liquid (92) into the membrane matrices displayed improved acid retention, excellent proton conductivity, and enhanced compatibility with polymer chains. The functional groups on the silica can form ionic bonds with PA molecules, while the capillary forces among the silica nanospheres can trap or hold more PA molecules, thus alleviate acid leaching. Another interesting application is to incorporate silica oxide into the PBI membranes and pre-treat the MEA at 250 °C (132, 133), which will form PA/phosphosilicate clusters in the membranes to get stabilized PA and reduced PA leaching.

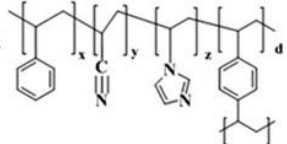
Other types of inorganic materials which can also reduce the PA leaching are the layered materials (33, 134-136, 140). Uregen et al. (140) prepared the PA doped PBI/graphene oxide (GO) nanocomposite membrane and investigated the effect of acid retention capability. Because GO has a hygroscopic nature which can trap PA to prevent excessive PA leaching, the acid loss degree of PBI/GO (69.8% acid loss for PBI/1 wt% GO, and 77.4% acid loss for PBI/2 wt% GO) is much lower than that of pristine PBI (85.2%). Similar results were also observed in the application of PBI modified GO/sulfonated poly(ether ketone) (SPEEK) membranes (134). In the acid-retention test, the inorganic membrane with highest GO content (3.0 wt%) showed the lowest weight loss.

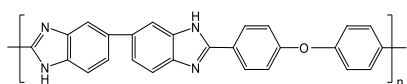
Furthermore, Jana's group prepared clay incorporated OPBI membranes (135). As the silicates of the nano-clays can trap PA in their nano-galleries and form hydrogen bonding interactions with the phosphate ions, PA molecules can be held in the membrane matrix. To measure membrane acid retention properties, the PA doped membranes were suspended in boiling water for 3 h and the membrane weight differences were recorded. The results showed that the PA leaching of clay incorporated membrane (around 50 wt% PA loss) is lower than the pure OPBI membrane (around 90 wt% PA loss). Another porous fibrous clay mineral, sepiolite, was utilized to be the additive in the poly(2,5-benzimidazole) (ABPBI) membrane to reduce PA leaching because of its natural hygroscopicity (32, 33). To improve proton conductivity and avoid phase separation after the incorporation of inorganic nanoparticles, sepiolite particles were functionalized by phenyltriethoxysilane to add sulfone groups onto the surface (33). The acid leaching test showed that the PA retention of ABPBI with 2 wt% silane-modified sepiolite has only 33.3 wt% acid loss which was less than that of pure ABPBI with 42.2 wt%. Similarly, one of our previous work (136), utilizing silica nanosheet as an inorganic filler into the polyethersulfone-polyvinylpyrrolidone (PES-PVP) membranes, also demonstrated that the trapping interactions between PA molecules and silica nanosheets lead to improved cell performance.

3.2.2 Introducing strong interactions between polymers and PA

Apart from the 'trapping' effect to reduce PA leaching from membranes, establishing strong molecular interactions between PA and membrane materials can also be another efficient method to tackle this problem. Many efforts (summarized in Table 3.2) have been made along several fronts. On the one hand, research on the introduction of acid-base interactions between PA and membrane polymers will be discussed in this section (89, 141-145). In addition, recent efforts focusing on covalent interaction to anchor the PA molecules in the membrane, show promising to solve the acid-leaching problem (146, 147).

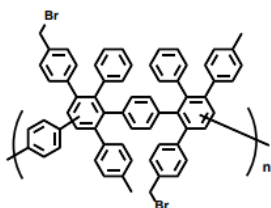
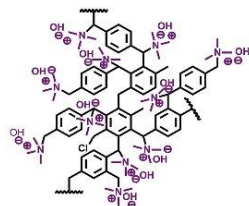
Table 3.2. Recent advances to introduce strong interactions to alleviate the PA leaching

Polymer	Modification	PA retention ability	Ref.
	Through photo-crosslinking	Less than 69.7 wt% loss in distilled water for 60 min	(141)



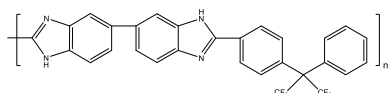
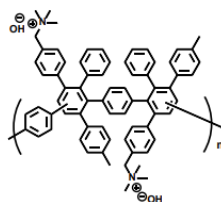
Crosslinking by Br-hyperbranched poly(p-xylene)

More than 80% (142) remaining at 24 h; 68.5% at 96 h at 80 °C and 40% RH



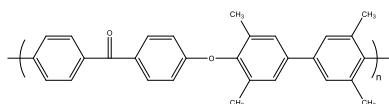
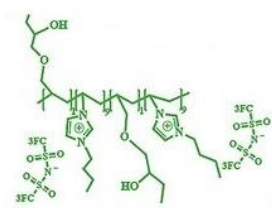
Quaternization

93 wt% remaining for (89) 44 h at 80 °C and 40% RH; 77 wt% remaining for 50 h at 220 °C and 0% RH



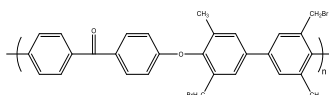
Adding cross-linkable polymeric ionic liquid

8.5 mol PA remaining (143) for 96 h at 80 °C and 40% RH

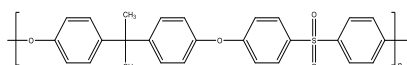
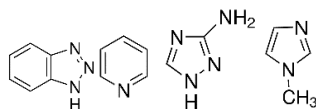


Bromination of PAEK

25 wt% remaining (144) after 325 min at 60 °C and 60% RH

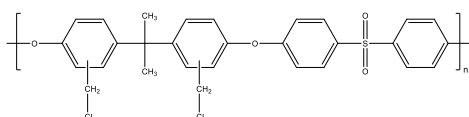


Then decorating with four kinds of nitrogen-heterocycles as shown below:

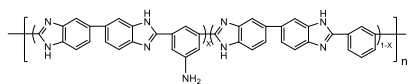


Polysulfone chloromethylation

8 wt% loss at 220 °C (145) and 0 RH for 48 h; 7 wt% loss at 80 °C and 40% RH for 48 h

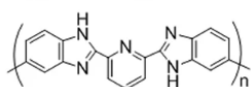
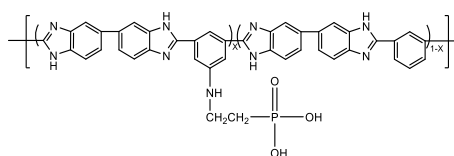


Then grafting quaternary benzyl-pyridinium cation as shown below:



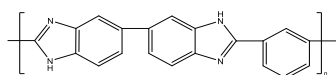
Grafting ethyl phosphonic acid groups onto the backbone NR

(148)



Use poly(vinylphosphonic acid) to replace PA

Free from acid leaching (146, 147)



Adding Al₂O₃ into the catalyst layer

Around 2 mg PA loss from exhaust after 360 h (93)

^aNR = not reported.

One approach to alleviate PA leaching out of the membrane is to introduce basic groups onto the polymer backbone to get stronger interactions between PA molecules and polymers. One of the applications is the preparation of crosslinked membrane with imidazole groups (141). The crosslinked membrane was prepared through photo crosslinking with a mixture containing vinylimidazole, acrylonitrile and styrene, and was then grafted with pendant imidazole groups. The PA retention was tested by measuring the PA weight loss after immersion in distilled water for 60 min. The result showed PA retention increased with the amount of imidazole groups in membranes, probably due to the formation of hydrogen bonding between PA and pendant imidazole groups.

Another basic group is the quaternary ammonium (QA) which was introduced into the polymer to reduce the PA leaching because of the strong ionic interactions between PA and QA (89, 142). Hu et al. (142) proposed a series of hyperbranched polybenzyl crosslinked OPBI membranes containing QA groups. Acid loss tests indicated that the acid loss of QA modified OPBI membrane was lower than the pure OPBI. Similar results were also observed in the application of PA doped QA-biphosphate ion-pair-coordinated polyphenylene (PA-doped QAPOH) membrane which can operate at 80-160 °C (89). The acid retention ability of the membrane was tested at different conditions (220 °C/0% RH, and 80 °C/40% RH), where the former condition (Fig. 3.3a) was used to measure the PA loss via evaporation and the latter condition (Fig. 3.3b)

tested PA loss through water condensation. To understand the reason why the PA leaching in the pristine PBI membrane was higher than the membrane containing basic groups, the intermolecular interaction energy between PA molecules and benzimidazole in pure PBI membrane was modelled and calculated as 17.4 kcal/mol, much less than the interaction energy between QA groups in QAPOH and PA (151.7 kcal/mol). Therefore, due to stronger interactions with PA molecules, PA doped QAPOH maintained a higher PA retention than that of PA doped PBI membrane.

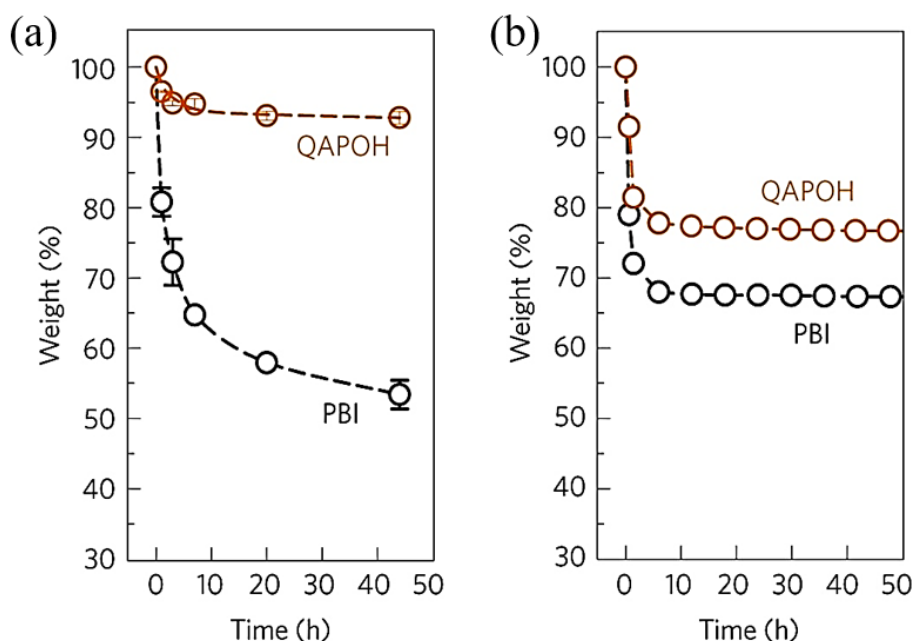


Fig. 3.3. Percentage weight loss of membranes (a) at 80 °C/40% RH and (b) at 220 °C/0% RH (89).

A cross-linkable polymeric ionic liquid (cPIL) was used by Liu et al. (143) to crosslink the fluorine-containing PBI membrane. The introduction of ionic liquid groups into the polymer backbone increased basic properties and strengthened the interactions with PA molecules. Consequently, the additional ionic liquid groups enhanced phosphoric acid retention of the membrane with increased the PA-doping sites. The acid retention property of the cPIL crosslinked membrane was measured by exposing at 80 °C and 40% RH and then weighting after wiping the membrane surface. It showed the PBI with 20 wt% cPIL still had higher ADL (8.5 mol) in the membrane than that of the pristine PBI (2.6 mol) after 96 h stability test, exhibiting excellent PA retention ability of cPIL crosslinked membranes.

Alternative approach to enhance PA retention properties of HT-PEMs is to graft nitrogen-heterocycles (1-methylimidazole, 3-amino-1,2,4-triazole, and 1H-benzotriazole pyridine) onto the polymer chains (144). In this study, because of the prominent basic property of imidazole, the imidazole groups from 1-methylimidazole were proved to be more effective than other three

nitrogen-heterocycles to improve proton conductivity and phosphoric acid retention. 1-methylimidazole modified poly (arylene ether ketone) membrane (BrPAEK-MeIm) was prepared and the acid retention test showed that PA doped BrPAEK-MeIm1.6 (1.6 imidazole per unit) had more acid retention than that of PA doped BrPAEK-MeIm1.0 or BrPAEK-MeIm1.3 because of the more basic groups in BrPAEK-MeIm1.6.

Similar to nitrogen-heterocycles, polycations have excellent acid retention due to strong interactions with PA molecules. Venugopalan et al. (145) developed a class of quaternary benzylpyridinium cation grafted polysulfone-PBI blend membranes (QPPSf-PBI). The 50: 50 QPPSf-PBI (50: 50 weight ratio) exhibited good acid retention at both conditions (220 °C and 80 °C/40% RH). This was explained by the strong interactions between cationic group in QPPSf and PA, where the polycations can anchor the phosphate anions of H_3PO_4 to prevent PA loss. The formation of pyrophosphoric acid from H_3PO_4 condensation at 220 °C was also responsible to the excellent acid retention since the produced pyrophosphoric acid is less volatile and stable at 220 °C (149).

Very recently, another approach to mitigate PA leaching is to graft ethyl phosphoric acid (EPA) onto the polymer chains (148): Wang's group prepared amino-modified PBI membranes with grafted ethyl phosphonic acid (named as PBI-NH₂-EPA-X, X represents the content of ethyl phosphoric acid in PBI). Through measuring the weight loss at 70 °C and 60% RH for 240 h, the PA doped PBI-NH₂-EPA-20 and PBI-NH₂-EPA-15 membranes still remained over 5 mol ADL, higher than that of pristine PBI membrane (4 mol ADL). It showed that the introduction of ethyl-phosphoric acid and amino groups onto the polymer chains improves the PA doping and acid retention ability.

A novel method to prevent excessive PA leaching from the membrane is to replace the PA with poly(vinylphosphonic acid) (PVPA) (146),(147). Because PVPA is a polymeric acid and its phosphonic acid groups can form hydrogen-bonding network with nitrogen sites of poly[2,2'-(2,6-pyridine)-5,5'-bibenzimidazole] (PyPBI), PVPA is bound to PyPBI backbones and facilitates the proton transfer through Grotthuss mechanism (82). This novel membrane without the use of PA molecules is free of acid leaching and has excellent durability.

Another interesting approach to decrease PA loss is by adding a small amount of Al_2O_3 (6 wt%) to the catalyst layer (93). The PA molecules which are leached out of the membranes can react with Al_2O_3 in the electrode and be converted to proton-conductive $\text{Al}(\text{H}_2\text{PO}_4)_3$. As a result, the formation of $\text{Al}(\text{H}_2\text{PO}_4)_3$ can not only reduce the PA loss of the MEAs, but the proton resistance of the MEA also reduced due to the increased proton conductivity in catalyst layer, demonstrating that the addition of Al_2O_3 to the electrode is a promising way to reduce PA loss in acid-based HT-PEMFCs.

3.3 Alleviating membrane oxidative degradation

Radicals (HO and HO₂) produced by the incomplete reactions at the cathode (see section 2.5.2), result in the degradation of membrane polymers and further cause performance deterioration (150). Recent developments on the alleviation of membrane oxidative degradation are through modifying the polymer structure to be radical inhibitors or incorporating some antioxidative materials. It is widely accepted that the synthesis of membranes with crosslinked or branched structures is an excellent method to increase the resistance of the polymer chains to radicals (151). Also, as hydroxyl radicals which have an electrophilic nature predominantly attack the electron-rich compounds (152), introducing the electron-withdrawing groups into the polymer chain or adding antioxidative materials into the membrane can facilitate the enhancement of the chemical stability of membrane (153-155). Research on these approaches to improve the oxidative stability will be outlined in the following paragraphs.

3.3.1 Crosslinking

To reduce attack from radicals and improve oxidative stability, the modification of a membrane via crosslinking can prepare more compact or dense structures, which can hinder the attack of radicals. A few papers have reported several approaches to enhance membrane oxidative stability by applying different crosslinkers. In this section, as shown in Table 3.3, crosslinkers containing alkyl groups or rigid benzene rings, epoxy based crosslinkers, macromolecular crosslinkers, and inorganic crosslinkers will be reviewed.

Table 3.3. Applications of acid-based PEMs with enhanced oxidative stability via crosslinking

Polymer	Crosslinker	Oxidative stability ^a	Ref.
OPBI	Hyperbranched crosslinkers decorated with imidazole groups	90 wt% remaining after 200 h at 68 °C	(156)
OPBI	Hyperbranched bromomethylated poly(p-xylene) decorated with quaternary ammoniums	88.1 wt% remaining after 200 h at 68 °C	(142)
PPO	1,7-octadiyne with alkyl groups with quaternary ammonium hydroxides	90 wt% remaining after 27h at 80 °C	(119)
PBI	P-xylylene dichloride	Less than 4 wt% loss after 96 h at 80 °C	(157)
Poly(arylene ether sulfone) with imidazole groups	P-xylylene dichloride	Keep complete shape for more than 360 h at 80 °C	(158)

Imidazolium-functionalized PPO	P-xylene dibromide	Keep its shape over 15 days at 80 °C	(159)
SPEEK containing imidazole groups	P-xylene dibromide	99 wt% remaining after 4 h at 80 °C	(160)
Sulfonated polyimides containing benzimidazole group	4,4'-diglycidyl (3,3',5,5'-tetramethyl biphenyl) epoxy resin (TMBP)	Became brittle after 1410 min at 80 °C	(161)
PBI with porous structure	TMBP	0.3 wt% loss after 24 h at 70 °C	(162)
PBI	TMBP	Broken onto pieces after 288 h at 85 °C	(163)
F6-PBI	Bisphenol A diglycidyl ether, or bisphenol A propoxylate diglycidyl ether, or poly(ethylene glycol) diglycidyl ether	Broken after nearly 110 h at 80 °C	(164)
SO ₂ PBI	Poly(vinylbenzyl chloride)	Less than 15 wt% loss after 350 h at 68 °C	(165)
PBI	Bromomethylated poly (aryl ether ketone)	93.4-94.5 wt% remaining after 24 h at 70 °C	(166)
Poly(ether ketone) bearing benzyl bromide groups	PBI	Broken after nearly 7.5 h at 80 °C	(167)
Sulfonated poly(imide benzimidazole)s	4,4'-bibromomethenyl diphenyl ether	2050 min dissolution time at 80 °C	(168)
PBI (PBI30OH) containing hydroxyl groups	(3-isocyanatopropyl)triethoxysilane (ICTES) and 1,4-phenylene diisocyanate (1,4-PDI)	Less than 5 wt% loss after 48 h	(169)
Poly(ether ketone)	(3-Aminopropyl)triethoxysilane	Broken after 15.3 h at 80 °C	(170)
PBI	(3-Glycidyloxypropyl)trimethoxysilane (KH560)	75 wt% remaining after 240 h	(171)
Poly(imide benzimidazole)	KH560	1450 min dissolution time	(172)

branched PBI	KH560	89.1 wt% remaining after 90 h	(16)
--------------	-------	-------------------------------	------

^atested in Fenton reagent.

PBI membranes with hyperbranched crosslinkers with imidazole groups (ImOPBI-x, x stands for the weight ratio of the hyperbranched crosslinker) (156) or quaternary ammonium hydroxides (142) were prepared by Wang's group. The chemical stability was tested by immersing the membranes in Fenton reagent and recording the remaining weight with time. The remaining weight of ImOPBI-x was within 90.0% after 200 h test without obvious damage, much higher than that of pure OPBI membrane (68.3%). Because imidazole groups in polymer backbone and alkyl groups in the crosslinkers are electron-rich sites which can be easily attacked, the initial decomposition will happen at these sites and protect the main chain with a relatively intact backbone (142). The pure OPBI membrane breaks into pieces in the first 100 h, owing to chain segment ruptures caused by oxidative degradation (99). Similar work was carried out on the preparation of poly(2,6-dimethyl-1,4-phenylene oxide) (PPO) with triazole groups crosslinked by 1,7-octadiyne with alkyl groups (119). The oxidative stability was tested in Fenton reagent at 80 °C. The results showed the crosslinked membranes (over 80 wt% remaining) had better chemical stability than the non-crosslinked membranes (only 75 wt% remaining).

Shen et al. (157) proposed a novel PBI membrane crosslinked by (p-xylylene dichloride) as shown in Fig. 3.4a. Additionally, the mixing with dibutyl phthalate (a kind of porogen) increased membrane porosity and further enhanced ADL and proton conductivity. From the result of 96 h Fenton test, the non-crosslinked porous PBI membranes with different porosities showed a mass loss of up to 7.2%, while the crosslinked porous membranes had a less than 3% weight loss. Even though the porous crosslinked PBI membranes had large surface area which can be easily attacked by the free radicals, the covalently crosslinked structure played an important role to obtain good oxidative stability. Wang et al. (158) used the same crosslinker (p-xylylene dichloride) to synthesize poly(arylene ether sulfone) with pendent imidazole groups (Fig. 3.4b). The membranes with 10-40% crosslinking degree kept their shape for more than 360 h in Fenton reagent, showing excellent oxidative stability. Similarly, Li et al. (159) and Jiang et al. (160) also used p-xylylene dibromide with the benzene rings as a crosslinker to prepare the crosslinked imidazolium-functionalized PPO and ionically crosslinked SPEEK containing imidazole groups (SPEEK-Im) (Fig. 3.4c), respectively. Due to the compact crosslinked structures, the mechanical properties and chemical stabilities of these prepared membranes have been greatly improved. In addition, the oxidative stability of crosslinked membrane increased with the degree of crosslinking.

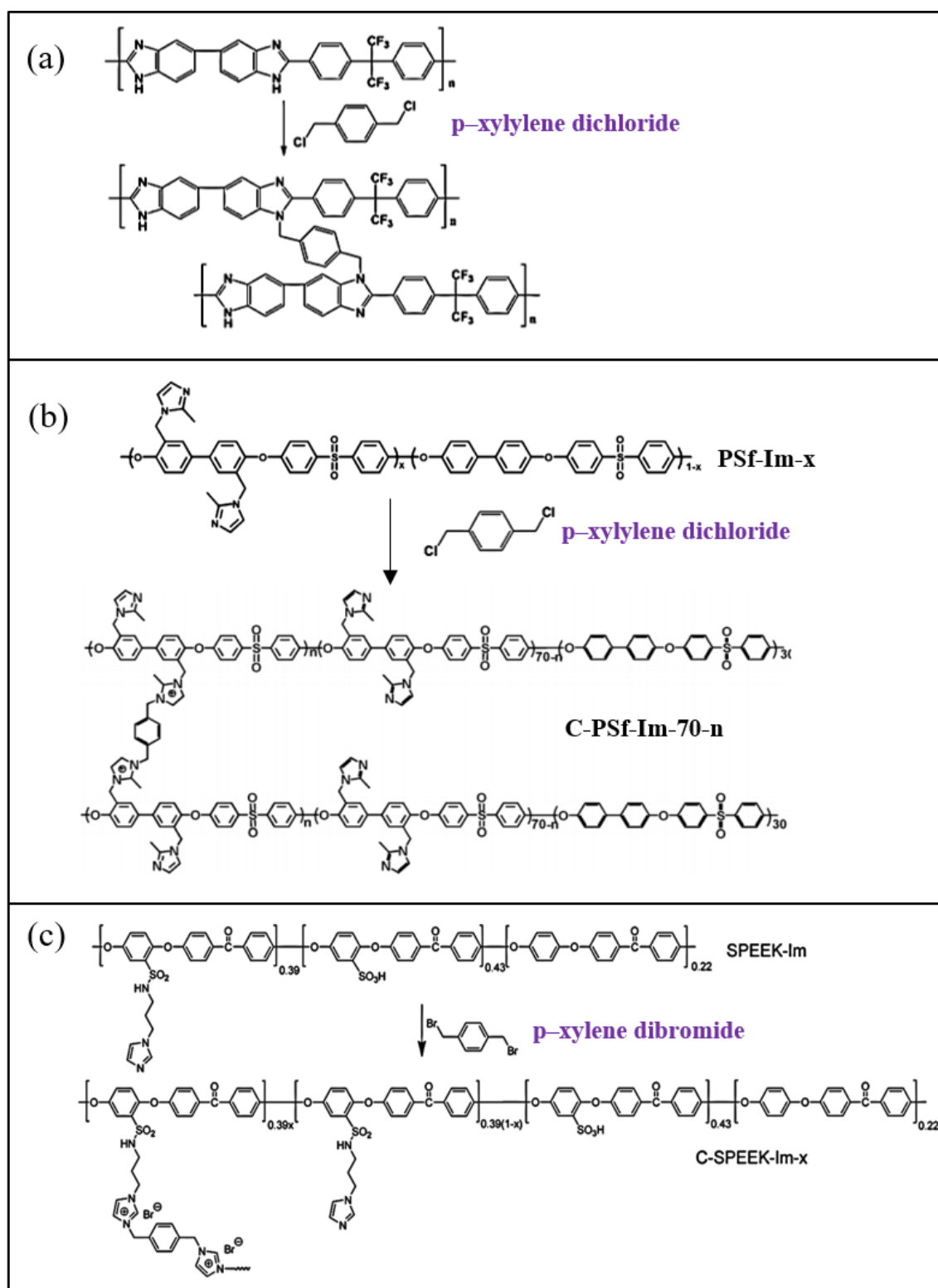


Fig. 3.4. Crosslinked membranes using p-xylylene dichloride or p-xylylene dibromide as the crosslinker. Synthetic route of (a) crosslinked PBI (157). (b) Crosslinked poly(arylene ether sulfone) (158). (c) Crosslinked PPO (159). (d) crosslinked SPEEK-Im (160).

Epoxy resin had been used as a crosslinker in several HT-PEM applications to improve membrane oxidative stabilities (161, 163, 164, 173). Pan et al. (161) prepared sulfonated polyimides

containing benzimidazole group (SPIBI) crosslinked by 4,4'-diglycidyl (3,3',5,5'-tetramethyl biphenyl) epoxy resin (TMBP). Because the ionic interactions between the sulfonic acid groups of the polymer and the benzimidazole groups of TMBP have higher chemical stability against the free radical reactions, all of the TMBP crosslinked SPIBI membranes displayed better oxidative stabilities than the pristine membranes. Similarly, comparing with the pure PBI, crosslinked PBI membrane using TMBP as a crosslinker also presented enhanced oxidative stability due to the incorporation of crosslinking bonds (163). Another application to improve the membrane oxidative stability is to use three different epoxides (bisphenol A diglycidyl ether (R_1), bisphenol A propoxylate diglycidyl ether (R_2) and poly(ethylene glycol) diglycidyl ether (R_3)) as crosslinkers (164). As shown in Fig. 3.5a, all PBI membranes crosslinked by these three epoxides showed improved oxidative stability. It is worth mentioning that the hexafluoropropylidene PBI (F6-PBI) membranes crosslinked by R_1 with rigid aromatic rings showed the higher tolerance in Fenton reagent than the membranes crosslinked by R_2 and R_3 with flexible alkyl chains (Fig. 3.5b). This might be explained that the aromatic ring in R_1 crosslinker has higher electrophilicity and steric effect than the crosslinker with flexible alkyl chain.

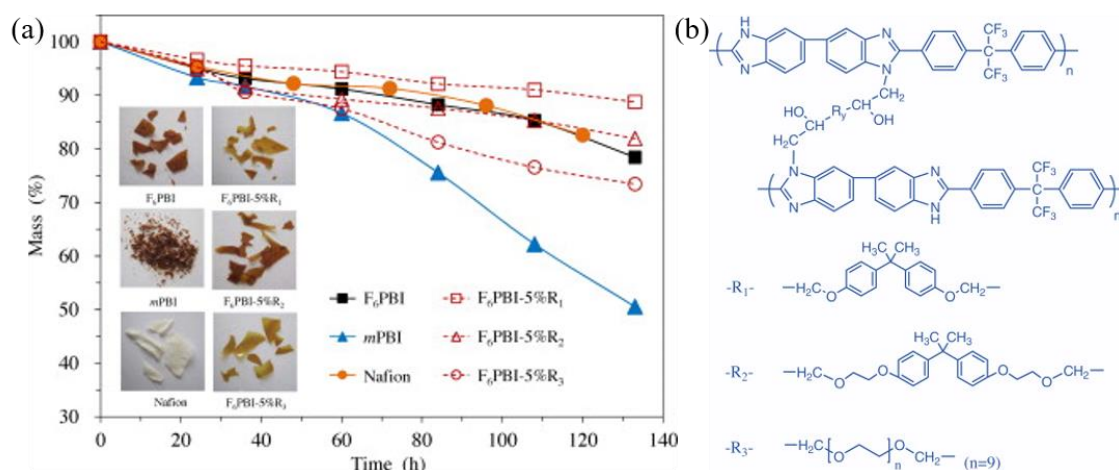


Fig. 3.5. (a) Fenton test results of F₆PBI, F₆PBI with 5 wt% R_1 , R_2 or R_3 , mPBI, and Nafion 115 membranes at 80 °C, and (b) structure of F₆PBI with R_1 , R_2 or R_3 . The inserted images are the appearance of membrane samples after 133 h Fenton test (164).

In acid-based HT-PEMs, membrane oxidative stability can also be improved by the membrane crosslinking using the macromolecular crosslinkers (165-167). Poly(aryl sulfone benzimidazole) (SO₂PBI) membrane crosslinked by poly(vinylbenzyl chloride) (PVBCl) had been prepared as the electrolyte in HT-PEMFC (165). The obtained crosslinked membranes refer to CL-x%SO₂PBI (x is the theoretical degree of crosslinking). The results of the Fenton tests showed that CL-33.5%SO₂PBI had a less weight loss (around 15 wt%) than that of pristine SO₂PBI membrane (around 29 wt%) after 350 h, illustrating that membrane oxidative stability was improved by the crosslinking. Similarly, the applications employing bromomethylated poly (aryl ether ketone)

(BrPAEK) (166) and poly(ether ketone) bearing benzyl bromide groups (Br-PEEK) (167) to crosslink PBI polymers had been developed, all of which showed improved oxidative stabilities. For example, the remaining weight of all BrPAEK crosslinked PBI membranes during the first 24h in Fenton reagent was in the range of 93.4-94.5 wt%, which was much higher than that of pristine PBI membrane (76.9 wt%). This can be explained that the dense crosslinked structure and covalent bond network increased the membrane resistance to the free radicals.

A series of covalently crosslinked sulfonated poly(imide benzimidazole)s (CBrSPIBIs) were synthesized using 4,4'-bibromomethenyl diphenyl ether as a crosslinker (168). All CBrSPIBI_x (*x* is the degree of crosslinking) membranes displayed better chemical stability than SPI/PBI blend membranes because of dense structure of CBrSPIBI_x membranes. The oxidative stability was evaluated by recording the time when the membrane was completely dissolved in Fenton reagent at 80 °C. PA doped CBrSPIBI₆₀ membrane showed the best chemical stability (more than 2050 min dissolution time), while the dissolution time of SPI/PBI blend membranes and pure poly(imide-benzimidazole) membranes was only 50-70 and 150-270 min, respectively.

Another category of crosslinked membrane with enhanced oxidative stability is the use of silane-based inorganic crosslinker such as (3-isocyanatopropyl)triethoxysilane (ICTES) (169), (3-Aminopropyl)triethoxysilane (APTES) (170) and (3-Glycidyloxypropyl)trimethoxysilane (KH560) (171, 172). The synthesis of a PBI copolymer containing hydroxyl groups (PBI30OH) crosslinked by ICTES or 1,4-phenylene diisocyanate (1,4-PDI) was developed by Shen et al. (169). The crosslinked membranes showed less than 5 wt% loss after 48 h in Fenton reagent, less than that of linear PBI30OH membrane (15% weight loss). In addition, as it is hard for radicals to penetrate the silica groups in ICTES to attack the polymer matrix, the results of Fenton test showed ICTES crosslinked PBI30OH has a better oxidative stability than 1,4-PDI crosslinked PBI30OH. Another organic-inorganic APTES-crosslinked quaternized poly(ether ketone) (QPEEK)-*x*%APTES (*x* is the ratio of -N-H to -CH₂Br) had been prepared (170). Its oxidative stability was evaluated by soaking the membrane in Fenton solution and measuring the breaking time when the membrane begins to break into pieces. The PA doped QPEEK-30%APTES has 15.3 h breaking time, while the pristine PA doped QPEEK membrane had only 1.5 h breaking time, showing membranes crosslinked by APTES had a great improvement in the oxidative stability. In the applications proposed by Wang et al. (171) and Yue et al. (172), PBI and poly(imide benzimidazole) were crosslinked by KH560, respectively. The membrane oxidative results showed that all KH560-crosslinked membranes displayed longer dissolution time (better oxidative stability) than their pristine membranes. Interestingly, the oxidative stability of the KH560-crosslinked membranes decreased with the increase of degree of crosslinking (171),(172), showing the opposite trend to other crosslinked membranes in which the oxidative stability usually improves with the increasing of degree of crosslinking. This can be explained that the C-

C and Si-O segments of KH560, which are the weakest parts in the crosslinked membrane, are easily attacked by radicals to lead to weight loss. Similar results were reported by Hu et al. (16): the oxidative stability of KH560-crosslinked branched OPBI membranes is more stable than the pure OPBI but decreases with increasing crosslinking degree.

3.3.2 Synthesis of polymer with branched structure

As discussed in above section, crosslinking is one of the effective methods to enhance the oxidative stability. However, the solubility of crosslinked membranes is relatively low in some common organic solvents, restricting their development in commercial markets (151). Recently, branched polymers have received increasing attentions in the applications of HT-PEMs because of their excellent acid retention abilities (discussed in the section of alleviating acid leaching), excellent oxidative stability and good solubility in common organic solvents (174). Although the oxidative stability of branched membranes increases with the degree of branching, the reduced interactions between the polymer chains in the branched structures usually lead to poor mechanical strength (151). Therefore, the compromise between mechanical strength and degree of branching should be controlled. In this part, different branched membranes which were applied in HT-PEMFCs will be introduced.

The first application of branched polymer in HT-PEMs is reported by Wang's group (174), where the branched PBI was prepared using 3,5-tri(4-carboxyphenoxy)benzene (B_3) as a branching agent ($PBI-B_3-x$, x is the molar percentage of B_3), as shown in Fig. 3.6a-b. The antioxidative stability and PA retention ability of the branching structures have been significantly improved, compared with the linear polymers. Although the branched PBI membranes can be attacked by radicals, the 3D branched structure with many connections between the polymer chains will not significantly break to get a decreased mass loss. As proven by the weight loss in Fenton solution at 80 °C for 60 h, the mass loss of $PBI-B_3-9\%$ is 6.9% while OPBI membrane has 14.7 wt% loss. However, the branched PBI membranes showed a decreased trend in mechanical strength with the increasing degree of branching. The tensile strength of $PBI-B_3-3\%$, $PBI-B_3-6\%$ and $PBI-B_3-9\%$ membranes are 10.89, 6.51 and 5.25 MPa, respectively, lower than the OPBI membrane (10.99 MPa). The reduced chain entanglement and decreased interactions between polymer chains in the branched membranes can explain this.

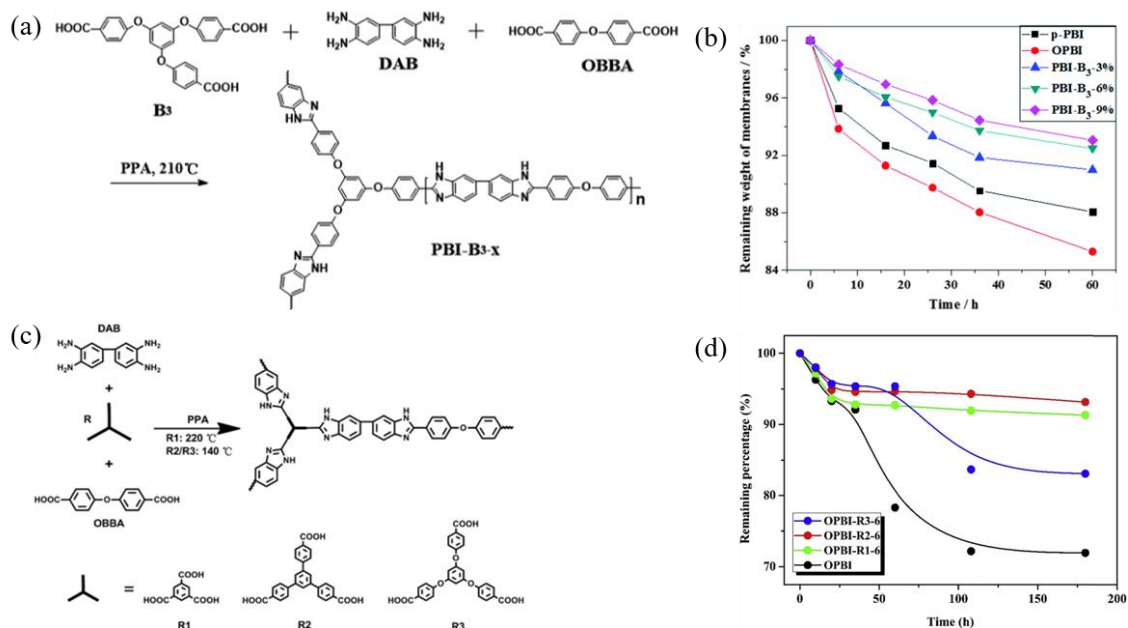


Fig. 3.6. (a) Synthesis route and (b) Fenton test results of PBI-B₃-x (174). (c) Synthesis route and (d) Fenton test results of branched OPBI using different branching agents (175).

Later, to investigate the functions of different branching agents in the branched membranes, three types of branched OPBI membranes prepared by introducing different branching agents (R1: trimesic acid; R2: 1,3,5-tri(4-carboxyphenyl) benzene; R3: 1,3,5-tri(4-carboxyphenoxy) benzene)) were explored by Wang's group as shown in Fig. 3.6c-d (175). The OPBI membrane showed largest weight loss (28.1%) after 180 h immersing time in Fenton reagent at 80 °C, comparing with the branched membranes prepared by R1 (8.7%), R2 (6.9%) and R3 (16.9%). All branched membranes showed better chemical stability than the pure OPBI membrane. Benefiting from the branched structures, when one segment of the branched polymer is attacked by radicals, the molecular weight and weight loss of branched membranes do not drastically change in the same way as OPBI to get improved oxidative stabilities (151). The reason why R3-based polymer has the worst weight loss among the three branched structures is that the ether bonds in R3 are vulnerable to be attacked by free radicals.

Because of the compact structure which can be induced by crosslinking, Hu et al. (16) tried to combine the crosslinking and branching to synthesize silane-crosslinked branched OPBI membranes with excellent oxidative stability and mechanical strength. SC-B-OPBI-x (x is the crosslinker ratio) is denoted as the silane-crosslinked branched OPBI membrane, while SC-OPBI-x (x is the crosslinker ratio) is denoted as crosslinked OPBI without branching. From the oxidative results in 90 h Fenton test at 80 °C, the weight loss of pure OPBI is highest (25.5%) while SC-B-OPBI-5 membrane has 12.8 wt% loss and branched OPBI without crosslinking has 17.3 wt% loss, illustrating both branching and crosslinking can improve the membrane oxidative stability. In addition, comparing with branched OPBI (36.0 MPa), the tensile strength of crosslinked branched

OPBI increased with degree of crosslinking (59.9 MPa for SC-B-OPBI-5, 72.7 MPa for SC-B-OPBI-10, and 78.4 MPa for SC-B-OPBI-20).

Very recently, star-shaped branched PBI polymers were reported by Wang et al. (176) as shown in Fig. 3.7a. Since the large free volumes of the branched structure and block PBI benefit nanophase separation, the prepared membranes have high ADL and excellent proton conductivity (0.15 S/cm at 160 °C) without fuel humidification. The Fenton test (Fig. 3.7b) showed the branched para-PBI block F6-PBI copolymer and branched F6-PBI block para-PBI copolymer showed better oxidative stabilities than the para-PBI, which can be attributed to the 3D branched structures. Wang et al. (177) also reported another novel crosslinker to crosslink the branched F6-PBI by polymeric crosslinking at 220 °C. The improved oxidative stability might result from the aliphatic fluorine ($-\text{C}(\text{CF}_3)_2-$) in these copolymer membranes, which is the electron-withdrawing group and will be discussed in the next section. Furthermore, the mass loss of the crosslinked branched membrane in the Fenton reagents was less than 3% after 168 h under the same conditions. This was attributed to more connections between PA and the branched copolymers than that of F6-PBI membranes (174).

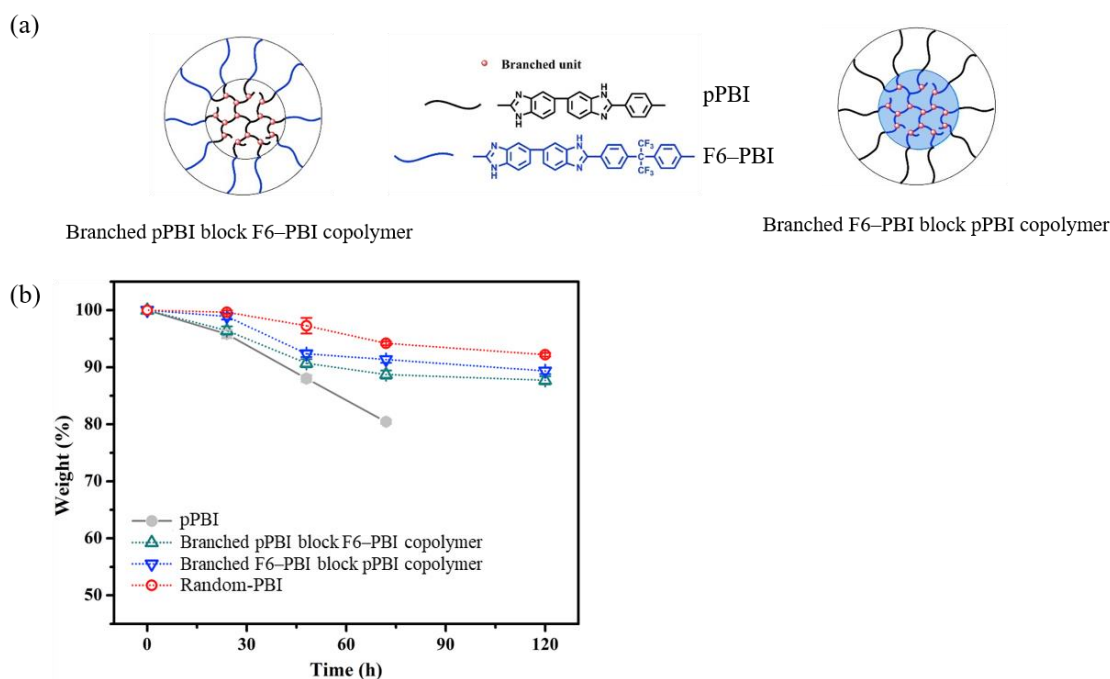


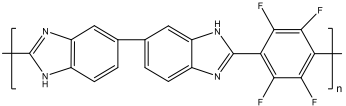
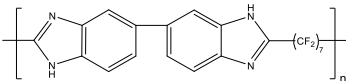
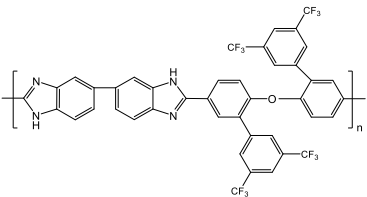
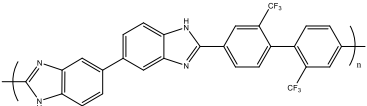
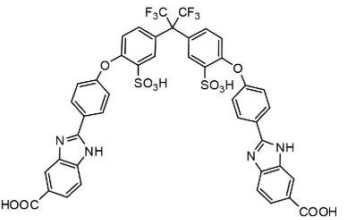
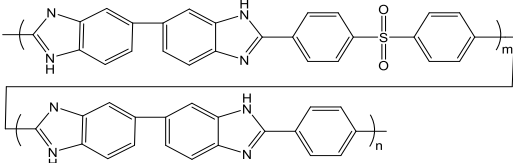
Fig. 3.7. (a) Scheme of branched pPBI block F6-PBI copolymer and branched F6-PBI block pPBI copolymer, and (b) Fenton results of PBI membranes (176).

3.3.3 Introducing electron-withdrawing group or stable polymers

Electron-withdrawing group, also named as electron-acceptor group, can draw neighbour electrons to reduce the electron density of neighbouring atoms. The incorporation of electron-withdrawing groups into the polymer chain can deactivate the electron-rich groups and further

increase the membrane oxidative stability. Since free radicals are liable to attack the sites where the electron cloud density is high and the hydrogen bonding in the polymer chain is electron-rich, it is effective to introduce electron-withdrawing groups into the polymer to stabilize the structure. It has been reported that the addition of electron-acceptor groups such as fluorine-containing groups (117, 123, 153, 177-183) and heteroatoms (such as sulfone groups) (154, 184-186) into the polymer showed improved oxidative stability. Another application to enhance membrane oxidative stability is polymer blending (see Table 3.4) (153, 179, 183, 187).

Table 3.4. Applications of HT-PEMs with enhanced oxidative stability via introducing electron-withdrawing groups

Polymer	Electron-withdrawing groups or polymers	Oxidative stability ^a	Ref.
	Fluorine-containing groups (-CF ₂ -, -C-F)	Without weight loss for 48 h at 80 °C	(123)
	Hexafluoroisopropylidene group (-C(CF ₃) ₂ -)	Less than 9 wt% loss after 200 h at 68 °C	(15)
	Trifluoromethyl groups (-CF ₃)	95 wt% remaining after 216 h at 68 °C	(180, 181).
	Trifluoromethyl groups (-CF ₃)	0.5 wt% loss after 24 h at 80 °C	(182)
	Fluorine groups (-CF ₃)	5 wt% loss after 48 h at 90 °C	(117)
	Sulfone group (-SO ₂ -)	Remained intact after 200 h at 68 °C	(154)

	Sulfone group (-SO ₂ -)	Around 5 wt% loss (184) after 5 days at 80 °C
	Sulfide linkages (-S-)	Stable for 1 h at (185) 80 °C
	Phenoxy	units less than 10 wt% loss (186) for 120 h at 70 °C
		2-4 wt% loss after (183) 144 h at 68 °C
		More than 75 wt% (187) remaining for 100 h at 70 °C
		Less than 9 wt% loss (179) after 120 h at 70 °C
		13.24 wt% loss after (153) 120 h
		7.89 wt% loss after (153) 120 h
		2.04 wt% loss after (153) 120 h

^atested in Fenton reagent.

Two kinds of fluorine-containing PBI membranes, poly(2,2'-(tetrafluoro-*p*-phenylene)-5,5'-bibenzimidazole) (4F-PBI) and poly(2,2'-tetradecafluoroheptylene-5,5'-bibenzimidazole) (14F-PBI), were prepared by Pu et al. (123) via a condensation polymerization method. The Fenton results showed that both 4F-PBI and 14F-PBI membranes were stable more than 48 h without weight loss in Fenton reagent. However, it only took 22.5 h for Hepta-PBI membrane to get flocculation with 1.5 wt% loss, and 37.0 h for meta-PBI membrane to occur flocculation with 1.7 wt% loss, showing the introduction of fluorine into the polymer backbone had a positive impact

to their oxidation stability. Also, Yang et al. (15) reported a fluorine-containing PBI (hexafluoropropylidene polybenzimidazole, F6-PBI) with excellent chemical stability. The introduction of a flexible spacer group $-\text{C}(\text{CF}_3)_2-$ can protect the adjacent aromatic rings by decreasing their electron density, while the introduced C-F bonds can reduce the density of C-H bonds in the backbones (178). Therefore, the probability of radical attacking the polymer backbones was reduced. This was verified in the Fenton test where the F6-PBI membrane had a less than 9 wt% loss after 200 h at 68 °C, compared with 23 wt% loss of poly[2,2'-m-(phenylene)-5,5'-bibenzimidazole] (mPBI).

Another fluorine-containing PBI membrane (P1-P5) was prepared from novel tetraamines using Eaton's reagent as a solvent as shown in Fig. 3.8a (181). The oxidative stability of the prepared membrane was measured in the Fenton reagent at 68 °C for 216 h where the remaining weights of P1, P2, P3 and mPBI were 83, 90, 96 and 78%, respectively (Fig. 3.8b). The chemical stabilities of mPBI, P1 and P2 were similar, but P3 displayed a superior oxidative stability. The bulky hydrophobic trifluoromethyl groups of P3 which can prevent the radicals from attacking polymer backbones might be the reason to explain the results in Fig. 3.8b (180, 181). Li et al. (182) used the solution-polymerization method to prepare fluorine-containing PBI (poly(2,2'-(2,2'-bis(trifluoromethyl)-4,4'-biphenylene)-5,5'-bibenzimidazole, BTBP-PBI) using Eaton's reagent. In the 24 h Fenton test, the weight losses of BTBP-PBI membranes at room temperature and 80 °C are 0 and 0.5 wt%, respectively. This is owing to the electron-withdrawing trifluoromethyl groups in BTBP-PBI which were very stable to radical attacking under harsh conditions.

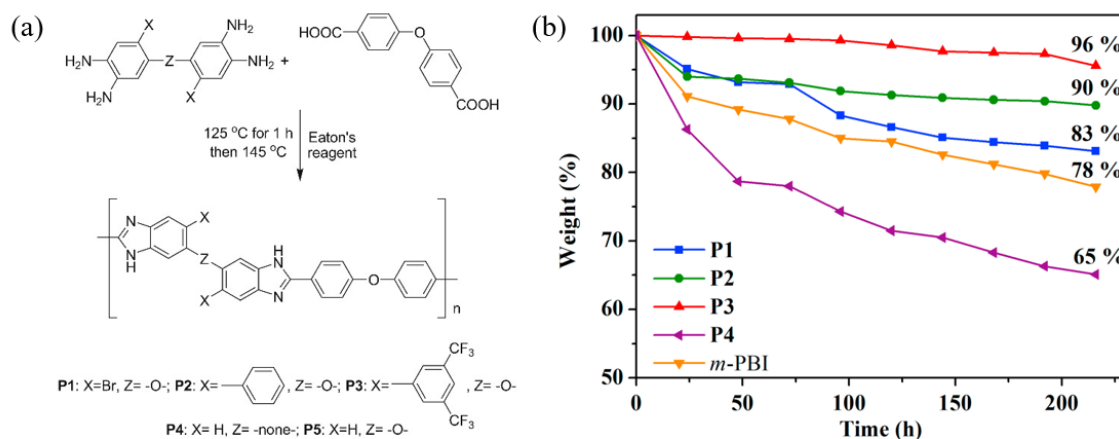


Fig. 3.8. (a) Synthesis of PBI membranes with the addition of electron-withdrawing groups in Eaton's reagent, and (b) Fenton results of fluorine-containing PBI membrane (P1-P5) (181).

Villa et al. (117) proposed two novel fluorine-containing PBI polymers: hexafluoropropylidene oxyPBI (F₆-oxyPBI) and bisulfonated hexafluoropropylidene oxyPBI (F₆-oxyPBI-2SO₃H). The weight loss of the F₆-oxyPBI and F₆-oxyPBI-2SO₃H in Fenton test at 90 °C after 48 h was only 2 and 5%, respectively. The excellent oxidative stability can be explained in three ways: (i) two -

CF₃ units in the backbone were more chemically stable than those obtained from similar non-fluorinated monomers. (ii) The presence of the sulfonic groups in F₆-oxyPBI-2SO₃H led to a higher mass change than that of F₆-oxyPBI (188), resulting in relatively higher loss in F₆-oxyPBI-2SO₃H. (iii) Polymers with low polymer intrinsic viscosity are less resistant to the Fenton test (99).

A different approach involves introducing sulfone groups into the polymer structures to achieve improved chemical stability (154),(184),(185). Yang et al. (154) prepared poly(aryl sulfone benzimidazole) (SO₂PBI) and its copolymers with poly[2,2'-p-(phenylene)-5,5'-bibenzimidazole] (pPBI). As the sulfone group is electron-withdrawing and can reduce the electron density of their surrounding molecules, the pure SO₂PBI membrane had the lowest weight loss among all tested membranes and remained intact after 200 h Fenton test. Similarly, a dense poly(aryl sulfone ether benzimidazole) (SO₂-OPBI) nanofiber was prepared using the newly electron-spun method (184). The incorporation of two spacer groups (sulfone and ether) into the polymers resulted in good physical-chemical properties. The SO₂-OPBI membrane displayed good oxidative stability (around 5% weight loss after 5 days in Fenton reagent at 80 °C). In addition, the highly sulfonated poly(phenylene sulphide nitrile) (XESPSN) copolymers were prepared by Lee et al. (185). After the chemical transformation from sulphide (-S-) linkages to electron-withdrawing sulfones (-SO₂-) under the exposure to H₂O₂, the prepared XESPSN showed improved oxidative stability. Another approach is to introduce phenoxy units into the polymer (186). The Fenton test showed the remaining weight of membrane increases with the increasing amounts of phenoxy moieties, suggesting that phenoxy units are also beneficial to the chemical stability. However, until now only three kinds of electron-withdrawing groups (fluorine-containing, sulfide-containing and phenoxy units) had been reported in the published papers. Further work is needed to fully explore other electron-acceptor groups (189) and incorporate them into the polymer for potential HT-PEMFC applications.

Another well-known application to enhance the membrane oxidative stability is polymer blending, which is an economic and facile method to prepare novel membranes with improved oxidative and mechanical properties (153, 179, 183, 187). Singha et al. (187) synthesized the blend membranes of PBI and poly(vinylidene fluoride) (PVDF) at different compositions by a solution casting method. In the Fenton test, the weight remaining of the 75/25 blend membrane (75 wt% PBI and 25 wt% PVDF), the 25/75 blend membrane and the 10/90 blend membranes are 75, 87 and 100%, respectively, showing that the oxidative stability of the blended membranes increased with the percentage of PVDF. Furthermore, it was found that the 75/25 membranes have higher PA doping level than pure PBI membrane, and the electronegativity of fluorine and the crystallinity of PBI can promote proton transport. This resulted in higher proton conductivity for the 75/25 membranes than pure PBI membrane. A similar application was studied by Jana's group

about blending PBI with poly(vinylidene fluoride-co-hexafluoropropylene) (PVDF-HFP) (179). The oxidative stability of the blended membrane increases with increasing content of PVDF-HFP. Another polymer blending application was developed by Li et al. (153). PBI, F6-PBI and SO₂PBI were blended with sulfonated partially fluorinated arylene main chain polymers (8b), respectively. In the Fenton test, all blended membranes showed excellent oxidative stability. Additionally, the Fenton results showed that the F6-PBI-8b and SO₂PBI-8b blend membranes had the lower mass loss than PBI-8b, which were attributed to the electron-withdrawing properties of the fluorine groups in F6-PBI and the sulfone group in SO₂PBI. Polymer blending is a facile method to obtain a stable membrane with excellent mechanical and oxidative stability. In the polymer-blending applications, however, the solubility of the mechanically stable polymer and the miscibility of two polymers are still limiting issues.

3.3.4 Inorganic additives with high oxidative stability

An alternative way to enhance membrane oxidative stability is to introduce inorganic additives as shown in Table 3.5. In general, the incorporation of inorganics into the polymer can attract or hinder the attack from radicals and then protect the polymer chain from radical attacking, but it might deteriorate membrane proton conductivity because of its poor conductivity. Therefore, the functionalization of inorganic materials using proton conductors is often used method to increase compatibility with polymers. Recently, to improve the membrane oxidative stability, many materials with porous, channelled or laminar structures such as clay (135) and sepiolite (33) have been studied as additives in acid-based HT-PEMFCs. In addition, the additives with good antioxidative properties (e.g. titanium-based nanoparticles and CeO₂) are also used as radical scavengers in the HT-PEMFC applications (190, 191). Finally, applications utilizing silica-based inorganics to improve the membrane oxidative stability will be introduced (92, 192, 193).

Table 3.5. Applications of HT-PEMs with enhanced oxidative stability via adding additives

Polymer	Additives	Oxidative stability ^a	Ref.
OPBI	Modified clays	70-80 wt% remaining after 100 h at 70 °C	(135)
ABPBI	Sulfonated sepiolite	More than 85 wt% remaining for 120 h at 70 °C	(33)
PBI	NanoCaTiO ₃	More than 90 wt% remaining for 120 h at 70 °C	(190)
ABPBI	Cs _x H _{3-x} PW ₁₂ O ₄₀ /CeO ₂	Around 5 wt% loss for 24 h at 80 °C	(191)
PBI	CeO ₂	20% weight loss after 220 h at 80 °C	(194)
OPBI	Protic ionic liquid modified silica	More than 50 wt% remaining for 240 h at 70 °C	(92)

PBI	Ionic liquid functionalized Si-O-Si network	80 wt% remaining for 120 h at 70 °C	(192)
PBIOH	Ionic-liquid-functional nanoparticles	silica 13 wt% loss after 96 h at 80 °C	(193)

^atested in Fenton reagent.

Singha et al. (135) prepared three surfactants-modified nanoclay/OPBI composite membranes by a solution blending method. Owing to the addition of the silicate layers and surfactant, the oxidative, mechanical and thermal stability of the composite membrane displayed great enhancement. In the Fenton test, the remaining weight of all surfactant modified clay/OPBI nanocomposite membranes was about 70-80 wt% after 100 h which was much higher than the pristine OPBI membrane (50 wt%). The nanoclay acted as a barrier to protect the vulnerable regions of the polymer backbones from the attack of hydroxyl radicals, especially in the regions where the polymer chains were intercalated within the nanoclay layers. In addition, the work also showed the membrane oxidative stability increased with the increasing amount of clay because more interfacial interactions occurred between the polymer chains and silicate layers.

Sepiolite is another type of clay mineral with high specific surface area, hygroscopic porous fibrous structure, micro-porous channels (195) and excellent water absorption ability (196, 197). Bao's group (33) prepared a series of poly(2,5-benzimidazole)/sulfonated sepiolite composite membranes (ABPBI/S-Sep). Since the hygroscopic sepiolite particles had excellent water-absorption ability and can form additional proton transfer pathways, the composite membranes can achieve much higher proton conductivities than that of PA-doped ABPBI membranes. From the results in the Fenton test, all ABPBI/S-Sep composite membranes had higher remaining weight comparing with pure ABPBI, showing that the composite membrane had a better membrane oxidative stability. This was attributed to enhanced crystallinity in the matrix where the polymer chains were stacked along sepiolite fibres through hydrogen-bonding interactions to shield ABPBI chains from the attack of radicals. Another novel perovskite structured nano calcium titanate (nanoCTO) was prepared and incorporated PBI membrane (190). The Fenton test showed all nanoCTO-PBI composite membranes had higher remaining weight than that of pure PBI, while the oxidative stability of the composite membrane increased with increasing nanoCTO content. This was also attributed to the hydrogen bonding between nanoCTO and polymer chains.

Another interesting work explored by Xie's group (191) is to introduce a catalyst ($\text{Cs}_x\text{H}_{3-x}\text{PW}_{12}\text{O}_{40}/\text{CeO}_2$) into the ABPBI membrane. As CeO_2 is an excellent free radical scavenger but with poor proton conductivity (198), 12-tungstophosphoric acid ($\text{H}_3\text{PW}_{12}\text{O}_{40}$) was used to functionalize this nanoparticle to increase its conductivity. The oxidative stability was

evaluated by the weight loss in Fenton reagent at 80 °C for 168 h. The mass loss of the composite membrane decreases with the increasing loading of $\text{Cs}_x\text{H}_{3-x}\text{PW}_{12}\text{O}_{40}/\text{CeO}_2$, and starts to increase when the amount of $\text{Cs}_x\text{H}_{3-x}\text{PW}_{12}\text{O}_{40}/\text{CeO}_2$ exceed 4 wt% due to the possible aggregation. The enhanced oxidative stability is attributed to the excellent antioxidative ability of CeO_2 . Later Hao et al. (194) also added 7 nm Ceria nanoparticles into PBI membranes to work as the free radical scavenger. The results showed that the PBI with 2 wt% CeO_2 only had 0.08 wt% loss per hour in the Fenton reagents (3 wt% H_2O_2 , 4 ppm Fe^{2+}), compared with 0.164 wt% loss in pure PBI membranes.

The functionalization of inorganic fillers with ionic liquid is a common method to increase the compatibility of inorganics and membrane. Maity et al. (92) reported OPBI composite membranes blended with ionic liquid modified silica (ILMS). The chemical stability of the composite membrane showed a higher remaining weight in Fenton reagent after 120 h at 70 °C, while the remaining weight of the composite membrane increased with the increasing concentration of ILMS. These were because of the hydrogen bonding interactions between ILMS and OPBI chains which can prevent the OPBI chains from the attack of radicals. Another approach to increase the membrane oxidative stability was reported by Wang's group (192) about the preparation of PBI membrane with ionic liquid (IL) functionalized Si-O-Si network. Firstly, the IL was introduced into the polymer matrix and then the IL functionalized Si-O-Si network formed after the hydrolysis of IL by being immersed in 1 M H_2SO_4 at 80 °C for 24 h. From the Fenton test at 70 °C after 240 h, the results showed that all the composite membranes had a higher remaining weight (around 80 wt%) than that of pristine PBI (66 wt%), showing that the introduction of IL functionalized Si-O-Si network into PBI matrix can improved the membrane chemical stability. Further, Wang's group (193) also prepared PBI with hydroxyl groups/ionic-liquid-functional silica composite membranes (PBIOH-ILS). Via an in-situ sol-gel reaction using the ionic-liquid-functional silane monomer and its hydrolysis reaction, the membrane with crosslinked inorganic-organic structure can be synthesized. The combination of crosslinking and the addition of functionalized inorganic materials was explored to enhance the oxidative stability without the sacrifices of proton conductivity and compatibility between PBI membrane and inorganic nanoparticles. From the results of Fenton test at 80 °C for 96 h (Fig. 3.9a), the PBIOH with 5 wt% ILS (PBIOH-ILS 5) had only 13 wt% loss which is lower than the pure PBIOH (around 18 wt% loss). As the incorporated ILS affords additional proton transferring pathways in the composite membranes, proton transferring in the membrane follows multiple mechanisms (Grotthuss and vehicle mechanism) as shown in Fig. 3.9b. Protons can transfer through hydrogen bonding networks via Grotthuss mechanism, and combine with PA molecules to diffuse through the membrane working as vehicles. Therefore, the proton conductivity of PBIOH-ILS 5 (0.106 S/cm)

showed the highest among all composite membranes at 170 °C, illustrating the PBIOH-ILS membranes are promising in HT-PEMFCs with the help of adding crosslinked inorganics.

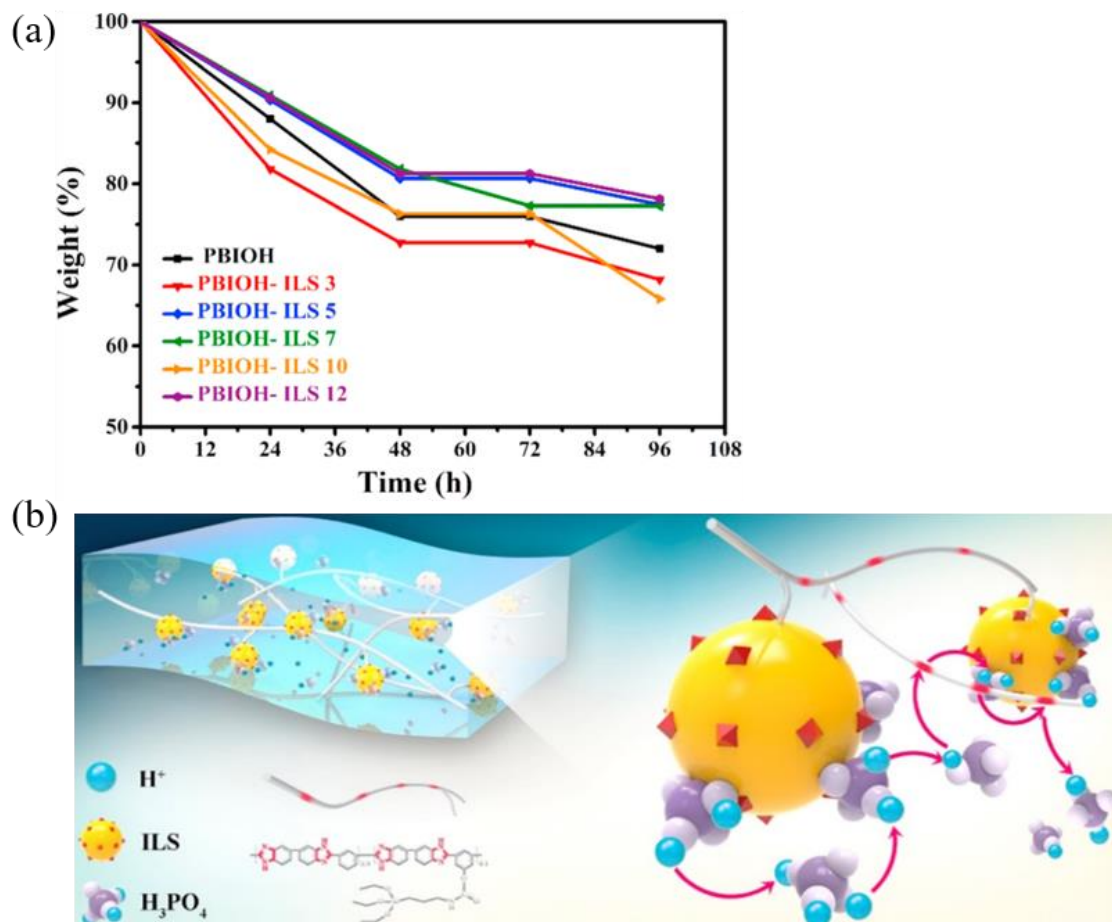


Fig. 3.9. (a) Fenton results and (b) proton transferring pathway in the PBIOH-ILS membranes (193).

3.4 Improving membrane mechanical strength

Since membrane degradation is the combination of mechanical, thermal and chemical effects, membrane mechanical degradation is of vital important as it can cause early life failure due to defects in the membrane or non-uniform stress along the membrane (111). In this section, approaches to alleviate the mechanical degradation will be described in four aspects, namely, crosslinking, blending with stable polymer, adding stable inorganic materials, and modifying membrane with designed structure.

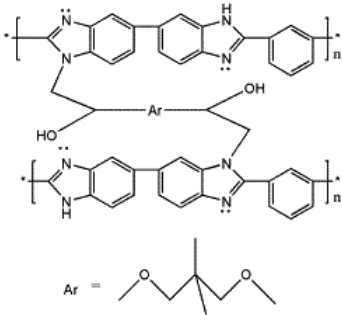
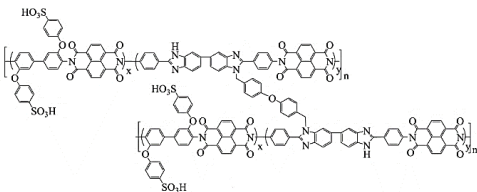
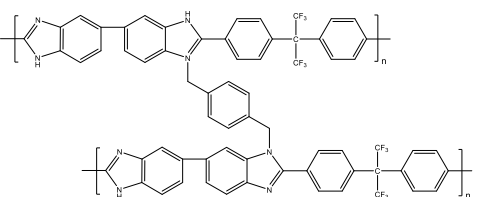
3.4.1 Crosslinking

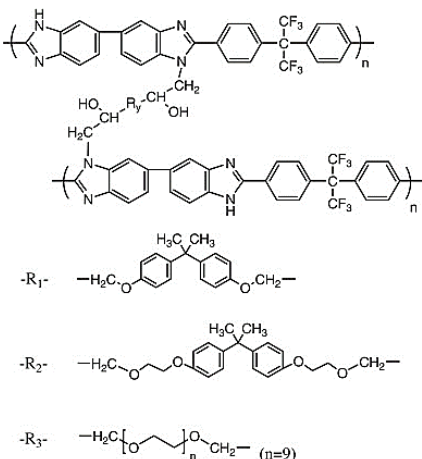
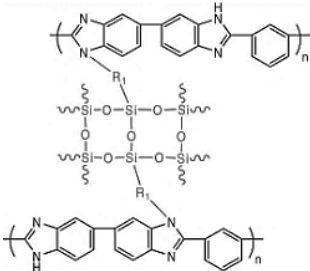
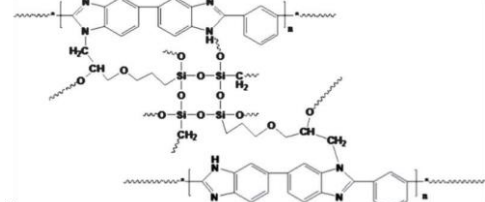
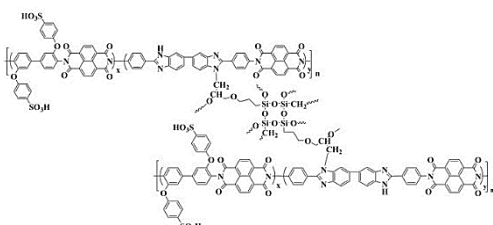
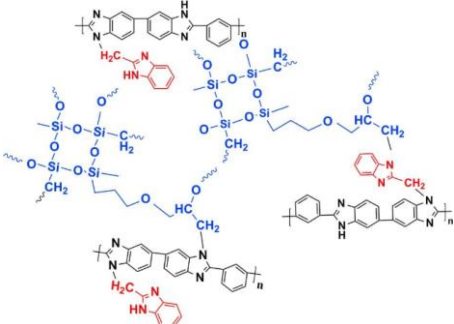
Compared with the introduction of hydrogen bonds or ionic interactions to compact the membrane structure with weak intermolecular connections and thermal stability (199), crosslinking is an efficient technique to get the compact structure with enhanced oxidative and mechanical stability

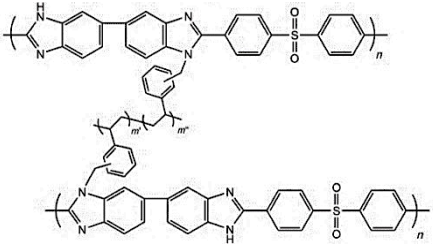
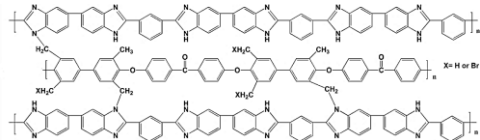
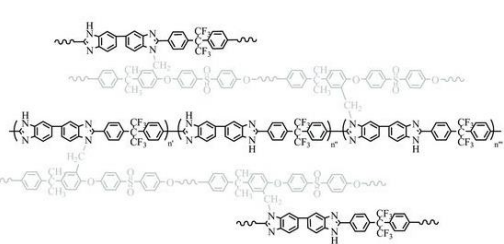
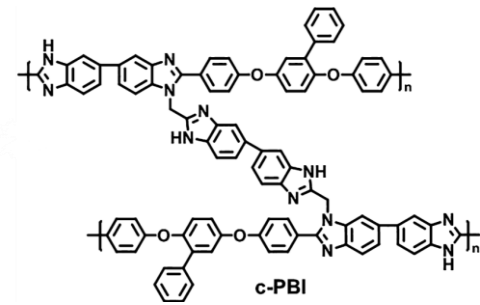
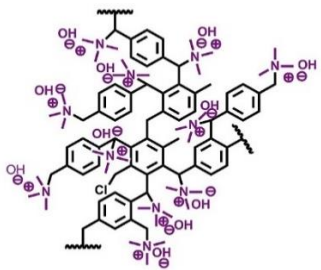
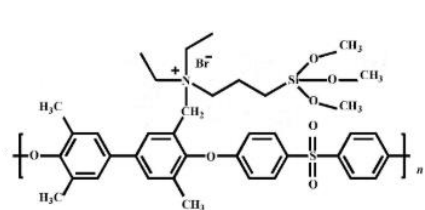
but usually at the expense with the consumption of N-H sites. The reduced available ionic sites for PA doping may reduce the membrane doping level and proton conductivity (200). Therefore, how to keep the balance between mechanical strength and proton conductivity is the main target when crosslinking.

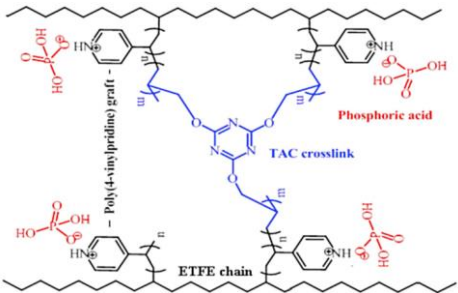
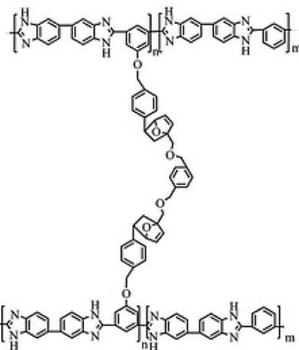
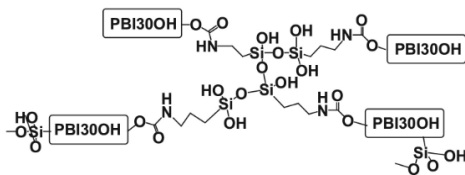
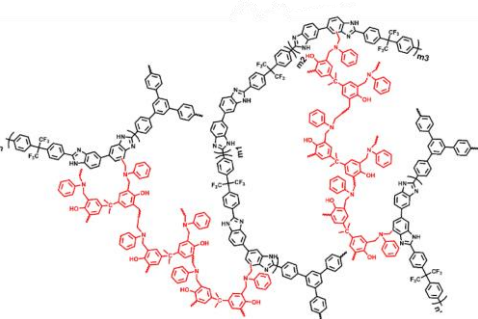
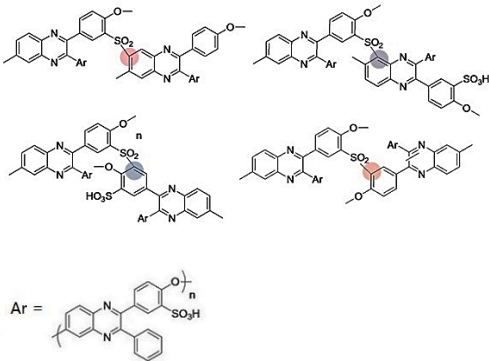
We already discussed crosslinking which can reduce PA leaching and alleviate membrane oxidation degradation in above sections. We focus here on the cases related to crosslinked applications which can improve mechanical properties (see Table 3.6). Four kinds of crosslinking will be discussed: 1. crosslinking at the expense of N-H sites (such as crosslinking using silane crosslinkers or macromolecular crosslinkers) (15, 157, 164-166, 168, 171, 172, 201, 202), 2. crosslinking with increased N-H sites (156, 203), 3. crosslinking without consuming N-H sites (119, 169, 177, 204-207), 4. crosslinking using special crosslinking methods such as thermal crosslinking or electron beam irradiation (208-210).

Table 3.6. Crosslinking for mechanical reinforcement of HT-PEMs

Polymer	Crosslinker	Structure	Tensile strength	Ref.
PBI	1,3-bis(2,3-epoxypropoxy)-2,2-dimethylpropane (NGDE)		101.61 MPa at RT ^b (undoped)	(162)
SPIBI	4,4'-bibromomethenyl diphenyl ether		137.8 ± 4.7 MPa at RT (undoped)	(168)
F6-PBI	p-xylylene dichloride		82.9 MPa at RT (undoped)	(157)

F6-PBI	bisphenol A diglycidyl ether (R ₁)/ bisphenol A propoxylate diglycidyl ether (R ₂)/ poly(ethylene glycol) diglycidyl ether (R ₃)	 <p>-R₁- $\text{—H}_2\text{C—O—C}_6\text{H}_4\text{—C(CH}_3)_2\text{—C}_6\text{H}_4\text{—O—CH}_2\text{—}$</p> <p>-R₂- $\text{—H}_2\text{C—O—CH}_2\text{—O—C}_6\text{H}_4\text{—C(CH}_3)_2\text{—C}_6\text{H}_4\text{—O—CH}_2\text{—O—CH}_2\text{—}$</p> <p>-R₃- $\text{—H}_2\text{C—[O—CH}_2\text{—CH}_2\text{—}]_n\text{—CH}_2\text{—}$ (n=9)</p>	0.8-8.7 MPa at (164) 10.6 mol ADL and 130 °C
PBI	((chloromethyl)phenylethyl)trimethoxysilane		1.4 MPa at 13.6 (201) mol ADL and 120 °C
PBI	(3-Glycidyloxypropyl)trimethoxysilane (KH560)		99.3 ± 8.6 at 7.13 (171) mol ADL and 130 °C
SPIBI	KH560		106.5 ± 11.5 MPa (172) at RT (undoped)
PBIIm	KH560		101.4 ± 3.9 MPa at (202) RT (undoped)

SO ₂ PBI	Poly(vinylbenzyl chloride)		10.4 MPa at 22 mol (165) ADL and RT
PBI	Bromomethylated poly (aryl ether ketone) (BrPAEK)		155.2 ± 3.0 MPa at (166) RT (undoped)
F6-PBI	Chloromethylated polysulfone		2.0 MPa at 22 mol (15) ADL and 130 °C
Ph-PBI	2,2'-Bis(chloromethyl)-5,5'-Bibenzimidazole (2BIM-2Cl)		13.6 MPa at 22 mol (203) ADL at RT
OPBI	poly(p-xylylene) with imidazolium groups		27.0 MPa at 3.69 (142) mmol/cm ³ and RT
QPAES	(N,N-diethyl-3-aminopropyl) trimethoxysilane		14 MPa at RT (204)

ETFE	Triallyl cyanurate (TAC)		43.6 ± 0.1 MPa at RT (undoped) (205)
PBI-VB	α,α' -difurfuryloxy-p-xylene (DFX)		101.36 ± 9.91 MPa at RT (undoped) (206)
PBI30OH	(3-isocyanatopropyl)triethoxysilane (ICTES)		74.18 MPa at RT (undoped) (169)
Branched F6-PBI	bis(3-phenyl-3,4-dihydro-2H-1,3-benzoxazinyl)isopropane (BA-a)		113 MPa at RT (undoped) (177)
ABPPQ	Sulfuric acid		99.5 ± 9.3 MPa at RT (undoped) (207)
PBI	Thermal curing	NR ^a	14.7 ± 0.9 MPa at 12.5 mol ADL and RT (208)

QPAEK	1,6-Diaminohexane and NR 4,4'- Diaminodiphenylmethane	64.0 MPa at RT (209) (undoped)
PBI	Electron beam irradiation NR	27 MPa at 6.87 mol (210) ADL and RT

^aNR = not reported. ^bRT = room temperature

Epoxy resins such as 1,3-bis(2,3-epoxypropoxy)-2,2-dimethylpropane (NGDE) (162) and 4,4'-diglycidyl (3,3',5,5'-tetramethyl biphenyl) (TMBP)(163, 173) (162, 163) have been reported as crosslinking agents to prepare crosslinked PBI membranes with improved mechanical properties. Because of the interactions between the imidazole rings of PBI chains and the epoxy groups of the crosslinkers which can restrict the movement of PBI chains, the crosslinked PBI-NGDE-15% (15% is the weight percent of epoxy resin in the crosslinked membrane) had better mechanical strength and displayed higher Young's modulus (3.02 GPa) and tensile strength (104.24 MPa), comparing with the pure PBI membrane with only 2.50 GPa Young's modulus and 77.76 MPa tensile strength.

Sulfonated poly(imide benzimidazole) (SPIBI) was crosslinked using crosslinker (4,4'-bibromomethenyl diphenyl ether) to prepare the crosslinked sulfonated poly(imide benzimidazole)s (CBrSPIBIs) (168). The tensile strength of CBrSPIBIs membrane increased from 73.7 MPa in non-crosslinked membrane to 137.8 MPa. The ionic interaction between the Lewis acid groups in SPIBI and basic -N=C- in the imidazole ring, and the covalent interactions between -NH groups and benzyl bromide, resulted in high density of polymers and improved mechanical strength.

Pioneer crosslinking work of Shen et al. (157) is porous fluorine-containing PBI (F6-PBI) crosslinked by p-xylylene dichloride and dibutyl phthalate (a kind of porogen). With the help of porosity and crosslinked network, good mechanical strength (0.9 GPa tensile modulus and 82.9 MPa stress) have been obtained. A similar approach (164) was proposed to compare different properties of F6-PBI membranes crosslinked by different epoxides (bisphenol A diglycidyl ether (R₁), bisphenol A propoxylate diglycidyl ether (R₂) or poly(ethylene glycol) diglycidyl ether (R₃)). As discussed in the part of alleviating oxidative degradation, the fluorine groups in the polymer and the aromatic-benzene-rings in R₁, R₂ and R₃ benefit enhanced oxidative stability. The mechanical strength was also improved from 0.4 MPa in original membrane to 0.8-8.7 MPa in the crosslinked membranes with 14 mol ADL at 130 °C. Especially, the long linear molecular chain of alkyl ether in R₃ caused low volume swelling and increased resistance to decompaction

of the polymer chains in R_3 crosslinked membrane, resulting in higher mechanical strength than other epoxides (R_1 and R_2) based membranes.

Alternatively, silane-based crosslinkers such as ((chloromethylphenylethyl)trimethoxysilane (201), 3-chloropropyltriethoxysilane (201), (3-Glycidyloxypropyl)trimethoxysilane (KH560) (16, 171, 172, 202), (N,N-diethyl-3-aminopropyl) trimethoxysilane (EPMS) (204), and ICTES (169), have been reported to crosslink the membranes. The silane-crosslinked structures can absorb more PA molecules onto their surface via electrostatic interactions to get improved PA stability in the membranes (171). In addition, all silane-crosslinked membranes displayed enhanced mechanical strength, improved dimensional stabilities as well as high conductivities as the dense crosslinked structures of Si-O-Si network were formed in the membranes by hydrolysing siloxane groups of silane-based crosslinkers (204). During the process of membrane preparation, the silane-based crosslinkers were firstly added into polymer solution to prepare membranes. Later, the isocyanate-hydroxyl reactions of silane-based crosslinkers in the membranes were conducted. Two common methods were used: 1) immersing the membrane in 1 M H_2SO_4 solution at 80 °C for 24 h to proceed the reactions (171, 172, 201, 202), 2) or drying the membrane at 110 °C for 1 day (169). As mentioned in the section of alleviating oxidative degradation, branched membranes have better chemical stability and proton conductivity than the crosslinked membranes. However, the branched polymer has larger free volume which can absorb more PA molecules and suffer relatively low mechanical strength. Very recently, to solve this problem, Wang's group have synthesized silane-crosslinked branched PBI membrane (16). After crosslinking by KH560, the crosslinked branched membrane has improved oxidative stability and mechanical strength, illustrating silane-crosslinking is one of the effective crosslinking methods to enhance the mechanical strength.

Similar to silane-based crosslinkers with big structure, novel macromolecular crosslinkers have many reactive functionalized groups and multiple crosslinked sites, leading to improved crosslinking connections and mechanical strength. In this approach, PVBCl (165), BrPAEK (166), and chloromethylated polysulfone (CMPSU) (15) have been prepared as macromolecular crosslinkers to reinforce PBI, SO_2 PBI and F6-PBI, respectively. Although the compact structures afford improved mechanical strength and oxidative stability, the proton conductivity are limited for the multiple-crosslinked membranes because of the consumption of acid doping sites for the multiple-crosslinked membranes. A balance is needed among proton conductivity, mechanical strength and oxidative stability. As reported by Yang et al. (15), good mechanical and oxidative stabilities perform improved stable durability (3500 h) for CMPSU crosslinked F6-PBI membrane at 10.4 mol ADL, comparing with similar stability of mPBI with lower ADL (6.2 mol). A good equilibrium was achieved among proton conductivity, getting compact structure and good mechanical strength in this work. This can be explained that the incorporated hexafluoro groups

(-C(CF₃)₂-) in the crosslinked structure gave free volume for more acid uptake without much membrane swelling.

Unlike the previous crosslinkers consuming the basic sites of polymers, a novel crosslinking agent, 2,2'-Bis(chloromethyl)-5,5'-Bibenzimidazole (2BIM-2Cl), was used to crosslink aryether-type poly(imide benzimidazole)s (Ph-PBI) to increase basic sites in the crosslinked network (203). c-PBI-X stands for the crosslinked membrane, and X is the molar ratio of -CH₂Cl in 2BIM-2Cl to -NH groups in Ph-PBI. Because of the additional basic sites in crosslinkers, excellent proton conductivity and tensile strength of the crosslinked membranes were observed although some N-H sites were consumed during crosslinking. The proton conductivity is 253 mS/cm at 200 °C which is two times larger than that of pure Ph-PBI membrane. Meanwhile, the tensile strength of c-PBI-20 is 13.6 MPa at 22.0 mol ADL, demonstrating outstanding dimensional-mechanical stability. In addition, different approaches by utilizing hyperbranched crosslinkers decorated with basic groups to crosslink OPBI polymers have been recently reported by Wang's group (142, 156). The hyperbranched crosslinkers with quaternary ammonium (QA) (142) or imidazolium groups (156) were reported as their large volumes which can immobilize PA molecules by hydrogen bonds and delocalization (211). Benefiting from the combined effect of crosslinking and additional basic QA groups which afford additional PA doping sites and proton transfer sites (Fig. 3.10a), the proton conductivity increases with crosslinking degree without loss of mechanical strength. For the undoped membranes, all crosslinked membranes have improved tensile strength comparing to the pure OPBI (Fig. 3.10b). After doping with PA which acts as a plasticizer to loosen the polymer chains, the tensile strength of PA doped membranes decreased but followed the same trend as the dry membranes. For instance, the tensile stress of PA doped membrane crosslinked by 15 wt% hyperbranched crosslinker with QA groups is 27.0 MPa at 3.69 mmol/cm³ acid content condition, which is still higher than the PA doped OPBI (18.5 MPa) at 3.30 mmol/cm³ as shown in Fig. 3.10c (142).

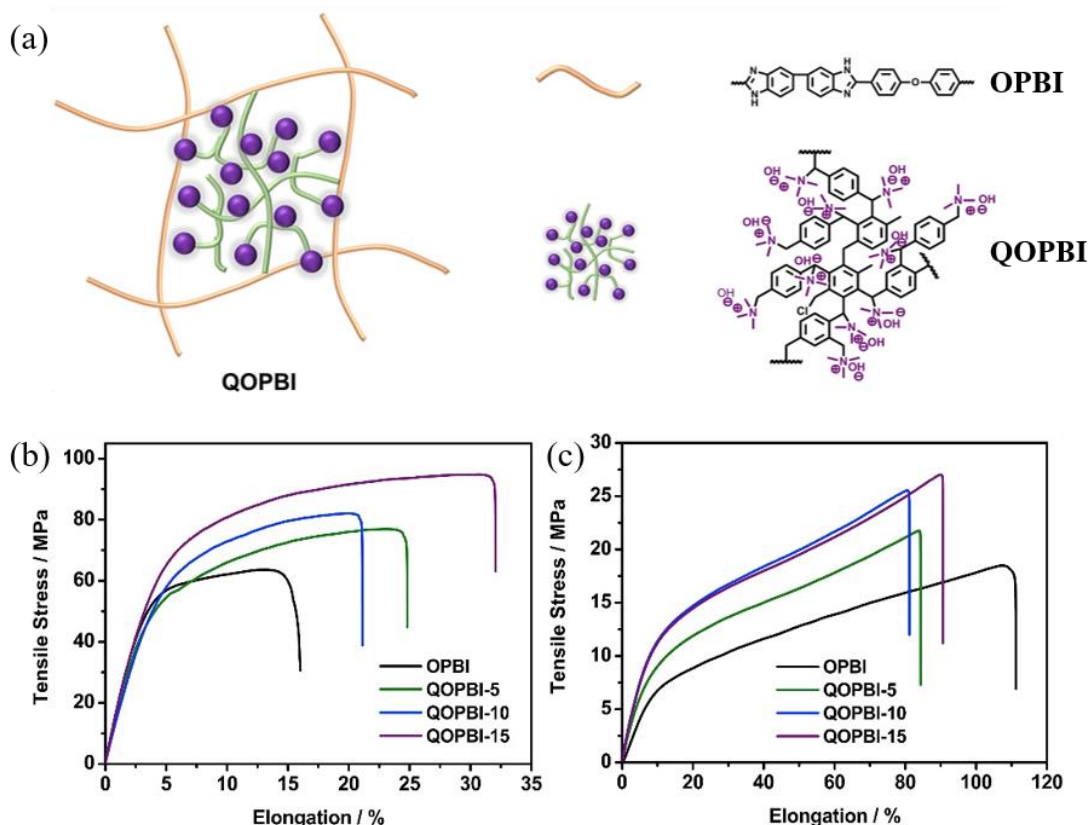


Fig. 3.10. (a) Structure of QOPBI, (b) mechanical properties of dry membranes and (c) PA-doped membranes (142).

In addition to the crosslinked membranes sacrificing N-H sites in polymer backbones, there is a different category of crosslinked membrane without occupying PA doping sites of the polymers. Triallyl cyanurate (TAC) (205) and 1,7-octadiyne (119) which have unsaturated bonds at their ends, were used to crosslink 4-vinylpyridine grafted ETFE and triazole modified poly(2,6-dimethyl-1,4-phenylene oxide), respectively. Both crosslinked membranes have improved tensile strength and elongation comparing with non-crosslinked membranes. Similar approaches were also reported that the crosslinkers, such as α,α' -difurfuryloxy-p-xylene (DFX), (3-isocyanatopropyl)triethoxysilane (ICTES), (N,N-diethyl-3-aminopropyl) trimethoxysilane (EPMS) and TAC were employed to crosslink the polymers containing hydroxyl groups (169, 204, 206), or sulfonic acid groups (207). For example, vinylbenzyl functionalized PBI was prepared using DFX to crosslink the hydroxyl groups in PBI-OH via a Diels-Alder reaction. The tensile strength of the crosslinked membranes increased from 45.2 to 101.4 MPa with increasing content of DFX (206). Wang et al. (177) reported another crosslinking application without sacrificing the N-H sites of polymers, which used the bis(3-phenyl-3,4-dihydro-2H-1,3-benzoxazinyl) isopropane (BA-a) as the novel crosslinker to synthesize crosslinked F6-PBI containing branched structures. Usually, for F6-PBI containing branched membranes or other

branched analogues, the mechanical strength is limited by free volumes and weak intermolecular force of the branched networks. However, the introduction of flexible side chains into the branched polymer can increase the entanglement of the polymer chain, and then improve the mechanical strength (151). Therefore, after being crosslinked by BA-a, the obtained membrane with bulky rigid structure has the reinforcement in the tensile strength comparing to that of non-crosslinked membrane.

A novel crosslinking method to produce mechanically-reinforced membranes is through a facile thermal curing method (208, 209). After thermally cured at 350 °C, a crosslinked PBI membrane becomes a thermosetting resin with a steeper slope of the stress-strain curve and lower elongation at break (208). For another thermal-curing application (209), 4,4'-Diaminodiphenylmethane and 1,6-Diaminohexane have been used as crosslinkers to prepare diamine-crosslinked poly(arylene ether ketone) containing pendant cationic quaternary ammonium group (QPAEK) membranes through thermal treatment at 100 °C. This simple and efficient thermo-curing crosslinking method shows a promising approach to synthesize cured membranes with improved mechanical toughness and chemical stability. Another interesting crosslinking method is by applying the electron beam irradiation to prepare ultra-thin crosslinked PBI membranes (210). After being irradiated by an electron beam, the membrane was crosslinked, resulting in better mechanical strength and chemical and thermal stability than the neat PBI membrane. The tensile strength of PA doped crosslinked membrane ranges from 19 to 27 MPa, higher than the pure PA doped PBI membrane (14 MPa) at similar doping level. However, the crosslinking methods through thermally curing or electron beam irradiation are limited by the characteristics of the polymers. More polymers are needed to be explored to get a crosslinked structure using these two facile methods.

3.4.2 Blending with a stable polymer

A facile approach to increase the membrane mechanical strength is the physical blending with other stable polymers such as PTFE and PVDF. During the blending procedure, two factors are usually considered: the solubility of blending polymers in organic solvent and the miscibility between polymers. Some blending applications (summarized in Table 3.7) have been studied in HT-PEMFCs conferring sufficient proton conductivity and mechanical strength.

Table 3.7. Polymer blending applications for mechanical reinforcement.

Polymer	Additives	Tensile strength	Ref.
PBI	PVDF-HFP	6.85 MPa at 5.61 mol ADL and RT ^a	(179)
MeIm-PAEK	PVDF or PVDF-HFP	2.1-6.9 MPa at RT	(212)

PVP	PES, PSU, PEK-c, PVDF or PVDF-HFP	0.5-1 MPa at 110 °C	(213)
PBI	Porous PTFE film	40.83 MPa at RT (undoped)	(214)
PES-PVP	Porous PTFE film	6.58 MPa at 6.5 mol ADL and RT	(215)
qPVBzCl ⁺	Porous PTFE film	56.23 MPa at 5 mol ADL and RT	(216)
PBI	QPPSf	11.9 MPa at RT	(145)
OPBI	PAPE	1.92 MPa at RT	(217)

^aRT = room temperature

As the fluoropolymers and engineered thermoplastics, both PVDF and PVDF-HFP have advantages such as different crystalline forms, hydrophobicity, good ionic conductivity, high chemical and thermal resistances. Hazarika et al. (179) reported the partially miscible blends of PBI and PVDF-HFP. Because the increasing content of PVDF-HFP reduces the volume swelling of the membrane, the mechanical strength of the blended membrane increases with the increasing content of PVDF-HFP. Another research reported by Yang et al. (212) used methylimidazolium poly (aromatic ether ketone) (MeIm-PAEK)/PVDF or MeIm-PAEK/PVDF-HFP. Similar to PBI/PVDF-HFP composite membrane, these blended membranes display higher mechanical strength and lower dimensional swelling than the pure MeIm-PAEK membrane. Also, Ren et al. (213) reported a series of polyvinylpyrrolidone (PVP) blended membranes by mixing with polyethersulfone (PES), polysulfone (PSU), polyetherketone-cardo (PEK-c), PVDF or PVDF-HFP. It was found that PVP blend membranes with aromatic polymers (PSU, PEK-c and PES) have more advantages (such as decreased volume swelling, improved mechanical strengths, and increased ADL and proton conductivities) than those blend membranes with aliphatic polymers (PVDF and PVDF-HFP).

PTFE is another well-known polymer with excellent thermal and oxidative stability and good mechanical strength. To improve the membrane mechanical properties and durability without sacrificing the proton conductivity, many applications using porous PTFE film as a supporting matrix have been developed in the HT-PEMFCs. All reinforced composite membranes which were prepared by penetrating the ionomer solution into the porous PTFE membrane showed prominent mechanical stabilities (214, 216, 218, 219). For example, the porous PTFE reinforced dimethylhexadecylamine partially quaternized poly (vinyl benzyl chloride) (qPVBzCl⁺) membrane prepared by Cao et al. (216) had a higher tensile stress (56.23 MPa) after PA doping, comparing with only 9.55 MPa tensile strength of PA doped pristine

qPVBzCl⁺ membrane, while the Young's Modulus of qPVBzCl⁺ membrane is 0.25 GPa which is also higher than the pure one (0.1 GPa).

In addition to fluoropolymers (PVDF, PVDF-HFP, and PTFE), there are a category of polymers which can form interactions with PA molecules and polymers to increase the mechanical strength with less reduced proton conductivities (145, 217, 220). As one of the polycations with strong electrostatic interactions with PA, chloromethylated polysulfone (CMPSf) was blended with PBI membrane at different volume ratios (145). The chloromethylated groups in CMPSf was then converted to quaternary benzylpyridinium chloride groups (QP) by immersing the membrane in pyridine to obtain the quaternary benzylpyridinium cation grafted polysulfone membrane (QPPSF). Since QPPSF promotes hydrogen conducting and facilitates PA uptake, this blended membrane showed excellent proton conductivity (0.3 S/cm at 240 °C). Also, good mechanical properties (11.9 MPa at break) were achieved, comparing with pure PBI (8.2 MPa at break). In addition, Koyilapu et al. (217) investigated a novel blend membrane containing OPBI and poly(aminophosphonate ester) (PAPE) polymers. The phosphonate ester and diamine groups in PAPE created hydrogen bonding with OPBI and PA, which promoted the stronger mechanical strength and good proton conductivity. The OPBI/PAPE 75/25 blend membrane (25% PAPE in OPBI) showed the best mechanical stability with 272% elongation and 1.92 MPa tensile strength at break. A similar behaviour was also found in the polymer blend of OPBI and poly(azomethine-ether) (PAME) (220). the storage modulus of the OPBI/PAME blend membranes are higher than that of the pure OPBI from 100-400 °C.

3.4.3 Incorporating inorganic materials

The mechanical properties can be improved by adding inorganic particles. Various types of inorganic materials have been used in published papers, including silica-based materials, clay-based materials, layered materials (GO, carbon nitride or Ti₃C₂T_x), hygroscopic oxides (TiO₂ and ZrO₂), heteropoly acids or perovskites (see in Table 3.8). Each of these materials possesses their own advantages and challenges, as will be discussed below.

Table 3.8. Inorganic additives for the mechanical reinforcement

Polymer	Additives	Mechanical strength	Ref.
PBI	SiO ₂	34 MPa at RT ^a (undoped)	(221)
PBI	Functionalized silica nanoparticles	98 MPa at RT (undoped)	(222)
ABPBI	Sulfonated silica	Not reported	(223)

PBI	Zwitterion-coated silica nanoparticle	67.5 MPa at 30 °C (undoped)	(131)
PBI	MDA-SBA-15	42.30 MPa at RT (undoped)	(224)
OPBI	mSiC modified by 3-aminopropyltriethoxysilane (KH550)	36.6 MPa at 9.1 mol ADL and RT	(225)
PBI	Clay	3.9-8.4 MPa at 8 mol ADL and 150 °C	(28)
ABPBI	Nanoclay cloisite Na ⁺	88.8 MPa at RT (undoped)	(226)
PBI	Radiation grafting graphene oxide	19.3 MPa at 12.5 mol ADL and RT	(227)
PBI	Sulfonated graphene oxide	36.4 MPa at 9.1 mol ADL and RT	(228)
Py-PBI	Phosphonic acid functionalized graphene oxide	7.14 MPa at 5.80 mol ADL and RT	(229)
PBI	Triazole modified graphene oxide	12.6 MPa at 12.2 mol ADL and RT	(230)
PBI	Electrochemically exfoliated graphene oxide	Around 12 MPa at 9.7 mol ADL and RT	(26)
PVP/pPPO	Graphitic carbon nitride	22.91-43.12 MPa at RT	(231)
PES-PVP	Graphitic carbon nitride	40.4-48.2 MPa at RT	(232)
PBI	Ti ₃ C ₂ T _x (MXene)	30.3 MPa at 3.23 mol ADL and RT	(233)
ABPBI	ZrO ₂	87.5 MPa at RT (undoped)	(234)
2,6-Py-PBI	ZrO ₂	7.5 ± 0.03 at 9.75 mol ADL and RT	(21)
Am-SPAEEKS	Functionalized TiO ₂	53.36-62.09 MPa at RT (undoped)	(155)
s-PBI	TiO ₂ /cellulose nanohybrids	Around 130 MPa at RT (undoped)	(235)
PBI	12-Silicotungstic acid	140 MPa at RT (undoped)	(236)
PBI	Ba _{0.9} Sr _{0.1} TiO ₃ /La _{0.9} Sr _{0.1} CrO _{3-δ}	24-48 MPa at RT (undoped)	(22)

^aRT = room temperature

PBI/SiO₂ composite membrane was prepared by Devrim et al. (221). The homogeneous SiO₂ dispersion in PBI membrane and the interactions between PBI and SiO₂ contribute to the

enhancement of tensile strength (34 MPa), higher than that of pristine PBI membrane (31.2 MPa). In addition, N-(p-carboxyphenyl)maleimide (pCPM) modified silica was synthesized via an ozone-mediated process to increase the compatibility between silica and PBI (222). The localized benzimidazole units of pCPM modified silica also induced the formation of additional proton-conducting channels to get an improved proton conductivity (50 mS/cm at 160 °C) which is 25% higher than that of original PBI. Interestingly, the mechanical strength increases with the increasing amount of silica (up to 20 wt%) and the highest proton conductivity occurs at 10 wt% silica. The excess silica might lead to aggregation which deteriorates the proton conductivity. Similar effects were observed in the sulfonated silica (223), zwitterion-coated silica (131), and melamine-based dendrimer amine (MDA) functionalized SBA-15 mesoporous silica (224), which formed nanoparticle clusters in ABPBI, F6-PBI, and PBI respectively. These functionalized groups (sulfonic acid, amino groups and MDA groups) on the surface of silica can interact with polymer and PA to form a hydrogen-bond network to get improved proton conductivity. It is worth mentioning that the functionalized SBA-15 mesoporous silica can display a better PA retention because of the porous structure with PA trapping sites. In addition to functionalized silica, other derivatives such as 3-aminopropyltriethoxysilane (KH550) modified silicon carbide (225) had also been developed to be the inorganic fillers in the membrane matrix. Comparing with OPBI/PA membrane, this PA doped organic-inorganic membrane showed an 35% increase in tensile strength (36.6 ± 3.9 MPa) and an 55.7% increase in proton conductivity (27.1 mS/cm at 170 °C), which were attributed to the strong interactions among the amino groups of KH550 modified silicon carbide, the imidazole rings of PBI and PA molecules.

Instead of silica-based materials described above, some researchers have studied the applications of inorganic minerals in HT-PEMFCs. Plackett et al. (28) reported the addition of ammonium or pyridinium salts-modified laponite clays (up to 20 wt% clay) to PBI to prepare homogeneous composite membranes. Increases in tensile modulus, elongation and tensile strength of PBI-clay membranes were observed, comparing with the pristine PBI membrane at similar ADL and temperature. The hydrogen crossover was also reduced which was five times lower than the unmodified PBI membrane. A similar approach had been studied by Bao et al. (226) with the incorporation of ionic liquid modified Cloisite Na⁺ (a kind of montmorillonite sodium nanoclay) into ABPBI matrix. The membrane containing 3 wt% Cloisite Na⁺ showed the highest mechanical strength and good ionic liquid absorption without aggregation. Due to the good dispersion and high exfoliation degree of nanoclay, the tensile strength and Young's modulus of the composite membrane had over 90% and 40% improvement, respectively. The improved mechanical properties were attributed to the high aspect ratio of rigid exfoliated nanoclay which can hinder and delay the propagation of micro-cracks in the membrane (226).

One of the most extensively explored inorganic materials are the two-dimensional (2D) layered fillers, such as graphene oxide (26, 227-230), carbon nitride (231, 232) and transition metal carbides (233). Because of its low manufacturing cost, outstanding mechanical properties and large surface area, graphene oxide (GO) has attracted tremendous attention (237). Specially, the hygroscopic oxygen-containing functional groups of GO such as epoxy, carboxyl and hydroxyl groups can interact with amino groups in the imidazole ring of polymers and further form hydrogen or ionic bonds to facilitate proton conduction (238). Therefore, the mechanical properties of this organic-inorganic composite membrane can be improved without the sacrifice of proton conductivity. Furthermore, to increase the processability and compatibility of GO in organic solvents, functionalized GO such as radiation grafted GO (227, 228), phosphonated GO (229), triazole modified GO (230), and electrochemically exfoliated graphene oxide (26), have been successfully synthesized and employed in HT-PEMs. All GO incorporated membranes showed increased mechanical strength, while the additional functionalized groups in GO can interact with PA via hydrogen bonding and result in improved ADL and proton conductivity. When the amount of GO exceeded a certain level, the homogeneous dispersion will not be formed because of aggregation, leading to deteriorated mechanical properties and proton conductivity. Similar to GO, graphitic carbon nitride is a 2D inorganic layered material with tri-s-triazine units and amino groups. Zou et al. (231) and Bai et al. (232) recently reported that graphitic carbon nitride was incorporated in PVP/phosphonated PPO blend membrane and PES/PVP blend membrane, respectively. The amino groups of graphitic carbon nitride can form hydrogen bonding with PA to enhance the Grotthuss-type proton conduction. Also, these nanocomposite membranes displayed enhanced mechanical properties because of the mechanical reinforcement effect of graphitic carbon nitride nanosheets. For example, in the PES/PVP membrane with 0.5 wt% graphitic carbon nitride, higher proton conductivity (0.104 S/cm) and increased tensile strength (6.0 MPa) were obtained at 160 °C, comparing with 0.076 S/cm and 3.75 MPa of the pristine membrane. Another 2D material is MXene, a kind of layered ceramics (ternary carbide and nitride) with metallic properties (239). Generally, the chemical formula is $M_{n+1}AX_n$ where M stands for an early transition metal, n equals 1, 2 or 3, A is the IIIA or IVA element, and X represents the carbon or nitrogen atom. It was found that the termination of MXene surfaces contains proton conducting groups such as oxygen, hydroxyl and fluoride groups (240). The application of MXene ($Ti_3C_2T_x$) in HT-PEMFC has been developed by Fei et al. (233). Due to the oxygen-containing groups which can interact with PA and PBI, there are some improvements in the proton conductivity (up to 1.4×10^{-2} S/cm) and mechanical properties (up to 30.3 MPa tensile strength), comparing to pristine PBI membrane (5.1×10^{-3} S/cm proton conductivity and 12.2 MPa tensile strength).

The ceramic and hygroscopic oxides, such as zirconia and titania, also showed attractions to improve membrane mechanical properties in fuel cells. Zheng et al. (234) studied the fabrication of ABPBI membranes with incorporated ZrO_2 nanoparticles. The resulting membrane showed improved tensile strength when the content of ZrO_2 increased from 5 to 15 wt%. This can be explained that the interactions between ZrO_2 and polymers strengthen the membrane stiffness and anti-deformation capability. However, the proton conductivity decreased when the content of ZrO_2 exceeds 10 wt%, which is lower than that of pure ABPBI, demonstrating that proton conductivity decreases with increasing inorganic materials at high concentration when the particle aggregation happens. The poor proton conductivity and incompatibility of hygroscopic oxides and dilution effect on the proton conductive groups lead to the poor conductivity. Similar results occurred in the ZrO_2 added 2,6-pyridine PBI membranes (21), where the addition of ZrO_2 in the membrane increased the tensile strength. Later, to obtain better interactions between hygroscopic oxides and polymers, the functionalization of these hygroscopic oxides have been developed, namely, titania/cellulose bionanocomposites (155) and functionalized titania with amino acid groups (235), all of which showed enhanced mechanical strength without loss of proton conductivity.

Heteropoly acids (HPA) have been studied in many areas, including biochemistry, chemical analysis, sensors, ion selective membranes and fuel cells (241). In the applications of fuel cells, HPA can work as a membrane inorganic additive or catalyst additives to improve ionic conductance (242). Recently, Nguyen et al. (236) used 12-silicotungstic acid as an inorganic filler and incorporated it into PBI membrane to get enhanced thermal stability, proton conductivity and tensile strength. Perovskite was also regarded as a suitable inorganic additive in HT-PEMs due to its excellent proton conductivity and good thermal stability (243). Hooshyari et al. (22) applied barium strontium titanate ($\text{Ba}_{0.9}\text{Sr}_{0.1}\text{TiO}_3$) and lanthanum strontium chromate ($\text{La}_{0.9}\text{Sr}_{0.1}\text{CrO}_{3-\delta}$) doped perovskite nanoparticles in PBI-based membranes. The addition of perovskites with oxygen vacancies showed increased mechanical properties without sacrifice of proton conductivity.

The incorporation of inorganic materials into the membrane matrix can benefit mechanical reinforcement, but at the expense of proton conductivity or phase separation if the inorganic nanoparticles cannot evenly disperse in the membrane matrix. Thus, the functionalization of these inorganic materials is important to modify their surface groups and therefore increase their processability and compatibility to strengthen membrane mechanical strength without loss of proton conductivity.

3.4.4 Modifying membrane with designed structure

Various methods, such as polymer crosslinking, polymer blending, and incorporating inorganic materials, have been applied to improve membrane mechanical properties. Even though there are some mechanical improvements for the membranes, their proton conductivities reduced to some extent as the PA absorption sites are occupied or diluted by the introduced groups or particles (244). Therefore, to seek an optimal compromise between proton conductivity and mechanical property of HT-PEMs is still facing challenges. Recently, it was reported that the mechanical strength will not deteriorate if the PA doping sites are separated from polymer backbones (244). One promising approach is to graft pendent side chains with functionalized groups such as imidazole (244, 245), tetrazole (246), and amine groups (89, 247, 248) away from the polymer backbones. On the other hand, fabrication of polymers with high molecular weight (109, 154, 208, 249, 250) or multilayer membranes (251-254) to strengthen membrane mechanical strength will also be discussed.

As reported by Bai et al. (244), poly(1-vinylimidazole) grafted polysulfone membranes were prepared via atom transfer radical polymerization. Different grafting degrees resulted in different lengths of imidazole side chains, which worked as PA doping sites and micro-phase separation for quick proton transfer. Meanwhile, the mechanical properties of the membrane will not decrease as the polymer backbones are not affected when the PA doping sites are away from backbones. The membrane showed outstanding proton conductivity (127 mS/cm at 160 °C) and excellent tensile strength (7.90 MPa). A similar trend was sought by Li et al. (245) by incorporating benzimidazole groups onto the Ph-PBI via N-substituted reaction. Because of the interactions between polymer chains and additional benzimidazole groups, the grafted Ph-PBI membrane exhibited excellent tensile stress (20 MPa), higher than the pure Ph-PBI membrane. Similarly, some functional groups like tetrazole (246), 2,4,6-tri(dimethylaminomethyl)-phenol (247), and quaternized 4-vinylbenzyl chloride (248) had been grafted to chitosan, BrPAEK and PSU, respectively. Unlike traditional PA doped membranes (Fig. 3.11a), all these N-substituted grafted membranes have prominent mechanical properties with improved Young's modulus since the N-substituted side chains can attract more PA molecules without plasticization of backbones as shown in Fig. 3.11b. However, the grafting degree of the membranes should be well-controlled as inappropriate grafting degree can lead to less or more free volumes for PA doping and have a negative impact on the membrane mechanical strength.

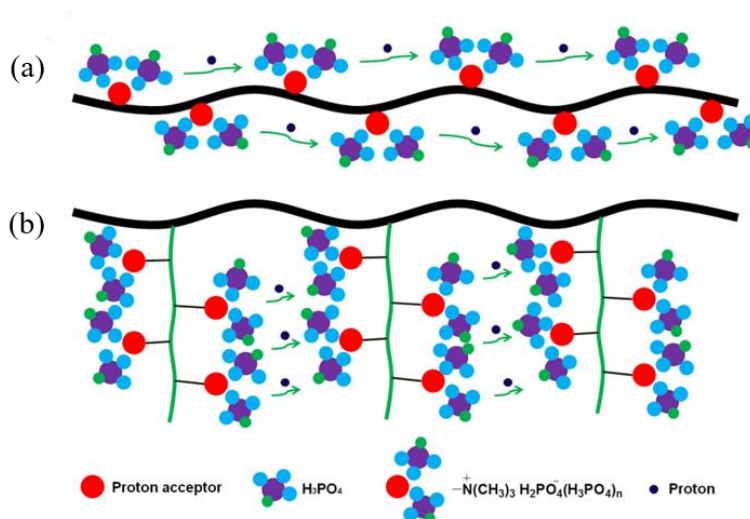


Fig. 3.11. (a) Traditional proton transferring pathway in a main chain structure and (b) side chain structure (248).

An alternative method that yields the improvement of the mechanical strength is the fabrication of high-molecular-weight polymers (109, 154, 208, 249, 250). Usually PBI polymer was synthesized by the polymerization of 3,3'-diaminobenzidine tetrahydrochloride and isophthalic acid with a molar ratio of 1: 1 using polyphosphoric acid (255). The molecular weight of PBI can be controlled by different reaction time and polymerization temperature. As the polymer's London force and induction interactions increase with the rise of polymer molecular weight (108), the membrane with high molecular weight has good mechanical strength. For instance, SO₂PBI and its co-polymers with poly[2,2'-p-(phenylene)-5,5'-bibenzimidazole] (pPBI) with high molecular weight were developed by Li's group through the polymer copolymerization (154). The obtained copolymers (Co-x%SO₂PBI, x is the molar percent of SO₂PBI) had excellent mechanical strength. The flexible aryl sulfone linkages of SO₂PBI segment can result in the good polymer solubility in the solvent, and the stiff para-phenylene of pPBI segment benefits excellent mechanical strength. As the PBI membranes with para structure have higher tensile strength than the PBI with meta structure (256), the tensile strength of Co-20%SO₂PBI membrane (16.4 MPa) is also better than that of SO₂PBI (9.4 MPa) and mPBI (5.8 MPa) at room temperature with similar ADL (around 11 mol). Another application is the copolymerization of 2,5-pyridine-PBI with the PBI containing para-, meta- or dihydroxy structure using polyphosphoric acid process (257). The Young's modulus of PBI membrane with para-structure also shows improved tensile properties and increases with the increase of molecular weight.

The mechanical properties can be improved by preparing multilayer membranes due to the mechanical reinforcement of membrane layers (251-254). The first application about the multilayer membrane described in the literature (251) was the three-layer membrane (graphene oxide reinforced PBI/porous PBI/graphene oxide reinforced PBI membrane, named as PBI-

RGO/PPBI/PBI-RGO) where the PPBI membrane was sandwiched by two PBI-RGO membranes. The tensile strength of PA doped PBI-RGO/PPBI/PBI-RGO membrane is in the range from 22.7 to 38.5 MPa, much higher than that of PA doped PBI membrane (7.9 MPa). Similarly, a three-layer membrane of PBI/GO/PBI was fabricated by Deng et al. (252) via a layer-by-layer method. Since the inner GO layer is less expandable after PA doping which helps decrease membrane swelling, the mechanical strength of the multilayer membrane (28.6 MPa) is higher than that of pure PBI membrane (12.2 MPa) at 150 °C. Another novel multilayer membrane was prepared using SPEEK and polyurethane (PU) through a layer-by-layer self-assembly technique (253). The noteworthy mechanical property was achieved due to the strong electrostatic interactions between sulfone groups in the SPEEK matrix and -C-N⁺ group in PU matrix. In another application reported by Park et al. (254), the porous hygroscopic-pre-treated PTFE membrane worked as a reinforcing membrane matrix and the PBI membrane was cast on it. This two-layer membrane showed 32.65 ± 0.61 MPa ultimate tensile strength, while the pure PBI membrane only had 17.54 ± 1.04 MPa tensile strength.

3.5 Durability of acid-based membranes

There are lots of ex-situ investigations to evaluate fuel cell performance such as testing the oxidative stability in Fenton reagents or evaluating PA retention over hot water. However, few studies have been conducted via the in-situ measurements for fuel cell performance, particularly long-term durability tests which can present a reliable and overall evaluation for fuel cell performance and degradation. Up to now, steady-state operation and dynamic-state operation have been developed to evaluate the actual fuel cell lifetime (258). As the most common testing mode, the steady-state operation conducts the cell running at a constant current or voltage for a certain time to accurately measure and access the performance and durability of fuel cells. Meanwhile, compared with the steady-state method which is time-consuming and expensive, the dynamic-state operation or accelerated stress tests can be utilized to investigate the performance and degradation in a shorter time (259) and get a better understanding for the performance aging mechanisms according to different operation conditions (55). Several dynamic durability testing protocols such as potential cycling durability tests, start-up/shutdown cycling durability tests and drive cycle tests (54) have been employed to evaluate the cell degradation properties. To evaluate how the electrochemical property changes with time, measurements such as hydrogen crossover, polarization curves, membrane resistance, and electrochemically active surface area can be in-situ tested periodically during the durability test.

This section will focus on the published literature which is related to the in-situ measurements to evaluate the durability of acid-based HT-PEMs. Three major aspects which enhanced membrane durability will be discussed, namely crosslinking, incorporating proton-conductive additives, or

modifying membrane structures (Fig. 3.12). In addition, a summary of membranes with improved durability according to the lifetime and degradation rate is displayed in Table 3.9-12 and a comparison of power density among these approaches has been proposed in Fig. 3.13 which will be discussed later.

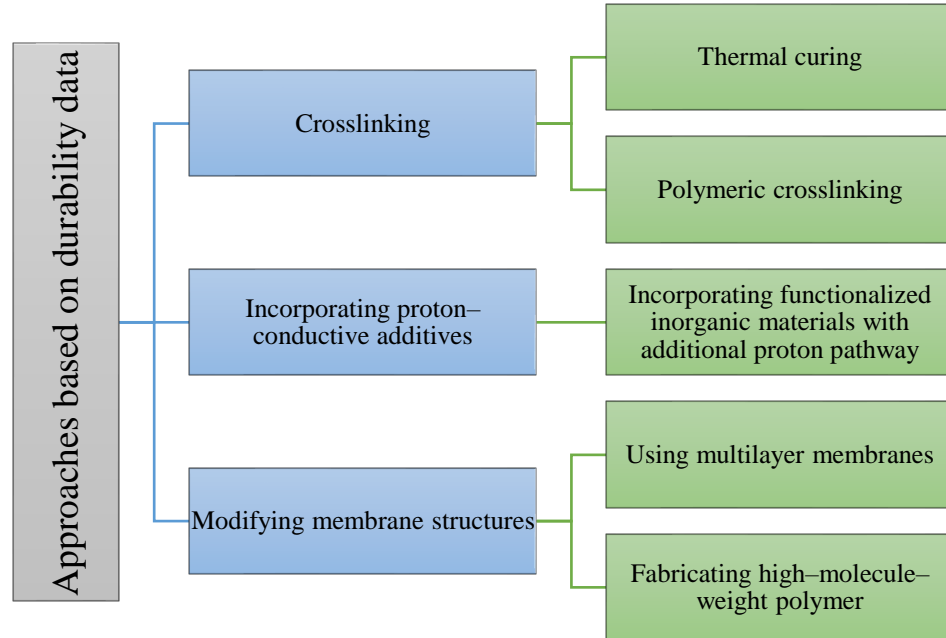


Fig. 3.12. A summary of approaches with excellent lifetime in HT-PEMFCs.

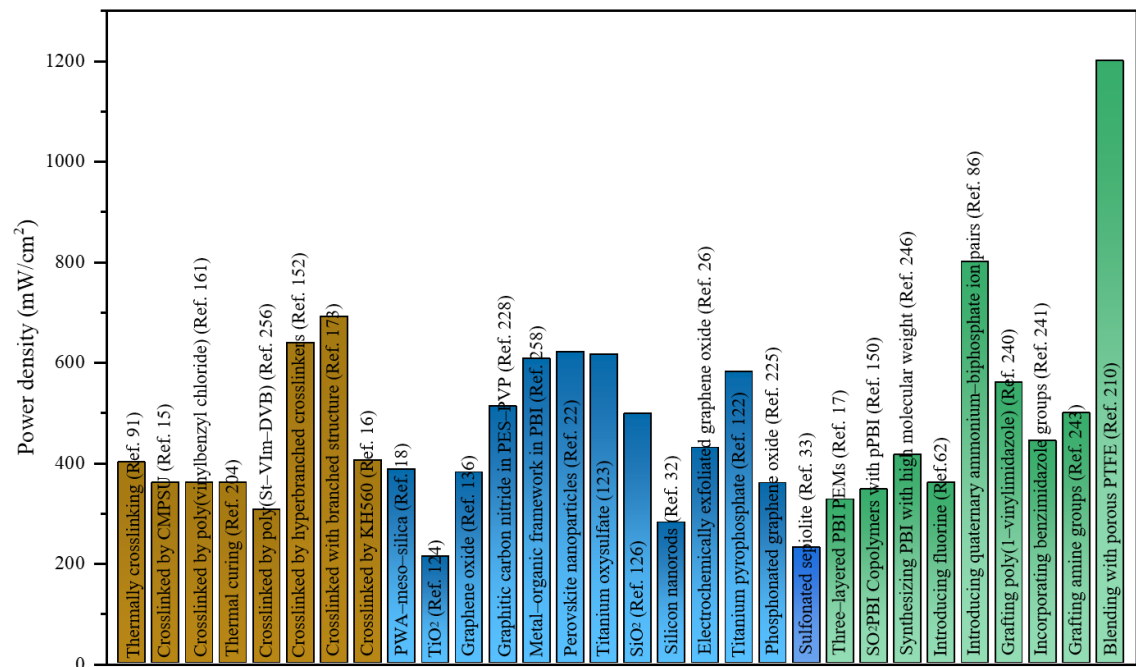


Fig. 3.13. Performance comparison of the reported applications based on the durability of HT-PEMFCs where brown, blue and green bars stand for the applications utilizing crosslinking, incorporating proton-conductive additives, and modifying membrane structures, respectively.

3.5.1 Crosslinking

Usually the improved mechanical properties will be observed in the crosslinked membranes as the compact structure of the crosslinked membrane benefits more interactions between polymer chains, which results in the reinforcement in mechanical strength and acid retention. Also, it becomes more difficult for radicals to arrive to the polymer chains to get enhanced chemical stabilities. However, the ADL and proton conductivity might be deteriorated because of the formation of dense structures. A compromise among mechanical strength, oxidative stability and proton conductivity should be considered. Until now, two major crosslinking approaches (thermal curing and polymeric crosslinking) had been reported to get a stable durability and lifetime as shown in Table 3.9.

Thermal curing is to treat the membrane at temperatures up to 350 °C to get a crosslinked structure. After thermal curing, the PBI membrane had similar features with a thermoset resin such as high swelling resistance, insolubility, and enhanced mechanical property. It was reported that the thermally crosslinked PBI membranes had long-term durability and low degradation rate (94, 208). Comparing with the membrane without thermally treating, a lower acid loss in the thermally crosslinked membrane was observed (94). The crosslinking using polymeric or macromolecular crosslinkers is another promising method for the durability enhancement of PA-doped HT-PEMs. As the polymeric covalently crosslinked membranes have 3D multi-crosslinked network with large free volume and ADL, the tensile strength and proton conductivity of the crosslinked membranes are higher than the corresponding linear membranes. Table 9 includes four major macromolecular crosslinkers, chloromethylated polysulfone (CMPSU) (15), poly(vinylbenzyl chloride) (165), poly(styrene-vinylimidazole-divinylbenzene) (poly(St-VIm-DVB)) copolymer (260) or hyperbranched crosslinkers (156). All membranes crosslinked by these crosslinkers showed a stable durability.

The crosslinking application with the best durability (13000 h) is the one using thermally crosslinking (94). Compared with the liner PBI membrane with 4.6 $\mu\text{V/h}$ decay rate, only 1.4 $\mu\text{V/h}$ decay rate was observed in the thermal crosslinking application where a better acid retention benefits the lower decay rate during the long-term operation. However, as shown in Fig. 15, the crosslinking application with highest power density is the one using the polymeric or macromolecular crosslinkers (638 mW/cm^2 in OPBI membranes crosslinked by hyperbranched crosslinkers, and 690 mW/cm^2 in F6-PBI membranes crosslinked with branched structure) (156, 177). This is probably due to the higher ADL and acid retention stability in these membranes with polymeric crosslinked structures.

Table 3.9. Summary of durability data for selected membranes via crosslinking.

Polymer	Thickness (μm)	Proton conductivity (mS/cm) ^a	PA retention ability	Oxidative stability ^b	Durability	Degradation rate	Modification	Ref.
m-PBI	40	NR ^c	25 wt% loss after 13000 h	NR	13000 h	1.4 $\mu\text{V/h}$	Thermally crosslinking	(94)
F6-PBI	NR	115 (160 °C)	NR	93 wt% remaining after 200 h	3500 h	4 $\mu\text{V/h}$	Crosslinked by CMPSU	(15)
SO ₂ PBI	NR	93 (160 °C)	NR	Less than 15 wt % after 350 h	2200 h	13.7 $\mu\text{V/h}$	Crosslinked by poly(vinylben zyl chloride)	(165)
PBI	20-80	60 (150 °C)	0.05 wt% loss per hour	NR	2000 h	43 $\mu\text{V/h}$	Thermal curing	(208)
PAEK containi ng four methyl groups	NR	117.3 (180 °C)	NR	NR	600 h	39 $\mu\text{V/h}$	Dual crosslinked by employing poly(St-VIm- DVB)	(260)
OPBI	NR	89 (160 °C)	67.9 wt% loss at 80 °C/40% RH after 96 h	90 wt% remaining after 200 h	390 h	No voltage degradation	Crosslinked by hyperbranche d crosslinkers	(156)
F6-PBI	40	73 (160 °C)	NR	NR	200 h	Stable open- circuit voltage	Crosslinked with branched structure	(177)
Branche d OPBI	40	44 (180 °C)	18.9 wt% loss at 80 °C/40% RH after 45 h	12.8 wt% loss after 90 h	200 h	No obvious loss	Crosslinked by KH560	(16)

^aIn-plane proton conductivity. ^btested in Fenton reagent. ^cNR = not reported.

Crosslinking is a promising method to get more interacted polymer structure, and the crosslinked membranes can trap or interact with PA molecules in the acid-based HT-PEMs, especially for the crosslinkers with additional basic sites (260). So far, thermal crosslinking of PBI membranes rises an interesting start point in the crosslinking direction. However, thermal crosslinking is not reported in other type of polymers which might be an issue to its further applications.

As supported in Table 9, one kind of crosslinking, covalent crosslinking using the crosslinker with ‘big and complex’ structure, benefits for the PEMs with good durable data, proving that covalent crosslinking is a powerful tool to improve mechanical strength, thermal and chemical stability. It can be noticed that the polymeric or hyperbranched crosslinkers which have larger free volume than the traditional small crosslinkers give a promising approach to figure out the PA leaching and degradation problems, resulted from the complex structure of crosslinker which can offer multiple crosslinking points with polymers to encapsulate PA molecules and largely reduce the attacking from radicals. Therefore, to seek novel crosslinking agents with multiple crosslinking points will show promising in the future market. Very recently, a membrane application of polyvinylchloride (PVC) crosslinked by 1-(3-aminopropyl)imidazole (APIm) has led to superior properties owing to multi-crosslinked network (261). Although the APIm does not have a macro-structure, the amino and imidazole groups of APIm can react with PVC through nucleophilic reaction. Superior thermal and mechanical stability and high ADL can be achieved due to the acid-base interactions between PA molecules and APIm groups. It seems that the crosslinkers with polymeric structure and basic sites can balance the compact structure and ADL to get a stable performance.

3.5.2 Incorporating proton-conductive additives

Table 3.10 contains applications with the incorporation of inorganic materials in the membranes. The membrane with the best long-term durability (2700 h) and lowest degradation rate (27 $\mu\text{V/h}$ at 200 °C and 200 mA/cm^2) is the PBI membrane with incorporated phosphotungstic acid impregnated mesoporous silica (PWA-meso-silica) (18). The in-situ formed phosphosilicate nanoparticles can immobilize PA in the cluster structures and subsequently inhibit excessive acid leaching from the composite membrane. It is noticeable that the additives can be divided into five-type porous hygroscopic materials: functionalized silica materials, functionalized graphene oxide, titanium related oxides, metal-organic framework or functionalized clay-related materials (Table 3.10). The addition of inorganic materials usually results in higher mechanical strength and extraordinary antioxidative ability but with sacrificing of proton conductivity. Therefore, the functionalization, such as introducing phosphonic acid groups (229), sulfonic acid groups (33) or

other acid-based groups (18) into the inorganic materials, becomes important to increase their conductivity and compatibility with polymers.

It seems that the applications with the addition of inorganic additives in Table 3.10 showed relatively lower durability than the applications with crosslinked or designed structures in Table 3.9 and Table 3.11. For instance, the applications with the best durability in Table 10 is 2700 h and the lifetime of the majority of these applications only has hundreds of operating hours. The possible reason might be that the incompatibilities between the inorganic fillers and the membrane matrix limit its further durable operations. Although all the inorganic additives had been functionalized to the related functionalized forms, it is urgent to develop the inorganic fillers with high compatible properties with membrane polymer.

Table 3.10. Summary of durability data for selected membranes via incorporating proton-conductive additives.

Polymer	Thickness (μm)	Proton conductivity (mS/cm) ^a	PA retention ability	Oxidative stability ^b	Durability	Degradation rate	Modification	Ref.
PBI	70	72 (250 °C)	NR ^c	NR	2700 h	27 $\mu\text{V/h}$	Incorporating PWA-meso- silica	(18)
PBI	NR	NR	7 μg PA loss per hour	NR	1100 h	2% voltage drop	Incorporating TiO_2 in membrane fuel cell stack	(128)
PBI	55 ± 5	129 (165 °C)	69.8 wt% loss in boiling water after 5 h	60 wt% remaining after 1 h	500 h	3.8% voltage loss	Incorporating graphene oxide	(140)
PES-PVP	72 ± 5	104 (160 °C)	NR	NR	200 h	No obvious loss	Incorporating graphitic carbon nitride	(232)
crosslinked branched PBI	45	100 (160 °C)	72.4 wt% remaining under	NR	187 h	36.0 $\mu\text{V/h}$	Incorporating metal-organic framework	(262)

			80 °C/40% RH after 72 h					
PBI	50	126 (180 °C)	1 mol PA loss in hot water after 2 h	Around 80 wt% remaining after 63 h	150 h	stable	Incorporating perovskite nanoparticles	(22)
PBI	10	47.7 (150 °C)	Stable in 80 °C water after 2 h	NR	149 h	127.1 μV/h	Incorporating titanium oxysulfate	(127)
Ph-PBI	60-80	232 (200 °C)	36 wt% loss in water vapor after 6 h	NR	108 h	11% conductivity loss	Incorporating crosslinking and SiO ₂	(130)
ABPBI	55	48 (180 °C)	Less than 33 wt% loss over boiling water for 5 h	NR	100 h	4.62% loss after 100 h	Incorporating silicon nanorods made from sepiolite	(32)
PBI	126-140 μm (after PA doping)	NR	NR	NR	70 h	11.4-16.5% voltage loss under accelerated stress test	Incorporating electrochemic ally exfoliated graphene oxide	(26)
PBI	50	3.85 (160 °C)	More than 29.7 wt% remaining over hot vapor after 5 h	92 wt% remaining after 120 h	24 h	Stable in 24 h	Incorporating titanium pyrophosphat e	(126)
Py-PBI	80-130	76.4 (140 °C)	NR	NR	20 h	Significant drops in the	Incorporating phosphonated	(229)

						first 5 h and slower decline until 20 h	graphene oxide	
ABPBI	Around 55	75 (90 °C)	33.3 wt% over boiling water for 5 h	7 wt% loss after 120 h	10 h	2.21% voltage loss	Incorporating sulfonated sepiolite	(33)

^aIn-plane proton conductivity. ^btested in Fenton reagent. ^cNR = not reported.

Because of the low cost, thermomechanical stability and hygroscopic properties of inorganic materials, through incorporating inorganic materials into the membranes usually results in improved proton conductivity, stability and cell performance in HT-PEMFCs. Meanwhile, to get a better dispersion in polymers and achieve additional proton transfer way, acid functionalized inorganic materials have received growing attention.

As shown in Table 3.10, hygroscopic inorganic nanoparticles (SiO₂ and TiO₂) and mineral-based materials such as perovskite-type materials and sepiolite and their related functionalized forms were applied in HT-PEMs, all of which have superior fuel cell performance. In addition, comparing with the fact that these zero-dimensional nanoparticles have a limited surface area and interaction points to the polymer chains and PA molecules, one-dimensional (1D) nanorods (32, 33) and 2D nanosheets (26, 229, 232) or metal-organic framework (262) are the promising candidates because of their large surface area and high aspect ratio which benefit excellent PA retention and strong mechanical strength. The related functionalized forms such as imidazolium-ionic-liquid functionalized silicon nanorods, sulfonated sepiolite or phosphonated GO are the interesting and promising approaches in the direction of organic-inorganic composite HT-PEMs.

Therefore, exploring the materials containing large surface area and effective interacting points can be an alternative way to develop novel additives in HT-PEMs. Especially, as the proton conductivities of 2D nanosheets and their related derivatives and hybrids have been reported in recent years (47, 263-265), the exploration of graphene or mica nanosheets in the HT-PEMs might propose a brand-new application in the future (136).

3.5.3 Modifying membrane with designed structure

Through modifying the polymer or membrane structure can also be an approach to increase the durability of fuel cell as shown in Table 3.11. One of the interesting modifications is to increase the membrane layers (17), where different layers have different functions. Another application

(214) using PTFE porous membrane as matrix to afford mechanical strength to blend with PBI also showed good proton conductivity and relatively stable durability.

In addition, another successful approach with a long-term durability is to graft or add some electron-withdrawing groups into the polymer structure, such as sulfone groups (154) or fluorine (117). In addition, the application with 2400-hour stability (154) indicates that the incorporation of phenylene with para structure and flexible aryl sulfone linkages helps to get high molecular weight copolymers with good solvent solubility, oxidative stability and mechanical strength. Similar research can also be found in the Yang's work (250), where PBI membranes with higher molecular weight result in better durability.

Another type of modification with improved durability is to introduce PA doping sites into the polymer side chains (89, 244, 245, 247). The introduced side chains with amine groups can work as PA doping sites and form micro-phase separation for fast proton conducting in membranes. Because the increased PA adsorption sites are away from the polymer backbones, the PA molecules will not deteriorate the membrane mechanical properties (244), resulting in minimization of the trade-off between mechanical strength and proton conductivity.

As shown in Table 3.11 and Fig. 3.13, one of the best performances among the applications with modified structures is the one introducing quaternary ammonium-biphosphate ion pairs into the polymer (800 mW/cm^2) (89). The strong interactions between PA molecules and quaternary ammonium-biphosphate groups can increase the membrane acid retention ability and afford excellent proton conductivity. In addition, it can be found that the performance is often related to the durability, while the application with higher power density usually shows higher proton conductivity but lower durability. For example, the application about blending PBI with porous PTFE shows highest proton conductivity (320 mS/cm) and power density (1200 mW/cm^2) but with only 50 h lifetime (214), where the higher acid content in the membrane tends to have a high acid loss rate and lead to shorter lifetime. Herein, how to achieve the balance between higher acid content and better acid retention is a tough issue and needs to be figured out in the future.

Table 3.11. Summary of durability data for selected membranes via modifying membrane structures.

Polymer	Thickness (μm)	Proton conductivity (mS/cm) ^a	PA retention ability	Oxidative stability ^b	Durability	Degradation rate	Modification	Ref.
PBI	90	330 (180 °C)	NR ^c	NR	10000 h	2.3-4.1 $\mu\text{V/h}$	Three-layered PEMs	(17)

SO ₂ PBI	NR	33 (160 °C)	NR	75 wt% remaining after 200 h	2400 h	6.4 mV/h	Copolymers with pPBI	(154)
PBI	70-80	140 (160 °C)	NR	19 wt% after 200 h	1500 h	1.5 μV/h	Synthesizing with high molecular weight	(250)
F6-oxyPBI	80 or 90	49 (120 °C)	NR	5.3 wt% loss after 48 h	1000 h	46 mV/h	Introducing fluorine to the polymer structure	(117)
QAPOH	80	60 (180 °C)	77 wt% remainin g at 220 °C and 0% RH after 50 h	NR	500 h	0.33 mA/(cm ² ·h)	Introducing quaternary ammonium-biphosphate ion pairs	(89)
Polysulfone	60 ± 5	127 (160 °C)	NR	51 h breaking time	200 h	No obvious loss	Grafted poly(1-vinylimidazole) as PA doping sites	(244)
Ph-PBI	60-80	127 (120 °C)	NR	NR	168 h	Only a slight decline in conductivity	Incorporating some benzimidazole groups	(245)
polysulfone	50	56 (160 °C)	NR	NR	150 h	Stable	Grafting amine groups	(247)
PBI	30	320 (160 °C)	NR	NR	50 h	No obvious loss	Blending with porous PTFE	(214)

^aIn-plane proton conductivity. ^btested in Fenton reagent. ^cNR = not reported.

The above described innovations are indeed suitable for the improvement of fuel cell performance with good durability data, but how to thoroughly solve out PA leaching, mechanical degradation and oxidative degradation is still a problem. Novel applications are therefore needed in the field

of acid-based PEMs, whilst the computational or theoretical approaches can also be employed to explore and understand how the degradation of HT-PEMs happens from a theoretical point (266). Additionally, it has been reported that PA leaching problems can be solved using poly(vinylphosphonic acid) to substitute movable PA molecules in the acid-based HT-PEMs (146, 147). Although a good durability was observed, the subsequent problems, insufficient ion-exchange capacity and low conductivity, can be a limiting issue for this kind of membranes.

3.6 Conclusion to this chapter

Because of the disadvantages of LT-PEMFCs (such as low carbon monoxide tolerance, complex water and heat management, and low reaction kinetics), HT-PEMFCs have attracted a lot of attention. However, the durability of HT-PEMFC limits its further development and commercialization. With respect to membrane durability, three issues including PA leaching, membrane oxidative degradation and mechanical degradation deteriorate the fuel cell performance. This review has tried to explain and conclude current applications to solve these three limitations.

PA works as the proton-conducting electrolyte and is the essential part for HT-PEMs, therefore, one of the most important and inevitable issues is the PA leaching. Meanwhile, as PA acts as a plasticizer in HT-PEMs, PA doped HT-PEMs display decreased mechanical strength especially when PA loading is high. Substituting PA with other possible acids like polymeric acid (146, 147) or other proton conductors like metal-organic frameworks can lower the dependency on PA (262), reduce the plasticization effect of PA, and have the potential to alleviate membrane mechanical degradation and acid leaching. Another attempt to solve this issue has been to modify membrane structure or polymer structure. While modifying membrane structure such as preparing multilayer membranes helps to reduce acid leaching and strengthen mechanical strength by applying physical membranes (17), the complex manufacturing procedures might limit its further commercialization. In addition, although modifying polymer structure like microphase separation structure is formed by moving the PA doping sites away from the backbones to get improved mechanical strength (244), the dependency on the PA molecules is still a tough issue. Herein, the most fundamental question, PA leaching, is not solved. It is still ambiguous for the understanding how PA leaching happens in actual running acid-based HT-PEMFCs. Developing a better understanding of acid distribution and investigating the different forms of phosphate groups during the actual operations might be important for the future applications.

Currently, many characterizations had been carried out to test PA leaching, chemical and mechanical stability, and durability. However, it is hard to find out the standardized methods to measure them, which will potentially rise concerns to comparatively evaluate the properties of different materials. To better simulate the real practice environment, it is advisable to use the

reformatted hydrogen or air as the normalized fuel supply sources to replace the common used pure hydrogen and oxygen. The scaling up in the fuel cell stack is another necessary step before the practice use. The standard testing protocol should also be emphasized such as fuel gas supply mode (dead-end or flow-through mode) (267), purging procedures (268, 269), optimal operating temperature range (270) and heating and cooling procedures (271). In addition, many ex-situ methods have been explored to measure the properties of PA doped HT-PEMs but lack of in-situ methods. Until now ex-situ methods have only been developed to test acid leaching and mechanical degradation. These ex-situ characterization methods do not necessarily directly convert to real HT-PEM performance. More work needs to be done for the in-situ measurement to explore how the degradation happens in the actual fuel cell operations.

As can be easily seen in the above review, crosslinking is an efficient way to fabricate crosslinked structures to solve these limitations. Especially by using crosslinker with multiple crosslinking points to synthesize the macromolecular or branched structures (142, 177), not only the PA molecules can be encapsulated inside the crosslinked structures, it also increased the difficulties for radicals arriving the N-H sites to avoid chain scissions. The compact structure will also benefit the improvement of mechanical strength. Nevertheless, if the ADL in the crosslinked membranes are too high, it is hard to maintain long-term stability because of the tendency of acid leaching. Therefore, to realize the practical applications of this crosslinked HT-PEMs, the low ADL without performance deterioration should be one of the practical approaches in the future. The combination of multi-point crosslinking and introducing proton-conducting groups into the polymer might afford a potential application to keep a relatively low acid loading without scarifying performance.

The second approach is to blend with stable polymers or graft antioxidative groups (fluorine-containing groups, phenoxy units, and sulfone groups) to improve the chemical and mechanical stabilities because of reduced plasticization effect of PA. However, the proton conductivity and acid retention of membranes might be deteriorated due to the lack of interactions between these organic additives and PA molecules. This topic has been extensively explored via the introduction of basic groups (imidazole groups, quaternary ammonium, ionic liquid groups, nitrogen-heterocycles and polycations) into the polymer structure. This might lead to increased intermolecular interactions with PA to get enhanced acid retention stability. Moreover, chemically linking organic free radical scavengers to the polymer backbones might offer another opportunity to get optimized membrane composition (272).

Another direction is to introduce the hygroscopic inorganic materials into the polymer matrix, such as clay-based minerals and metal oxides (titanium-based oxides and CeO₂). Further functionalization is also needed to add acid-based groups onto the surface of the inorganic

materials to increase their compatibility with the polymer (18, 33, 229). The strong hygroscopicity of inorganic material gives more opportunities to interact with PA molecules to maintain the proton conductivity with enhanced chemical and mechanical strength, especially for the polymer chains which are engaged into the nano-galleries of layered or porous material filler. However, when the inorganic fillers exceed a certain amount in the polymer matrix, possible aggregations might occur to result in voids or inner cracks in the membranes. Therefore, more detailed work should be performed in the field of getting homogenous dispersions and enhancing the interaction strengths between inorganic fillers and polymers, such as introducing covalent bonds other than hydrogen bonds (130, 273). Other physical approaches such as exfoliating the layered materials (136), applying electric field alignment (274, 275) and magnetic field alignment (276) or getting aligned arrangement by freeze casting (277, 278) can be further exploited in the near future.

To summarize, significant efforts have been addressed in the alleviation of membrane degradation, and corresponding solutions have been developed over years. This chapter is expected to give a better understanding of HT-PEMs, reveals the challenges and limitations, affords insights into the design of HT-PEMs, and contributes to promoting the commercialization of HT-PEMs in the future. According to the above literature review, the incorporation of hygroscopic inorganic fillers into the membranes can enhance the mechanical and chemical properties. The hygroscopic fillers, silica nanosheets and muscovite which are the first time to be introduced in HT-PEMs, can interact with phosphoric acid and polymers to build inorganics-PA and inorganics-polymer interactions to get improved acid retention ability and membrane oxidative stability in acid-based HT-PEMs. The next chapter is the experimental part which will focus on the preparation of clay-based fillers into the HT-PEMs, and the methods for the evaluation and characterization of HT-PEMs.

Chapter 4: Experimental work and characterization techniques

4.1 Introduction

In this chapter, how to choose and prepare clay-based materials as the fillers is introduced, along with functionalized forms of clay materials such as exfoliated and sulfonated fillers. Later, the selection of polymers in HT-PEMs and the preparation of membranes will be described. The subsequent section contains the preparation of membrane electrode assembly and the corresponding characterization techniques.

4.2 Preparation of clay-based materials

4.2.1 Why choose clay-based materials (vermiculite and muscovite)?

Incorporation of inorganic materials into proton exchange membranes is an efficient method to improve dimensional stability (reduce swelling), enhance mechanical properties, and reduce fuel crossover (279-281). Particularly, the incorporation of clay into the composite membrane is of interest due to the enhanced properties that clay nanofillers can provide to the membrane. The hygroscopic properties of clay contributing to increased humidity inside the membranes lead to a better proton conductivity (196). Clays have layered and siloxane structure which can provide strong interactions with polymer chains, resulting in fast ion transferring pathways (27, 282). Ion-exchange, intercalation or exfoliation of clay nanofillers also yields possibilities for improving proton conductivity and performance (263, 283, 284). To date, many different materials from the alumino-silicate family such as montmorillonite (30), laponite (28), bentonite (285), sepiolite (33), palygorskite (286), mordenite (280, 281, 287) and kaolinite (197) have been reported as membrane fillers in either LT-PEMFC or HT-PEMFC applications.

Vermiculite is a cheap, natural aluminosilicate clay mineral containing a $\text{MgO}_2(\text{OH})_4$ octahedral sheet sandwiched by two tetrahedral silica sheets where the cations (such as Mg^{2+} , Ca^{2+} , Na^+ and K^+) are exchangeable with ions (288). Its low price, excellent ion-exchange properties and layered structures have led to its widespread use as an electrode material (289), membrane filler in lithium batteries (290), nanofluidic-channel-networks (291), oil-water separation technology (292), and as an adsorbent membrane (293). Similar to vermiculite, muscovite ($\text{KAl}_2(\text{Si}_3\text{Al})\text{O}_{10}(\text{OH})_2$) contains negatively charged aluminosilicate layers and potassium interlayer cations, where an aluminosilicate layer comprises an aluminium octahedral ($\text{AlO}_4(\text{OH})_2$) layer between two silicate tetrahedral sheets (SiO_4) (Fig. 4.1) (294). Although muscovite was used in several applications such as absorbents (295), support materials (296) and

electronics (297), muscovite had been paid less attention in fuel cells because of its strong interlayer forces, non-expandable and low ion exchange properties (298).

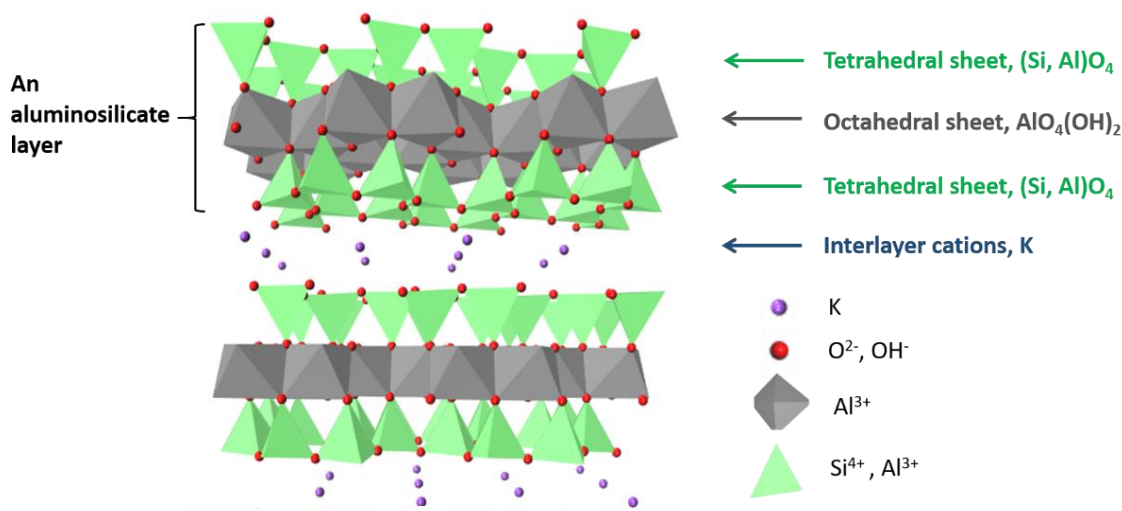


Fig. 4.1 Schematic representation of clay structure.

A recent application (263) reported few-layered clay (vermiculite and muscovite) exhibits promising as proton conductive membranes, but the complex preparation of mechanically exfoliated vermiculite and muscovite limits further exploration. However, since vermiculite and muscovite have similar hygroscopic properties and are excellent thermal and electrical insulators with a smooth surface and high aspect ratio (299), both clay-based inorganic fillers may offer more stable acid anchoring points than other clay-based materials in HT-PEMFCs. Additionally, as vermiculite and muscovite were reported as effective absorbents for phosphate (295, 300) and contain OH groups which can interact with polymer chains and PA molecules to benefit proton conducting (136), the vermiculite and muscovite incorporated membranes may retain PA molecules and offer additional proton-conducting pathways. The hydroxyl groups on the clay surface and the hygroscopic nature benefit the formation of clay-PA and clay-polymer crosslinks to facilitate proton transfer and good acid retention ability. The high aspect ratio and smooth surface may afford good dispersion in membranes and accessible PA anchoring points to get increased delocalized protons and enhanced ion conductivity. Clay-polymer crosslinks can limit the mobility of polymer chains to obtain stiffer membranes with good mechanical properties, while the vermiculite and muscovite with hygroscopic layered structure, large pore size and low porosity may act as barriers to block hydrogen crossover and alleviate membrane oxidative degradation.

4.2.2 Preparation of silica nanosheets

The original idea is to add vermiculite into the membrane without any modifications. However, we found vermiculite cannot survive in an acid environment and part of aluminium and

magnesium will leach out from vermiculite to obtain solids with high porosity and a large number of acidic sites. Meanwhile, acid treatment can remove the octahedral layer of silicates to form active groups (Si-OH groups) on the surface. The product after acid treatment is noted as silica nanosheets (SN). The possible interactions among Si-OH groups in SN, PA molecules and polymer chains inspire us to incorporate SN into the membranes to prepare the inorganic-organic composite membranes.

The SN were prepared through an acid-leaching method (301) as described below. 3 g vermiculite was added into 100 mL 2 M HCl solution, and magnetically stirred at 50 °C for 8 hours. The obtained mixture was filtered and washed with deionized water several times until pH 7. Then the filtrate was dried overnight at 70 °C under vacuum, and mechanically ground in an agate mortar for 15-20 min. The obtained SN was a fine white powder, lighter in colour than the raw vermiculite as shown in Fig. 4.2. Few-layer exfoliated silica nanosheets (E-SN) were synthesized via the liquid-phase exfoliation method (302, 303): 40 mg SN was dispersed in 40 mL absolute ethanol. Subsequently, the mixture was ultrasonicated for 2 h using a Hielscher Ultrasonic Processor (UP200St) instrument, equipped with a 7 mm sonotrode. The amplitude of ultrasound wave was kept constant at 70%. An ice bath was applied to avoid overheating. Unexfoliated SN was removed by centrifugation at 1000 rpm for 10 min. Finally, the product was decanted and dried at room temperature under vacuum overnight.

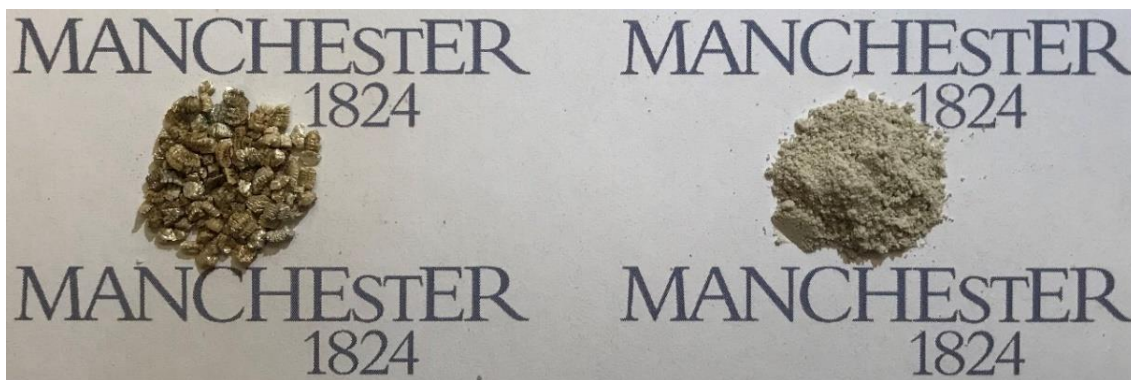


Fig. 4.2 Photographs of raw vermiculite (left) and SN (right).

4.2.3 Preparation of functionalized silica nanosheets

The functionalization of SN was prepared via silane condensation (304). Thiol (-SH) groups were firstly grafted onto the surface of SN by mixing SN with (3-mercaptopropyl)trimethoxy silane (MPTMS) and toluene (weight ratio 1:2:20) at 110 °C for 24 h. The reaction mixture was then centrifuged, filtered and washed with absolute ethanol and deionized water three times. The obtained filtrate was dried at 40 °C overnight, and mixed with 30 wt% H₂O₂ solution for 24 h to convert thiol groups into sulfonic groups. Subsequently, it was washed with absolute ethanol and deionized water three times, followed by filtering and drying at 40 °C overnight to obtain S-SN.

4.3 Preparation of membrane electrode assembly

By hot-pressing a proton exchange membrane (PEM) sandwiched by two electrodes can fabricate a membrane electrode assembly (MEA) (Fig. 4.3). In HT-PEMFCs, anode and cathode catalysts are platinum so the preparation procedures of anode and cathode are the same. We prepare the electrode using an airbrush to spray a microporous layer (MPL) and catalyst layer (CL) onto the carbon paper before hot-pressed with a membrane as shown in Fig. 4.4. The preparation procedure of each component will be introduced in detail as follows.

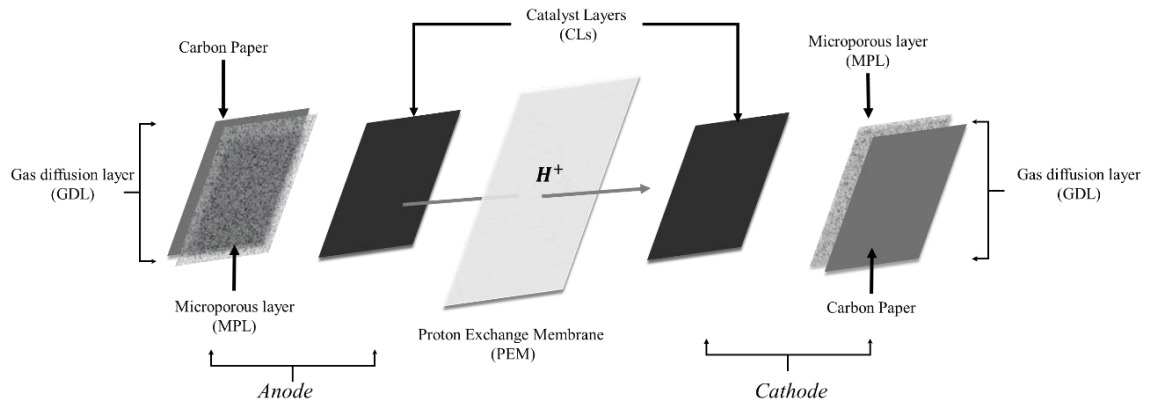


Fig. 4.3. Schematics of a membrane electrode assembly (MEA).

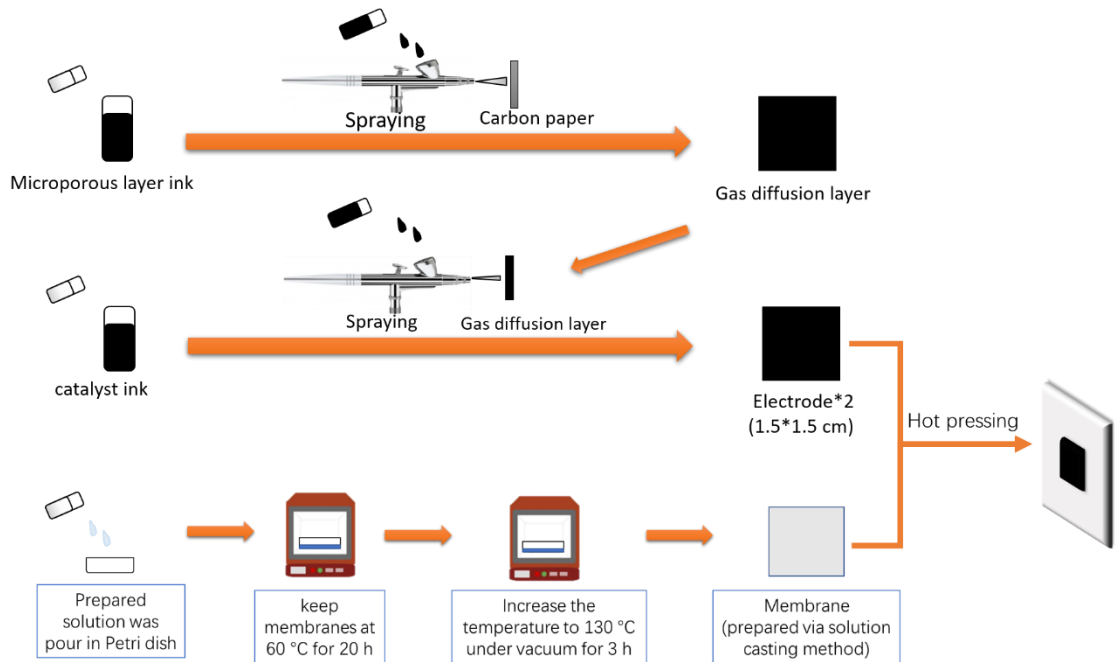


Fig. 4.4. Scheme and steps involved in MEA fabrication

4.3.1 Preparation of membranes

4.3.1.1 Why choose PES-PVP and PBI as the membrane polymers?

As the essential component in fuel cells, membranes transport protons and act as an electrical insulator to separate anode and cathode. Since the proton conductivity and durability of membranes play an important role on the performance of fuel cells, it is important to choose a suitable polymer as membrane material before the work starts. Recent representative papers using different polymers in HT-PEMFCs without humidification are summarized in Table 4.1, where the membrane materials, proton conductivity, power density and the operation temperature are compared. The order of different membrane polymers in the table is arranged by their proton conductivity.

Table 4.1. Comparison of different membrane materials in hydrogen fuel cells

Polymer	Membrane	Proton conductivity/ mS/cm	Power density/m W/cm ²	T/°C	Ref.
polyethersulfone-polyvinylpyrrolidone (PES-PVP)	PA doped PES-PVP (4:1) blended membrane	210	850	180	(72)
PES-PVP	Amino-functionalized mesoporous silica-based PES-PVP (7:3) composite membranes	152	480	180	(305)
PES-PVP/PTFE	PTFE reinforced PES-PVP composite	260	607	180	(215)
Poly(ether ketone sulfone)s (PEEK)	PA-doped PEEK with functionalized benzotriazole	118	562	180	(306)
PVDF-PVP	PVDF-PVP blended polymers	93	530	200	(307)
PES-PVP	Submicro-pore containing PES-PVP membrane	90	454	180	(308)
polyacrylamide-graft-chitosan (PAAm-g-CS)	H ₃ PO ₄ imbibed PAAm-g-CS membrane	83	453	165	(309)
PVP	PVP/phosphonated PPO/graphitic carbon nitride	61.3	294	180	(231)
poly(vinylidene fluoride-co-hexafluoropropylene), (poly(VDF-co-HFP))	phosphonic grafted silica nanoparticles added poly(VDF-co-HFP) membranes	54	800	80	(310)

Poly(2,5-benzimidazole)	poly(2,5-benzimidazole) (ABPBI)/sulfonated sepiolite composite membranes	51	230	180	(33)
Polybenzimidazoles (PBI)	PBI membranes blended CeO ₂	48	990	150	(194)
poly(ether sulfone)	Phosphoric acid-doped sulfonated poly(ether sulfone) based on Cr-MIL-101-NH ₂	41	238	160	(311)
polysulfone	PA doped imidazolium polysulfone membranes	38	269	160	(312)
chitosan	phosphorylated graphene oxide-based chitosan	31	107	160	(313)

From Table 4.1, the top 3 membranes with the highest proton conductivity are phosphoric acid doped polyethersulphone-polyvinylpyrrolidone (PES-PVP) membranes where the N-heterocycle of PVP acts as an excellent proton acceptor and PES affords the mechanical strength. In addition, the simple fabrication procedure of PES-PVP membrane has attracted attention (72). Herein, the PES-PVP membrane (2: 3 weight ratio) is chosen in this work (chapter 5-7) and is prepared using solution casting method. As PBI polymer has stable performance, to investigate the acid leaching along time, we use PBI as the objective in chapter 8 and prepare the membrane using the doctor blading method.

4.3.1.2 Solution casting method

In this procedure, the membrane was prepared through solution casting method under a vacuum oven. Here the membrane preparation procedure was chosen as the indirect mixing method as an example and the other different methods will be discussed in chapter 5. 0.12 g PES (Ultrason 7020P, BASF Co., Germany) was dissolved in 2 mL N,N-dimethylformamide (DMF, Sigma), and 0.18 g PVP (1300 kDa, Sigma) was dissolved in 3 mL DMF, respectively. Then PES and PVP solution were mixed under stirring for at least 12 h to get a homogeneous solution. Required amounts of SN, S-SN, or E-SN were dispersed in 2 mL DMF by ultrasonication for 10 min and mixed with the polymer solution. After 3 h magnetic stirring, the as-prepared homogeneous solution was cast onto a Teflon dish (Cowie Technology from Fisher). It was then dried at 60 °C for 20 h under ambient pressure and 130 °C for 3.5 h under vacuum. The composite membranes were labelled as P/xSN, P/xS-SN or P/xE-SN, where x (x = 0.1, 0.25, 0.5 and 0.75 wt%) represents the weight ratio of SN to polymer weight. The pure membrane, P/0SN, was prepared under the same conditions for comparison. In this work, the P/0.25SN membrane will be shown to have the optimal cell performance over other composition, so 0.25 wt% was chosen as the loading for P/xS-SN and P/xE-SN membranes. The average thickness of the composite membrane before and after 24h PA (Sigma) doping was 50 ± 5 μm and 80 ± 5 μm , respectively. The acid doping level

(ADL) of PA doped membranes as a function of doping time is shown in Fig. 4.5. Acid uptake of the membrane was calculated according to the mass difference before and after PA doping related to the weight of dry membrane. The acid doping level (ADL) was obtained by the following equations:

$$\text{ADL (mol)} = \frac{(W_{\text{wet}} - W_{\text{dry}})/98}{W_{\text{dry}} \times 0.6/111} \quad (4.1)$$

where W_{wet} and W_{dry} are the membrane weight after and before acid doping at room temperature, respectively. The area, thickness and volume swelling of the membranes were obtained by comparing area, thickness and volume differences before and after PA doping, respectively.

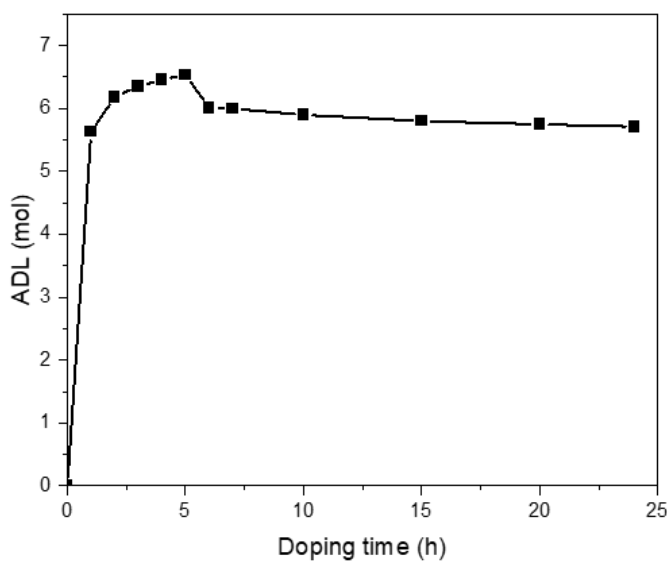


Fig. 4.5. ADL of pure PES-PVP membrane as a function of doping time.

4.3.1.3 Doctor blading method

The membranes were prepared using a doctor blade (Sheen Automatic Film Applicator 1133N) as shown in Fig. 4.6. Firstly, the required amount of muscovite was added into Dimethylacetamide (DMAc, Sigma) and ultrasonicated using a probe sonicator (Hielscher Ultrasonic Processor UP200 St) for 15 min. The well-mixed dispersion was then mixed with 20 mL 18 wt% PBI/DMAc solution (1 wt% lithium chloride as a stabilizer, PBI performance product, USA) to keep the final concentration of membrane solution as 15 wt%. After 3 h mixing using an overhead stirrer, the homogenous membrane solution was cast on a glass plate using a doctor blade with a blade gap of 200 μm and a rate of 50 mm s^{-1} . Afterwards, the wet film was dried at 60 $^{\circ}\text{C}$ in an oven for 20 h, and further dried at 130 $^{\circ}\text{C}$ under vacuum for 3 h to evaporate the solvent. After being immersed in deionized water for 30 min, the membrane can be easily delaminated from the glass plate. To further remove solvent residues, the delaminated membrane was transferred into deionized water at 60 $^{\circ}\text{C}$ for 1 h before being dried at 80 $^{\circ}\text{C}$ under vacuum for 1 h. The

PBI/muscovite composite membranes were labelled as PBI/xMus, where x ($x = 0.5, 1$ and 2 wt%) stands for the weight percentage of muscovite in the composite membrane. The pure PBI membrane, named as PBI/0Mus, was also prepared under the same conditions for comparison. For PA doping, membranes were soaked in 85 wt% PA solution at ambient temperature for 24 h to ensure the PA saturation. The ADL of PA doped membranes as a function of doping time is shown in Fig. 4.7. The membrane before doping had a thickness of 50 ± 5 μm , while the thickness of PA doped membrane was around 80 ± 5 μm .

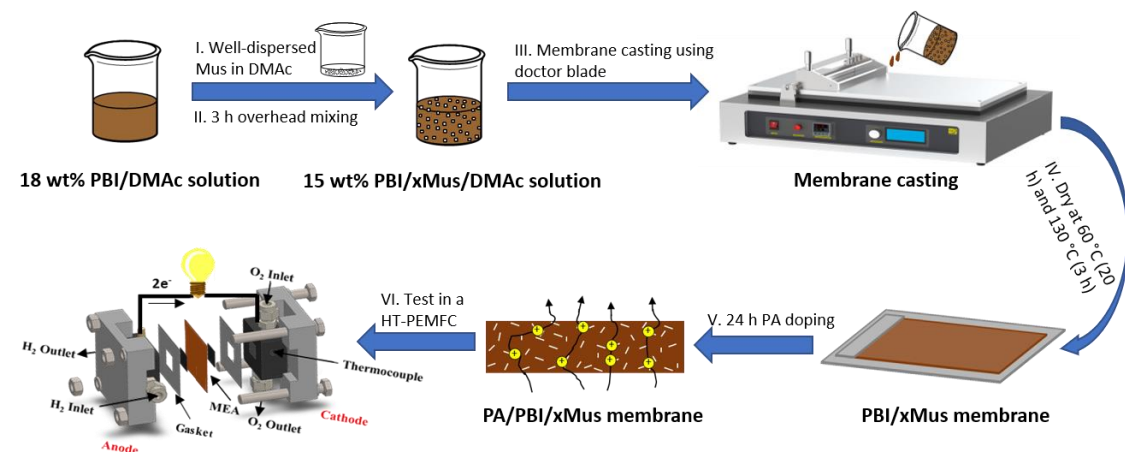


Fig. 4.6. Schematic representation of the preparation of PA doped composite membrane.

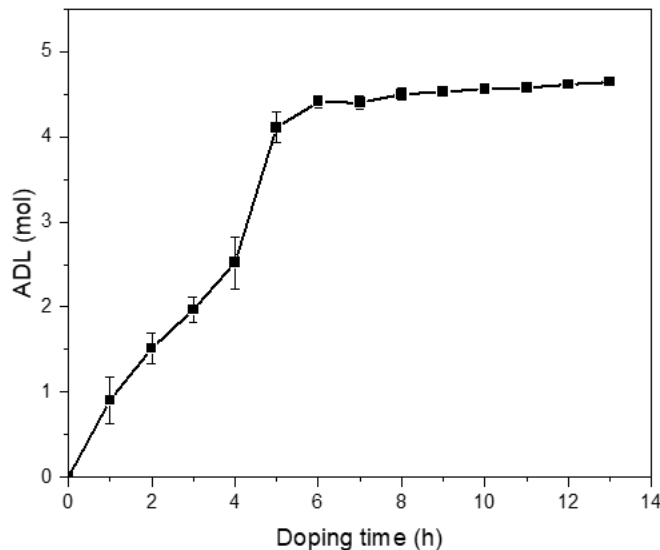


Fig. 4.7. ADL of pure PBI membrane as a function of doping time.

4.3.2 Preparation of microporous layer

A gas diffusion layer (GDL) was prepared by spraying the microporous layer (MPL) ink containing 10 wt% PTFE (made from 60 wt% PTFE dispersion in water, Sigma Aldrich) and 90 wt% Ketjen black (KB, EC-300J, AkzoNobel) onto a carbon paper (Toray Paper 90) and then drying in a muffle oven (Nabertherm) at 300 °C for 3 h. The calculation details and preparation

steps of MPL ink are shown in Table 4.2 and Fig. 4.8, respectively. The obtained MPL ink was stirred overnight and added into another 5 ml isopropanol (IPA) in the second day and sonicated for 1 h to get a homogenous mixture before spraying. After the preparation of MPL ink, we used a spray gun (KKmoon Professional Airbrush) to spray the MPL ink onto the carbon paper. The carbon paper was kept at 100 °C to promote isopropanol (IPA) evaporation and the spraying was carried out until the target mass was reached. The detailed spraying steps are described as below.

- A carbon paper with 13.5 cm² area (1.5 cm × 4.5 cm) was weighed. The weight added in the carbon paper should be 15 mg to keep the loading of KB as 1 mg/cm².
- The airbrush was cleaned with acetone and connected to nitrogen gas at 1 bar.
- MPL ink was placed in the airbrush and sprayed back and forth in straight lines to maintain a uniform layer. And the airbrush was placed perpendicularly at around 2.0 cm distance from carbon paper.
- The carbon paper was dried at 100°C on a hotplate to evaporate IPA.
- The steps of spraying and drying were repeat until the desired weight was arrived.
- Finally, following a procedure in Fig. 4.9, the prepared carbon paper was sintered at 300°C for 3 h in a muffle furnace to get the GDL.

Table 4.2. Calculation of parameters in microporous layer.

Parameters	Results
Weight ratio of KB and PTFE	9: 1
Target loading of KB	1 mg/cm ²
Weight percentage of PTFE in PTFE solution	60%
Area of carbon paper	13.5 cm ²
Waste factor	5
$m_{KB} = \text{Electrodes Area} \times \text{KB loading target} \times \text{Waste factor}$	67.5 mg
$m_{\text{PTFE solution}} = (\text{Amount of KB} \times 10 \text{ wt}\%) \div (90 \text{ wt}\% \times 60 \text{ wt}\%)$	12.5 mg
Total weight added in carbon paper = area of carbon paper × target loading of KB ÷ 90 wt%	15 mg



Fig. 4.8. Procedure for preparation of microporous ink.

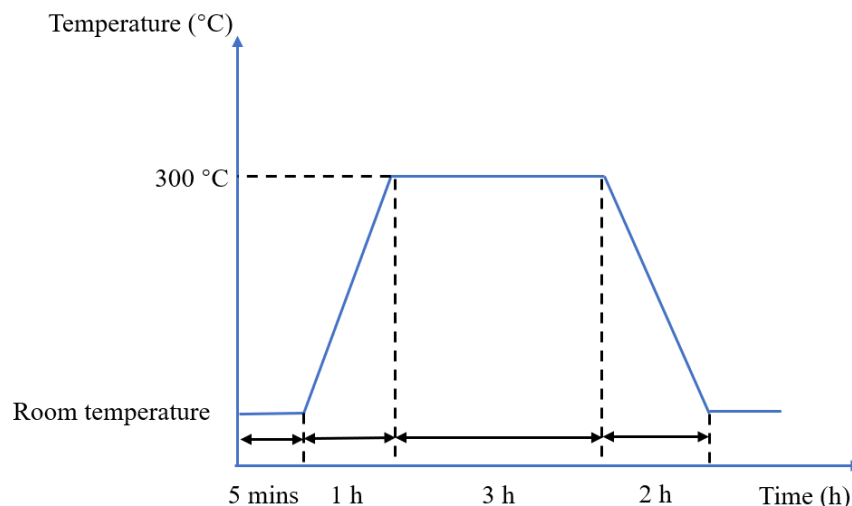


Fig. 4.9. The muffle furnace and GDL sintered temperature profile.

4.3.3 Preparation of catalyst layer

The catalyst ink was obtained by mixing Pt/C catalyst (60% Pt loading, Alfa Aesar) with PTFE dispersion (60 wt% PTFE dispersion in water, Sigma Aldrich) with the weight ratio of 4:1 in water-IPA solvent (314). Here PTFE works as catalyst binder to adjust PA distribution and trap the impregnated PA in the network to reduce phosphoric acid leaching and PA flooding (315). The reason why Nafion is not used as binder here is Nafion will lose its proton conductivity over 100 °C. The electrode was obtained by spraying the catalyst ink onto the GDL until target loading of platinum on electrode was arrived. The catalyst loading for PES-PVP and PBI based MEAs are 0.75 and 1 mg cm⁻² respectively. Taking the preparation of 0.75 mg cm⁻² loading catalyst as an example, the target weight and the experimental details are shown in Table 4.3, and the preparation procedures are shown below.

- 35.2 mg PTFE solution was added in 8 mL IPA, while 84.375 mg Pt/C was added into 7 mL deionized water.
- After being sonicated for 1 h to get homogenous dispersions, the two dispersions were mixed and sonicated for another 1 h to get the catalyst ink.
- After sprayed the catalyst ink by airbrush, the electrode was dried in a hotplate (100°C) and weighed until the increased weight arrived to 21.1 mg.

Table 4.3. Calculation of parameters in catalyst layer.

Parameters	Results
Weight ratio of carbon-based catalyst and PTFE	4:1
Target catalyst loading	0.75 mg/cm ²
Weight percentage of PTFE in PTFE solution	60%
Catalyst loading in carbon-based catalyst	60%
Area of carbon paper	13.5 cm ²
Waste factor	5
Carbon supported catalyst weight $m_{Pt/C} = \text{area of GDL} \times \text{target catalyst loading} \times \text{waste factor} \div \text{Catalyst loading in carbon-based catalyst}$	84.375 mg
$m_{PTFE \text{ solution}} = m_{Pt/C} \div \text{Weight ratio of carbon-based catalyst and PTFE} \div \text{Weight percentage of PTFE in PTFE solution}$	35.156 mg
Total weight added in GDL = $m_{Pt/C} \div \text{Waste factor} + m_{PTFE \text{ solution}} \div \text{Waste factor} \times \text{Weight percentage of PTFE in PTFE solution}$	21.094 mg

4.3.4 Hot-pressing

The detailed procedure of hot-pressing is given as follows:

- The PA doped membrane was sandwiched by two electrodes with the catalyst side close to the membrane.
- A PTFE template (0.15 mm thickness) acted as a barrier to prevent the electrode movement during the hot-press procedure.
- As there might have some PA leaching being pressed out to corrode the hot-press machine during the hot-press, another PTFE film (0.05 mm thickness) was applied to cover PTFE template and the MEA as shown in Fig. 4.10.
- The automatic hot-press machine (Geo Knight & Co Inc.) was adjusted to 140 °C and 80 psi before use. To achieve the thermal equilibrium of all components (anode, cathode, membrane and PTFE template), the assembly was preheated at 140 °C for 2 min without pressure in the machine and then hot-pressed at 140 °C, 80 psi for 2.5 minutes. For the preparation of PBI based MEAs, this procedure of hot-pressing was performed at 140 °C, 80 psi for 4.5 minutes.

- After that, the final MEA was taken out from the machine and sealed in a Ziplock bag before being tested in a fuel cell testing station.

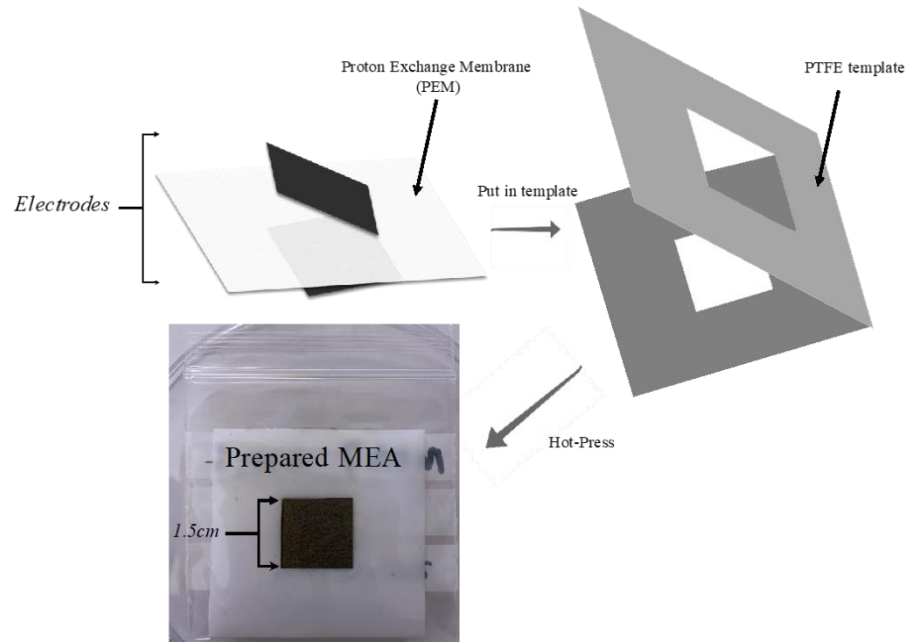


Fig. 4.10. Schematic of hot-pressing process and a prepared MEA.

4.4 Fuel cell testing

The testing of a single fuel cell performance was carried out in a HT-PEMFC work station as shown in Fig. 4.11 where four main parts (hydrogen and oxygen supply pipes, a HT-PEMFC setup, temperature controller, and electrochemical analysis potentiostat Gamry Interface 5000E) were connected and installed. A bit different from the LT-PEMFC, there were no humidifier in the HT-PEMFC testing station. This testing station was designed and made by workshop from the School of Chemical Engineering in the University of Manchester. The schematics of a fuel cell setup and its graphite bipolar plate with serpentine flow channels are given in Fig. 4.12.

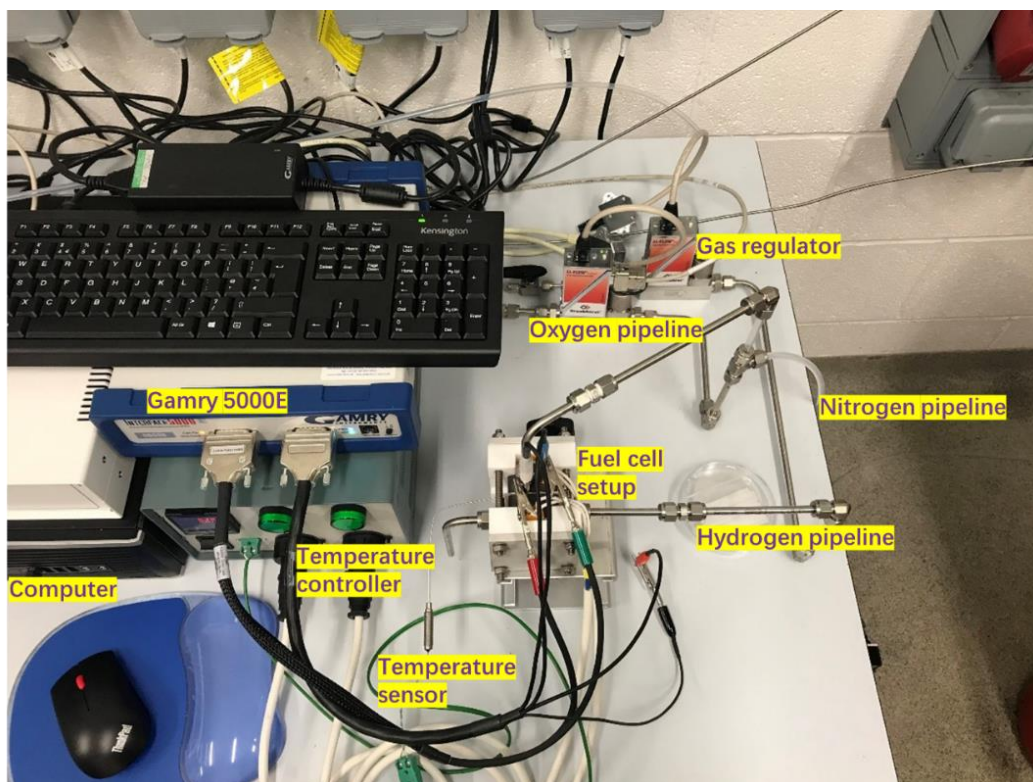


Fig. 4.11. HT-PEMFC testing station.

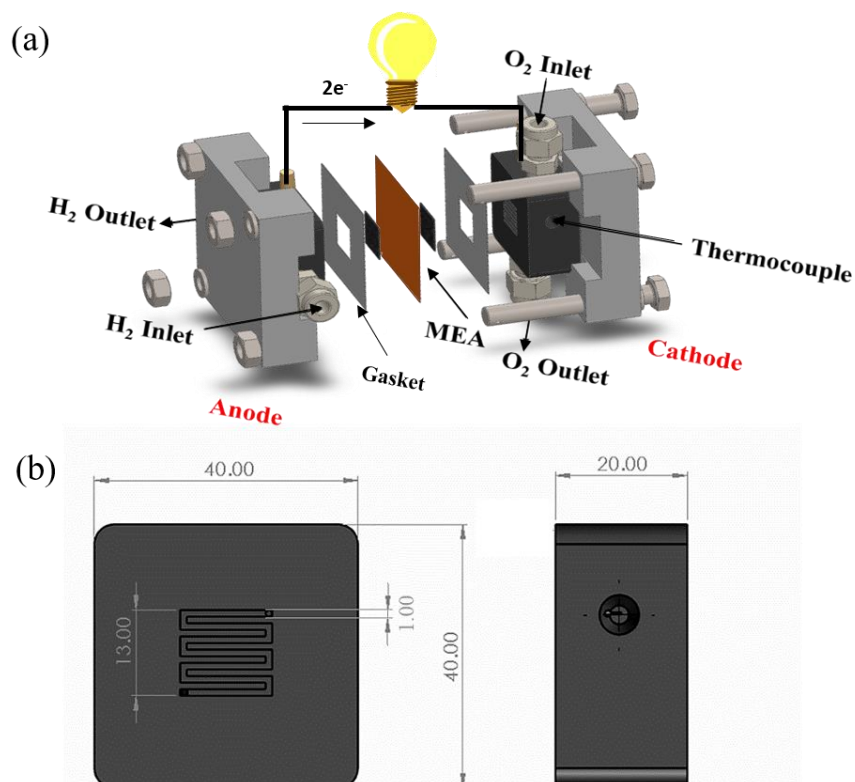


Fig. 4.12. (a) A HT-PEMFC setup and (b) a schematic of graphite bipolar plate with serpentine flow channels.

After the MEA was installed in the setup, the cell was tightened by screws applying a torque of 0.5 N m, and the dry H₂ and O₂ were connected to the cell under 100 mL/min flow rate. The performance of a MEA was evaluated by a Gamry Interface 5000E at a temperature range of 140 °C to 170 °C without humidification. Polarization curves were obtained after ten-polarization activation at 150 °C. The durability was evaluated at a steady-state test (0.6 V at 150 °C for PES-PVP membranes) or accelerated stress test (16 minutes at 1.0 A cm⁻², 4 minutes at 0.6 A cm⁻² and every 6 h 10 minutes at 0.0 A cm⁻² for PBI membranes). Electrochemical impedance spectroscopy (EIS) before and after durability test were performed at constant 0.6 A from 10000 Hz to 0.1 Hz at 150 °C. The corresponding EIS spectra were fitted by the equivalent circuits using Gamry Echem Analyst software. The initial ten-polarization activation of PA-doped HT-PEMFCs corresponds to the PA redistribution in the MEA (316). The polarization curves, Linear sweep voltammetry (LSV), EIS and the cell durability were tested by Gamry Interface 5000E potentiostat in this work. The steps are shown as below in details:

- After the MEA was assembled in the HT-PEMFC setup using 0.5 N·m torque force (Facom A.402), the Gamry potentiostat was connected to the cell where the reference and counter electrodes were connected to the anode side, and the working electrode and working sensor were connected with the cathode side.
- The temperature controller was turned on to 150 °C, while the nitrogen and hydrogen flowed to the cathode and anode chambers respectively at 100 mL/min flowrate.
- The oxygen replaced nitrogen to the cell when the cell temperature arrived 150 °C and was stable. This entire start-up procedure took approximately 15 min. This aimed to minimise the drying out of PA in the membrane (317).
- Ten polarization-curve activation was run by the Gamry potentiostat, and the tenth polarization curve was regarded as the final polarization curve.
- The following step was using Gamry potentiostat to test the EIS curves at different current (0, 0.1, 0.2, 0.3, 0.4, 0.5, 0.6 and 0.7 A) from 10000 Hz to 0.1 Hz at 150 °C.
- The next step was to measure the hydrogen crossover. After the nitrogen and hydrogen were supplied to cathode and anode at the flow rate of 100 mL/min respectively for 30 min, the LSV was tested by Gamry 5000E where the cathode worked as the working electrode at 1 mV/s from 0 to 0.7 V against anode.
- After that, oxygen was changed back in cathode and the durability test using accelerate stress test protocol (46) or recording the current response at a constant cell voltage of 0.60 V at 150 °C (136) were conducted using the Gamry potentiostat to test fuel cell lifetime.
- The polarization curve, EIS and LSV were successively performed to measure the fuel cell performance after the durability test.

4.4.1 Polarization curve

The polarization curve is also named as voltage-current-power curve which gives a complete picture of the MEA performance during fuel cell operation. The polarization curve consists of two plots: cell voltage profile (current density versus (vs) cell voltage, black line) and power density profile (current density vs power density, red line) as shown in Fig. 4.13. The power density profile was calculated from the cell voltage profile considering the electrode area. Since the current in Gamry 5000E potentiostat is up to 5 A and the range of voltage is from 0 V to 2 V to protect the device and the MEA, the current and voltage were automatically recorded by the potentiostat until the maximum current runs up to 5 A or the cell voltage is lower than 0.1 V. As introduced in part 2.3.2, there are three regions in the polarization curve (activation region, ohmic region and mass transfer region). In a HT-PEMFC, the humidifier is not required and there is no liquid water produced, therefore, the mass transfer resistance caused by water flooding can be almost neglected. However, the phosphoric acid flooding may be a factor to get increased mass transfer resistance especially for the degraded MEAs at high working current (318). The polarization curve at high-current-density region in Fig. 4.13 is fairly linear, illustrating the mass transfer resistance may not be the main issue in this example.

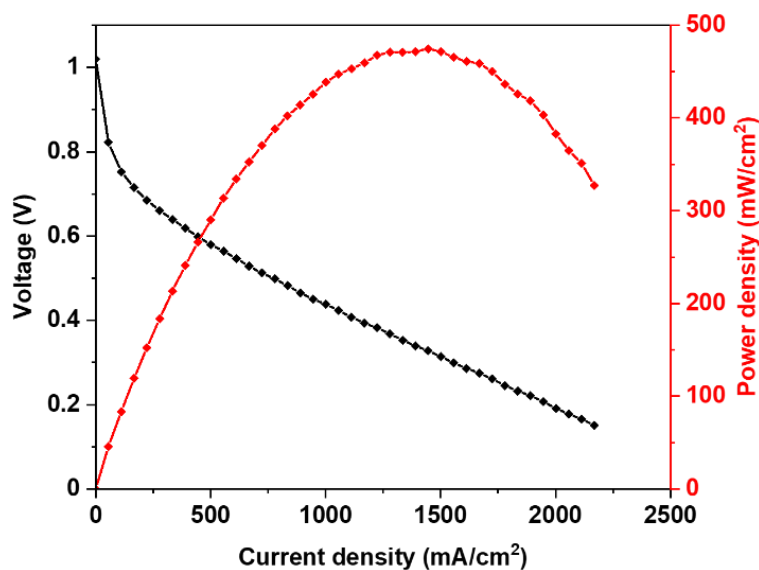


Fig. 4.13. Typical fuel cell polarization curve in a HT-PEMFC at 150°C.

4.4.2 Linear sweep voltammetry

In this work, LSV method was used to measure the hydrogen crossover. After hydrogen and nitrogen were supplied to anode and cathode respectively, Gamry 5000E potentiostat was employed to apply cathode potential from 0 to 0.7 V against anode at 1 mV/s to measure the hydrogen crossover. However, the measured LSV curves in this work (Fig. 4.14b) showed no limiting current platform which were different from the literature (Fig. 4.14a). Although 30 min

nitrogen supply was used to empty the oxygen in the cathode chamber, some gas residues (like oxygen absorbed by catalyst or from the outlet air) still existed and may have some negative impacts on the accuracy of LSV measurement. One explanation may be the oxygen residues in cathode can directly react with crossed hydrogen to produce mixed current and get decreased inaccurate hydrogen crossover limiting current. Herein, in this work, the calculation of hydrogen crossover using LSV limiting current was not applied. The comparisons of limiting current at a certain potential or the trend between different LSV curves were used to evaluate hydrogen crossover. As shown in Fig. 4.14b, four LSV curves standing for four different MEAs using different membranes after durability test were compared. The pure PBI membrane (black line) which had the highest hydrogen crossover current density indicates this membrane suffered the worst degradation and durability. The fuel cell setup can be updated with back pressure in future work to get accurate tested hydrogen crossover current density.

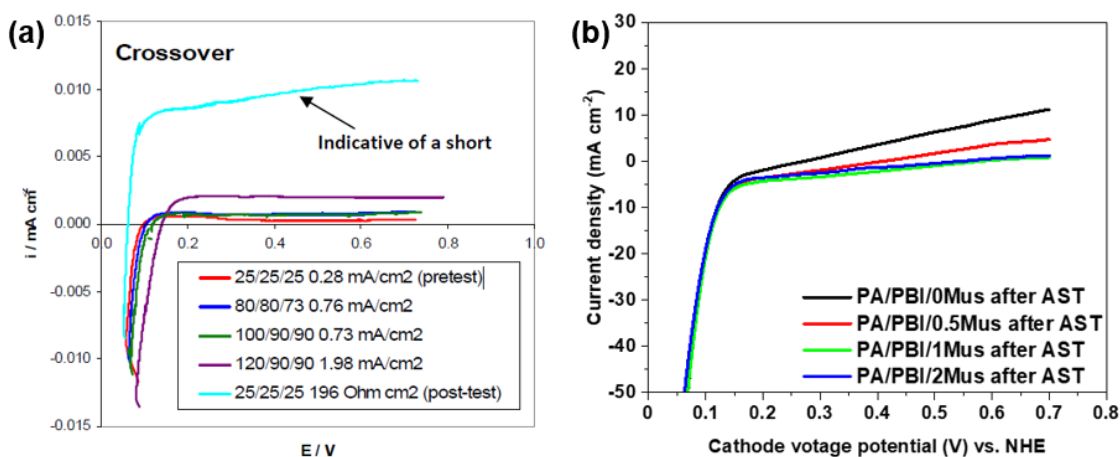


Fig. 4.14. (a) Hydrogen crossover data at different cell temperatures (51), and (b) hydrogen crossover current densities of PA/PBI/xMus membranes after accelerated stress test.

4.4.3 Electrochemical impedance spectroscopy

In this electrochemical impedance spectroscopy (EIS) experimental part, Gamry 5000E potentiostat was employed to test the impedance using the EIS method in the Gamry Instruments Framework software. The EIS curves were tested at different current (0, 0.1, 0.2, 0.3, 0.4, 0.5, 0.6 and 0.7 A) at 150 °C. In the EIS test, a small amplitude (0.015 A rms alternating current signal) needs to apply to the fuel cell from 10000 Hz to 0.1 Hz, so that the Gamry 5000E potentiostat can probe the response from the cell to generate impedance spectra according to impedance characteristics. In this work, EIS before and after durability test was performed at constant 0.6 A from 10000 Hz to 0.1 Hz at 150 °C. The corresponding EIS spectra are fitted by the equivalent circuits using Gamry Echem Analyst software. The proton conductivity was measured by the electrochemical impedance spectroscopy (EIS) using a Gamry 5000E at 0.6 A from 140 to 170 °C. The proton conductivity can be calculated using the equation below:

$$\sigma = \frac{L}{R \times A}$$

(4.2) where σ is the proton conductivity (S/cm), L is the membrane thickness (cm), R is the membrane resistance (Ω), and A is the membrane active area (cm^2).

In addition, by using Randles circuit model (Fig. 2.7b), Gamry Echem Analyst software was used to fit the EIS curves to obtain the equivalent circuits. An EIS example fitted by the Randles circuit model is shown in Fig. 4.15 where the well-fitted EIS curve illustrates that the Randles circuit model can stand for the equivalent circuits for this fuel cell. In the inset image of Fig. 4.15, the parameters (Y_0 and the dimensionless exponent α) are related to the properties of constant phase element. The unit of Y_0 is S s^α (siemens times second to the power of α). If $\alpha = 1$, Y_0 has the unit Farad (F) and represents an ideal capacitor. If $\alpha = 0$, Y_0 is the reciprocal of a resistor with the unit $\text{S} = \Omega^{-1}$ (319).

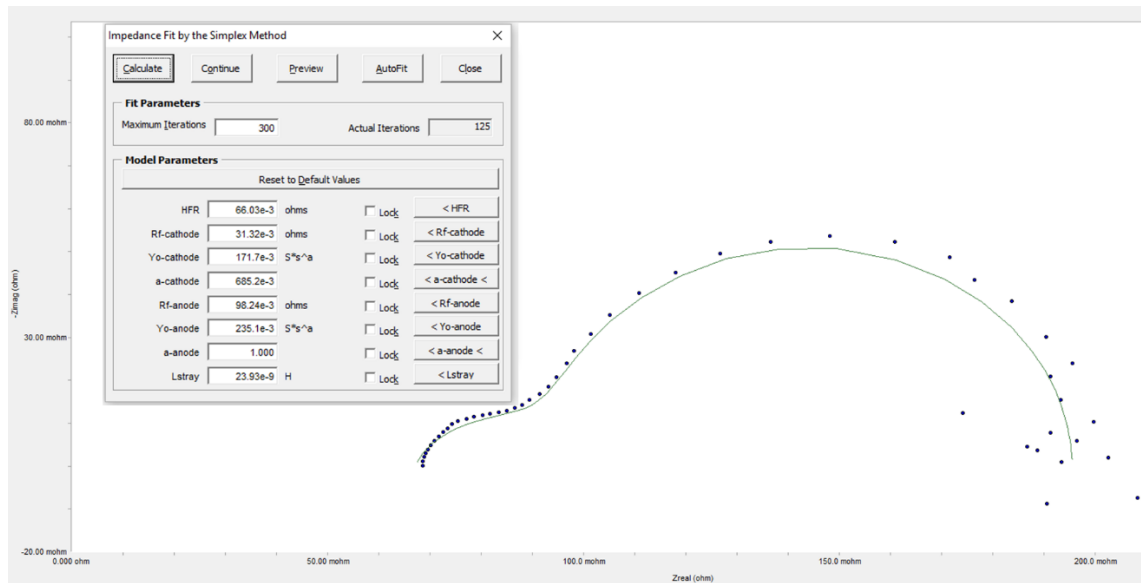


Fig. 4.15. An example of EIS curve and fitted curve with fitted impedance data using Randles circuit model in the Gamry software (Gamry Echem Analyst).

4.4.4 Durability test

Understanding fuel cell durability and analysing degradation mechanisms are important to evaluate and enhance the durability of HT-PEMFCs. In this work, the durability test of a single cell using PES-PVP membrane was evaluated using steady-state test at a constant cell voltage of 0.60 V and 150 °C for around 1200 min. The Chronoamperometry method was used to measure the cell durability using Gamry 5000E potentiostat.

In addition, considering that the majority of phosphoric acid (PA) in HT-PEMs especially at high acid doping level are free PA molecules and tend to leach out due to the relatively weak interactions with the polymer matrix, an accelerated stress test (at 0.6 A/cm² for 4 min, 1

A/cm² for 16 min, and open circuit voltage for 10 min every 6 h) which can accelerate electrolyte leaching was utilized to evaluate the PA retention ability of PBI membranes.

4.5 Characterization techniques

In this work, inorganic materials were incorporated into PES-PVP or PBI membranes to enhance the fuel cell performance. To better understand why and how there had some improvements in the cell, the chemical and physical characterizations of membranes and inorganic fillers were performed. In this section, several techniques are introduced in details and the related working mechanisms are also included as shown below.

4.5.1 Thermogravimetric Analysis

Thermogravimetric analysis (TGA) is applied in many types of research area such as materials science, material thermal durability, and the studies of reaction kinetics. TGA measures weight changes in response to the increases in temperature or time under protective gas atmosphere (Fig. 4.16). TGA can continuously record sample mass as the temperature increases over time, generally from room temperature to 1000 °C with sensitivities of several micrograms. Also, the temperature ramp or rising and decreasing speed inside the chamber can be pre-set by the TGA program. By controlling the temperature changing rate, types of gas, or operating temperature, several valuable information can be investigated such as thermal stability, sensitivity to oxidation, composition, decomposition kinetics, and the moisture content. For instance, when the temperature inside the chamber rises from room temperature up to 200 °C, the weight loss of the sample usually corresponds to the absorbed moisture.

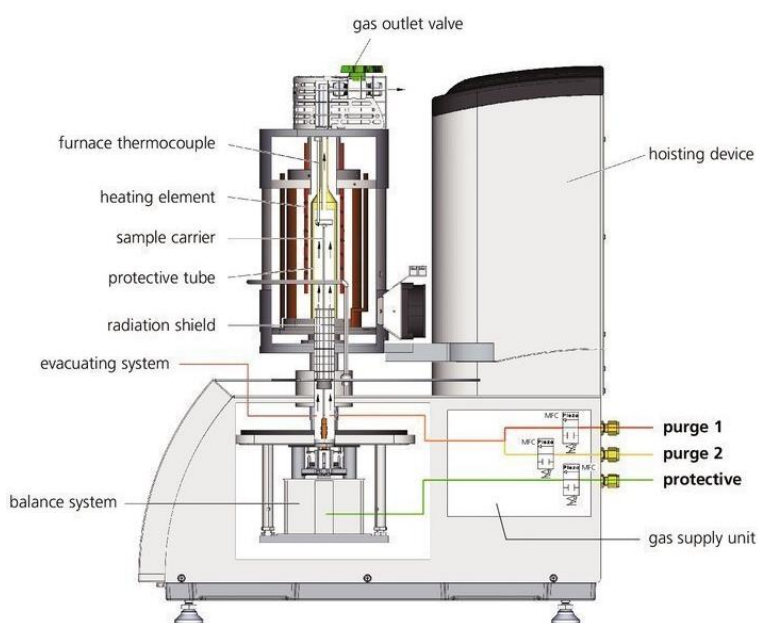


Fig. 4.16. Schematic representation of TGA (320).

Attentions should be paid for the moisture or air sensitive samples. For some samples which can easily absorb moisture from the air or react with air, the protective measurement such as transferring the samples inside the glove box to the TGA chamber can be taken. There are different sample pans according to its materials such as sample pans metal (stainless steel, aluminium, platinum, titanium, gold), or ceramic sample pans. In this work, aluminium pan was used, and the thermal stability of clay-based materials and membranes are tested at a heating rate of $10\text{ }^{\circ}\text{C min}^{-1}$ in a nitrogen atmosphere using Discovery TGA 550 from room temperature up to $800\text{ }^{\circ}\text{C}$.

4.5.2 Fourier-transform infrared spectroscopy

Fourier transform infrared spectroscopy (FTIR) is one of the most powerful tools for the determination of functional groups and possible chemical bonds in samples. In Fig. 4.17, the main component of a FTIR is schematically illustrated (321). The instrument produces a beam of IR irradiation which passes through interferometer where the spectral encoding takes place. The beam then goes through the sample and the specific frequencies of the beam are absorbed. The remaining signals are detected by the detector, which shows unique characteristics for each sample from the interferogram. Afterwards, the computer will simultaneously collect and process the special interferogram signal vs. time for all frequencies to produce the FTIR curve.

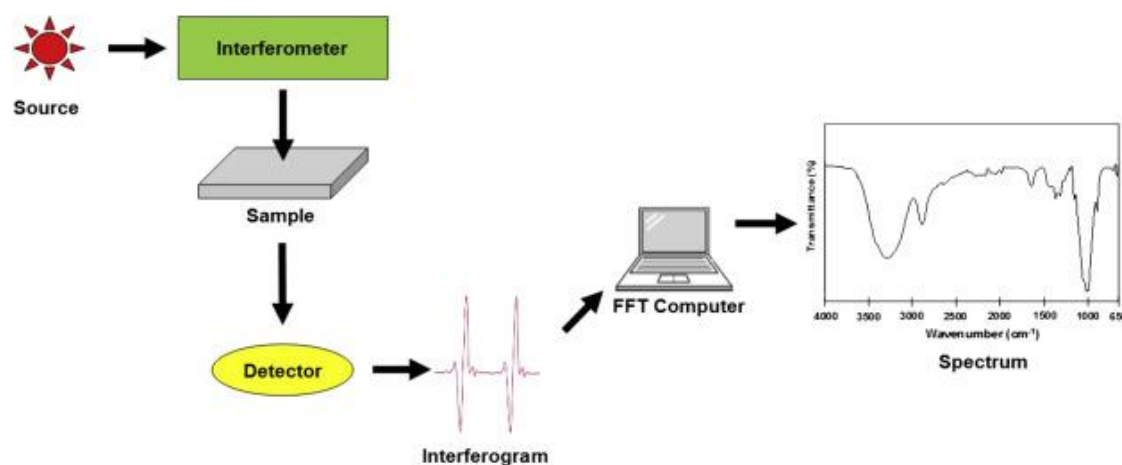


Fig. 4.17. Schematic representation of FTIR (321)

In the experimental procedure, FTIR spectra were determined using a Tensor 27 FTIR spectrometer. A reference working as the background without any samples needs to be performed before measuring any samples. The obtained spectrum of the reference ('empty' sample) will be selected as the background and automatically subtracted from the real sample spectrum by a spectroscopy software (OPUS, Bruker). In this work, different membranes and inorganic materials were tested by the FTIR spectroscopy at frequencies from 4000 to 400 cm^{-1} , and the

related peaks of FTIR spectra based on transmission were compared with the IR spectrum table to characterize chemical bonding in the tested samples.

4.5.3 X-ray diffraction

X-ray diffraction (XRD) is a powerful non-destructive technique to characterize the crystallinity of materials. It provides information on structures, phases, crystal orientations, and other structural parameters such as average grain size, crystallinity, strain and crystal defects. XRD peaks are produced by constructive interference of a monochromatic beam of X-rays which are scattered at specific angles from each set of lattice planes in a sample. The peak intensities are then determined by the distribution of atoms within the lattice (322). Currently there are two major types of XRD as shown in Fig. 4.18 (XRD with fixed goniometer or with fixed X-ray source), illustrating the geometry of the system and the layout of a typical diffractometer (323). When X-ray with the wavelength λ is produced from the source, it hits the sample crystal at an angle θ (an angle between the incident beams and diffracted beam) and diffracts in a pattern depending on the structure of the sample. The intensity of diffracted beam is then detected, processed, and counted. The interaction of the incident rays with the sample produces constructive interference (and a diffracted ray) when conditions satisfy the Bragg's law (equation 4-1). This law relates the wavelength of electromagnetic radiation to the diffraction angle and the lattice spacing in a crystalline sample. By scanning the sample through a range of 2θ angles, the graph (the intensity vs the angle of the detector) is then generated in the computer. Because each compound has a set of unique d-spacings, the identification of the compound can be attained by the conversion of the diffraction peaks to d-spacings.

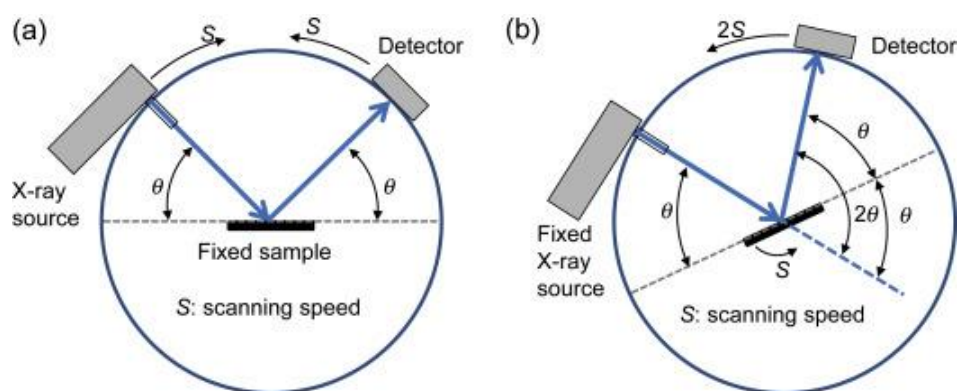


Fig. 4.18. Instruments for powder XRD with fixed goniometer (1), and with fixed X-ray source (2) (323).

In this work, an XRD instrument (the PANalytical X'Pert Pro X'Celerator diffractometer) was employed to measure the crystallinity of inorganic fillers and confirm the characteristic diffraction peaks. The scanning angles range from 2 to 60° with 1° min⁻¹ scan speed. The d-spacing of samples can be calculated via the Bragg's law:

$$2d \sin \theta = n\lambda \quad (4.1)$$

where d is the crystal planar spacing (nm), θ is the X-ray beam incident angle, n is a positive integer ($n = 1$), and λ is the wavelength of the incident wave ($\lambda = 0.154$ nm).

4.5.4 X-ray photoelectron spectroscopy

The typical X-ray photoelectron spectroscopy (XPS) instrumentation (Fig. 4.19) comprises an X-ray source, a vacuum system, an electron energy analyser and data system. The sample is placed in the ultrahigh vacuum chamber via load-lock or preparation chamber, and then irradiated with photons in the X-ray range. X-rays are created usually by impinging a high-energy (~ 10 keV) electron beam onto an anode. During this time, core holes are created by the emitted photoelectrons in the atoms of the anode material and the fluorescence X-rays are produced. Mg or Al K α radiation (1253.6 or 1486.6 eV) is usually used in XPS. During the measurement, anode is usually cooled by water because some incident electron energy is converted into heat. The photoelectrons which have a sufficient energy to escape from the irradiated sample into the vacuum chamber are then separated and counted by the energy dispersive analyser. When this X-ray flux is illuminating a sample, the spectrometer operation and data acquisition are controlled by the computer program.

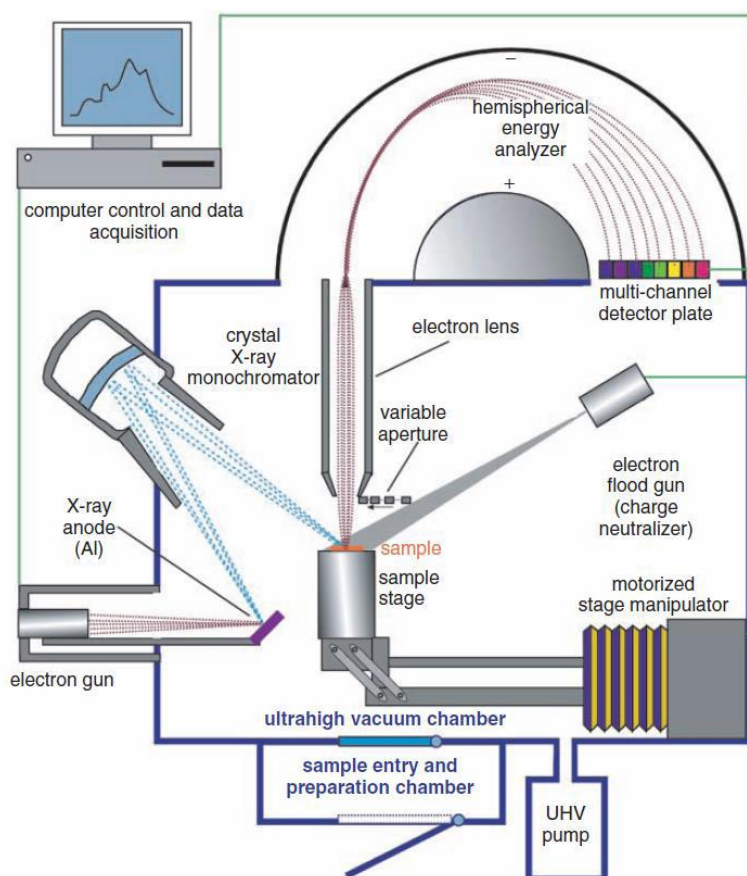


Fig. 4.19. Schematic representation of the XPS instrumentation (324).

In this work, the composition and functional groups of the clay-based materials were analysed using XPS (Kratoms Axis SUPRA) fitted with a monochromated Al K α X-ray source (1486.7 eV), 3 multichannel resistive plate, a spherical sector analyser, and 128 channel delay line detectors. All data was recorded at 150 W and a spot size of 700 x 300 μ m. Survey scans were recorded at a pass energy of 160 eV, and the high-resolution scans were recorded at a pass energy of 20 eV. Electronic charge neutralization was achieved using a magnetic immersion lens where filament current, charge balance, and the filament bias are 0.27 A, 3.3 V and 3.8 V, respectively. The sample data was recorded at a temperature of 294 K and a pressure below 10⁻⁸ Torr. The collected data was analysed using CasaXPS v2.3.20PR1.0.

4.5.5 Universal testing machine (mechanical testing)

Tensile testing is performed by elongating a specimen and measuring the load carried by the specimen using a test machine (Instron Universal Materials Testing Machine). By inputting the specimen dimensions into the Bluehill Universal software, the load and deflection data can be translated into a stress-strain curve. Fig. 4.20 shows a schematic image of an Instron universal testing machine and a diagram of the test configuration details where the sample jaws are different from different samples. For holding a thin film, rubber-surfaced grips are typically used to securely hold thin films. If necessary, abrasive papers can be attached to the jaws to hold the smooth thin samples.

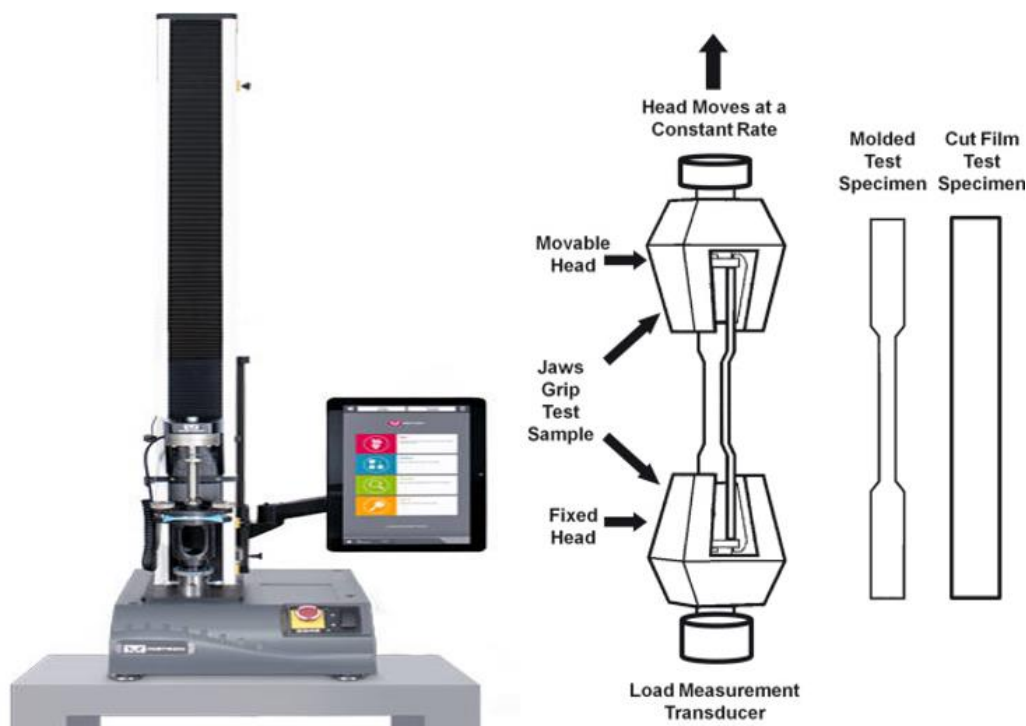


Fig. 4.20. Schematic representation of the tensile test instrument (325).

Before the testing of samples, a moulded test specimen needs to be applied in the testing machine to get the transducer calibrated. In this work, the tensile strength, elongation at break and Young's modulus of membranes ($0.5 \text{ cm} \times 5 \text{ cm}$) were tested by tensile test instrument (INSTRON 3344 with 100 N load cell) at a strain rate of 5 mm/min at room temperature.

4.5.6 Brunauer-Emmett-Teller (BET) Surface area

As shown in Fig. 4.21, BET surface area analyser contains two major components: the degassing and adsorption stations (326). The pre-cleaned sample tube is firstly loaded with 0.1-0.3 g sample, and connected to the degassing station. Degassing the sample is to remove physically adsorbed moisture and contaminants that accumulated during storage. Mild degassing temperatures and vacuum are used to degas the thermally sensitive solids. For fragile porous materials, inert gas will be introduced using the adsorbate path connected to the degassing station. After degassing, the sample tube will be removed from the degas port, weighed, and then installed onto the adsorption port for analysis. The weight difference between before and after degassing should be subtracted to get the weight of 'cleaned' sample. After the weight of sample is inputted, the adsorption cycle is performed by gradual introducing nitrogen with the calibration volume. The pressure difference between the measured and empty tube correlates with the number of moles of adsorbed nitrogen. During measurements, the cell is maintained at liquid nitrogen boiling point using a Dewar flask filled with liquid nitrogen to remain a low temperature. This can be explained that the low temperature can maintain the strong interaction between the gas molecules and the surface of the sample to measure the amounts of adsorbed gas onto the sample.

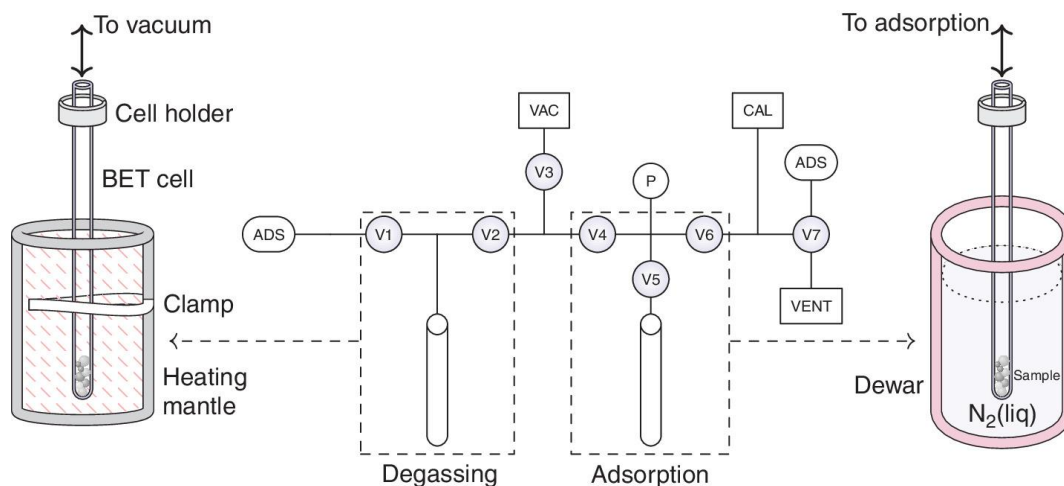


Fig. 4.21. Schematic representation of BET surface area analyser (vacuum (VAC), calibration (CAL), adsorbate (ADS), pressure gauge (P), V1-V7 valves) (326).

In this work, the specific surface area of samples was characterized within a relative pressure range (P/P_0) of 0.05-0.30 using a Micromeritics ASAP 2020 (Fig. 4.22). The pore volume was determined from the amount of N_2 adsorbed at the P/P_0 of 0.995, and the pore diameter was

obtained by applying the Barrett-Joyner-Halenda (BJH) model to the desorption isotherm. Before the analysis, the samples should be degassed at 120 °C for 6 h. The obtained BET data were processed by ASAP 2020 software.

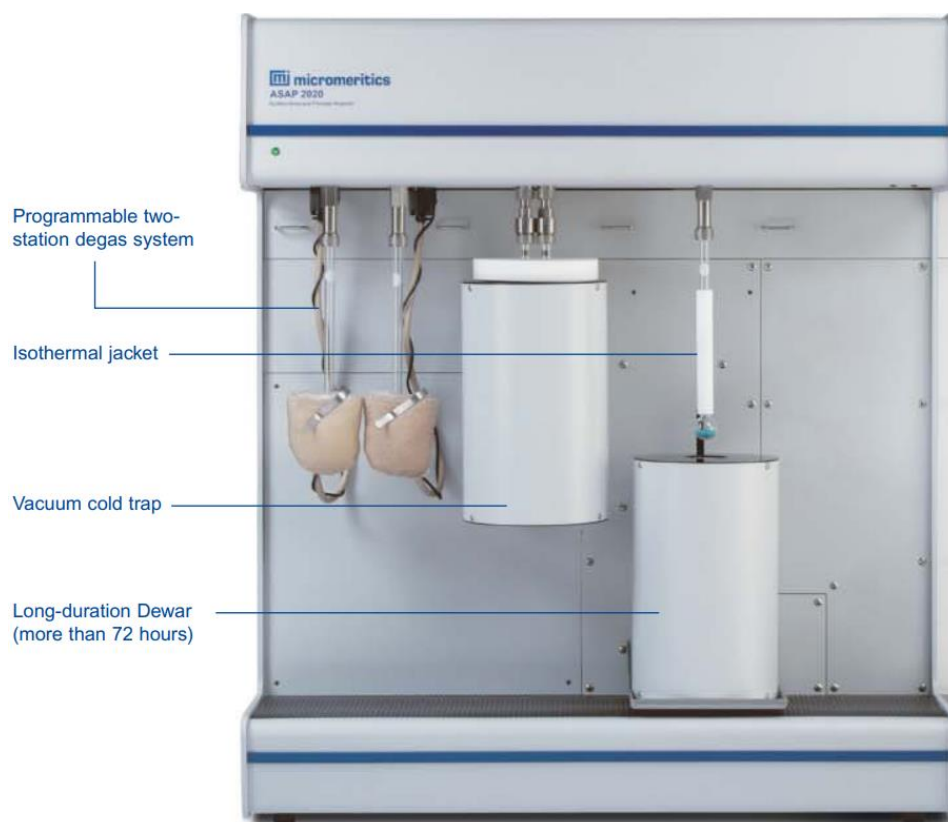


Fig. 4.22. Physical observation of Micromeritics ASAP 2020 (327).

4.5.7 Scanning electron microscopy

Scanning electron microscope (SEM) is a type of electron microscope that produces sample images by scanning its surface using a focused electron beam. The electron beam interacts with atoms in the sample to produce various signals and information about its surface topography and be collected by detectors. The detected signal is synchronized with known location of the beam on the sample, and the intensity of signal can modulate the corresponding image pixel. The in-series collected signals can be combined to form an image according to the scan pattern. A SEM can produce an image referring to the interactions of the electron beam with atoms at various depths within the sample, including secondary electrons, back-scattered electrons, characteristic X-rays, light, absorbed current and transmitted electrons. As shown in Fig. 4.23 (328), the SEM usually contains the electron gun (electron source and accelerating anode), electromagnetic lenses to focus the electrons, a vacuum chamber with sample stages, a selection of detectors to collect the signals emitted from the sample, related amplifier and the computer to show sample morphologies. There are usually three imaging modes in a SEM: the ‘high vacuum mode’ (a conventional SEM mode), the ‘low vacuum mode’ (where non-conductive samples can be imaged

without the need of a conductive layer), and the ‘ESEM mode’ (environmental SEM where the wet samples can be investigated in their “natural” state).

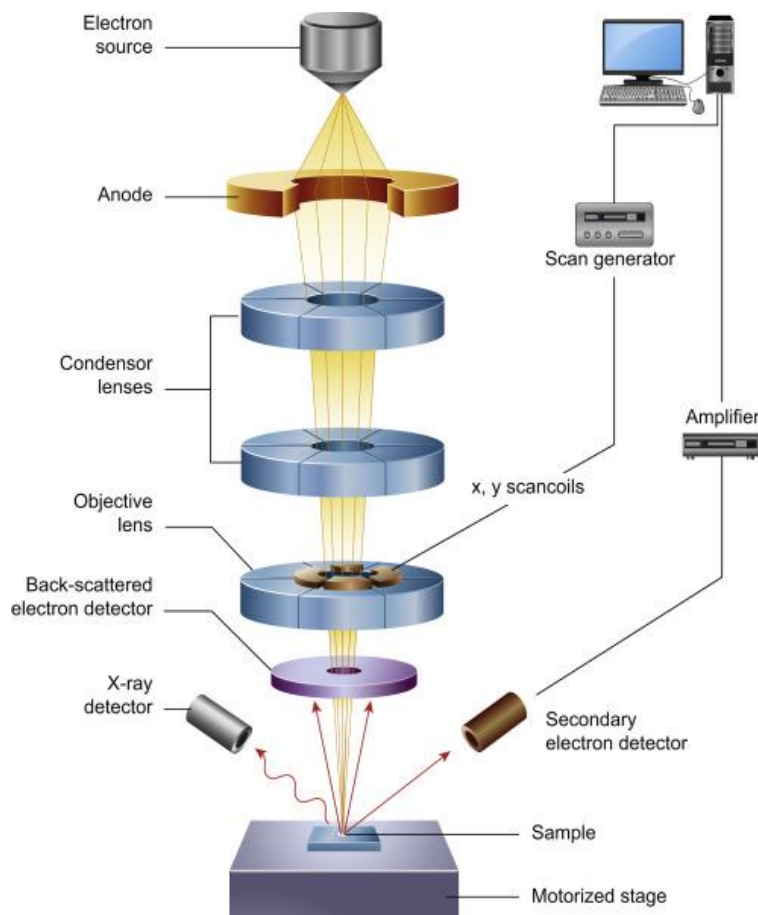


Fig. 4.23. Schematic representation of the core components of a SEM (328)

In this work, FEI Quanta 250 and TESCAN MIRA3 were used to analyse the morphology of clay-based fillers, the surface and cross-sections of membranes and MEAs. Before SEM analysis, all non-conductive samples were coated with a gold layer using a coating machine (Cressington 108 Auto Sputter Coater). The MEA was cut by a disposable scalpel No. 20 (Swann Morton) to get the MEA cross-section. For the configuration of Quanta 250, the source tilt and lens alignment were firstly adjusted. The spot size ranges from 1-6 and the beam energy is in the range from 0.5 to 30 kV in Quanta 250 where spot size ‘3’ or ‘4’ and 10-20 kV beam energy are usually selected. When the high magnification is needed, spot size ‘6’ can be chosen. The element (phosphorus) distribution in the MEA cross-section after AST was investigated using Energy Dispersive X-ray Spectroscopy (EDS, Oxford Instruments) mapping with QuantMap module in TESCAN MIRA3.

4.5.8 Transmission electron microscopy

Transmission electron microscopy (TEM) is a microscopy technique in which a beam is transmitted through a specimen to form an image. As shown in Fig. 4.24 (328), the schematic

representation of a TEM comprises an electron gun to emit the electrons, electrostatic lenses to focus the electrons before and after the specimen, electron detectors, and corresponding display system. A high energy beam of electrons will be produced and permeate through a very thin sample, and the interactions between electrons and the sample atoms collected by the detectors can reflect the crystal structure such as dislocations and grain boundaries.

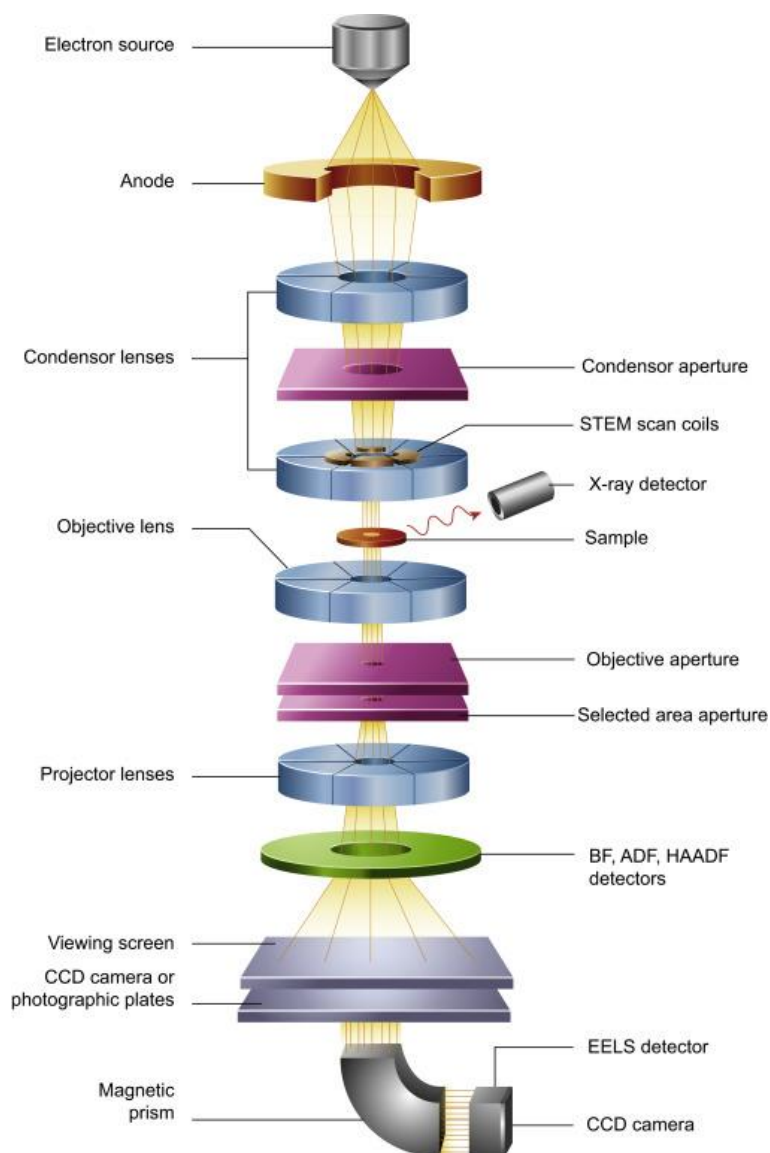


Fig. 4.24. Schematic representation of the key components of a TEM (328).

In this work, the structure of silica nanosheets and vermiculite were characterized by a Thermo Fisher Titan Scanning Transmission Electron Microscope (STEM) equipped with a Cs probe corrector and ChemiSTEM Super-X EDS detector. The STEM was fitted with a convergence angle of 21 mrad and a high angle annular dark field detector with an inner angle of 55 mrad at 200 kV. The element distributions of silica nanosheets and vermiculite were analysed by EDS mapping in STEM mode. The TEM samples were prepared by dispersing the materials in absolute

ethanol by 10 min ultrasonication and then drop-casting onto holey carbon coated copper TEM grids.

4.6 Conclusion to this chapter

This chapter explained the preparation procedures of microporous layer, catalyst layer and membrane. In addition, the testing methods of fuel cell performance (polarization curve, linear sweep voltammetry, electrochemical impedance spectroscopy, and durability test) and the sample characterization techniques, including thermogravimetric analysis (evaluating the thermal stability of inorganic fillers and membranes), Fourier-transform infrared spectroscopy (analysing functional groups or chemical bonds), universal testing machine (mechanical testing to measure the mechanical properties of membranes), X-ray diffraction (confirming the crystalline of inorganic fillers), X-ray photoelectron spectroscopy (analyzing the amount of functional groups on the surface of inorganic fillers), BET surface area (measuring the textual properties of inorganic fillers), scanning electron microscopy (analysing the morphology of inorganic fillers and membranes), and transmission electron microscopy (analysing the morphology and crystalline structure of inorganic fillers), are also introduced. The result and discussion of these experimental methods and their characterizations are explained in the following chapter.

Chapter 5: Performance of standard polyethersulfone–polyvinylpyrrolidone membranes

5.1 Introduction

High-temperature PEMFCs (HT-PEMFCs) work at temperatures ranging from 100 to 200 °C, and have been developed because they offer several advantages over low-temperature PEM, such as faster electrochemical reactions, higher fuel impurity tolerance and simple water management (329). Phosphoric acid (PA) doped polybenzimidazole (PBI) membranes have been extensively explored in HT-PEMFCs, allowing good proton conductivity and durability under higher operating temperatures (7). However, the poor processability of high-molecular-weight PBI and the toxicity of its raw materials have resulted in limited commercial development (8). As N-heterocycle of polyvinylpyrrolidone (PVP) is an excellent proton acceptor, recently PVP blended membranes have attracted attention due to their simple fabrication procedure and good fuel cell performance. However, pure PVP membrane is highly hydrophilic and swells extensively in water (213). Another thermally stable polymer is therefore needed to blend with PVP to afford mechanical stability. PVP membranes blended with phosphonated poly(2,6-dimethyl-1,4-phenylene oxide) (231), polyvinylidene fluoride (307) and polyethersulfone (PES) (72, 232) have been developed as HT-PEMs. As PES-PVP blended membrane showed the highest proton conductivity and comparable power density (Table 4.1), the PES-PVP blended membrane was chosen as the membrane in this work. The main objective in this chapter is the investigation of the optimal preparation method of the standard PES-PVP membrane.

The parameters in this chapter are different polymer molecular weights (PES: Ultrason E7020P and E6020P; PVP: PVP1300 and PVP360) and different polymer mixing methods (indirect and direct mixing). The blended membranes prepared using different preparation methods (Table 5.1) will be tested and evaluated by different membrane characterizations (FTIR, TGA, mechanical properties, and acid doping and swelling) and fuel cell performance (polarization curve, durability, hydrogen crossover, proton conductivity, and electrochemical impedance spectroscopy).

Table 5.1. Configurations of each prepared membrane.

Name	PES molecular weight (g/mol)	PVP molecular weight (g/mol)	Mixing method
PES/PVP-7020-Indirect	95,000	1,300,000	Indirect
PES/PVP-7020-Direct	95,000	1,300,000	Direct

PES/PVP-6020-Indirect	73,000	1,300,000	Indirect
PES/PVP360-Indirect	95,000	360,000	Indirect

5.2 Membrane preparation

5.2.1 PES/PVP-7020-Indirect

By following the steps in Fig. 5.1b which is the same procedure described in section 4.3.1.2, 0.12 g PES (Ultrason E7020P, molecular weight is 95,000 g/mol) was dissolved in 3 mL N,N-dimethylformamide (DMF), and 0.18 g PVP (PVP1300, molecular weight is 1300,000 g/mol) was dissolved in 4 mL DMF. Then PES and PVP solutions were mixed under stirring for at least 12 h to get a homogeneous solution. And the homogeneous solution was cast onto a Teflon dish. It was then dried at 60 °C for 20 h under ambient pressure and 130 °C for 3.5 h under vacuum. After being easily peeled from the Teflon dish, the membrane is labelled as PES/PVP-7020-Indirect.

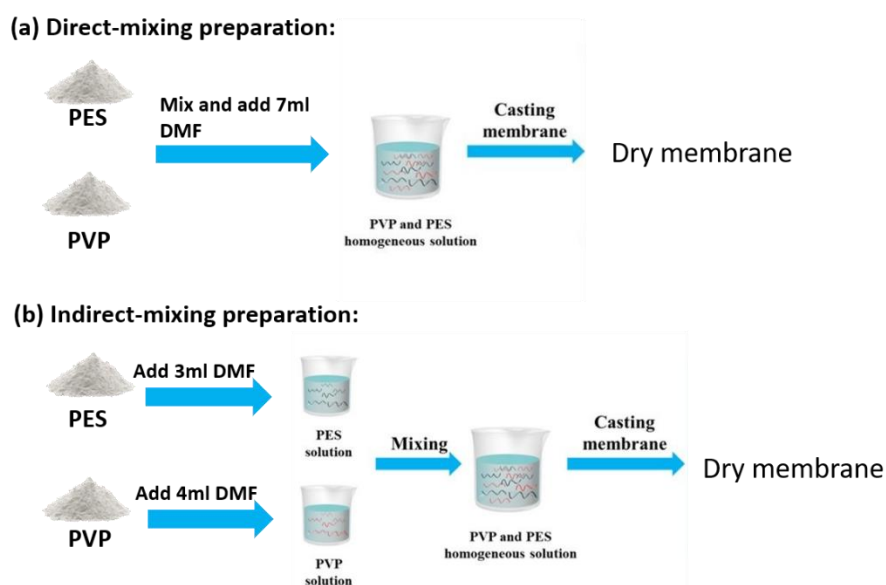


Fig. 5.1. Membrane casting methods: (a) direct-mixing preparation, and (b) indirect-mixing preparation.

5.2.2 PES/PVP-7020-Direct

PES/PVP-7020-Direct stands for the membrane prepared using Ultrason E7020P and PVP1300 as polymers and applying direct-mixing method. As shown in Fig. 5.1a, 0.12 g PES (Ultrason E7020P) and 0.18 g PVP (PVP1300) were directly mixed and then dissolved in 7 mL DMF. After being stirred overnight, the homogeneous solution was cast onto a Teflon dish and dried at 60 °C for 20 h under ambient pressure and 130 °C for 3.5 h under vacuum to get PES/PVP-7020-Direct.

5.2.3 PES/PVP-6020-Indirect

PES/PVP-6020-Indirect means the membrane is prepared using Ultrason E6020P and PVP1300 with indirect-mixing method. All other procedures such as membrane casting conditions are the same as the procedure in section 5.2.1.

5.2.4 PES/PVP360-Indirect

Via applying the same procedures in section 5.2.1 but using Ultrason E7020P and PVP360 as the polymers, the PES/PVP360-Indirect was prepared using indirect-mixing method.

5.3 Membrane characterization

5.3.1 Fourier-transform infrared spectroscopy analysis

Fourier-transform infrared spectroscopy (FTIR) was carried out to investigate the chemical components of PA doped blended membranes. As shown in Fig. 5.2, the vibration peak of at 1631 cm^{-1} presents the C=O in PVP. Also, a typical symmetric and asymmetric vibration peak of O=S=O is observed at 1146 cm^{-1} and the characteristic absorption peaks at 1577 cm^{-1} and 1485 cm^{-1} are attributed to the aromatic bands of the benzene ring in PES, indicating the existing of PES in all membrane samples. Due to the participation of free PA molecules, the band at the wavenumber of 966 cm^{-1} (C-C stretching vibration of PVP) has shifted to $1050\text{--}900\text{ cm}^{-1}$. There are no obvious differences between different membranes prepared using different methods, illustrating that PES-PVP blended membranes prepared using different molecular weights or blending methods contain the same chemical bonds.

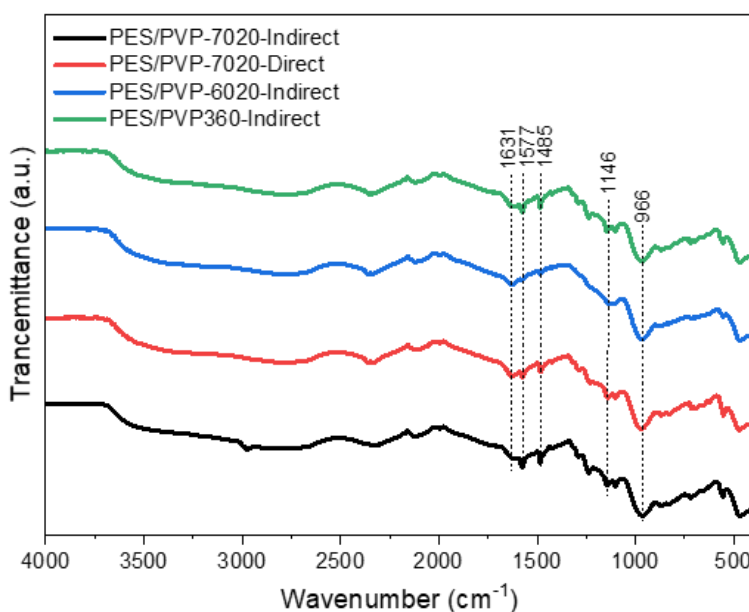


Fig. 5.2. FTIR spectra of PA-doped PES-PVP blended membranes.

5.3.2 Thermogravimetric analysis

As shown in Fig. 5.3, the thermal stabilities of all PES-PVP membranes were determined by Thermogravimetric analysis (TGA). The TGA curves of the all membranes prepared using different molecular weights or mixing methods showed overlapping and similar weight loss. The initial loss of all PES-PVP membranes happened when the temperature approached to 100 °C, which is attributed to the release of unbound moisture absorbed by the membranes. The second mass loss started from around 200 to 300 °C because of the removal of solvent residues in the polymer chains. Due to the decomposition of imidazole rings in PVP (72), we see the third mass loss when the temperature rises over 350 °C. This demonstrates that all PES-PVP membranes have intact structures under 350 °C and are able to be the HT-PEMs under HT-PEMFC operating temperatures (100–200 °C). Meanwhile, there are almost no differences on the weight loss of different membranes when the temperature is up to 400 °C, illustrating that all membranes show similar thermal stability.

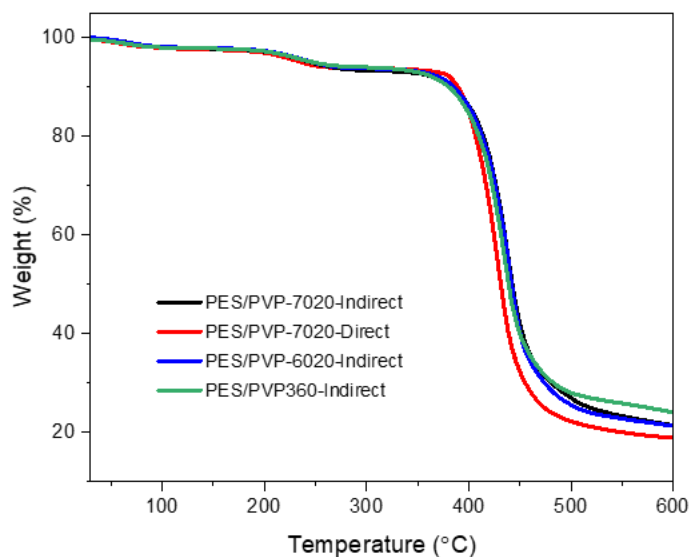


Fig. 5.3. TGA curves of PES-PVP blended membranes.

5.3.3 Mechanical properties

The stress-strain curves of membranes before and after acid doping were measured (Fig. 5.4) and the mechanical properties are summarized in Table 5.2. The phosphoric acid (PA) doped membranes (Fig. 5.4b) had lower tensile strength, higher elongation and lower Young's modulus than the dry membranes (Fig. 5.4a), suggesting that PA molecules act as plasticizers to the membrane (136). The PA doped high-molecular-weight membranes, which were prepared using high-molecular-weight PES and PVP, have higher tensile strength and elongation than the low-molecular-weight membranes, which show the same trend as the result from Yang's work (250). PES with large molecular weight has longer polymer chains to facilitate the formation of dense

structure to get increased tensile strength. PA doped direct-mixing membrane (PES/PVP-7020-Direct) had highest tensile strength (3.72 MPa), which had similar tensile strength for PES/PVP-7020-Indirect (2.93 MPa). For the undoped membranes as shown in Fig. 5.4a, PES/PVP-7020-Indirect membrane showed higher tensile strength (65.34 MPa) and elongation (6.03%), compared with only 58.83 MPa and 4.57% in PES/PVP-7020-Direct, respectively. In addition, all undoped membranes prepared using indirect mixing method (indirect-mixing membranes) had higher Young's modulus than PES/PVP-7020-Direct (Table 5.2). The Young's modulus was calculated by the initial slope of the linear part of the stress-strain curve, where the membrane dislocation is in the elastic deformation region and is practically reversible. The direct-mixing membranes may suffer uneven mixing during the preparation, which can possibly explain why the tensile strength and Young's modulus of the indirect-mixing undoped membrane had higher value than the direct-mixing one. Future work needs to be focused on the modelling of PVP and PES chain arrangement in the membranes prepared by different mixing methods.

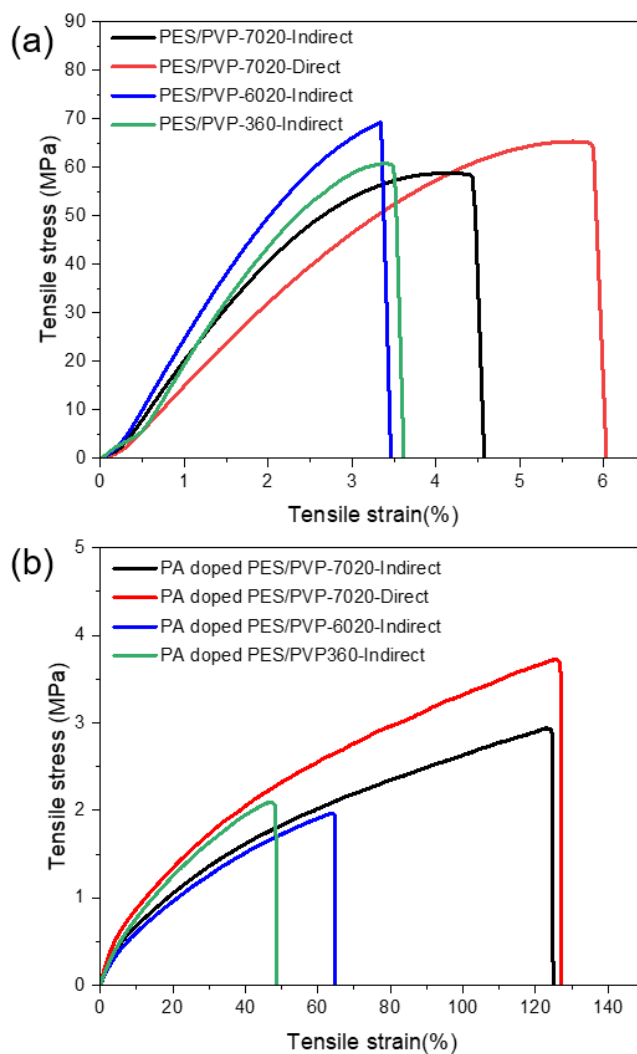


Fig. 5.4. Stress-strain curve of membranes (a) before and (b) after PA doping.

Table 5.2. Summary of mechanical properties of blend membranes before and after PA doping.

Membrane	Tensile Strength (MPa)		Break Elongation (%)		Young's modulus (MPa)	
	Doped	Undoped	Doped	Undoped	Doped	Undoped
PES/PVP-7020-Indirect	2.93	65.34	124.81	6.03	2.02	1396.6
PES/PVP-7020-Direct	3.72	58.83	126.95	4.57	2.02	1179.7
PES/PVP-6020-Indirect	1.96	69.27	64.7	3.46	2.51	2123.3
PES/PVP360-Indirect	2.09	60.78	48.49	3.61	2.79	1915.9

5.3.4 Acid doping and swelling

The acid uptake, acid doping level (ADL) and membrane swelling properties of different membranes are shown in Table 5.3. ADL is related to the acid uptake in membranes where the acids interact with PVP or exist as free acids inside membranes. Usually, the ADL can also reflect the membrane swelling properties as the membrane with more acids usually has greater swelling. Therefore, the density and PVP distribution of membranes can determine ADL and the swelling properties. Although PES/PVP-7020-Indirect had higher ADL than PES/PVP-7020-Direct, indirect-mixing method may benefit for homogeneous PVP distribution in membranes to obtain larger density and lower volume swelling than the direct-mixing method.

Regarding the impacts of different molecular weights on ADL and swelling properties, the low-molecular-weight membranes (PES/PVP-6020-Indirect and PES/PVP360-Indirect) showed larger volume swelling compared with high-molecular-weight membranes (PES/PVP-7020-Indirect). This can be explained that high-molecular-weight PVP and PES have longer macromolecular chains and are more resistant to rearrangement to get less swelling (250).

Table 5.3. Summary of acid uptake, ADL and swelling properties of prepared membranes.

Membrane	Acid uptake/%	ADL/mol	Area swelling/%	Thickness swelling/%	Volume swelling/%
PES/PVP-7020-Indirect/PA	322.60	5.96	52.00	64.55	150.13
PES/PVP-7020-Direct/PA	292.86	5.53	68.89	63.69	176.47
PES/PVP-6020-Indirect/PA	368.10	6.00	68.89	108.65	252.39
PES/PVP360-Indirect/PA	318.04	6.94	73.33	109.40	262.97

5.4 Fuel cell performance

5.4.1 Polarization curve

The polarization curves of all fresh MEAs based on different membranes (PES/PVP-7020-Indirect, PES/PVP-7020-Direct, PES/PVP-6020-Indirect, and PES/PVP360-Indirect) tested at 150 °C without humidification are shown in Fig. 5.5. Among all membranes, the PES/PVP360-Indirect showed the highest power density (437 mW/cm²), which is in consistent with highest ADL among all PA doped membranes in Table 5.3. The higher acid uptake and ADL usually corresponds to higher proton conductivity, therefore, the membrane with higher acid uptake performs higher power density as shown in Fig. 5.5. However, other properties such as durability and mechanical properties might behave in a reverse way because higher acid uptake usually means there are larger swellings and less dense structure in membranes to get higher tendency of acid leaching, further resulting in worse degradation and durability.

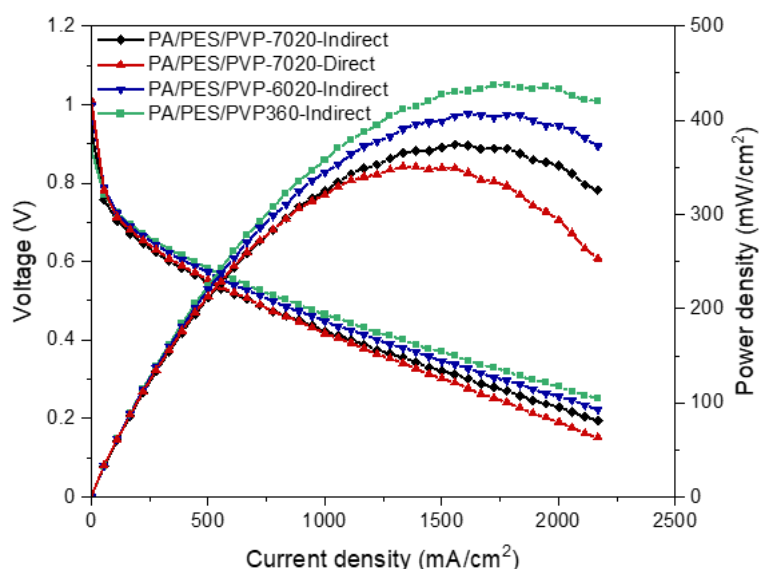


Fig. 5.5. Polarization curves of all fresh PES-PVP membranes at 150 °C without humidification.

5.4.2 Durability

To better investigate the fuel cell durability, the cell was operated at 0.6 V under a steady-state test at 150 °C for 1200 min. All MEAs showed decreased current density as shown in Fig. 5.6a, while the MEAs using high-molecular-weight polymers presented good stability and lower decay rates (Fig. 5.6b). For instance, PES/PVP-7020-Indirect and PES/PVP-7020-Direct only suffered 3.10 and 3.70 mA/cm²·h respectively, which are smaller than the decay rates of low-molecular-weight membranes (4.25 mA/cm²·h for PES/PVP-6020-Indirect and 5.50 mA/cm²·h for PES/PVP360-Indirect). The acid leaching from the membrane may result in decreased proton conductivity and deteriorated performance. Another factor is the chemical degradations of polymer chains. Since free radicals attack the hydrogen bonding and break polymer chains into

small parts (307), the high-molecular-weight membranes can survive longer time and have lower current density decay rates than the low-molecular-weight membranes. On the other hand, compared with direct-mixing membrane (PES/PVP-7020-Direct), the indirect-mixing membrane (PES/PVP-7020-Indirect) has lower decay rate, demonstrating that the indirect-mixing method may help to get homogenous structures, even acid distribution and improved durability.

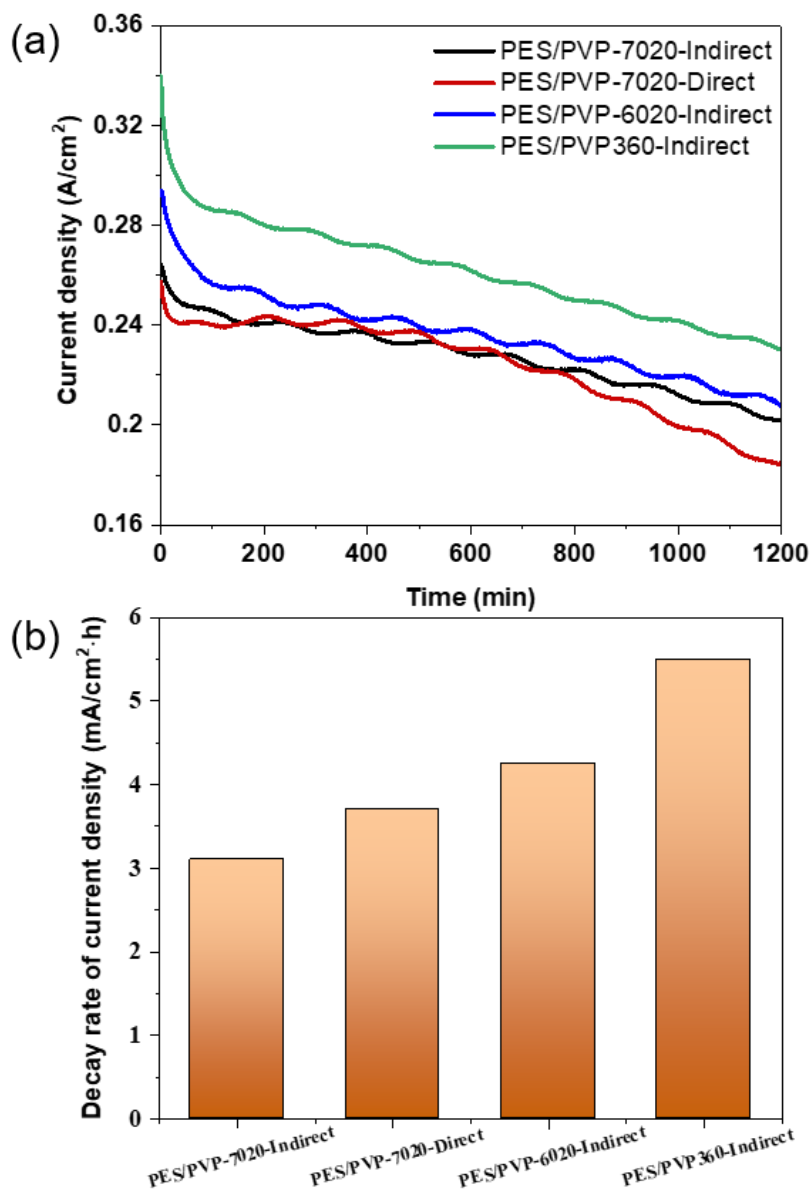


Fig. 5.6. (a) Durability test and (b) decay rate of PA doped PES-PVP membranes at 0.60 V and 150 °C during 1200 min durability test.

5.4.3 Hydrogen crossover

Hydrogen crossover through the MEA is a common indicator of membrane chemical degradation. Linear sweep voltammetry (LSV) was conducted to test hydrogen crossover for different PES-PVP membranes before and after durability test in this work. As presented in Fig. 5.7a, the LSV

results for different membranes before durability test were almost identical, indicating all fresh MEAs using different membranes had similar hydrogen crossover. After 1200 min durability test (Fig. 5.7b), however, the low-molecular-weight membranes (PES/PVP-6020-Indirect and PES/PVP360-indirect) had increased hydrogen crossover current density, whilst the PES/PVP-7020 (direct and indirect) membranes showed barely any increase. This can be explained that the low-molecular-weight membranes have greater swelling, suffer more radical attacks to get mechanical degradations, and further have more acid leaching to become thinner and get more hydrogen crossover. Therefore, the high-molecule-weight membranes perform better chemical stabilities than the low-molecule-weight membranes. There are no obvious hydrogen-crossover-current-density differences between indirect-mixing method and direct-mixing method, illustrating the preparation method (indirect or direct mixing) makes no differences in terms of membrane oxidative stability.

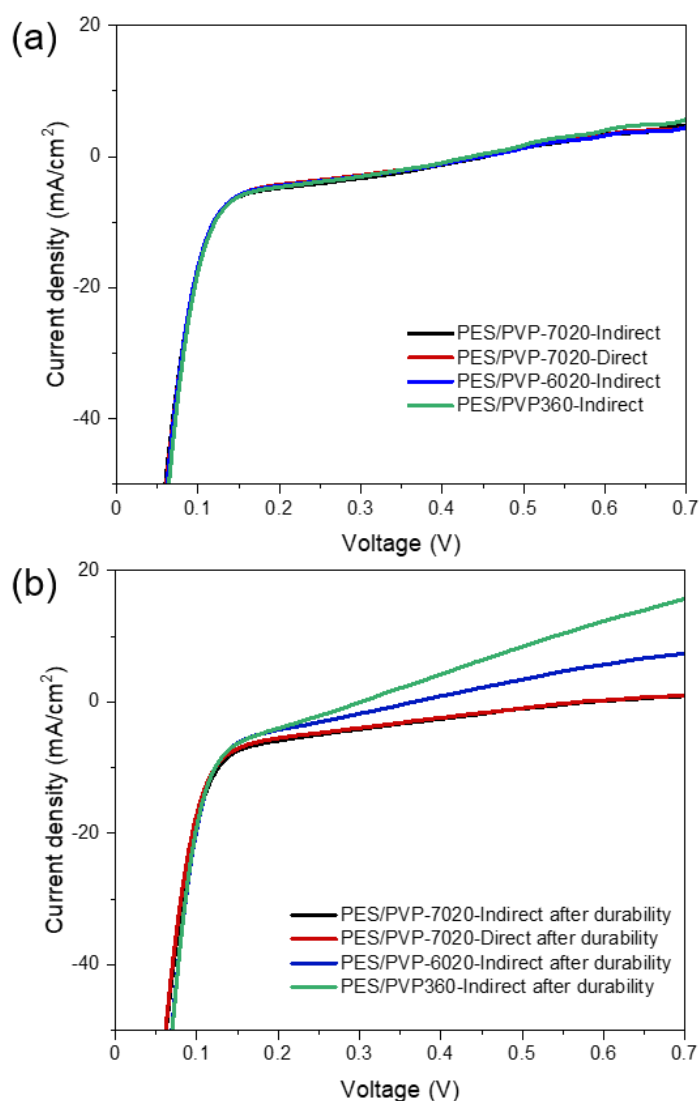


Fig. 5.7. Hydrogen crossover current density of different membranes (a) before and (b) after 1200 min durability test.

5.4.4 Electrochemical impedance spectroscopy and proton conductivity

The Nyquist plots of all PES/PVP membranes before and after durability tests were measured using electrochemical impedance spectroscopy (EIS) as shown in Table 5.4. All membranes after durability tests suffered reduced ohmic resistance and increased charge transfer resistance. The reduction in ohmic resistance after the durability test may be explained that the membrane became diluted and thinner than the fresh membranes (also explained in section 2.5.3.2) (330, 331), which had a good consistence with increased hydrogen permeability after durability test (Fig. 5.7b). In addition, PES/PVP360-Indirect had the largest ohmic resistance reduction, verifying that the membrane thinning (also explained in section 2.5.3.2) and hydrogen crossover were worse in the low-molecular-weight membranes. In terms of charge transfer resistance, all membranes significantly increase after the durability test. This may be explained by the catalyst aggregation, carbon corrosion, and electrode acid losses which can result in three-phase zone loss after durability test. The reduced three-phase zone means the proton transfer or active reaction points become less to get increased charge transfer resistance. The proton conductivities of all fresh membranes were also calculated in Table 5.4. PES/PVP-7020-Indirect and PES/PVP-7020-Direct had slightly lower conductivities (49–51 mS/cm) than the low-molecular-weight membranes (54–63 mS/cm). This is in accordance with the higher ADL for low-molecular-weight membranes (Table 5.3).

Table 5.4. Summary of ohmic resistance (R_0), anode charge transfer resistance (R_1), and cathode charge transfer resistance (R_2) before and after durability test, and the proton conductivity of fresh MEAs.

Membrane	$R_0/\Omega \text{ cm}^2$		$R_1/\Omega \text{ cm}^2$		$R_2/\Omega \text{ cm}^2$		Proton conductivity (mS/cm)
	Before	After	Before	After	Before	After	
PES/PVP-7020-Indirect	0.165	0.14	0.04	0.025	0.223	0.352	51.27
PES/PVP-7020-Direct	0.213	0.187	0.028	0.024	0.223	0.33	49.64
PES/PVP-6020-Indirect	0.192	0.164	0.031	0.023	0.239	0.274	54.16
PES/PVP360-Indirect	0.172	0.141	0.028	0.024	0.224	0.259	63.08

5.5 Conclusion to this chapter

The properties of membranes prepared using different molecular weights are significantly different, especially in terms of the mechanical and chemical properties. Compared with the properties of low-molecular-weight membranes (PES/PVP-6020-Indirect and PES/PVP360-Indirect), better mechanical and chemical properties of high-molecular-weight membranes

(PES/PVP-7020-Indirect and PES/PVP-7020-Direct) are mainly attributed to denser structure and longer polymer chains which have higher resistance to mechanical and oxidative degradation. Stable performances like low current density decay rate and hydrogen permeability also implied that high-molecular-weight membranes are more chemically and mechanically stable than the low-molecular-weight membranes.

Compared with the membrane preparation method using different molecular weights, different mixing methods (direct and indirect mixing) did not make obvious differences to membrane performance. However, different mixing methods indeed made some changes in terms of mechanical properties, ADL, swelling properties and durability. As indirect mixing method is the mixing process of two polymer solutions, this procedure may get more homogenous mixing than the direct-mixing method. The even distribution between PES and PVP in the indirect-mixing membrane may offer denser structure and better mechanical properties to get low decay rates. The relationship of PVP and PES chain distributions inside membranes prepared using different mixing methods needs to be clarified.

As a summary, the advantages and disadvantages of PES-PVP membranes prepared using different polymer molecular weights or different mixing methods are shown in Table 5.5. It was found that the membranes prepared using high-molecular-weight polymers and indirect-mixing method performed very well in terms of membrane properties and fuel cell performance. Therefore, in this work, the optimal membrane preparation procedure is employing high-molecular-weight polymers and indirect mixing method to prepare the standard PES-PVP membrane. The next chapter is focused on the performance improvements of the PES-PVP membranes by adding silica nanosheets.

Table 5.5. Summary of the impacts of different membrane preparation methods.

Method	Thermal stability	Mechanical property	Dimensional stability	Hydrogen crossover	Current decay rate
Low molecular weight	—	Worse	Worse	Worse	Worse
High molecular weight	—	Better	Better	Better	Better
Direct mixing method	—	Worse	Worse	—	Worse
Indirect mixing method	—	Better	Better	—	Better

Note: — indicates no obvious change.

Chapter 6: Performance of polyethersulfone–polyvinylpyrrolidone/silica nanosheets composite membranes

6.1 Introduction

As mentioned in Table 4.1, polyethersulfone–polyvinylpyrrolidone (PES–PVP) membrane which showed excellent proton conductivity and cell performance was selected as the target membrane in this work. In previous chapter, the membrane preparation conditions were optimized to use the high-molecular-weight polymer and indirect-mixing method to prepare the membranes. However, hydrogen crossover and acid leaching problems with PVP blended membranes limit their use in fuel cell applications.

As described in section 4.2.1, the incorporation of clay-based inorganic fillers into the high-temperature proton exchange membranes (HT-PEMs) may be a potential approach to solve these limitations. The fuel cell applications using vermiculite or its derivations have not been reported until now. In this chapter, vermiculite was used to synthesize two-dimensional (2D) silica nanosheets (SN) via a simple and environmentally benign acid-treatment method. To obtain a good dispersion and interfacial interactions between SN and the membrane polymers, which can reduce hydrogen crossover, exfoliated SN (E-SN) and sulfonated SN (S-SN) were also prepared. Finally, the as-prepared SN, E-SN and S-SN were incorporated into PES–PVP blended membranes as inorganic fillers to explore their influence on the proton conductivity, hydrogen crossover, power density, and the durability of the composite membranes. While clays have been used as fillers in fuel cell membranes, including the work of our group (280, 281, 287), this study is the first time to apply the exfoliated and sulfonated nanosheets made from clays in HT-PEMs.

6.2 Characterization of SN, E-SN and S-SN

6.2.1 Elemental analysis

A schematic of the preparation of SN, E-SN and S-SN synthesized from vermiculite is displayed in Fig. 6.1. The chemical formula of the natural vermiculite had been reported as $(\text{Al}_{0.30}\text{Ti}_{0.04}\text{Fe}_{0.63}\text{Mg}_{2.00})(\text{Si}_{3.21}\text{Al}_{0.79})\text{O}_{10}(\text{OH})_2\text{Mg}_{0.13}\text{Na}_{0.02}\text{K}_{0.10}(\text{H}_2\text{O})_n$ (332) which is consistent with the composition determined by Scanning Transmission Electron Microscope equipped with an Energy Dispersive X-ray Spectroscopy (STEM EDS) analysis results (Table 6.1). Fig. 6.2 also illustrates the uniform distributions of Si, O, and Mg elements in the SN. SN was prepared by treating natural vermiculite with 2M HCl through a simple and low-cost acid-leaching method, where most of Mg^{2+} , Al^{3+} and Fe^{3+} are dissolved and acidic sites of the clay minerals are increased (Table 6.1) (333). This acid-leaching process can increase the specific surface area and dissolve partial mineral impurities (334). Unlike silica nanoparticles (221, 335) and silica nanoclusters

(18), these 2D SN can afford more hydroxyl groups to interact with polymer backbones and protons, aiding a high dispersion of SN through the membranes and additional continuous proton transfer channels. In order to introduce the additional sulfone groups to get increased proton transfer pathway, the silane condensation (304) was used to add sulfone groups on the surface of SN to prepare the sulfonated SN (see the detailed preparation in section 4.2.2). The exfoliated SN was also prepared to investigate the effects of flake size and different layered structure on the membrane performance.

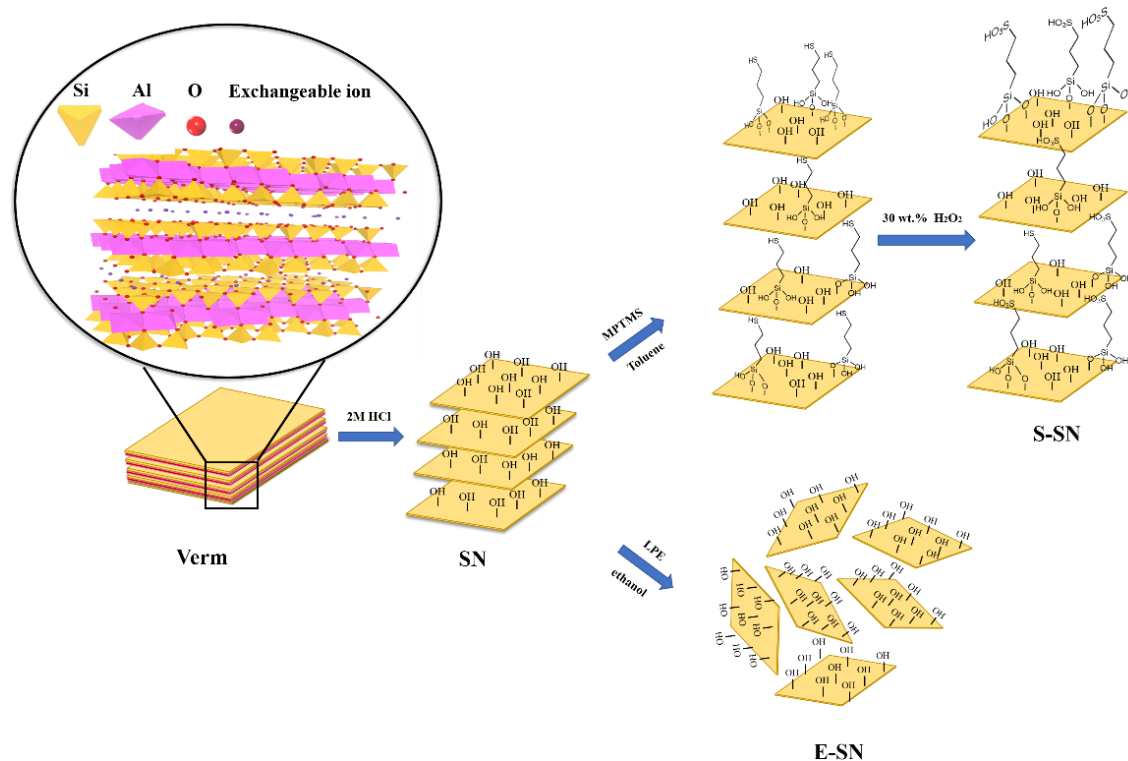


Fig. 6.1 Schematic for the preparation of SN, E-SN and S-SN.

Table 6.1. Elemental composition of vermiculite and SN determined from STEM EDS mapping results.

Sample	Elemental composition (at.%)								
	Si	Mg	Al	O	C	Ti	K	Fe	Cu
Verm	3.96	5.31	2.14	55.50	32.20	0.05	0.13	0.46	0.22
SN	2.31	1.23	0.34	64.91	31.02	<0.01	<0.01	0.04	0.13

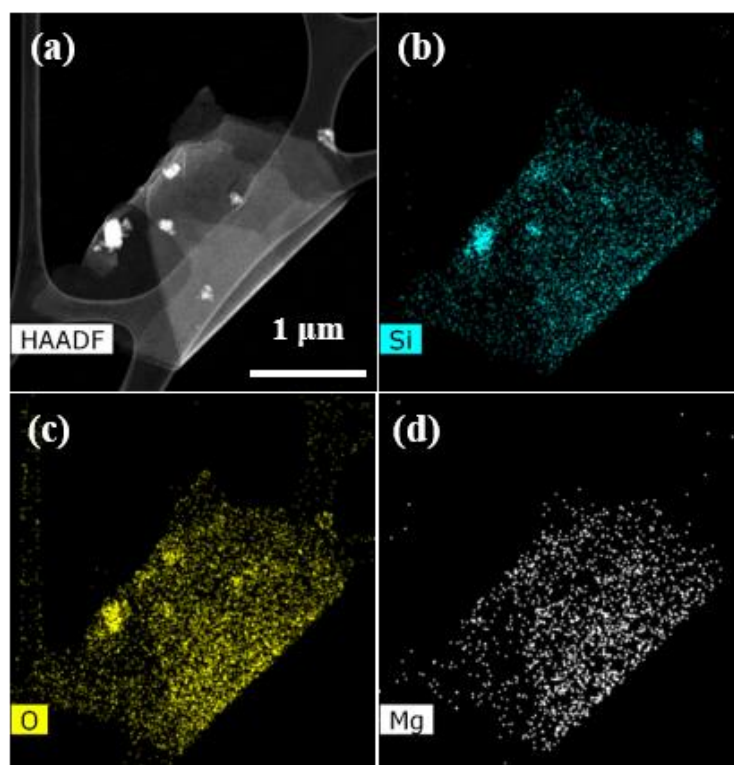


Fig. 6.2. (a) HAADF-STEM image of SN and (b-d) corresponding EDS elemental maps for Si, O, and Mg, respectively.

6.2.2 Morphology and textural property analysis

The raw vermiculite has the expected lamellar particulate morphology (around 25–200 μm) (Fig. 6.3a–b and Fig. 6.4a) and the expected crystalline lattice spacings (Fig. 6.5a). These are compared to similar data for the SN materials. The SEM and HAADF-STEM images of SN show preservation of the flake-like morphology although with a higher concentration of smaller diameter (around 0.1–5 μm) and thinner flakes (Fig. 6.3d–e and Fig. 6.4b), which is in good agreement with the increased BET specific surface area from 7 m^2/g for vermiculite to 413 m^2/g for SN (Table 6.2). The SEM images of E-SN and S-SN (Fig. 6.3c–d) showing that these exfoliated nanosheets have similar morphologies to the SN, as confirmed by the histograms of lateral flake size in Fig. 6.4, respectively. The HAADF-STEM image of vermiculite show the flake structure while the SN also present the preservation of the flake-like morphology (Fig. 6.5). The crystallographic structure of SN was studied at an atomic scale using High-resolution TEM (HRTEM). Compared with the obvious crystallinity of vermiculite (Fig. 6.5a inset), HTTEM imaging of the SN was unable to detect any crystallinity (Fig. 6.5b inset), suggesting the formation of amorphous silica during the acid treatment.

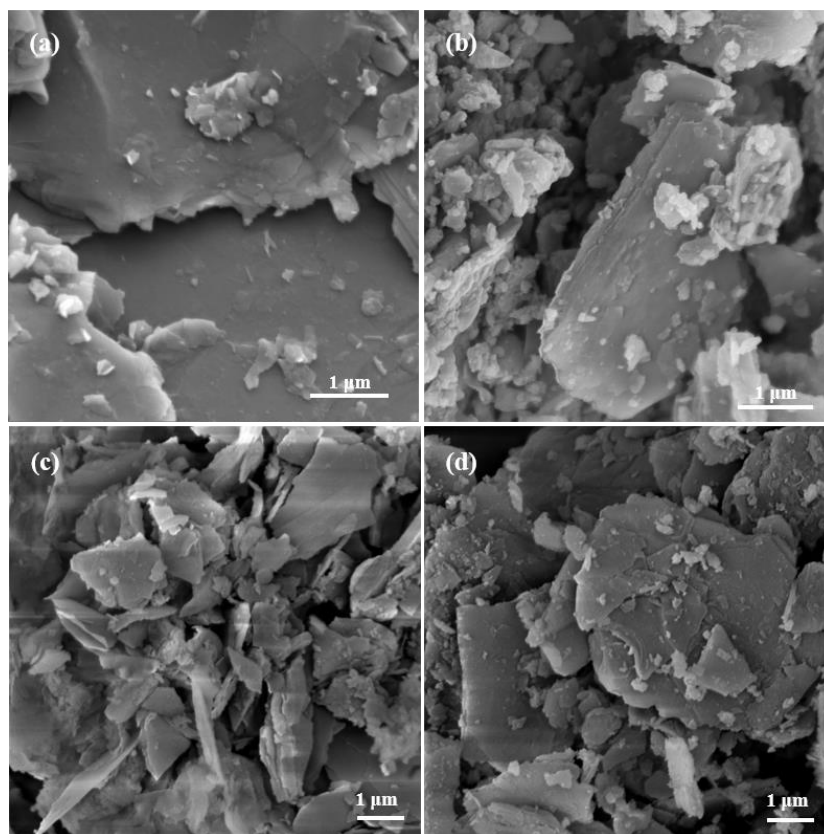


Fig. 6.3. Typical SEM images of (a) vermiculite, (b) SN, (c) E-SN and (d) S-SN.

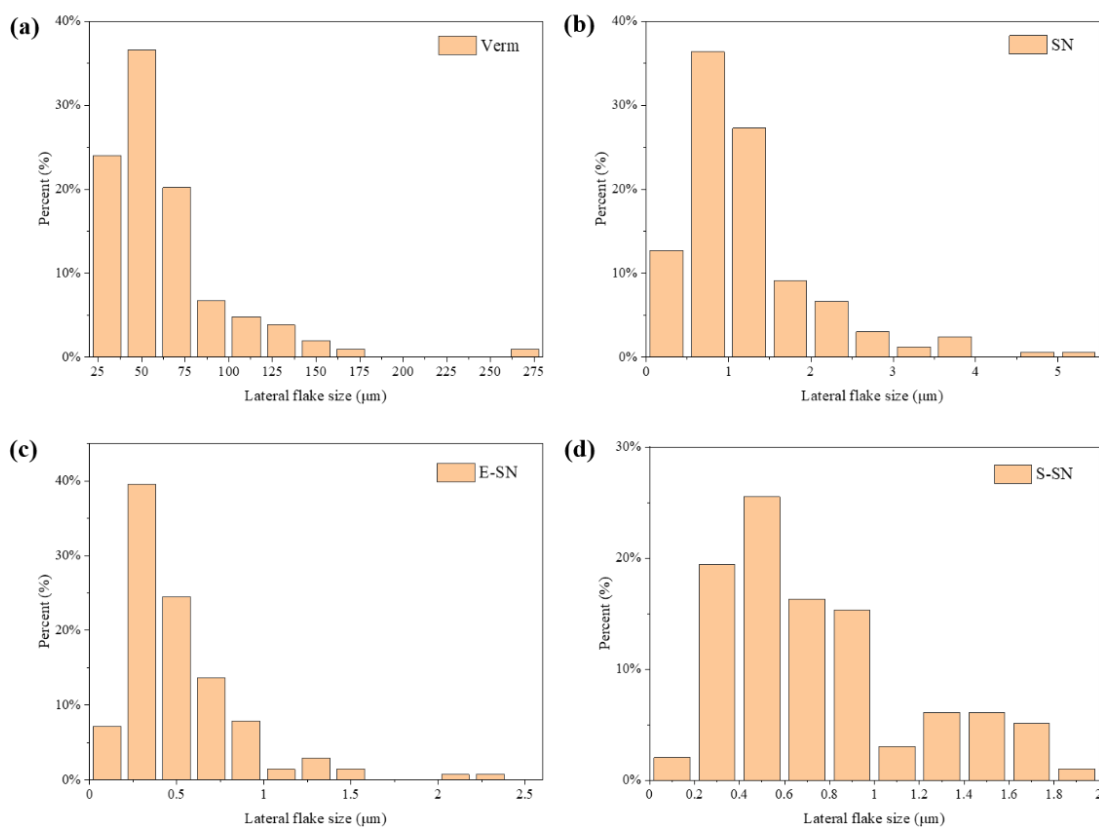


Fig. 6.4. Histograms of lateral flake size of (a) vermiculite, (b) SN, (c) E-SN, and (d) S-SN.

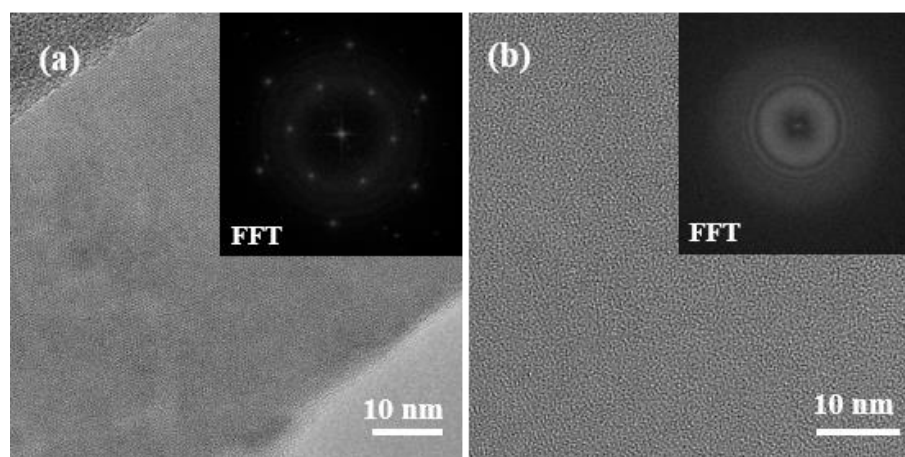


Fig. 6.5. HAADF STEM images (a) and HRTEM images (b) of vermiculite and SN, respectively. The insets in (a) and (b) are the corresponding FFT images.

Table 6.2. Textural properties of vermiculite and SN.

Samples	S_{BET} (m^2/g)	V_{p} (cm^3/g)	D_{p} (nm)
Verm	7	0.02	13.56
SN	413	0.37	4.03

6.2.3 X-ray diffraction analysis

The crystallinities of inorganic fillers were confirmed by the XRD results as shown in Fig. 6.6. The XRD pattern of vermiculite displays the characteristic diffraction peaks at 6.39° ($d = 1.38$ nm, 002), 12.27° ($d = 0.72$ nm, 004), 18.93° ($d = 0.47$ nm, 006), and 25.35° ($d = 0.35$ nm, 008). However, the XRD spectrum of SN, E-SN and S-SN show decreased intensities and broad reflections, indicating the octahedral and tetrahedral crystalline structures had been severely modified and partially transformed to amorphous silica (333, 336), which is consistent with the results in Fig. 6.5b inset.

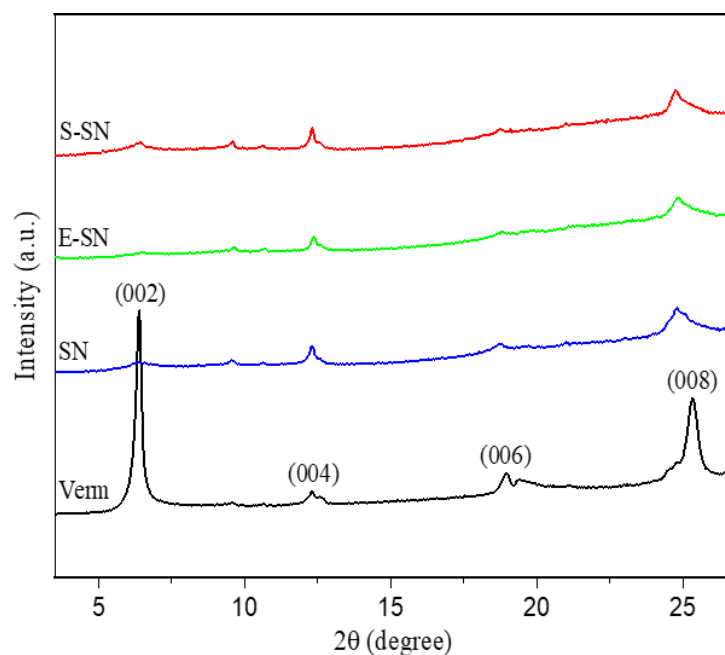


Fig. 6.6. XRD patterns for vermiculite, SN, E-SN and S-SN.

6.2.4 Fourier-transform infrared spectroscopy analysis

The chemical structures of vermiculite, SN, E-SN and S-SN were further analysed by FTIR in Fig. 6.7. All samples show a band at 650 cm^{-1} because of the Si-O stretching vibration. The new bands at 800 and 1060 cm^{-1} in SN, E-SN and S-SN are attributed to the bending and stretching vibrations of SiO_4 tetrahedra (337), also supporting the formation of amorphous silica. Another band at 960 cm^{-1} in SN, E-SN and S-SN illustrates the formation of Si-OH groups because the Al^{3+} and Mg^{2+} ions are leached and replaced by H^+ from acid. The FTIR spectrum of S-SN does not have the distinct peaks at $1420\text{--}1310\text{ cm}^{-1}$ and $1235\text{--}1145\text{ cm}^{-1}$ which are assigned to the sulfonic group. This can be explained by the fact that they are overlapped with the peaks of Si and Al tetrahedral units (338).

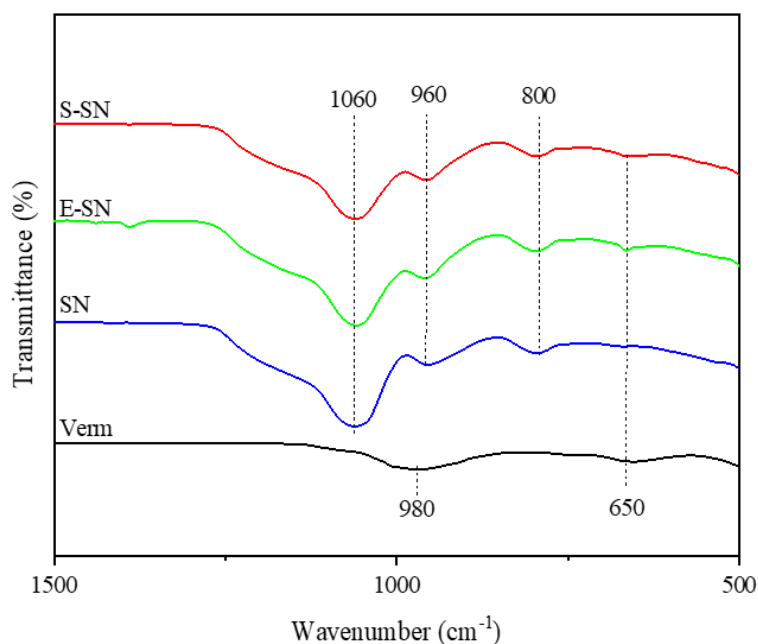


Fig. 6.7. FTIR spectra for vermiculite, SN, E-SN and S-SN.

6.2.5 X-ray photoelectron spectroscopy analysis

High-resolution XPS was employed to analyse the functional groups and surface composition of vermiculite, SN and S-SN and confirm the existing of hydroxyl groups in SN and sulfonic groups in S-SN. The survey spectra of vermiculite and SN in Fig. 6.8a show that vermiculite and SN mainly contain Si, O and Mg elements as expected from the vermiculite chemical formula. SN shows higher intensity peaks for Si and lower intensity peak for Mg than that the original vermiculite which again supports the dissolution of Al and Mg after acid treatment. The XPS survey spectrum of S-SN (Fig. 6.8a) contains additional sulphur element, supporting the existence of sulphur elements in S-SN. The presence of C peaks in all survey spectra is related to surface-absorbed carbon-based contaminants (339). To explore and confirm the partially condensed Si-OH groups during sulfonation reactions, the high-resolution O 1s XPS spectra of S-SN and SN are presented in Fig. 6.8b inset tables, showing that SN contains around 2.55 wt% Si-OH groups which decreased to 2.44 wt% Si-OH in S-SN after sulfonation reaction. The O 1s XPS spectra of S-SN can be deconvoluted into two peaks at approximately 532.9 eV and 534.8 eV which are attributed to Si-O-Si and Si-O-H, respectively. The additional O 1s binding energy of SN at 531.2 eV presents absorbed carbon-based oxides (C-O). S 2p XPS spectrum of S-SN is displayed in Fig. 6.8c to further confirm the existence of sulfonic groups in S-SN. It can be seen that the peak at around 168.8 eV represents the sulphur in sulfonic group (338). Two deconvoluted peaks can be observed at around 168.5 eV and 169.7 eV, which are attributed to the doublet structure in the regions of S 2p_{3/2} and S 2p_{1/2}, respectively (340).

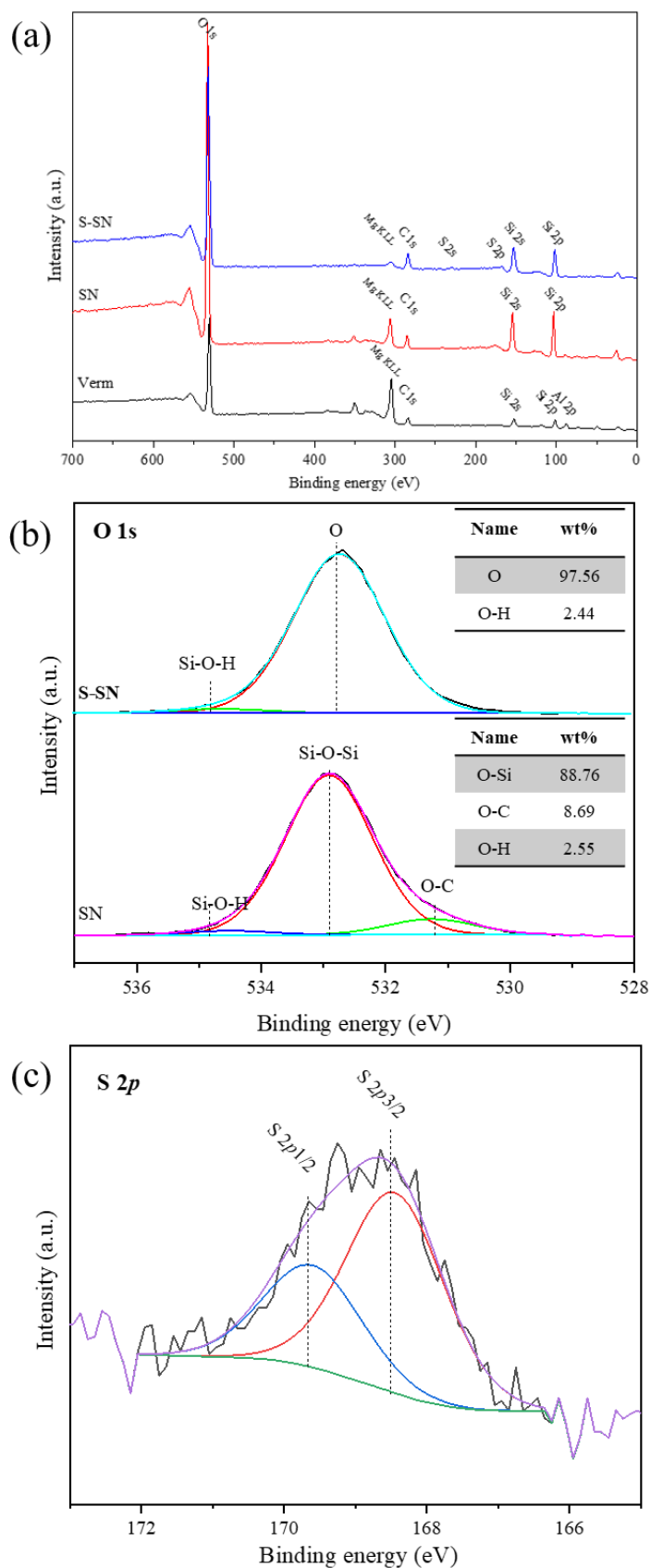


Fig. 6.8. (a) XPS spectra of vermiculite, SN and S-SN. High-resolution XPS near (c) O 1s for SN and S-SN, and (d) S 2p for S-SN.

6.3 Characterization of composite membranes

6.3.1 Morphology analysis

The SEM images of the SN-based membranes show a dense structure without any macroscopic defects (Fig. 6.9a-f). The cross-section images of these inorganic-organic composite membranes in Fig. 6.9b-f suggest the SN are well-dispersed in the membranes. Compared with the pure membrane (P/0SN in Fig. 6.9a), the composite membranes with increased loadings of SN show increased rough cross-sections with wrinkles (341, 342), especially when the SN loading is more than 0.5 wt% (Fig. 6.9c and d). This might result from the incompatibility between SN and polymers. P/0.25E-SN membrane in Fig. 6.9e has a rougher cross-section than that of P/0.25SN membrane in Fig. 6.9b, indicating that the exfoliated flakes of E-SN might have poor compatibility with polymers. This was improved in the P/0.25S-SN membrane although the average flake sizes of S-SN (Fig. 6.4d) are smaller than SN (Fig. 6.4b). The sulfonic groups on the surface of S-SN might contribute to attractive interactions and improved interfacial compatibility with polymers to get a smooth cross-section (Fig. 6.9f).

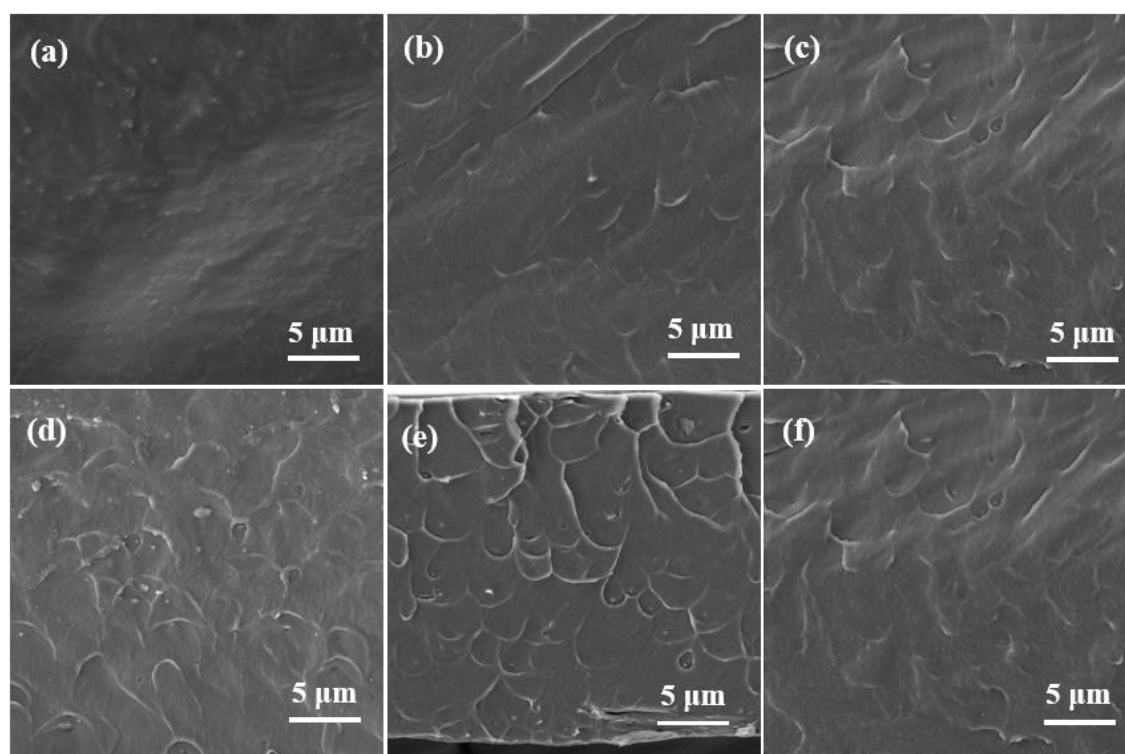


Fig. 6.9. Cross-sectional SEM images of (a) P/0SN, (b) P/0.25SN, (c) P/0.50SN, (d) P/0.75SN, (e) P/0.25E-SN, and (f) P/0.25S-SN membranes.

6.3.2 Thermogravimetric analysis

The thermal stabilities of inorganic fillers and membranes were determined by TGA (Fig. 6.10). For the inorganic fillers, only up to 15 wt% loss is observed when the temperature rises to 600 °C.

This is because of the evaporation of physically absorbed water (below 120 °C) and hydrogen-bonded water (120 to 220 °C) on the surface and interlayers of the SN (223). The extra weight loss (around 8%) of S-SN from 350 to 600 °C is assigned to the loss of alkyl groups and sulfonic groups of S-SN (223), which also supports the successful sulfonation of SN. For the membranes, the initial loss occurs when the temperature is up to 280 °C, which is assigned to the release of absorbed and hydrogen-bonded moisture. The second mass loss starts from 350 °C due to the decomposition of imidazole rings in PVP (72). It should be noted that the temperature at which all composite membranes started to degrade is around 350 °C, which demonstrates that these inorganic-organic composite membranes are probably to be stable at HT-PEMFC operating temperatures.

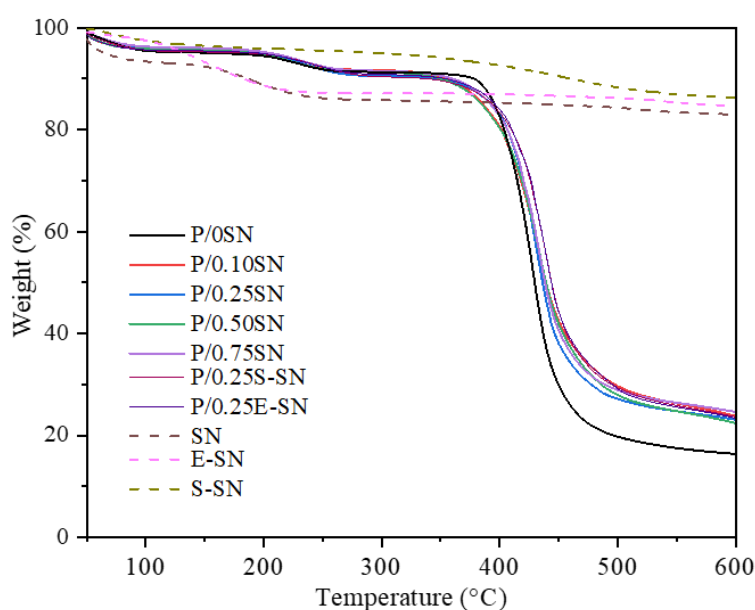


Fig. 6.10. TGA curves of SN, E-SN, S-SN and P/xSN composite membranes.

6.3.3 Mechanical properties

The tensile stress of the composite membranes before and after acid doping were measured (Fig. 6.11) and the mechanical properties are summarized in Table 6.3. The PA doped membranes have lower tensile strength and higher elongation than the corresponding dry membranes, indicating that the PA molecules work as the plasticizer to loosen the compact structure of the membranes. The PA doped pure PES-PVP membrane has highest tensile strength (5.3 MPa), which is consistent with the Zhang's work (343). The PA doped inorganic-organic membranes showed excellent tensile strength (3.1–4.2 MPa), elongation at break (57–128%) and Young's modulus (14.1–20.2 MPa). Interestingly, the P/0.25E-SN/PA and P/0.25S-SN/PA membranes have higher Young's modulus than other membranes, probably because of the well-dispersed distribution of inorganic materials in the membranes and increased interactions with PA molecules. The tensile strength of P/0.25SN and P/0.25SN/PA showed promising among the SN incorporated

membranes. This might result from the desirable dispersion and good compatibility of SN, comparing with the membranes with higher loadings which probably lead to the formation of inner cracks and voids to inhibit a good tensile strength (344, 345).

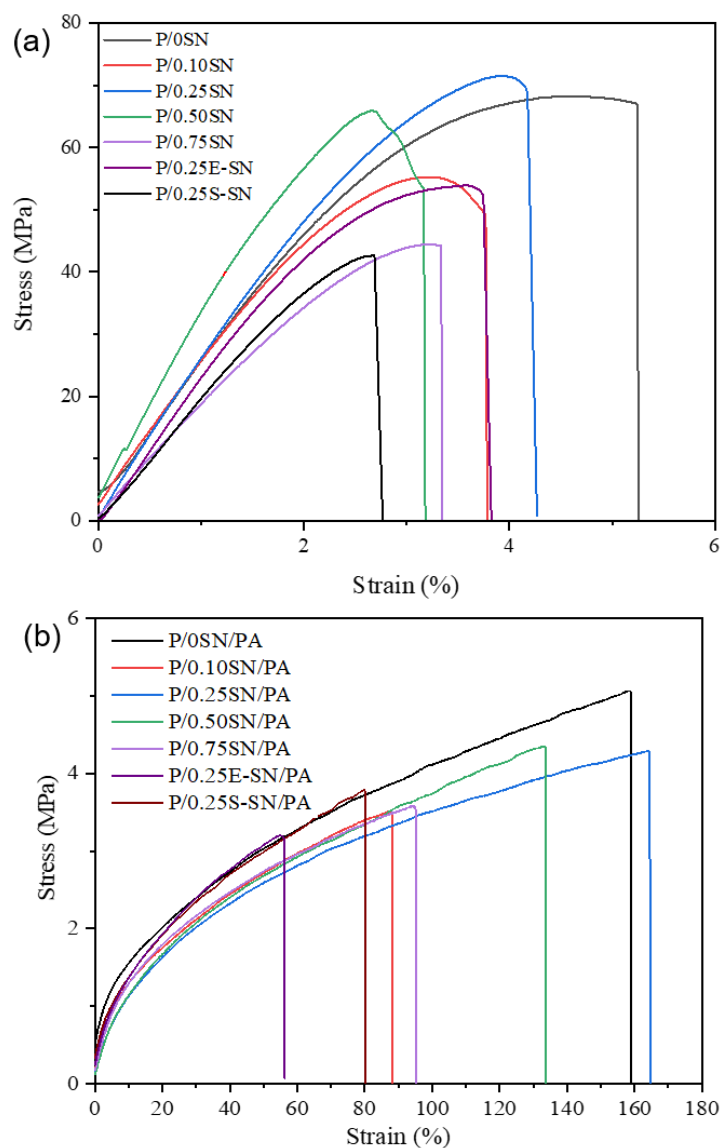


Fig. 6.11. Stress-strain curves of (a) undoped and (b) PA doped P/xSN, P/0.25E-SN and P/0.25S-SN membranes.

Table 6.3. Summary of mechanical properties of composite membranes before and after PA doping at ambient temperature and humidity.

Samples	Tensile strength (MPa)		Elongation at break (%)		Young's modulus (MPa)	
	Undoped	Doped	Undoped	Doped	Undoped	Doped
P/0SN	67 ± 19	5.3 ± 0.3	3.7 ± 1.2	153 ± 17	3007 ± 789	18.0 ± 1.5
P/0.10SN	63 ± 13	3.2 ± 0.2	3.1 ± 0.4	77 ± 16	2734 ± 632	15.7 ± 2.0

P/0.25SN	69 ± 16	4.2 ± 0.6	3.9 ± 0.3	128 ± 49	2575 ± 674	16.5 ± 1.0
P/0.50SN	58 ± 16	3.8 ± 0.5	3.7 ± 1.2	123 ± 35	2393 ± 634	14.1 ± 2.0
P/0.75SN	47 ± 21	3.6 ± 0.1	4.8 ± 1.8	91 ± 36	1927 ± 609	15.5 ± 4.0
P/0.25E-SN	55 ± 1	3.1 ± 0.4	4.1 ± 0.6	57 ± 9	1924 ± 4	18.5 ± 0.8
P/0.25S-SN	45 ± 4	3.2 ± 0.5	2.9 ± 0.4	66 ± 20	1942 ± 303	20.2 ± 1.9

6.3.4 Acid doping and swelling

The PA uptake and ADL decrease with the increasing loading of SN-based materials (Table 6.4), which can be explained that the free volume of the membrane matrix was occupied by the SN (222). However, the acid uptake of composite membranes containing 0.25 wt% S-SN shows a similar level to that of pristine P/0SN membranes, suggesting that sulfonic groups in S-SN might absorb additional PA via hydrogen bonding compared with unmodified SN. The hydrophobicity of the alkyl chains in S-SN can introduce hydrophobicity into the polymer matrix to avoid moisture absorption and give more opportunities to interact with the PA molecules. Additionally, the ADL of PA/0.25E-SN/PA is around 5.94 mol, similar to the pure membrane (5.96 mol ADL). This can be explained by the exfoliation and smaller flake size of E-SN, which gives more interaction sites to PA molecules, compared with SN. The membrane swelling area and volume were also tested to show the membrane dimensional properties as shown in Table 6.4. The addition of SN into the membranes produces reduced swelling with the P/0.75SN/PA having the best dimensional stability.

Table 6.4. Acid uptake, ADL, area and volume swelling of the PA doped composite membranes.

Samples	Acid uptake (wt%)	ADL (mol)	Area swelling (%)	Volume swelling (%)
P/0SN/PA	316 ± 11	5.96 ± 0.21	60.4 ± 0.6	157 ± 9
P/0.10SN/PA	308 ± 3	5.82 ± 0.05	59.9 ± 0.2	152 ± 14
P/0.25SN/PA	307 ± 6	5.79 ± 0.12	59.3 ± 0.3	145 ± 10
P/0.50SN/PA	303 ± 5	5.72 ± 0.09	58.2 ± 0.5	142 ± 8
P/0.75SN/PA	302 ± 3	5.70 ± 0.05	57.6 ± 0.3	139 ± 8
P/0.25E-SN/PA	315 ± 6	5.94 ± 0.12	60.1 ± 0.4	156 ± 11
P/0.25S-SN/PA	315 ± 4	5.95 ± 0.16	60.3 ± 0.4	155 ± 14

6.3.5 Fourier-transform infrared spectroscopy analysis

To determine the chemical bonds between the SN and the polymer, the PA doped membranes were tested by FTIR. In Fig. 6.12, the characteristic bands at 1486 and 1577 cm^{-1} are assigned to the C_6H_6 ring stretch of PES, while the small peaks at approximate 1624 cm^{-1} show the $\text{C}=\text{O}$ stretch of PVP (305). The broad peaks at 900–1050 cm^{-1} show the existence of PA in membranes. The FTIR curves of P/0SN/PA, P/0.25SN/PA, P/0.25E-SN/PA, P/0.25S-SN/PA have characteristic bands at the same wavenumbers, illustrating that there are no chemical bonds between polymer matrix and SN (232).

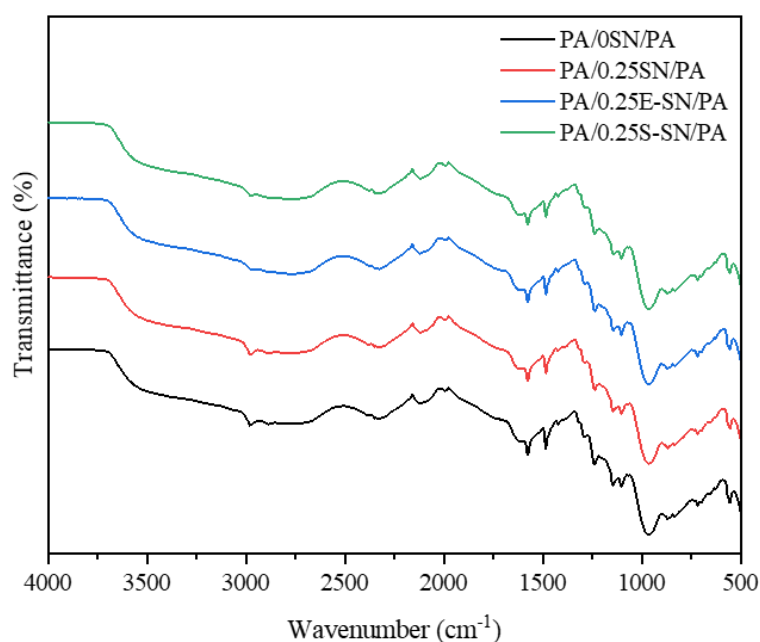


Fig. 6.12. FTIR spectra of PA doped P/xSN, P/0.25E-SN and P/0.25S-SN membranes.

6.3.6 Proton conductivity

Despite having no chemical-structure differences, detectable by FTIR, all inorganic-organic composite membranes show higher proton conductivities than pure P/0SN/PA membranes at the same temperature as shown in Fig. 6.13. The conductivity is obtained from the average conductivity of three different samples, and the error bar is calculated from the corresponding standard deviation. The P/0.25SN/PA membrane has a 48.2 mS/cm proton conductivity, compared with only 34.8 mS/cm for PA doped pristine membrane at 150 °C. This can be explained by hydrogen bonding formed among polymer chains, Si-OH groups, and PA molecules adsorbed by the SN (221, 335). These hydroxyl groups and adsorbed PA molecules afford additional faster and easier proton transfer pathways governed by the Grotthuss mechanism (83). In addition, the TGA data indicates that bound water still exists in the interlayer of SN from 120 to 220 °C (Fig. 6.10), so the interlayer H_2O could also participate in additional proton-conducting paths at the operating temperature of 140–170 °C. The SN act as fixed species, while the functional

groups on the surface and the bound water molecules in the interlayers can give a continuous proton-hopping route in the PES-PVP membranes.

The proton conductivities of P/xSN/PA membranes depend on SN loading, firstly increasing to 0.25 wt% and then starting to decrease. This is probably due to the aggregation of SN which results in blocked proton transport channels and pores or defect areas (193). In principle, the E-SN composite membranes should have higher proton conductivity than the corresponding SN incorporated membranes because of the better dispersion and the greater surface area of the exfoliated nanosheets which can afford traps and interact with PA molecules and polymer chains (31). However, we observe P/0.25E-SN/PA has a lower proton conductivity of 46.1 mS/cm at 150 °C, likely due to the tortuous proton pathways and the newly exfoliated interlayers which might not be fully protonated during the acid-treatment, so it could result in decreased proton conductivity compared with P/0.25SN/PA. Further functionalization is needed to achieve better dispersion without deterioration of proton conductivity. The SN functionalized by $-\text{SO}_3\text{H}$ groups can form additional hydrogen bonds with PA molecules compared with SN. Although a small number of hydroxyl groups were consumed during S-SN preparation, the P/0.25S-SN/PA membrane has the highest proton conductivity (57.6 mS/cm) at 170 °C. This is probably due to the significant contribution from $-\text{SO}_3\text{H}$ groups in S-SN to the proton conductivity (346).

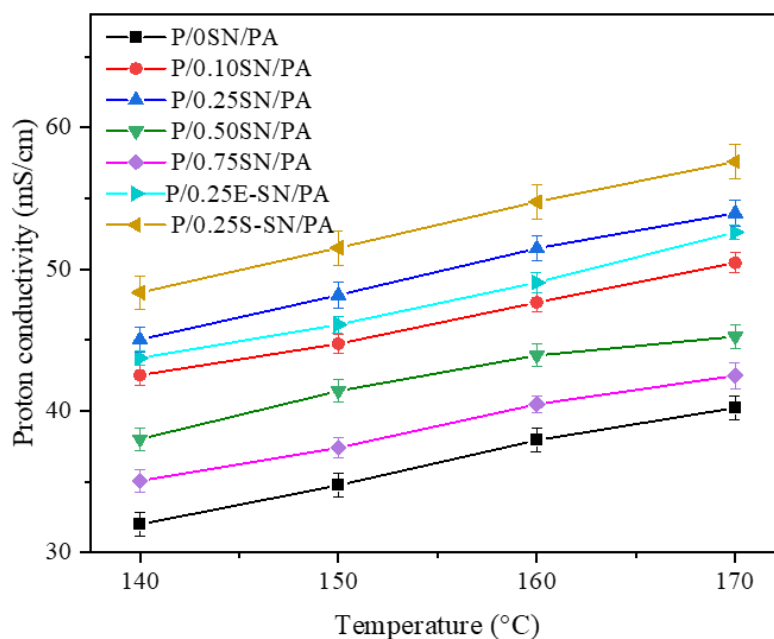


Fig. 6.13. Proton conductivity of PA doped P/xSN, P/0.25E-SN and P/0.25S-SN membranes at different temperatures.

6.4 Evaluation of the composite membranes in a HT-PEMFC

6.4.1 Polarization curve

The composite membranes with different loading of SN described previously were evaluated in a HT-PEMFC, with the conditions described in the experimental section. All the membranes with SN showed improved performance compared with pure polymer membranes (Fig. 6.14). Performance improves when the loading of SN is increased up to an optimum value of 0.25 wt%, after which the performance starts to decrease. The membrane with 0.25 wt% SN showed a peak power density of 495 mW/cm², 34% improvement on pristine polymer membrane without any additions (370 mW/cm²). When further SN is added into the membrane, a gradual decrease of cell performance has been observed. However, the performance is still better than the pure PES-PVP membranes, as confirmed by the trend of proton conductivity in Fig. 6.13. The E-SN and S-SN were incorporated into the membranes to further achieve a better fuel cell performance with excellent filler dispersion.

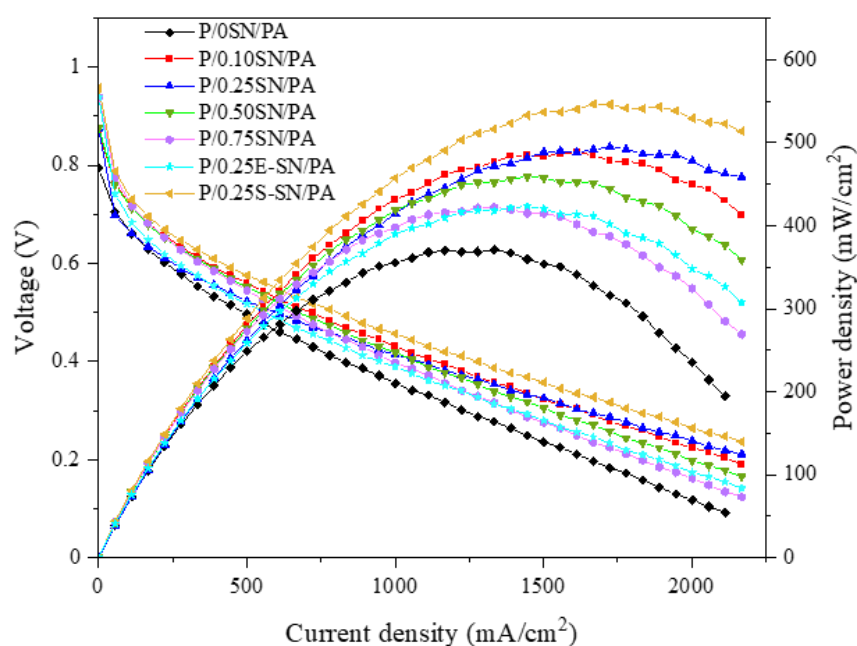


Fig. 6.14. Cell performances of P/xSN/PA, P/0.25E-SN/PA and P/0.25S-SN/PA membranes at 150 °C.

Optimization of the loading of SN in membranes was determined according to the measured cell performance. As shown in Fig. 6.15, P/0.25SN/PA has the highest proton conductivity and power density, indicating that 0.25 wt% is the optimal loading. Therefore, 0.25 wt% was also chosen as the loading for E-SN and S-SN incorporated membranes. The cell performance of P/0.25S-SN/PA displays 546 mW/cm² peak power density at 150 °C which is the highest among all tested membranes and 48% higher than the pure membrane. The power density of P/0.25E-SN/PA

membrane only reaches 423 mW/cm^2 which is consistent with the decreased proton conductivity in Fig. 6.13 compared to that of P/0.25SN/PA. As open circuit voltage (OCV) and hydrogen crossover values are interrelated (347), the OCV values have also been evaluated and displayed in Table 6.5. The OCV values of P/0.25E-SN/PA and P/0.25S-SN/PA membranes before durability test are 0.91 V and 0.93 V, respectively, illustrating the PES-PVP membranes with good filler dispersions can reduce hydrogen crossover.

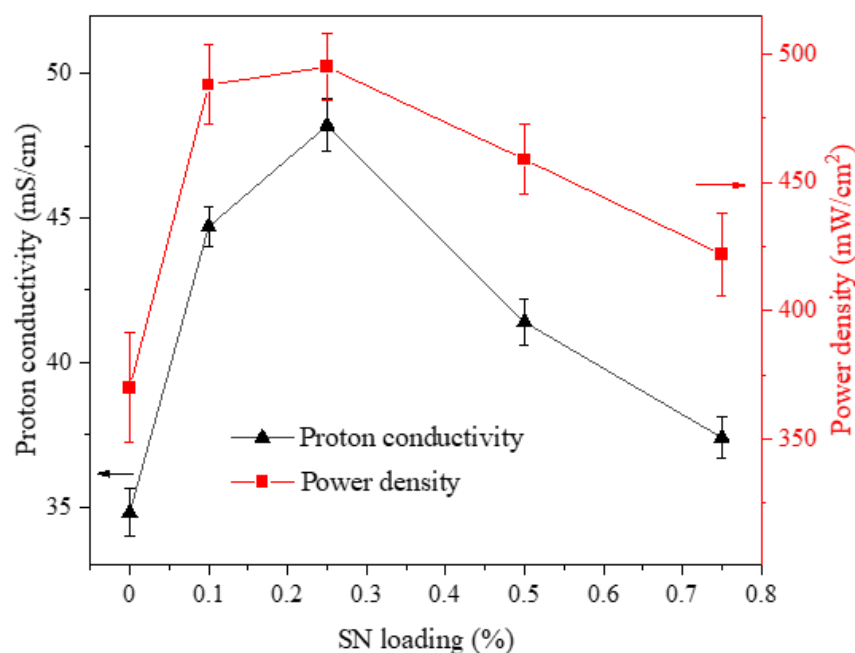


Fig. 6.15. Proton conductivity and power density of P/xSN/PA with different loadings of SN at 150°C .

Table 6.5. OCV values of composite membranes before and after durability test at 150°C .

Samples	OCV before durability test (V)	OCV after durability test (V)
P/0SN/PA	0.84 ± 0.02	0.75 ± 0.03
P/0.10SN/PA	0.87 ± 0.01	0.80 ± 0.02
P/0.25SN/PA	0.88 ± 0.05	0.81 ± 0.04
P/0.50SN/PA	0.88 ± 0.04	0.81 ± 0.03
P/0.75SN/PA	0.88 ± 0.02	0.82 ± 0.02
P/0.25E-SN/PA	0.91 ± 0.03	0.82 ± 0.02
P/0.25S-SN/PA	0.93 ± 0.05	0.82 ± 0.07

The performance comparison among 2D SNs in this chapter and silica nanoparticles or other 2D materials in HT-PEMs is shown in Table 6.6. As the SN with layered structure have high aspect ratio and large surface area, the microstructure of the membrane can be finely tuned with 2D nanosheets to get continuous proton pathways and achieve tortuous paths to reduce fuel crossover (348, 349). Compared with the HT-PEM applications using silica nanoparticles, the SN incorporated membranes showed comparable HT-PEMFC performance. Additionally, compared with other 2D fillers (carbon nitride or graphene oxide), the 2D SN fillers can be prepared from nature vermiculite using a green and facile acid-leaching method, affording a cheaper and more competitive approach to synthesize 2D inorganic fillers.

Table 6.6. Performance comparison of PA doped organic-inorganic HT-PEMs without humidification.

Membranes	Temperature (°C)	Proton conductivity (mS/cm)	Peak power density (mW/cm ²)	Reference
P/0.25SN/PA	150	48.2	495	This work
P/0.25E-SN/PA	150	46.1	423	This work
P/0.25S-SN/PA	150	51.5	546	This work
10 wt% PWA-NH ₂ -HMS /PES-PVP	180	175	420	(343)
PA/PES-PVP-NH	180	152	480	(305)
PBI/SiO ₂ /PA	165	86.6	250	(221)
PBI/SNP-PBI-10	160	50	650	(222)
Al-Si(12%)/PBI-4.75PA	150	31	370	(344)
c-PBI-20-SiO ₂ -2	160	180	497	(130)
m-PBI/Al-MCM-41	160	356	516	(350)
P/carbon nitride-0.5/PA	160	104	512	(232)
PBI/2%graphene oxide	150	-	429	(26)

6.4.2 Durability

The short-term fuel cell durability was performed at 150 °C under 0.6 V without gas humidification (Fig. 6.16a). The cell current density of P/0SN/PA decreases from 0.28 to 0.21

A/cm² after 1200 min durability test with an average decay rate of around 3.20 mA/cm²·h (Fig. 6.16b) which is the largest loss among all the tested membranes. This might be due to acid leaching and the formation of pyrophosphoric acid in the membranes, leading to reduced proton conductivity and further deteriorated durability (351). The oxidative degradation of polymer chains is another factor affecting the degradation in performance durability. The attack by the free radicals on the hydrogen-containing bonds results in the degradation of PVP in membranes (307). After the addition of SN, E-SN or S-SN into the membranes, the cell durability tested at 0.6 V has been enhanced as shown in Fig. 6.16b. The cell decay rate drops with the increase of SN content. The lowest decay rate is 1.01 mA/cm²·h when the content of SN is 0.75 wt%, indicating the addition of inorganic materials into the PES-PVP membranes can benefit stability and durability. This improvement is probably due to the formation of phosphosilicate species to aid acid retention (352). The layered structures with excellent hydrophilicity and large pore volume (Table 6.2) may reduce acid leaching out of the cell by trapping PA molecules in their nanogalleries (135). In addition, the SN act as barriers to protect the PVP polymer chains from the attack by radicals, especially for the chains intercalated in the SN galleries (135). The hydroxyl groups and sulfonic groups of SN participate in the formation of hydrogen bonding with polymer chains which can also protect the terminal bonds of PVP and improve fuel cell durability (129). For P/0.25E-SN/PA membranes, the desirable durability (1.75 mA/cm²·h) is probably contributed by the barrier function of exfoliated nanosheets. It is noteworthy that the decay rates of all organic-inorganic membranes are around 1.01–2.83 mA/cm²·h, which are comparative with the quaternary ammonium-biphosphate ion-pair-coordinated polyphenylene membrane in recent published work (0.33 mA/cm²·h) (89). More work needs to be focused on the combination of functionalization and exfoliation of SN.

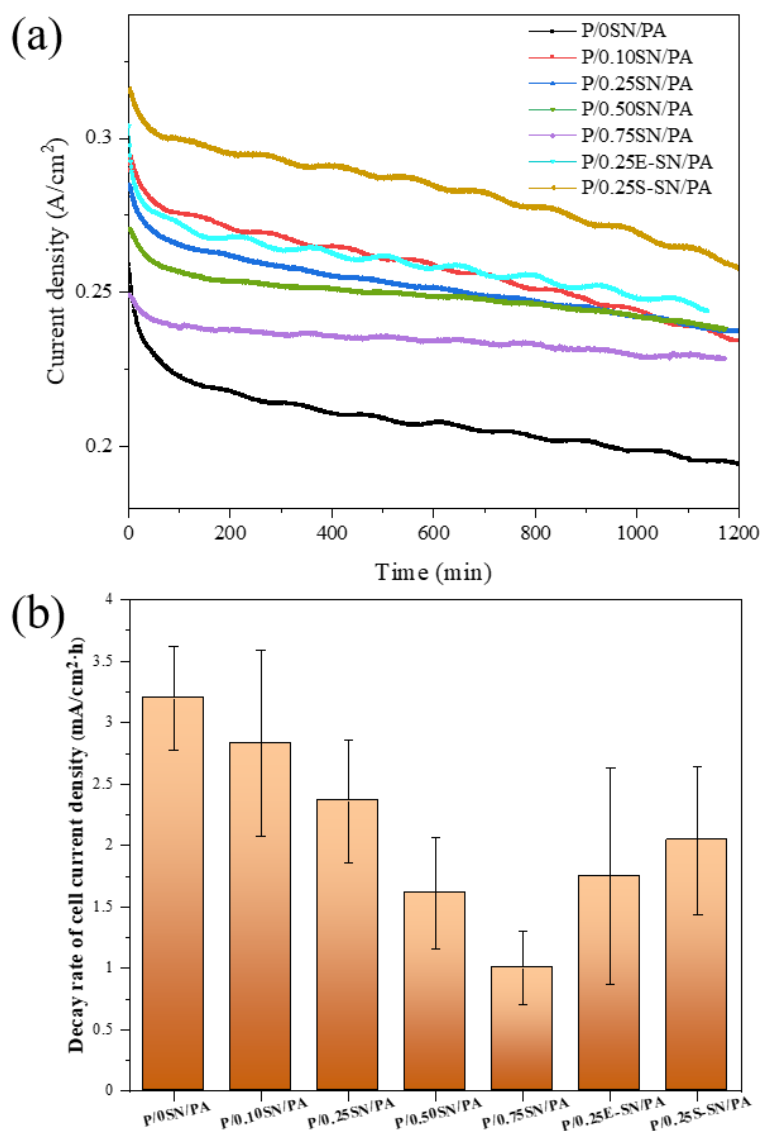


Fig. 6.16. (a) durability test and (b) decay rate of PA doped PES-PVP/SN composite membranes at 0.60 V and 150 °C during 1200 min durability test.

6.4.3 Electrochemical impedance spectroscopy

Further investigation of the membrane degradation over time was obtained by analysing the EIS Nyquist spectra measured at 0.6 A and 150 °C before and after durability test. The EIS data was fitted using the equivalent circuit $R_0L_1(R_1||CPE_1)(R_2||CPE_2)$ which can be divided into three parts: R_0 and L_1 represent the ohmic resistance and inductance of the cell, respectively; R_1 and CPE_1 represent the anode charge transfer resistance and a constant phase element at high frequency, respectively; R_2 and CPE_2 represent the cathode charge transfer resistance and a constant phase element at low frequency, respectively. As shown in Fig. 6.17, all tested membranes after durability test performed decreased ohmic resistance and increased charge transfer resistance. The decreased ohmic resistance can be explained that the diluted and thinner membranes had formed

after durability test (330, 331), although the possible PA leaching out of the membrane might deteriorate the proton conductivity and increase the ohmic resistance. During the short-term durability test in this work, therefore, the phosphoric acid leaching might not be the main problem. The increased hydrogen crossover after durability test reflected by the decreased OCV values (Table 6.5) also confirmed the membrane thinning (331). In addition, membrane creep (115), clamping pressure on the MEA (353), and membrane oxidative degradation (354) can also result in membrane thinning problems. All fitted impedance parameters are listed in Table 6.7. The P/0SN/PA had the largest ohmic resistance loss from 0.24 to 0.20 Ωcm^2 among all the membranes, indicating the thinning degree of P/0SN/PA membrane might suffer the worst. In addition, the charge transfer resistances of all the membranes are slightly increased after durability test because of catalyst agglomeration, carbon corrosion and acid loss from the electrodes (355). Compared with EIS resistance change of pure membrane before and after durability, the reduced ohmic resistance loss and charge transfer resistance of the inorganic-organic membranes suggest that the addition of SN, E-SN or S-SN is resistant for membrane thinning and benefits for the improvement of membrane durability.

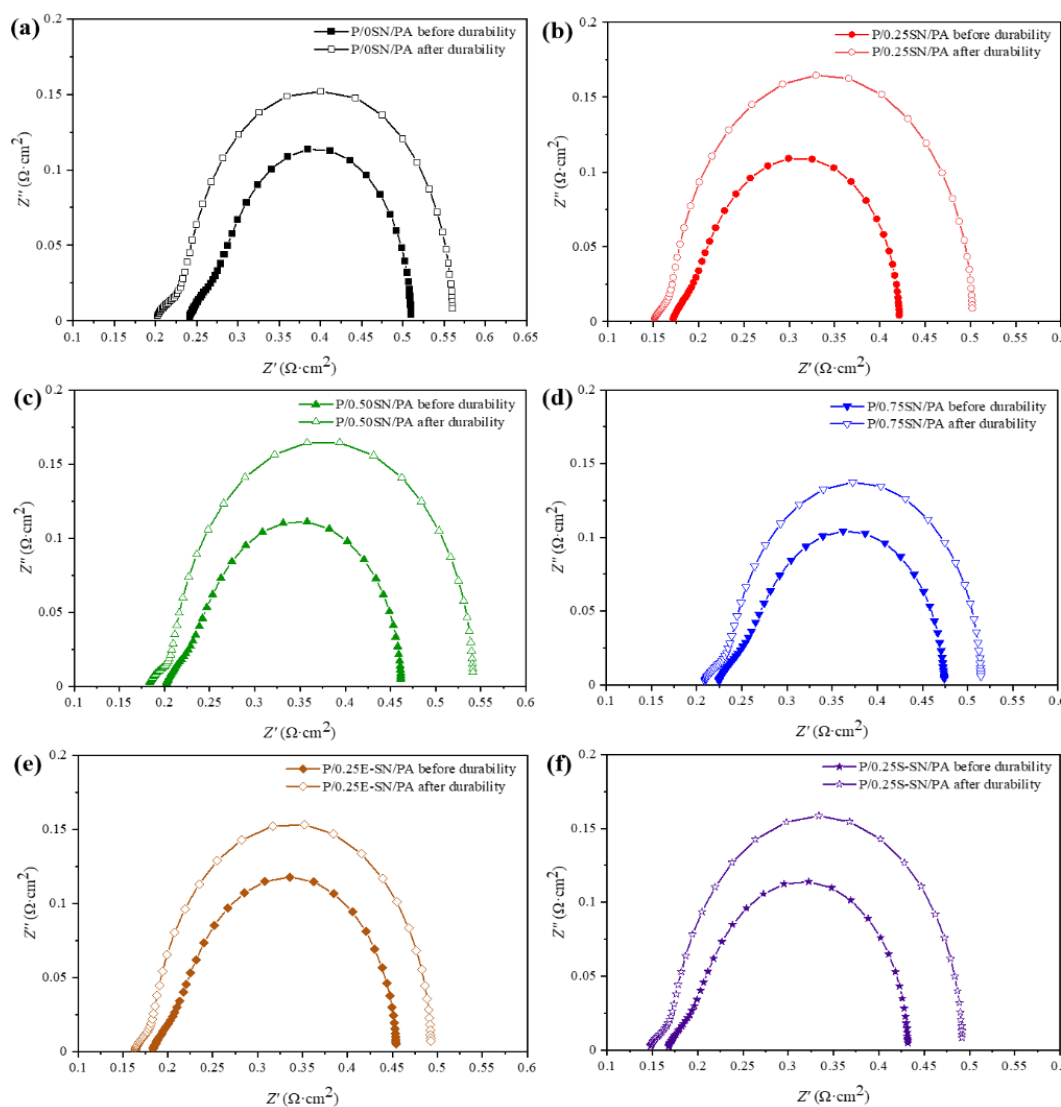


Fig. 6.17. EIS Nyquist plots of (a) P/0SN/PA, (b) P/0.25SN/PA, (c) P/0.50SN/PA, (d) P/0.75SN/PA, (e) P/0.25E-SN/PA, and (f) P/0.25S-SN/PA.

Table 6.7. Summary of ohmic resistance (R_0), anode charge transfer resistance (R_1), and cathode charge transfer resistance (R_2) before and after durability test obtained from equivalent circuits.

Samples	$R_0/\Omega \cdot \text{cm}^2$		$R_1/\Omega \cdot \text{cm}^2$		$R_2/\Omega \cdot \text{cm}^2$	
	Before durability	After durability	Before durability	After durability	Before durability	After durability
P/0SN/PA	0.2417	0.2030	0.0538	0.0495	0.2169	0.3360
P/0.10SN/PA	0.1843	0.1603	0.0340	0.0286	0.2196	0.3380

P/0.25SN/PA	0.1718	0.1515	0.0412	0.0259	0.2104	0.3267
P/0.50SN/PA	0.2021	0.1847	0.0590	0.0329	0.2115	0.3276
P/0.75SN/PA	0.2249	0.2093	0.0565	0.0387	0.1953	0.2698
P/0.25E-SN/PA	0.1835	0.1637	0.0493	0.0284	0.2237	0.3033
P/0.25S-SN/PA	0.1679	0.1480	0.0488	0.0333	0.2176	0.3130

6.5 Conclusion to this chapter

In this work, a novel type of PES-PVP composite membrane with the incorporation of SN was prepared by a simple blending method. The SN with high surface area, increased pore volume and functionalized Si-OH groups were synthesized by a simple and facile acid treatment of vermiculite. After the addition of layered SN, the power density and durability of the inorganic-organic membranes are improved due to the increased proton conductivity and acid retention ability. In the type of SN-based membranes, the membrane with 0.25 wt% SN show highest proton conductivity (48.2 mS/cm) and improved power density (495 mW/cm²) at 150 °C without any humidification, while P/0.75SN/PA has the lowest current density decay rate during the durability test. Subsequent exfoliation and surface modification of SN were performed to get the membranes with good filler dispersion. Although the cell performance of P/0.25E-SN/PA is not the best, the ADL, hydrogen permeability and durability show promise among these composite membranes. The P/0.25S-SN/PA membranes exhibit an excellent proton conductivity (51.5 mS/cm) and peak power density (546 mW/cm²) at 150 °C, which represents a 48% improvement compared with the pure polymer membranes under the same conditions. The results in this work illustrate that 2D silica nanosheet is a promising filler material in HT-PEMs. To further explore and develop more clay-based materials in HT-PEMs, another inorganic filler, muscovite was added into PES-PVP membrane membranes, which are introduced in the next chapter.

Chapter 7: Performance of polyethersulfone–polyvinylpyrrolidone/muscovite composite membranes

7.1 Introduction

The clay-based material, silica nanosheets derived from vermiculite, have been proven (see chapter 6) as an efficient filler in PES-PVP membranes to get enhanced proton conductivity, power density and durability. As discussed in section 4.2.1, muscovite, $\text{KAl}_2(\text{Si}_3\text{Al})\text{O}_{10}(\text{OH})_2$, is a phyllosilicate mineral and is regarded as the main mineral in the mica subgroup of clay minerals (356). Since it has similar elemental composition and layered structures to vermiculite, several studies had been developed in the field of adsorption and electrode material. However, no studies have demonstrated the effect of muscovite working as a filler material in HT-PEMs. To further explore other potential clay-based alternatives, the muscovite which has the same surface hydroxyl groups with silica nanosheets (SN, explored in chapter 6) has studied in this work. The hygroscopic and barrier properties may offer enhanced performance by increased proton pathway and reduced degradation.

As the hydroxyl groups on the surface of muscovite can benefit for fast proton transfer and the layered structure may protect the polymer chains from the radical attack, as-received natural muscovite was incorporated into PES-PVP matrix through solution casting method to prepare the PES-PVP/muscovite composite membranes. The characterizations of muscovite (such as the morphology, crystallinity, elemental composition, functional groups and thermal stability) and PES-PVP/muscovite composite membranes (including membrane cross-section, acid doping level, dimensional stability and mechanical properties) have been investigated in this chapter. The polarization curves, electrochemical impedance spectroscopy and the durability (tested at 0.6 V under 1200 min steady state) of PES-PVP/muscovite membranes containing different loadings of muscovite (0–0.75 wt%) are also explored.

7.2 Characterizations of muscovite

7.2.1 Morphology analysis

The SEM image of as-received muscovite shows the samples used in this work have crystalline flaky morphologies (Fig. 7.1a) and the corresponding average size distribution histogram of as-received muscovite illustrates the size of flakes is in the range of 0.2–10 μm as shown in Fig. 7.1b. Compared with vermiculite ($62.99 \pm 36.63 \mu\text{m}$), the as-received muscovite has the similar layered structure but with different flake sizes. Benefitting from the lower flake size ($5.31 \pm 4.57 \mu\text{m}$), the as-received muscovite can be potentially incorporated into HT-PEMs directly to get homogenous structure.

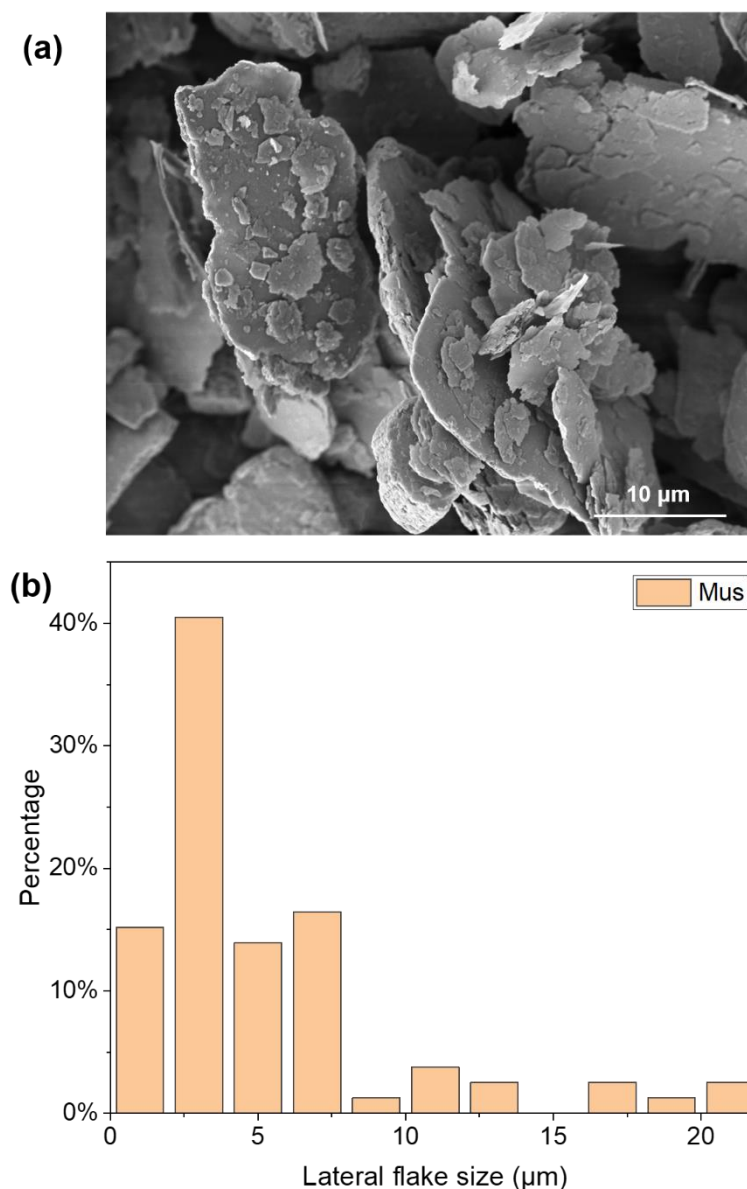


Fig. 7.1. (a) SEM image, and (b) histogram of flake size of raw as-received muscovite.

7.2.2 X-ray diffraction analysis

To evaluate the crystal structure of muscovite, the XRD pattern was obtained as shown in Fig. 7.2. The as-received muscovite can be identified as muscovite mineral by its sharp peaks detected at $2\theta = 9.10^\circ$, 18.03° , 27.05° , 36.21° , and 45.67° , which were attributed to (002), (004), (006), (008), and (0010) crystallographic planes, respectively (295). The remaining peaks at $2\theta = 12.6^\circ$ (001), 25.15° (002), and 37.95° (003) correspond to the kaolinite impurities (357, 358). Although the as-received muscovite has some kaolinite impurities, the similar layered structure and surface hydroxyl groups of kaolinite seem there are no obvious negative impact to work as membrane filler materials (359).

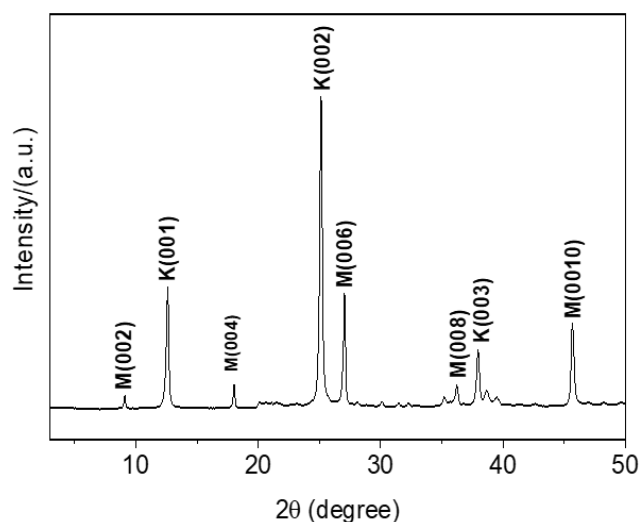


Fig. 7.2. XRD curve (K-kaolinite, M-muscovite) of muscovite.

7.2.3 Fourier-transform infrared spectroscopy

The FTIR was performed to confirm the surface functional groups of muscovite as shown in Fig. 7.3 and the full FTIR assignment of muscovite is concluded in Table 7.1. Several bands at 3688, 3651, 3618, 1113, 1026, 1000, 910, 788, 748, 527, and 458 cm^{-1} were observed in Fig. 7.3. The bands at 3688 and 3651 cm^{-1} indicate outer surface hydroxyl groups, and the characteristic band at 3618 cm^{-1} represents the inner hydroxyl groups (360). The remaining main groups are Si-O bonds with apical oxygen (1113 and 748 cm^{-1}), Si-O bonds with basal oxygen (1026, 1000 and 788 cm^{-1}), Al-OH bending inner hydroxyl groups (910 cm^{-1}), and Si-O-Si stretching (527 and 458 cm^{-1}) (360, 361). The surface hydroxyl groups in muscovite which may afford potential interactions with PA molecules and polymer chains in HT-PEMs can be used as inorganic fillers in HT-PEMs.

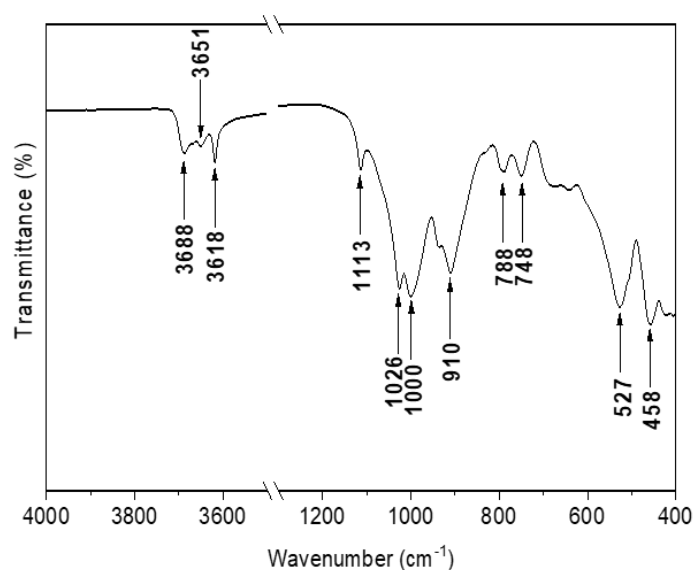


Fig. 7.3. FTIR spectra of muscovite.

Table 7.1. Full FTIR assignment of muscovite.

FTIR of muscovite	Assignment
3687	$\dot{\nu}_{\text{OH}}$
3651	δ_{OH}
3618	δ_{OH}
1113	$\delta_{\text{Si-O}}$
1026	$\delta_{\text{Si-O}}$
1000	$\delta_{\text{Si-O}}$
935	$\delta_{\text{Al-O-H}}$
910	$\delta_{\text{Al-O-H}}$
788	$\delta_{\text{Si-O-Al}}$
748	$\delta_{\text{Si-O-Al}}$
680	$\delta_{\text{Si-O}}$
527	$\delta_{\text{Si-O-Si}}$
458	$\delta_{\text{Si-O-Si}}$
424	$\delta_{\text{Al-O}}$

7.2.4 X-ray photoelectron spectroscopy analysis

The elemental composition and surface functional groups of muscovite were investigated using XPS. The spectra in Fig. 7.4a show that muscovite contains Si, Al, and O elements and the presence of C is assigned to surface-absorbed carbon-based contaminants. The O 1s spectrum of muscovite (Fig. 7.4b) can be deconvoluted into two species, the lattice oxygen (O^{2-}) and surface hydroxyl group ($-\text{OH}$) (362), where the percentage of surface hydroxyl groups in muscovite is 55.98%. This high loading of hydroxyl groups make muscovite as one of promising fillers to interact with PA molecules and polymer chains and further get a good dispersion in HT-PEMs. In addition, the chemical composition further confirmed by EDS comprises O (57.45 at.%), Si (19.73 at.%), Al (18.44 at.%), K (3.83 at.%), Fe (0.32 at.%), and Ti (0.21 at.%), while the corresponding formula is $\text{KAl}_{4.81}\text{Si}_{5.15}\text{O}_{15}\text{Fe}_{0.09}\text{Ti}_{0.06}$ (Table 7.2). The slightly different

stoichiometry from the $\text{KAl}_2(\text{Si}_3\text{Al})\text{O}_{10}(\text{OH})_2$ results from the kaolinite impurities detected by XRD (Fig. 7.2).

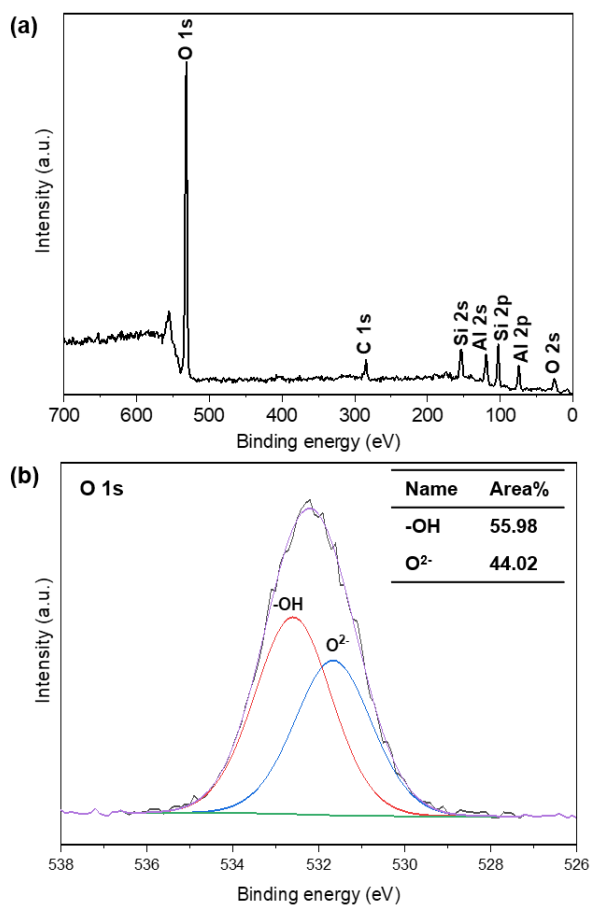


Fig. 7.4. (a) XPS survey spectrum and (b) XPS O 1s spectrum of muscovite.

Table 7.2. The main chemical compositions and formula of muscovite.

Sample	Elemental composition (at.%)						Formula
	O	Si	Al	K	Fe	Ti	
Mus	57.45	19.73	18.44	3.83	0.32	0.21	$\text{KAl}_{4.81}\text{Si}_{5.15}\text{O}_{15}\text{Fe}_{0.09}\text{Ti}_{0.06}$

7.2.5 Thermogravimetric analysis

The thermal stability of muscovite was displayed in Fig. 7.5. When the temperature rises up to around 220 °C, the weight loss is only around 0.2 wt% which is related to the absorbed moisture in muscovite. The major weight loss occurs when the temperature reaches around 400 °C, illustrating muscovite is stable under 400 °C and meets the requirement of HT-PEMFCs. As the hydroxyl groups exist in the muscovite confirmed from the FTIR results (Fig. 7.3) and XPS curves

(Fig. 7.4b), it is highly probable that the incorporation of muscovite in HT-PEMs may introduce Mus-PBI and Mus-PA crosslinks to afford facile proton hopping pathways and further benefit the enhancement of proton conductivity in HT-PEMFCs (140).

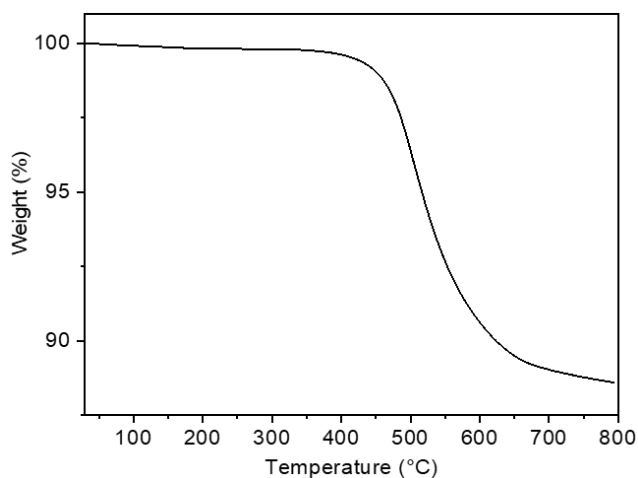


Fig. 7.5. TGA curve of muscovite.

7.2.6 Textural property analysis

The BET analysis was also conducted to characterize the porosity and surface area of muscovite. From the BET results (Table 7.3), the $6.72 \text{ m}^2 \text{ g}^{-1}$ specific surface area, $0.04 \text{ cm}^3 \text{ g}^{-1}$ pore volume and 24.93 nm pore diameter of muscovite flakes may afford possible trapping points in their nano-galleries for PA molecules in PA doped HT-PEMs (135). In this work, therefore, the as-received muscovite was added into PBI membranes in HT-PEMFCs, and the related fuel cell performances were explored.

Table 7.3. Textural properties of muscovite.

Sample	S_{BET} ($\text{m}^2 \text{ g}^{-1}$)	V_{p} ($\text{cm}^3 \text{ g}^{-1}$)	D_{p} (nm)
Mus	6.72	0.04	24.93

7.3 Characterization of composite membranes

7.3.1 Morphology analysis

The membrane with a flat and dense structure is an important character in HT-PEMs. The crack or rough morphology usually result in low mechanical strength and poor durability. In this work, the morphology of membranes was characterized by SEM as shown in Fig. 7.6. Dense structures without macroscopic defects are observed in the cross-sectional SEM images of all membranes, illustrating that membranes with well-dispersed muscovite had been successfully prepared.

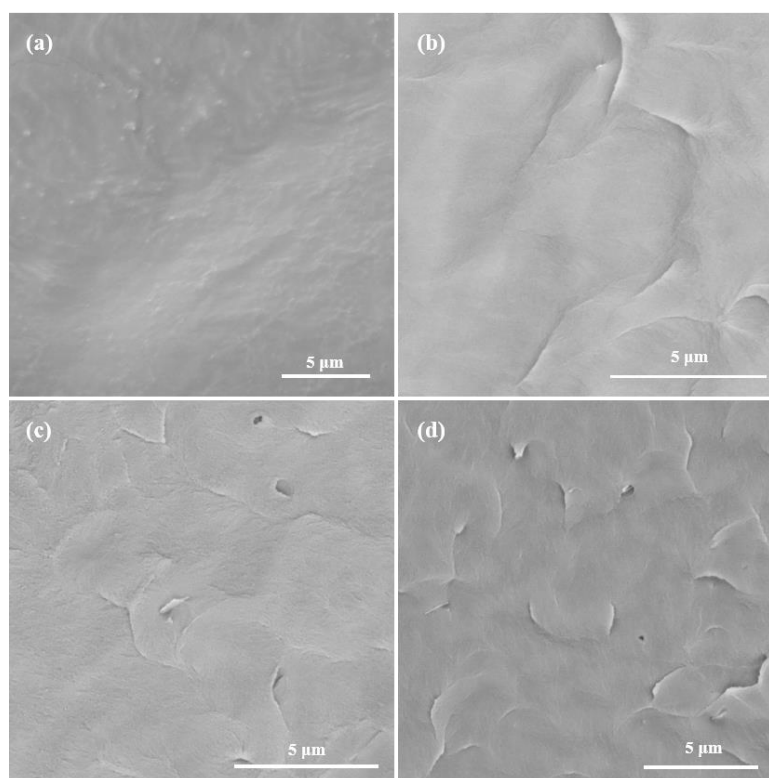


Fig. 7.6. Cross-sectional SEM images of (a) P/0Mus, (b) P/0.25Mus, (c) P/0.50Mus, and (d) P/0.75Mus membranes.

7.3.2 Fourier-transform infrared spectroscopy analysis

To explore chemical bonding of undoped and acid doped PES-PVP/Mus composite membranes, Fourier-transform infrared (FTIR) spectroscopy was conducted (Fig. 7.7) and the full FTIR assignment of all membranes is shown in Table 7.4. As shown in Fig. 7.7a, all membranes show all peaks at the same wavenumber, illustrating that the chemical bonding in pure PES-PVP or composite membranes is the same. The characteristic bands at 1486 and 1576 cm^{-1} are assigned to the C_6H_6 ring stretch of PES, while the small peaks at 1657 cm^{-1} show the $\text{C}=\text{O}$ stretch of PVP. These peaks which correspond to the bonds in PES or PVP confirm the successful preparation of PES-PVP membranes. However, the incorporated muscovite in PES–PVP matrix cannot be distinguished by FTIR ($4000\text{--}500\text{ cm}^{-1}$) because the amide groups in PVP overlapped the O–Si–O bands in muscovite. In order to investigate the differences, the wavenumber range from 500 to 400 cm^{-1} is presented as shown in Fig. 7.7b where the band at 423 cm^{-1} in the composite membranes corresponds to Al–O bands, confirming the existence of muscovite in the composite membranes. The FTIR curves of PA doped membranes are shown in Fig. 7.7c. The new broad peaks at approximately 960 cm^{-1} show the existence of PA in membranes. In addition, it can be seen that some peaks are in the same or slightly shifted positions of undoped membranes (Fig. 7.7a). This can be explained that the introduced PA and water in acid doped membranes can interact with PVP chains to get some bond vibrations.

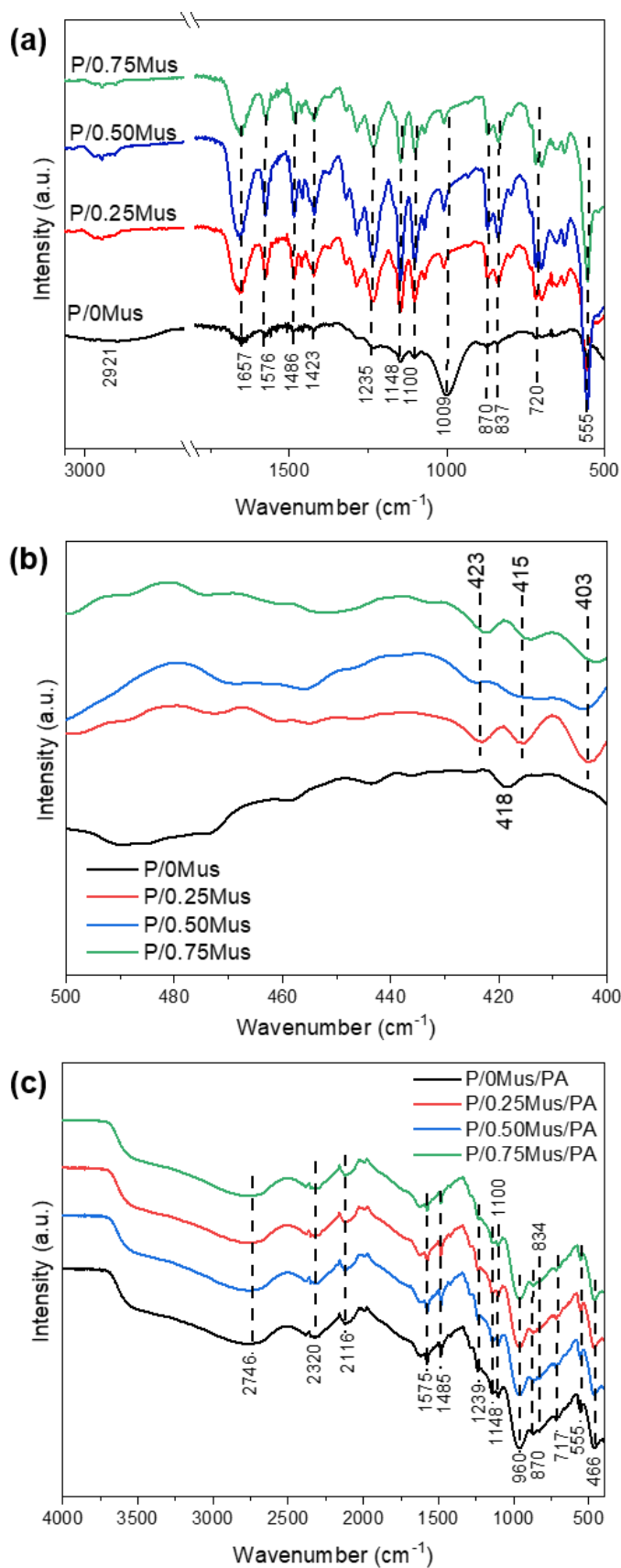


Fig. 7.7. FTIR spectra of undoped PES-PVP membrane in (a) 3100–500 cm^{-1} and (b) 500–400 cm^{-1} , and (c) PA doped PES-PVP/Mus membranes (4000–400 cm^{-1}).

Table 7.4. Full FTIR assignment of undoped and acid doped PES-PVP/Mus membranes.

Wavenumber	Assignment	Related polymer
2921	C–H asymmetric stretch	PVP
2746	N–H	PVP
2320	O–H	PVP, PES
2116	C–N stretching vibration	PVP
1657	C=O stretch	PVP
1576	C ₆ H ₆ ring stretch	PES
1486	C ₆ H ₆ ring stretch	PES
1423	Pyrrolidinyl	PVP
1235	C–O asymmetric stretch	PES
1148	S=O symmetric stretch	PES
1100	C–N vibration	PVP
1009	C–C	PVP
960	Phosphoric acid	Phosphoric acid
870	C–H bending	PES
837	CH ₂	PVP
720	C–S stretch	PES
555	N–C=O in-plane bending	PVP
423	Al–O	muscovite

7.3.3 Acid doping and swelling

Acid uptake and acid doping level (ADL) are related to the acid amount in the membranes, which have direct relationship to the proton conductivity of membranes. Higher acid uptake or ADL usually represent higher proton conductivity since there are more free acids inside the membrane to transfer protons through the membranes via Grotthuss mechanism. However, higher acid uptake tends to more acid leaching and lower dimensional stability, which may result in poor

mechanical strength and cell degradation. As shown in Table 7.5, the acid uptake and ADL of all composite membranes decrease with the increased loading of muscovite in membranes. This is in good agreement with the enhanced dimensional stability (reduced volume swelling) in the composite membranes. Among all the composite membranes, P/0.75Mus/PA membrane has best dimensional stability (154% volume swelling).

Table 7.5. Summary of acid uptake, ADL and swelling properties of PES-PVP/Mus membranes.

Membrane	Acid uptake/%	ADL/mol	Area swelling/%	Volume swelling/%
P/0Mus/PA	316 ± 11	5.96 ± 0.21	60.4 ± 0.6	157 ± 9
P/0.25Mus/PA	315 ± 11	5.95 ± 0.22	60.7 ± 2.0	156 ± 3
P/0.50Mus/PA	310 ± 9	5.85 ± 0.18	62.2 ± 3.88	155 ± 6
P/0.75Mus/PA	305 ± 2	5.76 ± 0.04	62.2 ± 3.50	154 ± 5

7.3.4 Mechanical properties

The reinforcing effects of muscovite on PA doped PES-PVP membranes are evaluated by tensile stress-strain behaviour as shown in Fig. 7.8 and Table 7.6. The reduction of tensile strength is observed in both acid undoped and doped PES-PVP/muscovite composite membranes, which is consistent with the mechanical results in the PES-PVP/SN in section 6.3.3. Although the interactions between muscovite and PVP can limit the mobility of PVP polymer chains to obtain stiffer ordered PVP domains, the incorporation of muscovite cannot enhance the tensile strength of the composite membranes. This may be explained that muscovite has no interactions with PES which offer the main mechanical strength for PES-PVP membranes. Therefore, the incorporation of muscovite can dilute the polymer chain arrangement of PES to get a reduced tensile strength in composite membranes. The elongations at break of all composite membrane are also lower than pure PES-PVP membranes (Table 34). Interestingly, the Young's modulus of acid doped membranes was enhanced with increasing muscovite loading (Table 7.6), which is probably due to the hydrophilicity of muscovite which introduce interactions between PA molecules and the polymer chains. For example, the Young's modulus of the membrane with 0.50 wt% muscovite was 20.3 MPa, compared with only 18 MPa for the pure membrane.

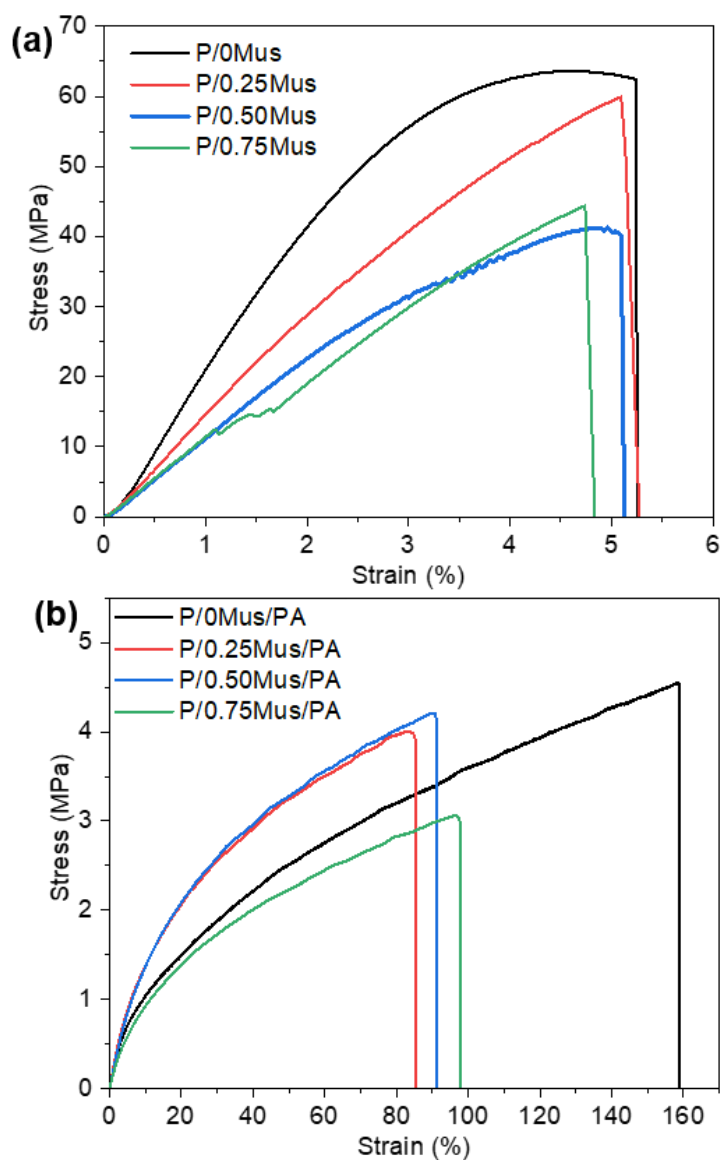


Fig. 7.8. Stress-strain curves of (a) undoped and (b) PA doped PES-PVP/Mus membranes.

Table 7.6. Summary of mechanical properties of PES-PVP/Mus composite membranes before and after PA doping at ambient temperature and humidity.

Samples	Tensile strength (MPa)		Elongation at break (%)		Young's modulus (MPa)	
	Undoped	Doped	Undoped	Doped	Undoped	Doped
P/0SN	67 ± 19	5.3 ± 0.3	3.7 ± 1.2	153 ± 17	3007 ± 789	18.0 ± 1.5
P/0.25Mus	62 ± 6	3.9 ± 0.3	6.1 ± 1.0	76 ± 17	1243 ± 73	17.5 ± 5.7
P/0.50Mus	45 ± 7	3.8 ± 0.5	4.8 ± 0.8	90 ± 20	1107 ± 270	20.3 ± 5.0
P/0.75Mus	47 ± 4	3.8 ± 0.7	4.3 ± 0.6	92 ± 30	1053 ± 205	23.0 ± 3.3

7.4 Evaluation of the composite membranes in a HT-PEMFC

7.4.1 Polarization curve

In this chapter, muscovite was introduced into PES-PVP membranes to prepare corresponding MEAs and test the performance. Three different loadings (0.25, 0.50 and 0.75 wt%) of muscovite were used to prepare the composite PES-PVP membranes, named as P/0.25Mus, P/0.50Mus, P/0.75Mus, respectively. The addition of muscovite was found to have some improvements on the power density as shown in Fig. 7.9. The power density was enhanced from around 370 mW/cm² in pristine membrane to 553 mW/cm² in P/0.50Mus/PA, around 49% higher than the unaltered PES-PVP membrane. The possible reason is the addition of muscovite with surface hydroxyl groups can facilitate the proton transfer through the membranes and enhance the power density. However, when the loading of muscovite rises to 0.75 wt%, the power density of P/0.75Mus/PA decreased to 495 mW/cm². This may be due to the possible aggregation of muscovite flakes when the loading of muscovite is over than 0.5 wt%. Therefore, from the viewpoint of power density, the optimal ratio of muscovite is 0.5 wt% in the composite membranes.

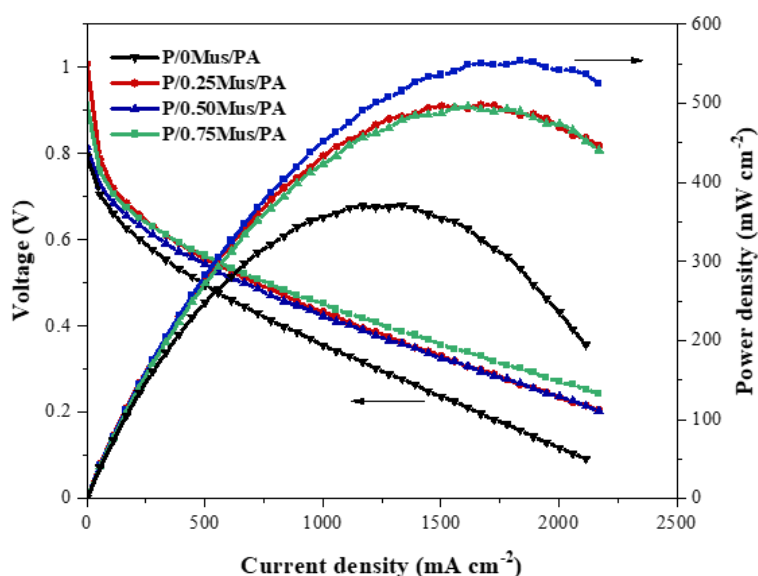


Fig. 7.9. Polarization curves of fresh muscovite incorporated PES-PVP membranes.

7.4.2 Durability

To explore the durability of the muscovite incorporated PES-PVP membranes, a 1200 min steady-state durability test was performed in this chapter. The fuel cell was operated at a constant voltage (0.6 V) without humidification and the corresponding current was recorded. All membranes had decreased current density during the durability test as shown in Fig. 7.10a. The membranes with different loadings of muscovite showed different decay rates (Fig. 7.10b) where the membrane

with higher loading of muscovite presented lower decay rates. For instance, the P/0.75Mus/PA had the lowest decay rate ($0.9 \text{ mA/cm}^2\cdot\text{h}$) which is comparable with the PES-PVP membrane with 0.75 wt% SN ($1.01 \text{ mA/cm}^2\cdot\text{h}$) described in chapter 6. This interesting result is consistent with the SN added PES-PVP membranes (section 6.4.2), illustrating the muscovite may has similar functions with SN to promote the cell performance and alleviate degradations due to the layered structures which can protect the intercalated polymer chains from radical attack.

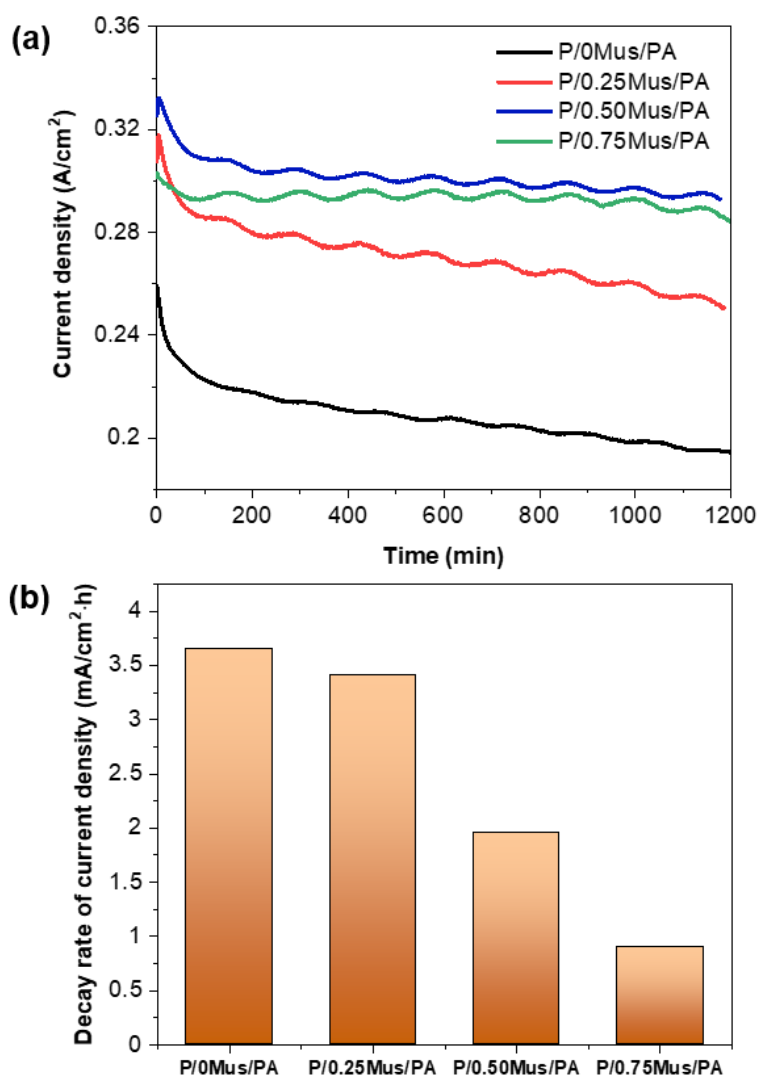


Fig. 7.10. (a) durability test and (b) decay rate of PA doped PES-PVP/muscovite composite membranes at 0.60 V and 150°C during 1200 min durability test.

7.4.3 Electrochemical impedance spectroscopy

The impedance properties of fresh muscovite added composite membranes were also investigated by the EIS Nyquist spectra which were fitted using Randles circuit model and measured at 0.6 A and 150°C without humidification (Fig. 7.11). The detailed EIS data are shown in Table 7.7. After the addition of muscovite, the ohmic resistance decreased from $0.2417 \Omega\cdot\text{cm}^2$ in pristine

membrane to $0.1719 \Omega \cdot \text{cm}^2$ in P/0.50Mus/PA, while the polarization resistances of composite membranes including anode and cathode charge transfer resistance were also reduced. This may be explained that the hydroxyl groups on the surface of muscovite can benefit for the enhancement of proton conductivity to get reduced resistances.

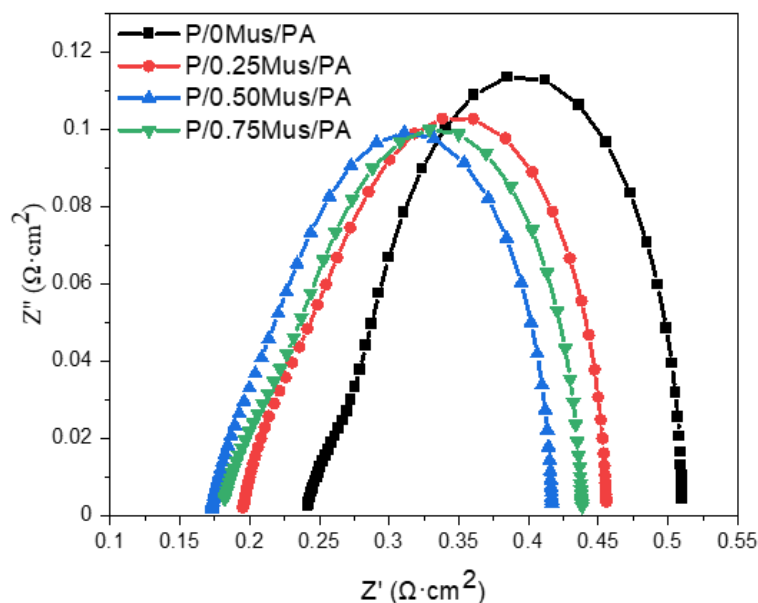


Fig. 7.11. EIS Nyquist plots of PA doped PES-PVP/muscovite composite membranes measured at 0.6 A and 150 °C without humidification.

Table 7.7. Summary of ohmic resistance (R_0), anode charge transfer resistance (R_1), cathode charge transfer resistance (R_2), and proton conductivity of fresh MEAs obtained from equivalent circuits.

Samples	$R_0/\Omega \cdot \text{cm}^2$	$R_1/\Omega \cdot \text{cm}^2$	$R_2/\Omega \cdot \text{cm}^2$
P/0SN/PA	0.2417	0.0538	0.2169
P/0.25Mus/PA	0.1952	0.0801	0.1817
P/0.50Mus/PA	0.1719	0.0684	0.1767
P/0.75Mus/PA	0.1790	0.0842	0.1756

7.5 Conclusion to this chapter

In addition to the SN fillers which were studied in chapter 6, muscovite was used as the alternative clay-based filler in this chapter. It was found that the addition of muscovite into PES-PVP membrane gave improved performance and durability. The hydroxyl groups on the surface of

muscovite may offer additional proton transfer pathway to get reduced ohmic resistances and improved power density. Meanwhile, the layered structure of muscovite affords polymer anchoring points and protects them from the radical attack to reduce decay rate during the 1200 min steady-state durability test at 150 °C without humidification. The PES-PVP/muscovite composite membranes showed highest power density (553 mW/cm²) when the muscovite loading is 0.5 wt%, which has a 49% enhancement compared with the pure PES-PVP membrane. Better durability (0.9–3.4 mA/cm²·h decay rate) was also observed in the composite membranes, compared with 3.65 mA/cm²·h in pure membranes.

To better analyse the effects of two clay-based filler (SN and muscovite) on the performance of HT-PEMs, the comparisons between SN and muscovite are summarized in Table 7.8. It is clear that there are no big differences in terms of membrane properties (ADL and ohmic resistance) and decay rate. However, the muscovite incorporated membranes showed higher improvement (49%) in terms of power density than the SN added membranes (34%). The possible reason may be that the muscovite with higher concentration of surface hydroxyl groups has better compatibility with the polymer chains to get a better distribution and faster proton transfer in PES-PVP/muscovite membranes. Therefore, the muscovite used without any modification is regarded as the cheap and promising inorganic filler in HT-PEMs. To examine the reason why the performances of composite membranes get improved, the next chapter will focus on the investigation of the degradation mechanisms of the muscovite incorporated membranes.

Table 7.8. Performance comparison between silica nanosheets and muscovite in HT-PEMs

Membrane	Filler loading (wt%) ^a	ADL (mol) ^a	Ohmic resistance (Ω·cm ²) ^a	Peak power density (mW/cm ²)	Improvement compared to pure membrane	Lowest voltage decay rate (mA/cm ² ·h)
P/SN/PA	0.25	5.79	0.1718	495	34%	1.01
P/muscovite/PA	0.50	5.85	0.1719	553	49%	0.9

Note: ^a indicates the best filler loading in terms of power density.

Chapter 8: Investigation of acid retention ability in polybenzimidazole/muscovite composite membranes

8.1 Introduction

There are very few studies focused on the durability degradation and deactivation mechanisms of the organic-inorganic composite membrane-based HT-PEMFCs. Zhang et al. (18) demonstrated the in-situ formed PA/phosphosilicate nanoclusters at 250 °C can lead to reduced acid leaching and good durability. Ossianer et al. (363) and our group (136) used electrochemical characterization techniques such as polarization curves and electrochemical impedance spectroscopy (EIS) to reveal that the membrane short circuits and membrane thinning may result in cell degradation. Krishnan et al. (364) and Wu et al. (262) reported that the enhanced durability of HT-PEMs is attributed to good PA retention of metal-organic frameworks and the covalent bonds between the polymer and the filler, respectively. However, there is a lack of substantial evidence to show mechanisms related to the cell degradation. As mentioned in section 3.2, PA leaching inevitably occurs in PA doped HT-PEMs during the operation of HT-PEMFCs (365). In addition to being mechanically squeezed by the fuel cell setup, PA can migrate from cathode to anode due to PA diffusion and electrochemical pumping (91) and can also leach out from HT-PEMs by dissolving in the water produced at the cathode. PA leaching can cause PA loss in membrane, catalyst poisoning, and the fuel pathway blockage in gas diffusion layer, thereby decreasing the proton conductivity of the membrane, reducing the activity of the oxygen reduction reaction, and increasing the mass transfer resistance, respectively (354). Therefore, in this chapter, how to alleviate acid leaching and understand the mechanism of acid leaching is regarded as the main objective.

Since muscovite (studied in chapter 7) showed similar improvements of membrane properties and cell performance compared with SN (studied in chapter 6), the cheap and as-received muscovite was chosen as an inorganic filler to investigate the effect of acid retention ability of inorganic-organic composite HT-PEMs. In addition, as the PES-PVP membrane suffered a relatively poor durability and the acid leaching occurs after a longer fuel cell operation (46), the stable polybenzimidazole (PBI) was used as polymer matrix in this chapter. PA doped PBI/muscovite composite membranes were prepared using the doctor blading method, while the deactivation mechanisms were investigated by several in-situ and ex-situ techniques. In-situ electrochemical techniques such as linear sweep voltammetry (LSV) and EIS were performed to evaluate the hydrogen crossover and resistances, respectively. To efficiently explore the durability and acid retention ability of the membranes in a relatively short time, an accelerated stress test (AST) running at high current density was carried out to test the durability (55). Further, the deactivation

mechanisms and acid retention ability of composite membranes were studied for the first time to explore the phosphorus distribution via Energy Dispersive X-ray Spectroscopy (EDS) and to validate the relationship between muscovite and PA molecules via X-ray photoelectron spectroscopy (XPS) and thermogravimetric analysis (TGA). In addition, since the method for membrane preparation (doctor-blade casting technique) is an industrially scalable process (366), we hope the method will facilitate the commercialization of PBI/muscovite composite membranes.

8.2 Characterization of composite membranes

8.2.1 Morphology analysis

As the compatibility and dispersion status of the inorganic filler in membranes have critical effects on the mechanical property and proton conductivity of membranes, the morphologies of PBI composite membranes were explored. There are slight colour differences among the membranes with different loadings of muscovite as shown in Fig. 8.1 where the physical observation of membranes shows decreased transparency with increased loading of muscovite. The surfaces of all membranes present similar flat and smooth surfaces (Fig. 8.2), while the cross-sectional images show good muscovite distribution (Fig. 8.3). The incompatibility between muscovite and PBI polymer could explain the aggregation when the loading of muscovite rises to 2 wt%. This aggregation may lead to the formation of voids or cracks in the membranes, thus further deteriorating the performance of membranes (350). However, more muscovite loadings may increase connections with PA molecules and PBI polymer chains via hydrogen bonds to get improved PA retention ability and durability. It is probably that the impacts between the muscovite aggregations and the increased nano-galleries affording trapping points for PA molecules and polymer chains need to be balanced, which will be discussed in later sections. To further confirm the good distribution of muscovite in the PBI matrix, surface morphology and element mapping of PBI/1Mus composite membrane are shown in Fig. 8.4. The smooth surface in Fig. 8.4a shows muscovite has good compatibility with PBI matrix, while the element mapping of Al and Si (Fig. 8.4e-f) which only exist in muscovite confirms the uniform dispersion of muscovite in the PBI matrix. In addition, muscovite aggregation occurs in PBI/2Mus membranes (red ovals in Fig. 8.3d) where the flake sizes of muscovite are less than 5 μm , which show smaller than the flake sizes of raw muscovite in Fig. 7.1 (up to 10 μm). This can be explained that the as-received raw muscovite was firstly mixed with DMAc and then ultrasonicated using a probe sonicator for 15 min during the preparation of composite membrane.



Fig. 8.1. Physical observation of (a) PBI membrane, (b) PBI/0.5Mus, (c) PBI/1Mus, and (d) PBI/2Mus.

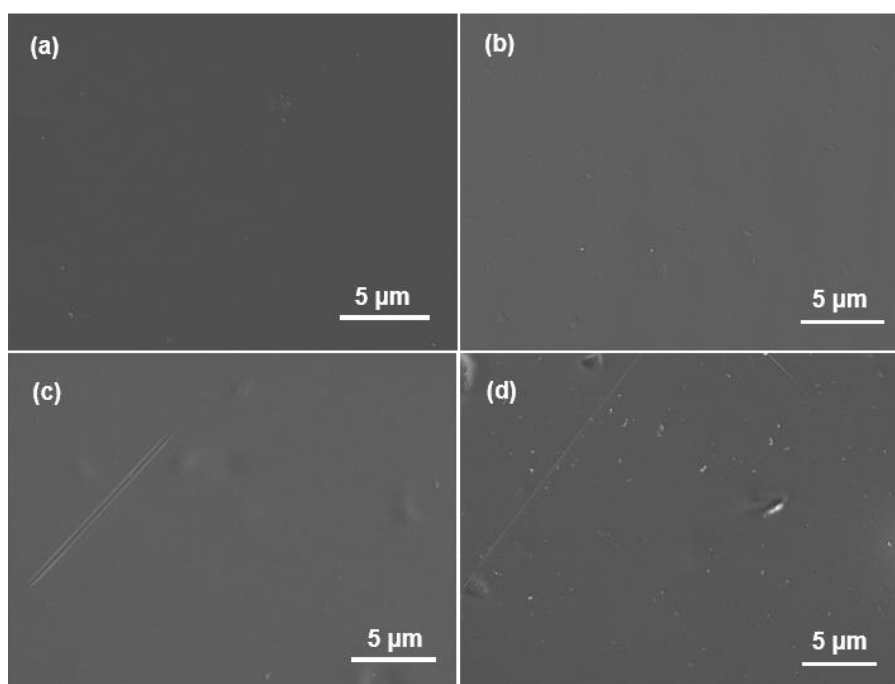


Fig. 8.2. Surface SEM images of (a) PBI/0Mus, (b) PBI/0.5Mus, (c) PBI/1Mus, and (d) PBI/2Mus.

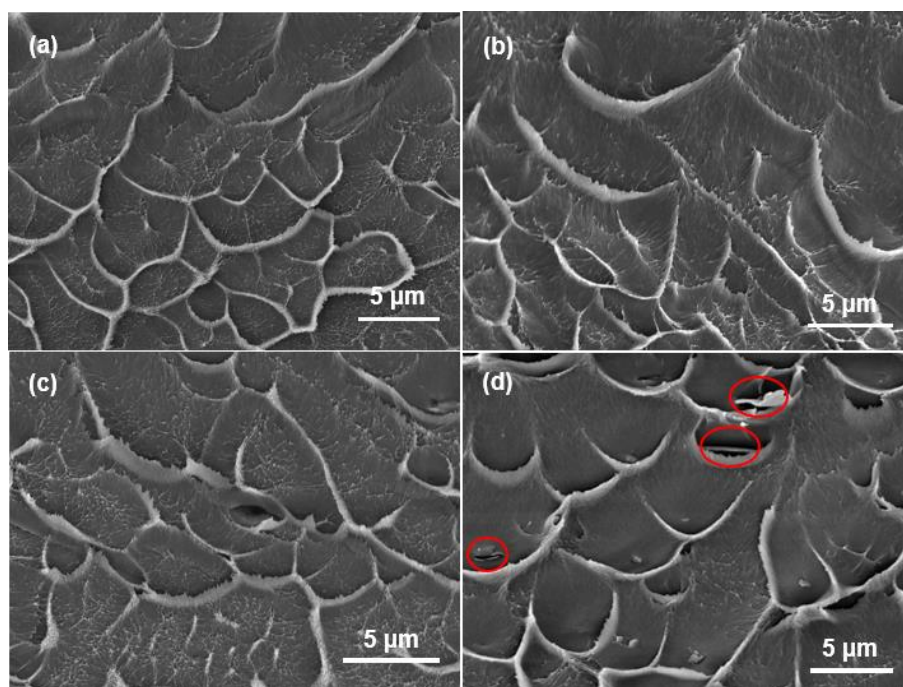


Fig. 8.3. Cross-sectional SEM images of (a) PBI/0Mus, (b) PBI/0.5Mus, (c) PBI/1Mus, and (d) PBI/2Mus.

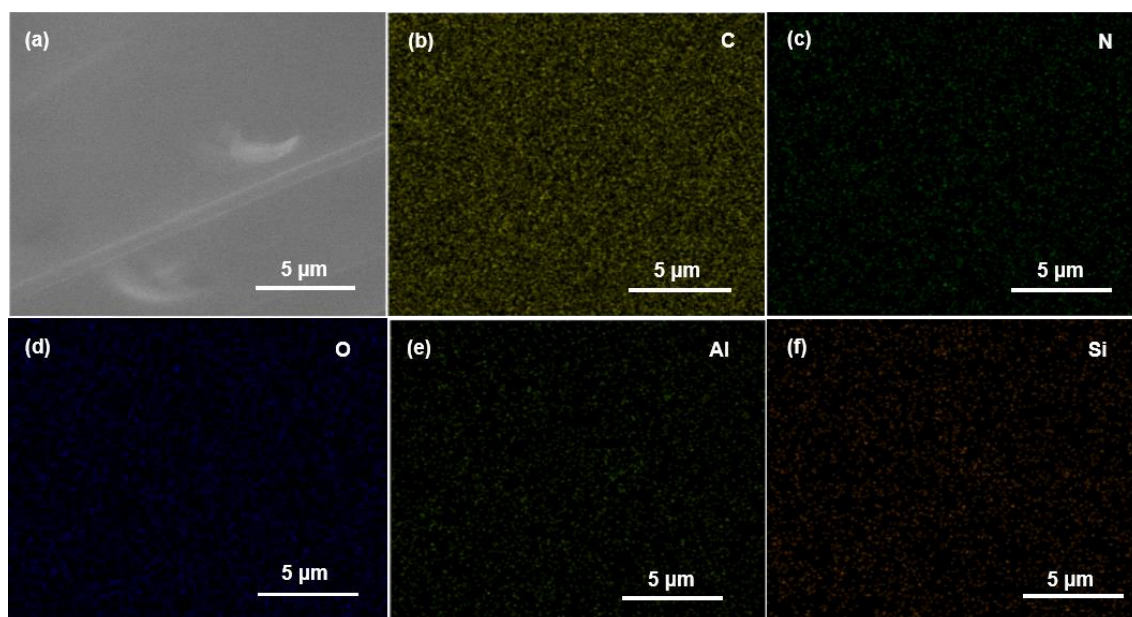


Fig. 8.4. (a) Surface morphology, and elemental distribution mappings of (b) C, (c) N, (d) O, (e) Al, and (f) Si in the PBI/1Mus composite membrane.

8.2.2 Fourier-transform infrared spectroscopy analysis

FTIR was used to characterize the chemical bonds in membranes as shown in Fig. 8.5, and the full FTIR assignment of membranes is concluded in Table 8.1. The band at 3614 cm^{-1} is ascribed to water, which can be explained by the absorbed water in membranes (Fig. 8.5a). The wide band at $3400\text{--}3000\text{ cm}^{-1}$ stands for the N-H stretching vibrations in which two peaks at 3378 and 3036

cm^{-1} indicate the N-H without involved in hydrogen bonding and hydrogen-bonded N-H, respectively (367). The reduced intensity in this range is observed in the composite membranes, indicating that muscovite may disrupt the hydrogen bonding in polymer chains and form hydrogen bonds with N-H groups of PBI to get decreased intensity of N-H mode (368). The bands at 1608 cm^{-1} (C=N and C=C stretching vibrations), 1438 cm^{-1} (C-H stretching vibration), 796 cm^{-1} (heterocyclic ring vibration), and 685 and 454 cm^{-1} (C-H stretching vibration) indicate the existing of PBI polymer in membranes (369). Compared with pure PBI at 454 cm^{-1} (Fig. 8.5a inset), the reduced intensity of PBI/1Mus suggests that the aromatic groups become less staggered and more coplanar conformation (370), further supporting that muscovite acts as a plasticizer to disrupt the interchain hydrogen bonding interactions in the composite membrane. For the PA doped membranes (Fig. 8.5b), the bands over 2000 cm^{-1} can be assigned to N-H and O-H stretching modes, while the bands below 2000 cm^{-1} are related to different forms of P-O modes. The broad peaks at $3000\text{--}2500\text{ cm}^{-1}$ and $2500\text{--}2250\text{ cm}^{-1}$ are identified as N-H and O-H stretching, respectively (371). Because of the participation of PA molecules, the peak which is ascribed to C=C and C=N stretching is shifted from 1608 to 1633 cm^{-1} (Fig. 8.5b inset). The FTIR results confirm that the muscovite acts as a plasticizer in membranes and the PBI/muscovite composite membranes are successfully prepared.

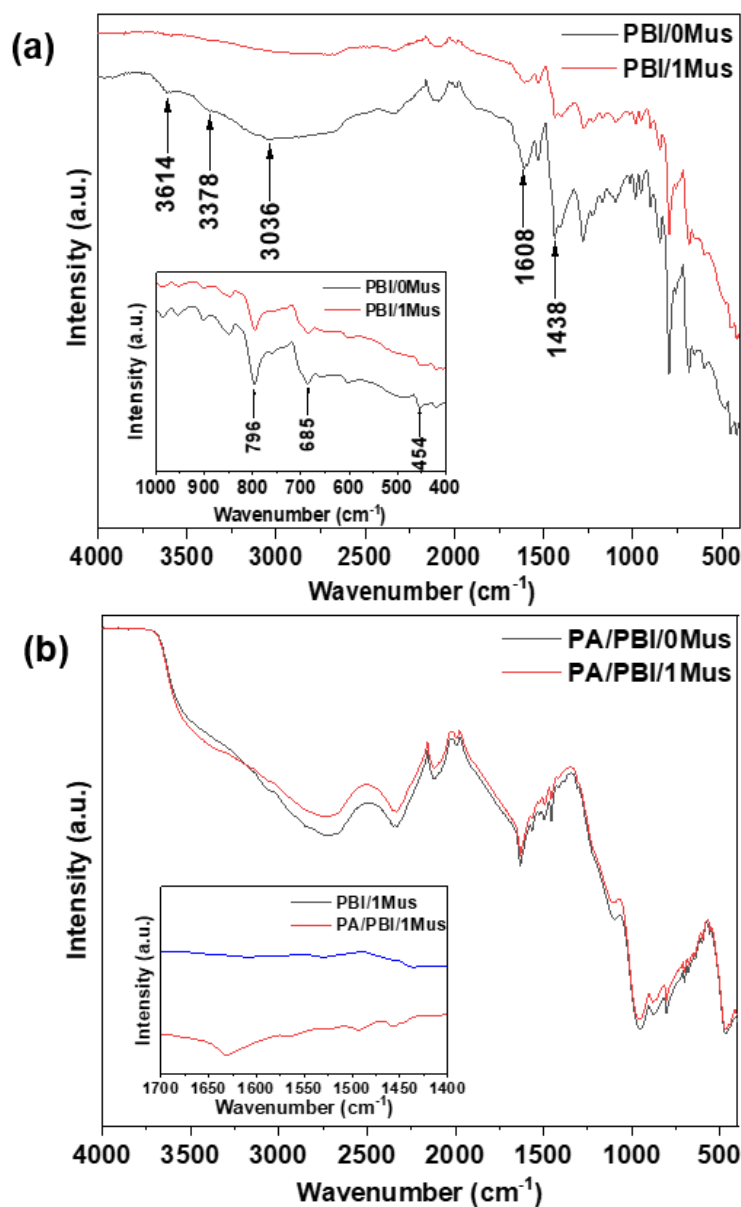


Fig. 8.5. FTIR spectra of (a) undoped PBI/0Mus and PBI/1Mus membranes (inset: a comparison of PBI/0Mus and PBI/1Mus from 1000 to 400 cm^{-1}) and (b) PA doped PBI/0Mus and PBI/1Mus membranes (inset: a comparison of PBI/1Mus and PA/PBI/1Mus from 1700 to 1400 cm^{-1}).

Table 8.1. Full FTIR assignment of PBI/xMus and PA/PBI/xMus.

FTIR of PBI/xMus	Assignment ^{a,b}	FTIR of PA/PBI/xMus	Assignment ^{a,b}
3614	Aqueous δ_{OH}	2725	δ_{NH}
3378	Free δ_{NH}	2345	δ_{OH}
3036	Hydrogen-bonded δ_{NH}	1633	$\nu_{\text{CC}} + \nu_{\text{CN}} + \delta^{\text{ip}}_{\text{XH}}$
1608	$\delta_{\text{XH}}^{\text{ip}} + \nu_{\text{CC}}^{\text{ip}}$	1566	$\delta^{\text{ip}}_{\text{CH}} + \nu^{\text{ip}}_{\text{CC}}$

1592	$\delta_{\text{CH}}^{\text{ip}} + \nu_{\text{CC}}^{\text{ip}}$	1496	$\delta^{\text{ip}}_{\text{NH}} + \delta^{\text{ip}}_{\text{CH}} + \nu^{\text{ip}}_{\text{CC}} + \nu^{\text{ip}}_{\text{CN}}$
1531	$\delta_{\text{CH}}^{\text{ip}}$	1457	$\delta^{\text{ip}}_{\text{XH}} + \nu^{\text{ip}}_{\text{CC}} + \delta^{\text{ip}}_{\text{CNC}}$
1458	$\delta_{\text{CH}}^{\text{ip}} + \delta_{\text{XH}}^{\text{ip}} + \nu_{\text{CC}}^{\text{ip}}$	1415	$\nu^{\text{ip}}_{\text{CN}} + \delta^{\text{ip}}_{\text{CH}}$
1438	$\delta_{\text{CH}}^{\text{ip}} + \delta_{\text{XH}}^{\text{ip}}$	1379	$\delta^{\text{ip}}_{\text{NH}} + \delta^{\text{ip}}_{\text{CH}} + \nu^{\text{ip}}_{\text{CC}}$
1408	$\delta_{\text{XH}}^{\text{ip}}$	1308	$\delta_{\text{P(OH)}_2} + \delta_{\text{P(OH)}} \text{H}_{11}\text{P}_4\text{O}_{16}^-$
1279	$\delta_{\text{XH}}^{\text{ip}} + \nu_{\text{CC}}^{\text{ip}} + \delta_{\text{CH}}^{\text{ip}}$	1225	$\delta_{\text{POH}} + \nu_{\text{P=O}} [\text{H}_3\text{PO}_4]_4$
1227	$\delta_{\text{XH}}^{\text{ip}} + \nu_{\text{CC}}^{\text{ip}} + \nu_{\text{CN}}^{\text{ip}}$	1095	$\delta_{\text{POH}} + \nu_{\text{P=O}} [\text{H}_3\text{PO}_4]_4$
1171	$\delta_{\text{CH}}^{\text{ip}} + \delta_{\text{XH}}^{\text{ip}} + \nu_{\text{CC}}^{\text{ip}} + \nu_{\text{CN}}^{\text{ip}}$	958	$\delta_{\text{POH}} + \nu_{\text{POH}} [\text{H}_3\text{PO}_4]_4$
1099	$\delta_{\text{CH}}^{\text{ip}}$	873	$\nu_{\text{P(OH)OO}^-} + \nu_{\text{P(OH)3}} \text{H}_{11}\text{P}_4\text{O}_{16}^-$
1017	$\delta_{\text{CH}}^{\text{ip}}$	803	$\delta_{\text{CH}}^{\text{oop}}$
986	$\nu_{\text{CC}}^{\text{ip}}$	702	$\delta_{\text{NCN}}^{\text{oop}}$
954	$\delta^{\text{oop}}_{\text{CH}}$	678	$\delta_{\text{CH}}^{\text{oop}}$
902	$\delta^{\text{oop}}_{\text{CH}}$	645	$\delta^{\text{oop}}_{\text{NH}}$
848	$\delta^{\text{oop}}_{\text{CH}}$	601	$\delta_{\text{POH}} \text{H}_{11}\text{P}_4\text{O}_{16}^-$
796	$\delta^{\text{oop}}_{\text{CH}}$		
761	$\delta^{\text{oop}}_{\text{CH}}$		
685	$\delta_{\text{CH}}^{\text{oop}}$		
655	$\delta_{\text{CH}}^{\text{oop}} + \delta_{\text{CCC}}^{\text{oop}}$		
600	$\delta_{\text{CCC}}^{\text{ip}}$ (ring)		
480	$\delta^{\text{oop}}_{\text{CH}} + \delta_{\text{CCN}}^{\text{oop}}$		
454	$\delta^{\text{oop}}_{\text{XH}}$		
419	$\delta^{\text{oop}}_{\text{NH}}$		

^aThe correlative assignments are based on the previously published results (370, 372).

^b δ : bending; ν : stretching; ip: in-plane; oop: out-of-plane; X indicates the motions of N and C atoms.

8.2.3 Mechanical properties

To explore the mechanical and thermal stabilities of the composite membranes, the stress-strain and TGA tests have been performed. As shown in Table 8.2 and Fig. 8.6, the tensile strength goes up from 103 MPa in PBI/0Mus to 123-135 MPa in PBI/muscovite composite membranes. Although the elongation is slightly smaller than PBI/0Mus, the Young's modulus of the composite membranes is improved to 2476-2589 MPa. As expected, since PA molecules can loosen the compact nature of membranes and have a plasticizing effect on polymer chains, the tensile strength of PA doped membranes reduces, and the elongation goes up (Fig. 8.6). Compared with PA/PBI/0Mus (6.8 MPa tensile strength and 118% elongation), the tensile strength of PA doped PBI/muscovite composite membrane ranges from 6.8 to 7.5 MPa while the elongation is enhanced to 121-134%. The improved mechanical strength may be explained by the good dispersion of muscovite in membranes (as shown in Fig. 8.3 and Fig. 8.4) and the formation of hydrogen bonds between muscovite and PBI polymer (confirmed by FTIR in Fig. 8.5). Interestingly, the tensile strength improves with the muscovite loading from 0 to 1 wt% before decreasing in the filler range from 1 to 2 wt%. The initial positive correlation between tensile strength and the muscovite loading (0-1 wt%) may be due to the formation of Mus-PBI crosslinks which can limit the mobility of polymer chains to obtain stiffer ordered domains. At high muscovite loadings (1-2 wt%), however, possible muscovite aggregation may form filler-filler crosslinks to dilute the density of Mus-PBI crosslinks, resulting in the decreases of membrane cohesiveness to obtain reduced tensile strength (373).

Table 8.2. Summary of mechanical properties of membranes before and after PA doping at ambient temperature and humidity.

Samples	Tensile strength		Elongation at break		Young's modulus	
	(MPa)		(%)		(MPa)	
	Undoped	Doped	Undoped	Doped	Undoped	Doped
PBI/0Mus	103 ± 4	6.8 ± 0.4	25.0 ± 1.4	119 ± 2	2254 ± 211	42.9 ± 3.4
PBI/0.5Mus	123 ± 4	7.0 ± 0.4	13.6 ± 1.3	121 ± 13	2545 ± 214	35.5 ± 1.3
PBI/1Mus	135 ± 3	7.5 ± 0.1	14.4 ± 1.7	130 ± 1	2476 ± 227	32.1 ± 6.6
PBI/2Mus	124 ± 7	6.8 ± 0.3	22.5 ± 2.1	134 ± 12	2589 ± 62	29.1 ± 3.7

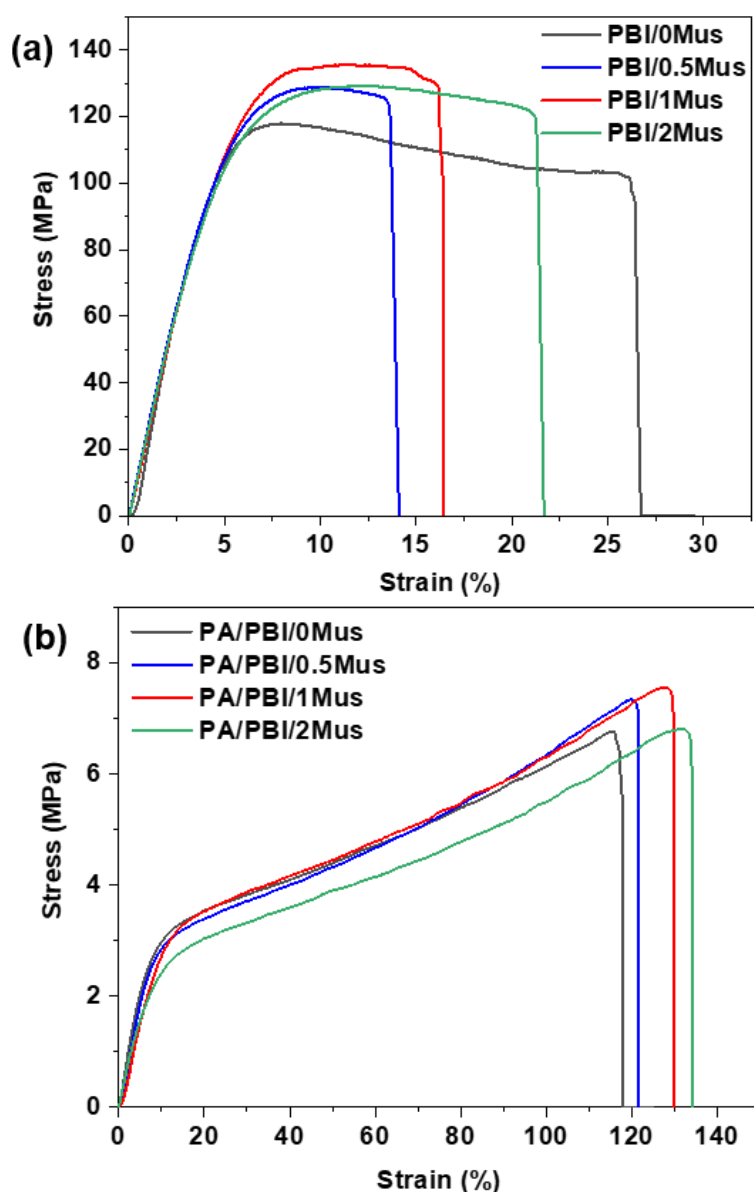


Fig. 8.6. Stress-strain curves of (a) undoped and (b) PA doped PBI/xMus membranes.

8.2.4 Thermogravimetric analysis

In Fig. 8.7, the TGA results show all membranes experience up to 10 wt% initial weight loss below 150 °C, which can be due to the evaporation of absorbed water from the PBI matrix due to the hygroscopic nature of PBI (374) and is consistent with the FTIR result in Fig. 8.5. After a period of stability from 150 to 400 °C, the membranes start decomposition from 400 °C due to the thermal decomposition of the PBI backbones. It is noticeable that the thermal stabilities of composite membranes increase with the increasing muscovite loading and all membranes are stable under 400 °C, demonstrating that these composite membranes have excellent thermal stabilities under the HT-PEMFC operating temperatures.

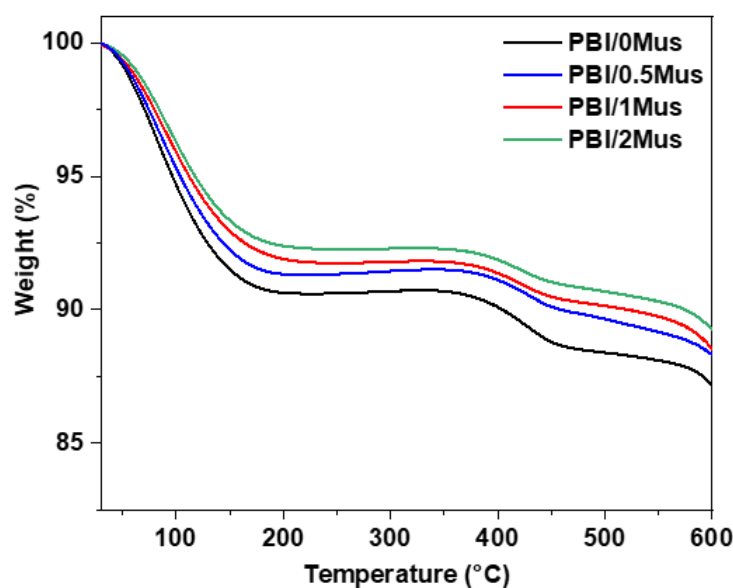


Fig. 8.7. TGA curves of PBI/xMus membranes.

8.2.5 Acid doping level and dimensional property

Compared with PA/PBI/0Mus (12.87 mol), the ADL and PA uptake show highest in PA/PBI/1Mus (13.65 mol) and start to decrease in PA/PBI/2Mus (13.57 mol) (Table 8.3). Possible aggregation of muscovite in PA/PBI/2Mus (Fig. 8.3) may occupy the free volume in the PBI membranes to result in lower ADL, PA uptake and blocked proton transport channels. Dimensional stability of membranes is another important parameter in fuel cell membranes as excessive swelling of acid doped membranes will result in poor mechanical strength and further shorten the lifetime of fuel cells. In this chapter, the area and volume swelling of membranes are displayed in Table 8.3. After the addition of muscovite, all composite membranes show reduced area and volume swelling, while PA/PBI/1Mus membrane has best dimensional stability (70.99% area swelling and 202 volume swelling), indicating the positive impact of muscovite on the dimensional stability of membranes.

Table 8.3. Properties of the PA doped PBI composite membranes with different muscovite loadings.

Samples	ADL, mol	PA uptake, %	Area swelling, %	Volume swelling, %
PA/PBI/0Mus	12.87 ± 0.43	409 ± 14	74.11 ± 2.5	232 ± 5
PA/PBI/0.5Mus	13.41 ± 0.12	427 ± 4	73.99 ± 3.3	229 ± 7
PA/PBI/1Mus	13.65 ± 0.19	434 ± 6	70.99 ± 3.3	202 ± 6
PA/PBI/2Mus	13.57 ± 0.21	432 ± 7	71.13 ± 3.5	211 ± 6

8.2.6 Proton conductivity

Fig. 8.8 shows the proton conductivities of composite membranes from 140 to 170 °C without humidification. The proton conductivity increase with the increasing muscovite loading but start to decrease when the loading exceeds 1 wt%. For instance, the proton conductivity of PA/PBI/0Mus at 150 °C is 39.5 mS cm⁻¹, which has been improved to 40.7, 42.4 and 41.7 mS cm⁻¹ for PA/PBI/0.5Mus, PA/PBI/1Mus and PA/PBI/2Mus, respectively. Compared with the pristine PBI membrane, the higher proton conductivities in composite membranes illustrate that muscovite can facilitate the proton transfer through the membranes. This can be explained by the formation of Mus-PBI and Mus-PA interactions. Specifically, the incorporation of muscovite into the membrane may introduce Mus-PBI crosslinks (confirmed by the FTIR results in Fig. 8.5) to get reduced density of hydrogen bonding among polymer chains (373), facilitating polymer chain relaxations and long-range proton migration in the membrane. The interactions between muscovite and PA also result in the increased delocalized protons to increase the conductivity (367). In addition, higher ADL of the composite membranes (Table 8.3) can be another factor to higher proton conductivity (375). Three proton pathways, including proton transfer at the PBI-PBI or Mus-PBI interfaces, and at the delocalization bodies, happened in the composite membranes and performed improved proton conductivity (376).

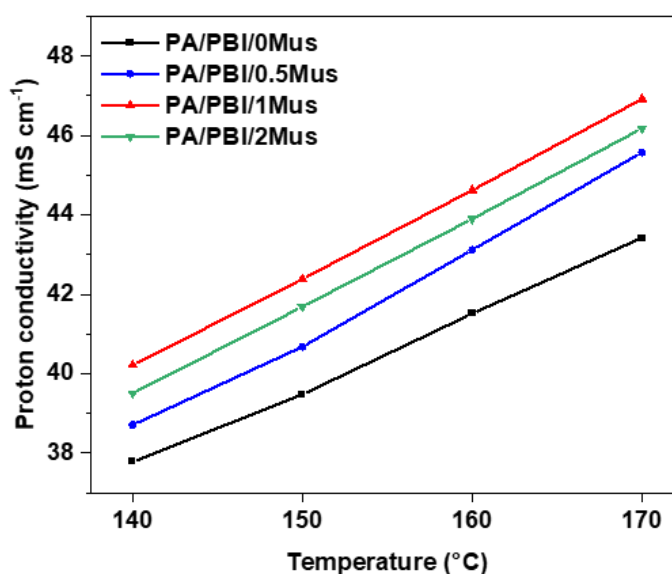


Fig. 8.8. Proton conductivity of PA/PBI/xMus at 140-170 °C.

8.3 Performance of the composite membranes in a HT-PEMFC

8.3.1 Polarization curve

The addition of muscovite convinced the addition of muscovite into PES-PVP membranes can get improved performance. However, the main objective in this chapter is to explore the acid retention of composite membranes. As the PES-PVP membranes suffer relatively higher decay

rate (Fig. 6.16) and PBI membranes perform good stability (26), using PBI membranes as substitute can give better understanding to the effect of acid leaching problems on the cell performance in a relatively longer lifetime. Therefore, the following results were focused on the incorporation of muscovite in PBI membranes.

The PA doped PBI membranes were applied in a HT-PEMFC to explore the influence of muscovite on the performance and acid leaching issues. As shown in Fig. 8.9, fuel cell performances are different according to different muscovite loadings. The PA/PBI/1Mus shows the best power density (586 mW cm^{-2}) among all the membranes, 24% higher than the PA/PBI/0Mus membrane (474 mW cm^{-2}) at 150°C without humidification. This improvement is in accordance with the enhanced proton conductivities of PBI/muscovite composite membranes (Fig. 8.8). Regarding to the proton conductivity and power density, the best loading of muscovite in PBI membrane is 1 wt%. The performance comparisons among PBI/muscovite composite membranes and other inorganic materials based PBI membranes are summarized in Table 8.4, illustrating that the PBI/muscovite composite membranes have comparable performance with the literature. Additionally, as the muscovite used in this work is as-received state, this cheap and comparable performance may afford the promising commercialization in the area of inorganic-organic HT-PEMs.

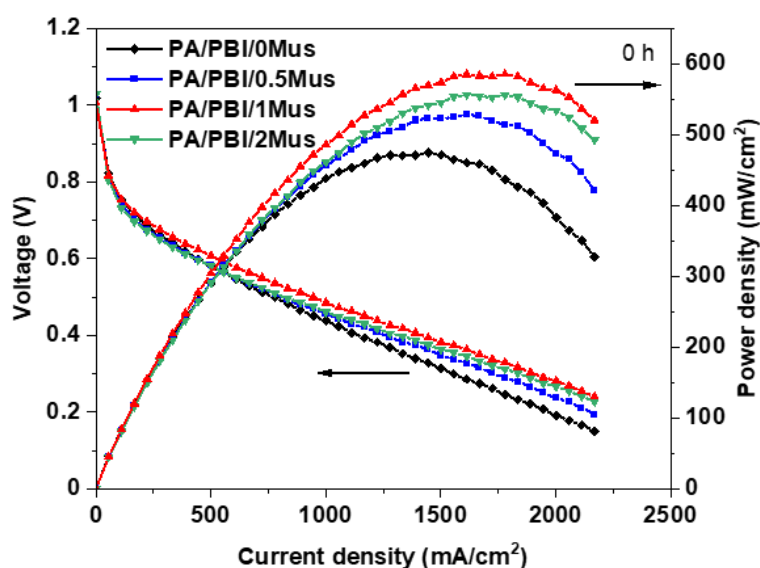


Fig. 8.9. Polarization curves of muscovite incorporated PBI membranes at 0 h.

Table 8.4. Performance comparison of PA doped PBI-based composite membrane without humidification.

Membranes	σ (mS cm^{-1})	Peak power density (mW cm^{-2})	Improvement in power density	Reference
-----------	-------------------------------------	---	---------------------------------	-----------

PA/PBI/1Mus	42.4	586 @ 150 °C	24%	This work
PBI/SiO ₂ /PA	86.6	250 @ 165 °C	20%	(221)
ABPBI/2S-Sep-1.92PA	51	230 @ 180 °C	28%	(33)
PBI/2%EGO	-	429 @ 150 °C	29%	(26)
m-PBI/Al-MCM-41	356	516 @ 160 °C	31%	(350)
PBI/SNP-PBI-10	50	650 @ 160 °C	25%	(222)
PBI-SGO 2 wt%	29.30	100 @ 150 °C	66%	(377)
F ₆ PBI(10)	2.14	498 @ 150 °C	38%	(178)

8.3.2 Accelerated stress test

The acid retention ability is also important as the acid leaching will deteriorate cell performance and durability (17). To evaluate the acid retention ability and check the durability of the membranes, a method which can test the durability in a shorter time (around 70 h), an accelerated stress test (AST) (running at 1.0 A cm⁻² for 16 min, at 0.6 A cm⁻² for 4 min, and at OCV for 10 min every 6 h) was chosen in this work (55). This AST method employs fuel cell running at high loads to produce a large amount of water vapor which may extract the acids and redistribute along the electrode. The acids will then be dragged from membrane to gas diffusion layer and flow field to result in acid loss (91). In addition to the factor of water extraction, the increased heat production at high working current may also accelerate the acid vaporization to result in acid loss (79, 88). Therefore, as this AST can lead to strong electrolyte leaching, especially when the cell is running at high current density, it is easy to assess the cell degradation (durability and acid retention ability) via this durability test. As presented in Fig. 8.10a, all membranes show degraded trend but with different decay rates at different current densities. The polarization curves and power density of the cell performance after 70 h AST were also measured (Fig. 8.10b). Interestingly, compared with the lowest power density of pure PBI membrane (319 mW cm⁻²) after 70 h AST, the PA/PBI/1Mus and PA/PBI/2Mus have almost the same power density (413 mW cm⁻²). In addition, from the high current density region of polarization curves, PA/PBI/0Mus and PA/PBI/0.5Mus suffer apparent mass transfer loss after running 70 h AST (378). This may be explained that the PA/PBI/0Mus and PA/PBI/0.5Mus membranes have the worst degradation in terms of acid loss from the electrodes (see later discussion in the EDS part) (355). The leached acid may increase the degree of carbon corrosion to cause the detachment between carbon support and catalysts, resulting in catalyst aggregation, loss of cathode void volume and porosity, and the

increase of cathode hydrophilicity (379, 380). The leached acid and the increased cathode hydrophilicity can cause acid flooding to get increased mass transfer loss.

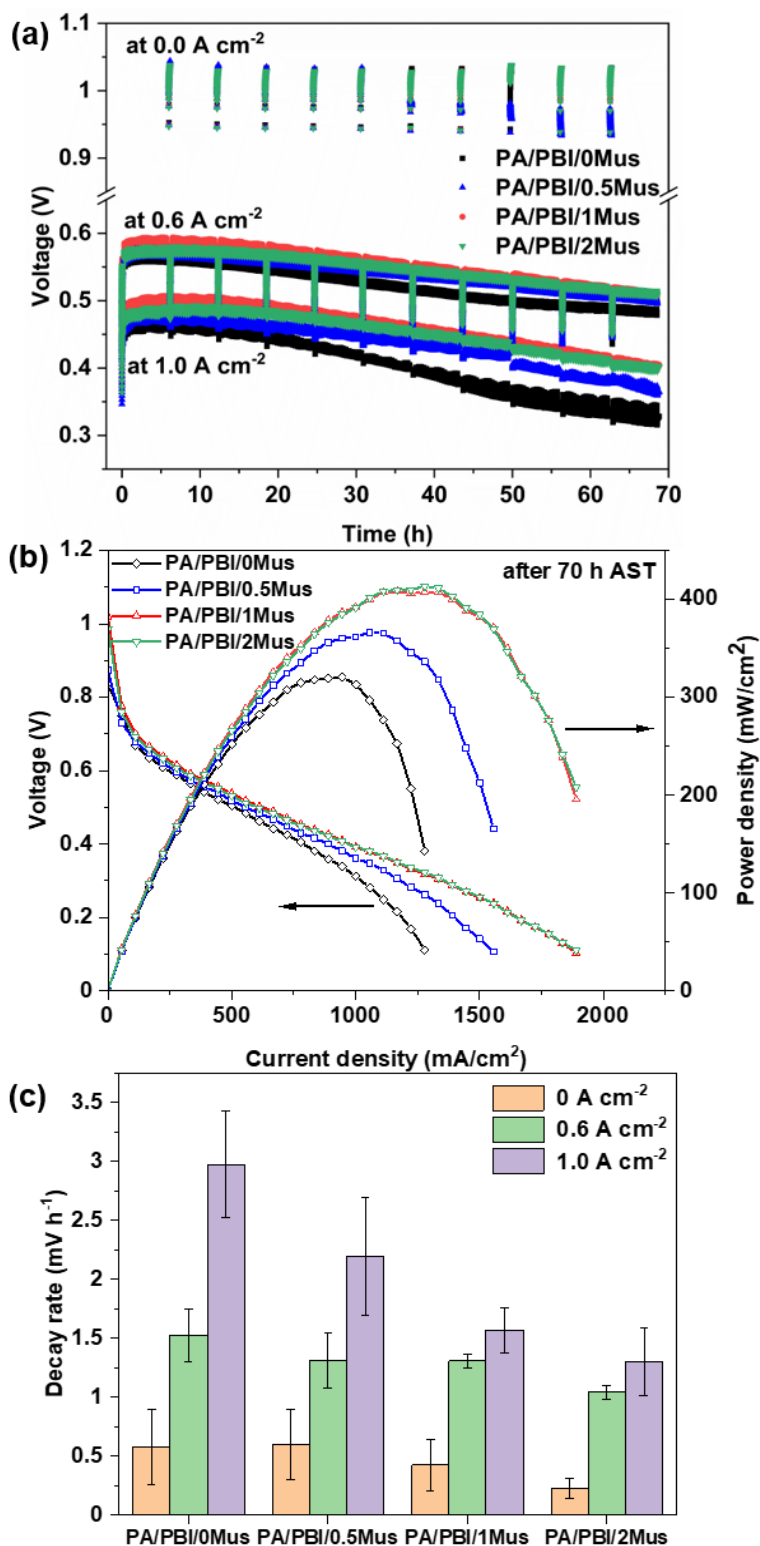


Fig. 8.10. (a) Durability test under AST conditions, (b) polarization curves after 70 h AST, and (c) decay rate at 0, 0.6, and 1.0 A cm⁻² of PA/PBI/xMus membranes at 150 °C without humidification.

Compared with the pristine PBI membrane with the highest decay rate (0.575 mV h^{-1} at OCV, 1.525 mV h^{-1} at 0.6 A cm^{-2} , 2.975 mV h^{-1} at 1.0 A cm^{-2}), the degradation rate of composite membranes decreases with the increasing loading of muscovite (Fig. 8.10c). For instance, the PA/PBI/2Mus suffers the lowest decay rate especially at high current density (0.226 mV h^{-1} at OCV, 1.042 mV h^{-1} at 0.6 A cm^{-2} , 1.298 mV h^{-1} at 1.0 A cm^{-2}), indicating the addition of muscovite can largely avoid PA leaching to alleviate performance degradation (55). Although the proton conductivity and power density are limited by the possible flake aggregation, PA/PBI/2Mus has promising durability and decay rate. This may be attributed to the trade-off between proton conductivity and acid retention ability of PA/PBI/2Mus. Moreover, oxidative degradation can also explain the deterioration of cell performance. Since muscovite has layered structures with large pore diameter (Table 7.3), the possible formation of the Mus-PA and Mus-PBI crosslinks in the interlayers and pores of muscovite can act as barriers to reduce acid loss and protect the PBI chains to alleviate performance degradation. Therefore, improved cell performance and durability were observed after the addition of muscovite into PBI membranes.

8.3.3 Hydrogen crossover

Since hydrogen crossover from the anode side to the cathode side can decrease fuel efficiency, lead to cathode potential depression, and produce harmful radicals (43), hydrogen permeability is an important factor to determine the membrane degradation. Therefore, LSV was conducted on the membranes before and after AST. As shown in Fig. 8.11a, the hydrogen crossover of all membranes before AST show almost the same. However, the PA/PBI/0Mus showed a large increase in hydrogen crossover current density after AST, while the hydrogen crossover of composite membranes showed barely any changes particularly when the muscovite loading is high (Fig. 8.11b), illustrating the pure PBI membrane suffers worst hydrogen crossover and this situation is alleviated in the composite membranes. Therefore, after the addition of muscovite, the PBI/muscovite composite membranes have better chemical stabilities than the pure PBI membrane, which is similar to Parnian's work (381). The reduced hydrogen crossover can be attributed to three reasons: (1) after the incorporation of muscovite into the membranes, the gas pathways through membranes will become tortuous because of the low porosity of muscovite ($0.04 \text{ cm}^3 \text{ g}^{-1}$ porosity in Table 7.3). (2) From the results of the swelling properties (Table 6.4), the reduced swelling volume of the acid doped composite membrane benefits the lower porosity than the pure membranes after PA doping, supporting the lower hydrogen crossover in the composite membranes. (3) Compared with the pure PBI membrane, the reduced membrane thinning of composite membranes after durability test (see later discussion in the EIS part) may be another factor to get reduced hydrogen crossover.

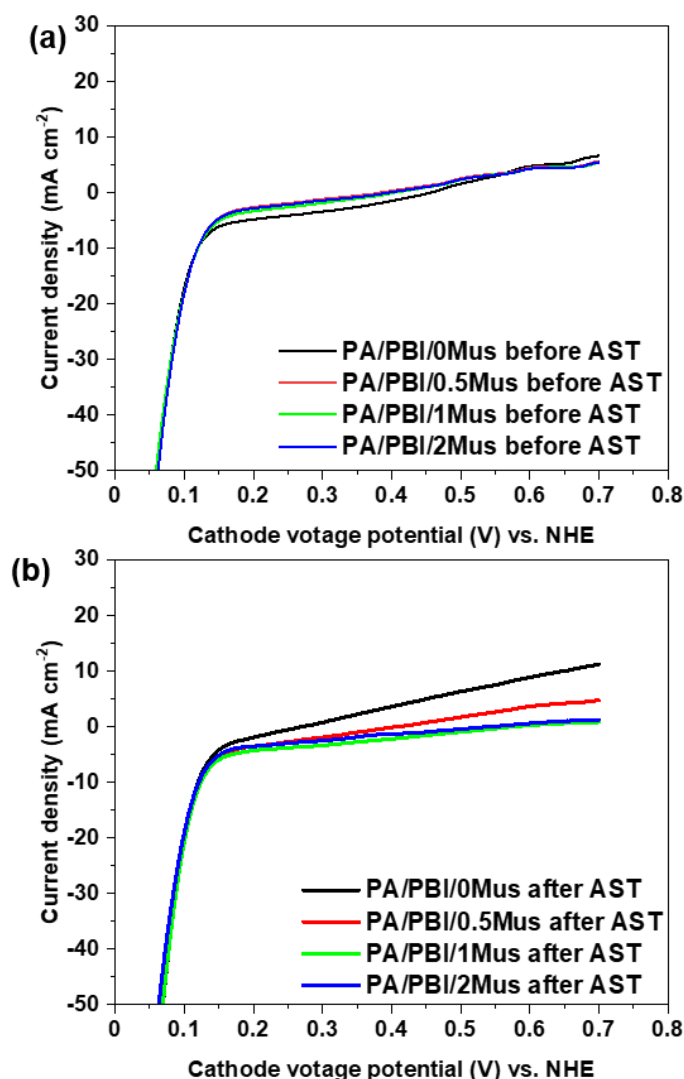


Fig. 8.11. Hydrogen crossover current densities of (a) PA/PBI/xMus membranes before AST and (b) PA/PBI/xMus membranes after AST.

8.3.4 Electrochemical characterizations of the membranes

To better understand the electrochemical properties of membranes, the EIS was performed before and after 70 h AST. The EIS spectra were fitted using the equivalent circuit (Fig. 2.7b). Usually, the EIS curves contain three loops: high frequency loop (anode charge transfer resistance), intermediate frequency loop (cathode charge transfer resistance) and low frequency loop (mass transfer resistance) (98). However, it seems only two arcs exist in these EIS curves (Fig. 8.12), which is not consistent with the apparent mass transfer loss in the membranes tested after 70 h AST (Fig. 8.10b). This is probably due to the instabilities such as acid content and reactant diffusion in the fuel cell (17, 382). All tested membranes after 70 h AST present reduced ohmic resistance and increased polarization resistance (the sum of anode and cathode charge transfer resistance and mass transfer resistance), which are consistent with our previous work (136).

Because the increased hydrogen crossover reflected by OCV and LSV (Fig. 8.10c and Fig. 8.11b) and possible membrane creep caused by clamping pressure on the MEA can lead to membrane thinning, the ohmic resistance of all membranes decreases. Meanwhile, the change in the ohmic resistance loss (Table 8.5 and Fig. 8.12) reduces with the increasing loading of muscovite, indicating that the addition of muscovite benefits the alleviation of membrane thinning. Moreover, as the acid leaching out of membranes can lead to the decrease of proton conductivity to get an increased membrane resistance, the reduced membrane resistance after 70 h AST in Fig. 8.12 illustrates acid leaching would not be the main factor for the membrane degradation. In terms of polarization resistance, the PA/PBI/0Mus has the largest increase from 0.2358 to 0.3308 $\Omega \text{ cm}^2$, indicating the pure PBI membrane suffers the worst degradation, which is also consistent with the deteriorated cell performance and pronounced mass transfer loss from Fig. 8.10b. The reason why the polarization resistance of pure PBI membrane suffers the worst will be discussed in the following section.

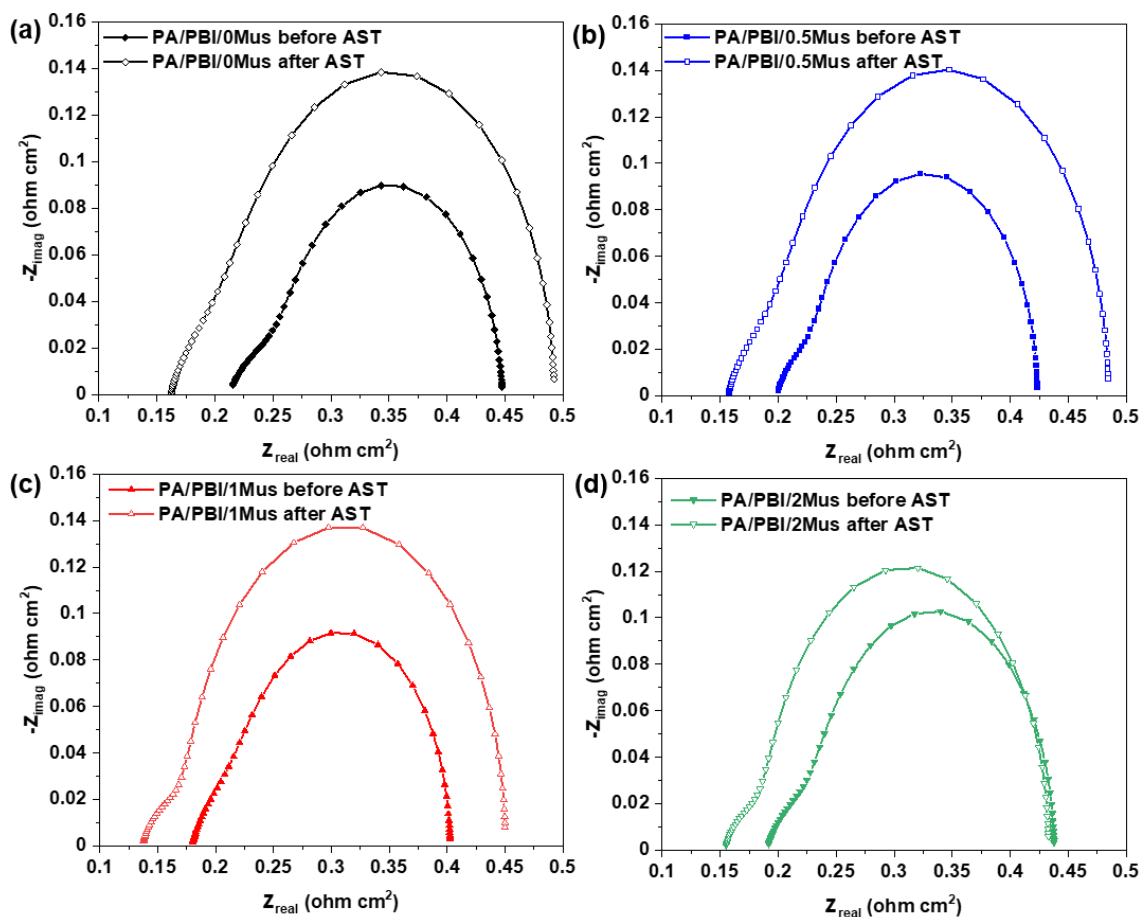


Fig. 8.12. EIS comparisons of (a) PA/PBI/0Mus, (b) PA/PBI/0.5Mus, (c) PA/PBI/1Mus, and (d) PA/PBI/2Mus before and after AST.

Table 8.5. Summary of ohmic resistance (R_0), anode charge transfer resistance (R_1), and the sum of cathode charge transfer resistance and mass transfer resistance (R_2) before and after durability test obtained from equivalent circuits.

Samples	R_0 ($\Omega \text{ cm}^2$)		R_1 ($\Omega \text{ cm}^2$)		R_2 ($\Omega \text{ cm}^2$)	
	Before AST	After AST	Before AST	After AST	Before AST	After AST
PBI/0Mus/PA	0.2153	0.1625	0.0573	0.0746	0.1785	0.2572
PBI/0.5Mus/PA	0.1991	0.1565	0.0405	0.0606	0.1698	0.2678
PBI/1Mus/PA	0.1793	0.1366	0.0534	0.0427	0.1698	0.2709
PBI/2Mus/PA	0.1919	0.1551	0.0513	0.0403	0.1964	0.2387

8.3.5 Phosphorus distribution of the composite membranes after durability test

The membrane with poor acid retention will result in reduced three-phase zone with less catalyst active area and make the proton transfer more difficult to get increased polarization resistances (355, 383, 384). Because PA/PBI/2Mus showed the smallest increase in polarization resistance after AST (Fig. 8.12a-d), we suppose that the composite membranes have better acid retention ability when the amount of muscovite is higher. To validate this assumption, the phosphorus distribution after 70 h AST achieved by EDS was performed to characterize the cross-sections of MEA. As shown in Fig. 8.13, the dark colours such as blue and black indicate less intensities of phosphorus while the bright colours such as white and pink represent more phosphorus. Compared with the cathode GDL (lower side) with less acid, all the anode GDL (upper side) contains more acids. This can be explained that the water produced in cathode side can accelerate more acid leaching than that in the anode side. Moreover, Fig. 8.13 also shows that the membrane with higher amount of muscovite has lower phosphorus loss. This demonstrates that the membrane with higher muscovite loading has better acid retention ability. The sufficient acid in the composite membrane and electrode will act as essential proton carriers during the operation of fuel cells, and this phenomenon will be more notable in the membrane with more muscovite loadings. Furthermore, since the composite membrane with the increasing loading of muscovite filler has better acid retention ability, it seems that the acid concentration in the interfaces between membrane and the catalyst layers also increases with the increase of muscovite loading (Fig. 8.13). As the leached acids distributed in the interfaces help to form three-phase zones to reduce polarization resistance, the composite membranes with higher muscovite loadings can facilitate

the better durability which is in accordance with the reduced decay rate in Fig. 8.10c. While the EDS mapping is considered semi-quantitative and there are no big differences between different MEAs with different membranes, the results predict a trend that the addition of muscovite can successfully alleviate the acid leaching out of the membranes. The less leached acid in composite membrane will have reduced negative impacts on catalyst degradation and the increase of polarization resistance. Therefore, compared with the pure PBI membrane, the composite membrane with higher muscovite loading has less leached acids to get better durability.

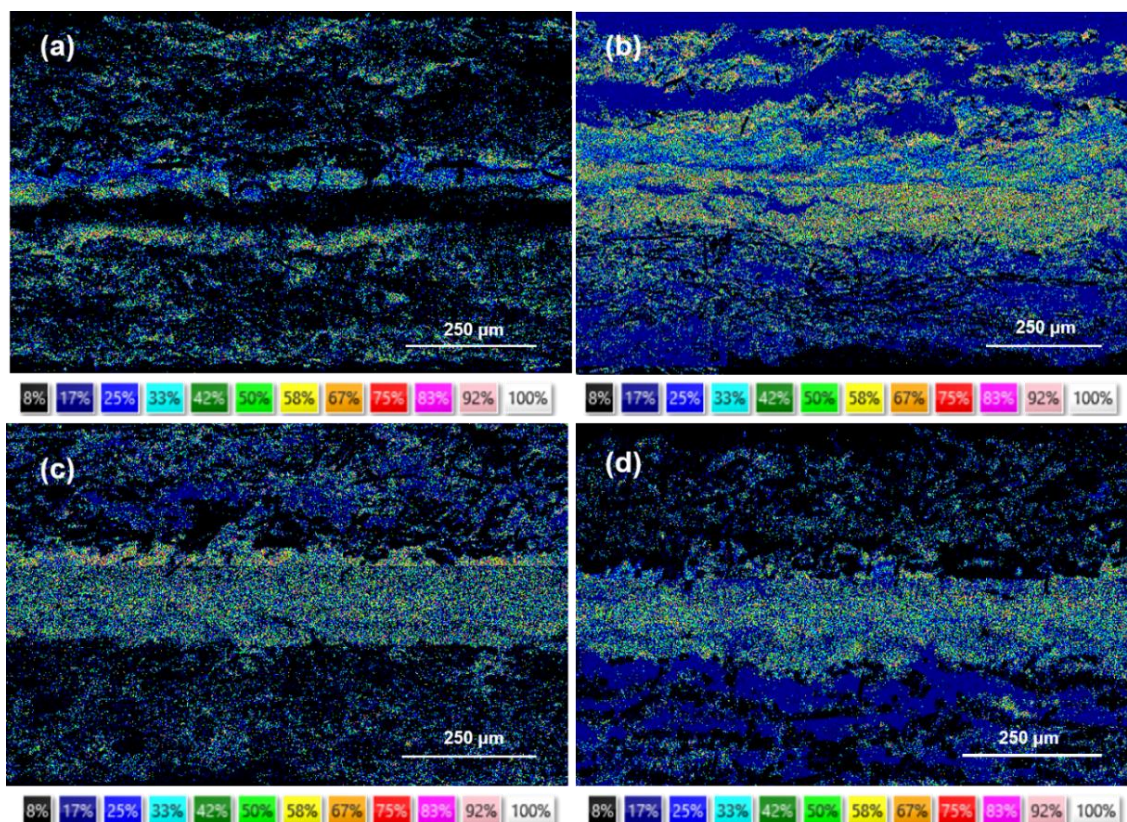


Fig. 8.13. Phosphorus distribution of the cross-sectional MEAs with (a) PA/PBI/0Mus, (b) PA/PBI/0.5Mus, (c) PA/PBI/1Mus, and (d) PA/PBI/2Mus after 70 h AST.

8.3.6 Investigation of interactions between muscovite and phosphoric acid

To investigate why muscovite can increase acid retention ability of the composite membranes, the interactions between muscovite and PA were characterized by TGA and XPS. Firstly, 5 g muscovite was added into 85% PA solution and stirred at room temperature for 24 h. Afterwards, the mixture was rinsed with deionized water and absolute ethanol until pH 7. The mixture was then dried under vacuum at 70 °C overnight to obtain PA absorbed muscovite, named as P-muscovite. The TGA curves in Fig. 8.14a show muscovite and P-muscovite have a slightly different thermal stability. The weight loss of P-muscovite occurs when the temperature rises above around 160 °C, suggesting that the amount of absorbed PA in P-muscovite is around 0.5 wt% and the strong interactions between PA molecules and muscovite meet the temperature

requirement in HT-PEMFCs. Abukhadra (295) proposed the chemical interaction and electrostatic attractions are the main forces between muscovite/phillipsite composite and phosphate ions. In this work, to analyse the mechanism for phosphoric acid retention ability of PBI/muscovite membranes, the content of surface hydroxyl groups in P-muscovite was also carried out by XPS. Since the surface hydroxyl groups of muscovite have strong interactions with PA molecules to get reduced available OH groups on the muscovite surface, the percentage of surface hydroxyl groups decreased from 55.98% in muscovite (Fig. 7.4b) to 33.37% in P-muscovite (Fig. 8.14b). Therefore, from the XPS results, the formation of electrostatic attractions between muscovite and PA molecules is the main mechanism to retain PA molecules inside the composite membrane to get improved acid retention ability. In detail, the improved acid retention ability of the PA doped composite membrane can be due to two processes (367). After the first process of dissociation of PA molecules from H_3PO_4 to H_2PO_4^- , the H_2PO_4^- molecules can interact with the surface hydroxyl groups of muscovite and bind to the muscovite surface to create Mus-PA crosslinks. These two processes can lead to the formation of delocalized protons and Mus-PA crosslinks, and further improve the ionic conductivity and acid retention ability in the composite membranes.

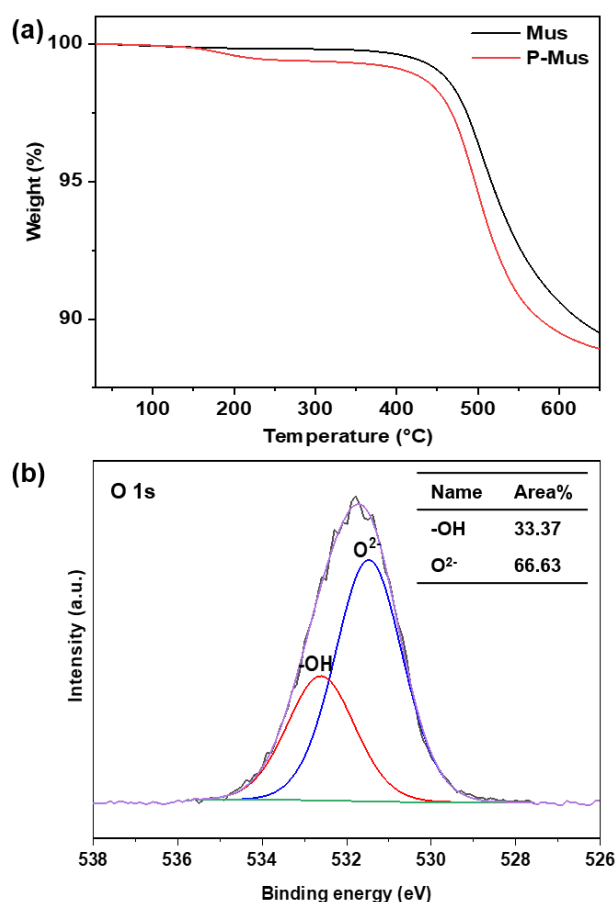


Fig. 8.14. (a) TGA curves of muscovite and P-muscovite. XPS O 1s spectra of (b) P-muscovite.

8.4 Conclusion to this chapter

In this chapter, an inorganic clay material, muscovite, was incorporated into PBI membranes by the doctor blade method to explore the effect of clay addition into HT-PEMs on the acid leaching issue. Because hygroscopic layered muscovite and its surface hydroxyl groups benefit the formation of Mus-PA and Mus-PBI crosslinks to interact with PA molecules and polymer chains, the acid retention ability, proton conductivity and the durability of PBI/muscovite composite membranes were enhanced. The PBI membrane with 1 wt% muscovite shows maximum proton conductivity of 42.4 mS cm^{-1} and highest power density of 586 mW cm^{-2} at 150°C without humidification, whilst the composite membranes show improved durability with the increase of muscovite loading. Compared with the PA/PBI/0Mus (0.575 mV h^{-1} at OCV, 1.525 mV h^{-1} at 0.6 A cm^{-2} , 2.975 mV h^{-1} at 1.0 A cm^{-2}), the PA/PBI/2Mus has the lowest decay rate (0.226 mV h^{-1} at OCV, 1.042 mV h^{-1} at 0.6 A cm^{-2} , 1.298 mV h^{-1} at 1.0 A cm^{-2}) over 70 h AST. In addition, the deactivation mechanisms of the organic-inorganic composite membranes are explored by several in-situ and ex-situ methods. The results from LSV and EIS illustrated the composite membranes have better chemical stabilities than the pure PBI membrane. It was also found that acid leaching is not the main problem in terms of membrane degradation but has a negative impact on the catalyst degradation. Based on the results from EDS, TGA and XPS, the Mus-PA crosslinks could improve the acid retention ability of PBI/muscovite composite membranes to alleviate catalyst degradation. These results indicate a great potential of cheap muscovite as a filler material in HT-PEMs and propose feasible characterization methods to investigate the deactivation mechanisms of the fuel cell performance.

Chapter 9: Conclusion and future prospect

9.1 Summary

In this work, the main objective is focused on the performance enhancement of phosphoric acid (PA) doped high-temperature proton exchange membranes (HT-PEMs). The main learnings of this PhD thesis work are summarized in three subsections as follows.

9.1.1 Optimization of the preparation procedures of PES-PVP membrane

The polyethersulfone-polyvinylpyrrolidone (PES-PVP) membrane was chosen as the HT-PEM due to its simple preparation and reduced environmentally harmful synthesis method. The optimal preparation condition of PES-PVP membranes was firstly studied according to different polymer molecular weights and different polymer mixing methods. It was found that the membranes using high-molecular-weight polymer or indirect mixing method had better chemical stability and durability than the high-molecular-weight or direct-mixing membranes.

9.1.2 Improvement of SN and muscovite incorporated PES-PVP membranes

Cheap clay-based fillers including silica nanosheets (SN), exfoliated SN, sulfonated SN and muscovite, were incorporated into PES-PVP membranes. Benefiting from the surface functional groups (hydroxyl or sulfonic groups) and layered structures of inorganic fillers that enable the formation of additional proton-transferring pathways and protect the intercalated polymer chains from radical attacking, the inorganic-organic membranes displayed enhanced power density and durability. These improvements illustrated that these inorganic fillers are the potential promising clay-based materials in HT-PEMs.

9.1.3 Investigation of acid retention ability of clay added HT-PEMs

As polybenzimidazole (PBI) membranes have a longer lifetime, the as-received muscovite was added into PBI membranes to explore the possible mechanisms why the addition of clay-based fillers can alleviate acid leaching and enhance cell performance. Due to the formation of Mus-PBI and Mus-PA crosslinks, the composite membranes have enhanced mechanical strength, reduced dimensional swelling, improved power density and durability. The decreased ohmic resistance and increased polarization resistance after durability test are related to the membrane thinning and the loss of catalyst active area, respectively. The strong interactions between muscovite and PA molecules lead to improved acid retention ability, thus less leached acid from the composite membrane reduces the negative effects on the catalyst degradation to alleviate degradation on cell performance and durability.

9.2 Conclusion

To the best of the author's knowledge, the optimization of the preparation procedure of PES-PVP membranes is the first work in scientific literature involving the use of different polymer molecular weights and polymer mixing methods. On top of this, the addition of cheap clay-based fillers (silica nanosheets and muscovite) into HT-PEMs brings significant advantages to the previously reported approaches in terms of fuel cell performance and scalability potential. Additionally, very good quality of durability and acid retention ability in HT-PEMs have been achieved via adding the clay-based filler, as proven by several in-situ and ex-situ characterization methods, named as linear sweep voltammetry, electrochemical impedance spectroscopy, accelerated stress test, elemental mapping using Energy Dispersive X-ray Spectroscopy, X-ray photoelectron spectroscopy and thermogravimetric analysis.

This original work on development of new PES-PVP membranes and inorganic-organic composite membranes should serve mainly as: (i) the PES-PVP membranes using high-molecular-weight polymers and indirect-mixing method can be used as one of potential cheap HT-PEMs; (ii) this proof-of-concept study could open the way to future developments including alleviating acid leaching by incorporating cheap clay-based fillers, and setting a basis and practical guidelines to characterize acid leaching which may motivate further research in the field.

9.3 Future prospects

Suggestions for future work are divided in five areas described below.

9.3.1 Molecular modelling

As demonstrated in chapter 5, the membrane using high-molecular-weight polymer or indirect-mixing method had better membrane properties and cell performance. However, the understanding why these membranes prepared using different preparation methods performed differently should be explored in terms of microstructure at the molecular level. Different preparation methods may result in different arrangements of polymer chains in membranes. The molecular modelling may offer a solution to figure out why these membranes with the same elements and chemical bonds showed different performances.

9.3.2 Filler functionalization

Filler functionalization can introduce functional groups onto the surface of inorganic fillers to strengthen the interactions with polymer chains and PA molecules. In future work, SN and muscovite can be functionalized by carboxylic acid, protic ionic liquids, heteropoly acids or phosphonic acid to investigate the effect of different functional groups on the membrane properties and fuel cell performance.

9.3.3 Filler alignment in membranes

Clay-based fillers which contain proton-conducting groups (hydroxyl groups and sulfonic groups) proved that the filler-PA and filler-polymer crosslinks could get improved performances. Nevertheless, as the protons pass faster through the membrane in a through-plane direction, the unordered distribution of fillers can result in uncontrollable crosslinks in inorganic-organic membranes to get longer proton pathway. Consequently, through-plane alignment of fillers would offer a shorter proton pathway and better interactions with polymer chains and PA molecules to achieve upgraded proton conductivity and mechanical properties. Many approaches such as applying electric field alignment and magnetic field alignment or using freeze casting might offer possible through-plane filler alignment to promote the performance of HT-PEMs.

9.3.4 Filler functionalized polymer

No matter how high degree of functionalization in inorganic fillers, the interactions between fillers and polymer chains or PA molecules are hydrogen bonds which can easily form phase separation and voids in membranes. The attempt to connect inorganic fillers with organic polymers using stronger chemical bonding interactions can be the future direction. For instance, the growth of polymers on the surface of fillers or employing in-situ synthesis of polymers to connect with the functional groups of the filler surface using covalent bonds can be explored.

9.3.5 Selection of clay-based filler using machine learning

This thesis demonstrated that the incorporation of vermiculite and muscovite into HT-PEMs can improve the membrane and fuel cell performances. It will be worth to explore other potential clay-based fillers in HT-PEMs. After analysing the structure of all related clay-based fillers, machine learning can be utilized to get the optimal clay structure which may offer a promising application in HT-PEMs.

9.3.6 In-situ analysis for inorganic-organic membranes

PA leaching from the membrane is regarded as the main degradation mechanism of HT-PEMFCs. The addition of different clay-based fillers into membranes in this work is to improve the chemical and mechanical stabilities, as well as the acid retention ability of HT-PEMs. However, the acid leaching happened in operando HT-PEMFCs using different inorganic-organic HT-PEMs is not fully understood and studied. Meanwhile, the distribution of different forms of PA anions inside MEAs is still unclear. In situ X-ray absorption spectroscopy, operando neutron imaging and operando X-ray computed tomography can be combined to explore how the different forms of PA anions diffuse in the MEAs, how the electrochemical performance fluctuates (using in-situ electrochemical techniques such as polarization, electrochemical impedance spectroscopy, and cyclic voltammetry) during fuel cell operations, and how the current density and hot spots form or distribute among ribs, channels and the current collectors.

References

1. Thomas JM, Edwards PP, Dobson PJ, Owen GP. Decarbonising energy: The developing international activity in hydrogen technologies and fuel cells. *J Energy Chem.* 2020.
2. Eriksson ELV, Gray EM. Optimization and integration of hybrid renewable energy hydrogen fuel cell energy systems – A critical review. *Appl Energ.* 2017;202:348-64.
3. Larminie J, Dicks A, McDonald MS. Fuel cell systems explained: J. Wiley Chichester, UK; 2003.
4. Michele Bozzolo GF, Philippe Gorse, Benjamin Oszfolk. Moving towards climate neutrality – fuel cell technology for future energy and propulsion systems 2020 [Available from: <https://www.mtu-solutions.com/au/en/technical-articles/2020/moving-towards-climate-neutrality-fuel-cell-technology-for-future-energy-and-propulsion-systems.html>].
5. Iqbal MZ, Rehman A-U, Siddique S. Prospects and challenges of graphene based fuel cells. *J Energy Chem.* 2019;39:217-34.
6. Wang S, Jiang SP. Prospects of fuel cell technologies. *National Science Review.* 2017;4(2):163-6.
7. Bose S, Kuila T, Thi XLN, Kim NH, Lau KT, Lee JH. Polymer membranes for high temperature proton exchange membrane fuel cell: Recent advances and challenges. *Progress in Polymer Science.* 2011;36(6):813-43.
8. Li Q, Jensen JO, Savinell RF, Bjerrum NJ. High temperature proton exchange membranes based on polybenzimidazoles for fuel cells. *Progress in polymer science.* 2009;34(5):449-77.
9. Hong BK, Kim SH. Recent advances in fuel cell electric vehicle technologies of Hyundai. *Ecs Transactions.* 2018;86(13):3.
10. Yoshida T, Kojima K. Toyota MIRAI fuel cell vehicle and progress toward a future hydrogen society. *The Electrochemical Society Interface.* 2015;24(2):45.
11. Tanaka S, Nagumo K, Yamamoto M, Chiba H, Yoshida K, Okano R. Fuel cell system for Honda CLARITY fuel cell. *eTransportation.* 2020;3:100046.
12. Kwon K, Yoo DY, Park JO. Experimental factors that influence carbon monoxide tolerance of high-temperature proton-exchange membrane fuel cells. *Journal of Power Sources.* 2008;185(1):202-6.
13. Valdes-Lopez VF, Mason T, Shearing PR, Brett DJL. Carbon monoxide poisoning and mitigation strategies for polymer electrolyte membrane fuel cells - A review. *Prog Energ Combust.* 2020;79.
14. Asensio JA, Sanchez EM, Gomez-Romero P. Proton-conducting membranes based on benzimidazole polymers for high-temperature PEM fuel cells. A chemical quest. *Chemical Society Reviews.* 2010;39(8):3210-39.
15. Yang JS, Li QF, Cleemann LN, Jensen JO, Pan C, Bjerrum NJ, et al. Crosslinked Hexafluoropropylidene Polybenzimidazole Membranes with Chloromethyl Polysulfone for Fuel Cell Applications. *Advanced Energy Materials.* 2013;3(5):622-30.
16. Hu MS, Ni JP, Zhang BP, Neelakandan S, Wang L. Crosslinked polybenzimidazoles containing branching structure as membrane materials with excellent cell performance and durability for fuel cell applications. *Journal of Power Sources.* 2018;389:222-9.

17. Kannan A, Aili D, Cleemann LN, Li QF, Jensen JO. Three-layered electrolyte membranes with acid reservoir for prolonged lifetime of high-temperature polymer electrolyte membrane fuel cells. *International Journal of Hydrogen Energy*. 2020;45(1):1008-17.
18. Zhang J, Aili D, Bradley J, Kuang HH, Pan C, De Marco R, et al. In Situ Formed Phosphoric Acid/Phosphosilicate Nanoclusters in the Exceptional Enhancement of Durability of Polybenzimidazole Membrane Fuel Cells at Elevated High Temperatures. *J Electrochem Soc*. 2017;164(14):F1615-F25.
19. Özdemir Y, Üregen N, Devrim Y. Polybenzimidazole based nanocomposite membranes with enhanced proton conductivity for high temperature PEM fuel cells. *International Journal of Hydrogen Energy*. 2017;42(4):2648-57.
20. Lee S, Seo K, Ghorpade RV, Nam K-H, Han H. High temperature anhydrous proton exchange membranes based on chemically-functionalized titanium/polybenzimidazole composites for fuel cells. *Materials Letters*. 2020;263:127167.
21. Nasef MM, Fujigaya T, Abouzari-Lotf E, Nakashima N, Yang Z. Enhancement of performance of pyridine modified polybenzimidazole fuel cell membranes using zirconium oxide nanoclusters and optimized phosphoric acid doping level. *international journal of hydrogen energy*. 2016;41(16):6842-54.
22. Hooshyari K, Moradi M, Salarizadeh P. Novel nanocomposite membranes based on PBI and doped-perovskite nanoparticles as a strategy for improving PEMFC performance at high temperatures. *Int J Energ Res*. 2020;44(4):2617-33.
23. Hooshyari K, Rezaia H, Vatanpour V, Salarizadeh P, Askari MB, Beydaghi H, et al. High temperature membranes based on PBI/sulfonated polyimide and doped-perovskite nanoparticles for PEM fuel cells. *Journal of Membrane Science*. 2020;612:118436.
24. Sun P, Li Z, Jin L, Wang S, Yin X. Construction of proton channels and reinforcement of physicochemical properties of oPBI/FeSPP/GF high temperature PEM via building hydrogen bonding network. *International Journal of Hydrogen Energy*. 2017;42(21):14572-82.
25. Wang S, Sun P, Li Z, Liu G, Yin X. Comprehensive performance enhancement of polybenzimidazole based high temperature proton exchange membranes by doping with a novel intercalated proton conductor. *International Journal of Hydrogen Energy*. 2018;43(21):9994-10003.
26. Chen J, Perez-Page M, Ji Z, Zhang Z, Guo Z, Holmes S. One step electrochemical exfoliation of natural graphite flakes into graphene oxide for polybenzimidazole composite membranes giving enhanced performance in high temperature fuel cells. *Journal of Power Sources*. 2021;491:229550.
27. Ray SS, Okamoto M. Polymer/layered silicate nanocomposites: a review from preparation to processing. *Progress in polymer science*. 2003;28(11):1539-641.
28. Plackett D, Siu A, Li Q, Pan C, Jensen JO, Nielsen SF, et al. High-temperature proton exchange membranes based on polybenzimidazole and clay composites for fuel cells. *Journal of membrane science*. 2011;383(1-2):78-87.
29. Ublekov F, Penchev H, Georgiev V, Radev I, Sinigersky V. Protonated montmorillonite as a highly effective proton-conductivity enhancer in p-PBI membranes for PEM fuel cells. *Materials Letters*. 2014;135:5-7.
30. Singha S, Koyilapu R, Dana K, Jana T. Polybenzimidazole-Clay Nanocomposite Membrane for PEM fuel cell: Effect of organomodifier structure. *Polymer*. 2019;167:13-20.

31. Ghosh S, Sannigrahi A, Maity S, Jana T. Role of clays structures on the polybenzimidazole nanocomposites: potential membranes for the use in polymer electrolyte membrane fuel cell. *The Journal of Physical Chemistry C*. 2011;115(23):11474-83.
32. Zhang X, Fu X, Yang S, Zhang Y, Zhang R, Hu S, et al. Design of sepiolite-supported ionogel-embedded composite membranes without proton carrier wastage for wide-temperature-range operation of proton exchange membrane fuel cells. *J Mater Chem A*. 2019;7(25):15288-301.
33. Zhang XX, Liu QT, Xia L, Huang DY, Fu XD, Zhang R, et al. Poly(2,5-benzimidazole)/sulfonated sepiolite composite membranes with low phosphoric acid doping levels for PEMFC applications in a wide temperature range. *Journal of Membrane Science*. 2019;574:282-98.
34. Grove WR. LXXII. On a gaseous voltaic battery. *The London, Edinburgh, and Dublin Philosophical Magazine and Journal of Science*. 1842;21(140):417-20.
35. Andújar JM, Segura F. Fuel cells: History and updating. A walk along two centuries. *Renewable and sustainable energy reviews*. 2009;13(9):2309-22.
36. Hoogers G. *Fuel cell technology handbook*: CRC press; 2002.
37. Zhang J, Xia Z, Dai L. Carbon-based electrocatalysts for advanced energy conversion and storage. *Science advances*. 2015;1(7):e1500564.
38. Lucia U. Carnot efficiency: why? *Physica A: Statistical Mechanics and its Applications*. 2013;392(17):3513-7.
39. Aili D, Bjerrum N, Christensen E, Li Q, Berg R, Bleha M, et al. Proton conducting polymeric materials for hydrogen based electrochemical energy conversion technologies. 2011.
40. Zhang J, Tang Y, Song C, Zhang J, Wang H. PEM fuel cell open circuit voltage (OCV) in the temperature range of 23 C to 120 C. *Journal of power sources*. 2006;163(1):532-7.
41. Ma TY, Dai S, Jaroniec M, Qiao SZ. Metal–organic framework derived hybrid Co₃O₄-carbon porous nanowire arrays as reversible oxygen evolution electrodes. *Journal of the American Chemical Society*. 2014;136(39):13925-31.
42. Kim O-H, Cho Y-H, Kang SH, Park H-Y, Kim M, Lim JW, et al. Ordered macroporous platinum electrode and enhanced mass transfer in fuel cells using inverse opal structure. *Nature communications*. 2013;4(1):1-9.
43. Cheng X, Zhang JL, Tang YH, Song CJ, Shen J, Song DT, et al. Hydrogen crossover in high-temperature PEM fuel cells. *Journal of Power Sources*. 2007;167(1):25-31.
44. Shan J, Gazdzicki P, Lin R, Schulze M, Friedrich KA. Local resolved investigation of hydrogen crossover in polymer electrolyte fuel cell. *Energy*. 2017;128:357-65.
45. Jung A, Oh J, Han K, Kim MS. An experimental study on the hydrogen crossover in polymer electrolyte membrane fuel cells for various current densities. *Applied Energy*. 2016;175:212-7.
46. Guo Z, Chen J, Byun JJ, Perez–Page M, Ji Z, Zhao Z, et al. Insights into the performance and degradation of polybenzimidazole/muscovite composite membranes in high-temperature proton exchange membrane fuel cells. *Journal of Membrane Science*. 2022;641:119868.
47. Holmes SM, Balakrishnan P, Kalangi VS, Zhang X, Lozada-Hidalgo M, Ajayan PM, et al. 2D crystals significantly enhance the performance of a working fuel cell. *Advanced Energy Materials*. 2017;7(5):1601216.

48. Pei P, Wu Z, Li Y, Jia X, Chen D, Huang S. Improved methods to measure hydrogen crossover current in proton exchange membrane fuel cell. *Applied Energy*. 2018;215:338-47.
49. Wu J, Yuan XZ, Wang H, Blanco M, Martin JJ, Zhang J. Diagnostic tools in PEM fuel cell research: Part I Electrochemical techniques. *International journal of hydrogen energy*. 2008;33(6):1735-46.
50. Ramani V, Kunz H, Fenton J. Stabilized composite membranes and membrane electrode assemblies for elevated temperature/low relative humidity PEFC operation. *Journal of power sources*. 2005;152:182-8.
51. Center FSE. Procedure for performing PEM single cell testing. Test Protocol for Cell Performance Tests Performed Under DOE Contract# DE-FC36-06G016028 vol DOE# DE-FC36-06G016028 US Department of Energy, Arlington, Virginia. 2009.
52. Yuan X-ZR, Song C, Wang H, Zhang J. *Electrochemical impedance spectroscopy in PEM fuel cells: fundamentals and applications*: Springer Science & Business Media; 2009.
53. Bardini L. EIS 101, an introduction to electrochemical spectroscopy. What was a website is now available as a self-contained PDF Available online: https://www.researchgate.net/publication/280009629_EIS_101_an_introduction_to_electrochemical_spectroscopy_What_was_a_website_is_now_available_as_a_selfcontained_PDF (accessed on 24 April 2020). 2015.
54. Zhao J, Li X. A review of polymer electrolyte membrane fuel cell durability for vehicular applications: Degradation modes and experimental techniques. *Energy Conversion and Management*. 2019;199:112022.
55. Schonvogel D, Rastedt M, Wagner P, Wark M, Dyck A. Impact of accelerated stress tests on high temperature PEMFC degradation. *Fuel Cells*. 2016;16(4):480-9.
56. Bandlamudi V, Bujlo P, Linkov V, Pasupathi S. The effect of potential cycling on high temperature PEM fuel cell with different flow field designs. *Fuel Cells*. 2019;19(3):231-43.
57. Ahn C-Y, Park JE, Kim S, Kim O-H, Hwang W, Her M, et al. Differences in the Electrochemical Performance of Pt-Based Catalysts Used for Polymer Electrolyte Membrane Fuel Cells in Liquid Half-and Full-Cells. *Chemical Reviews*. 2021.
58. Leng Y, Ming P, Yang D, Zhang C. Stainless steel bipolar plates for proton exchange membrane fuel cells: Materials, flow channel design and forming processes. *Journal of Power Sources*. 2020;451:227783.
59. Song Y, Zhang C, Ling C-Y, Han M, Yong R-Y, Sun D, et al. Review on current research of materials, fabrication and application for bipolar plate in proton exchange membrane fuel cell. *International Journal of Hydrogen Energy*. 2020;45(54):29832-47.
60. Marappan M, Palaniswamy K, Velumani T, Chul KB, Velayutham R, Shivakumar P, et al. Performance Studies of Proton Exchange Membrane Fuel Cells with Different Flow Field Designs–Review. *The Chemical Record*. 2021;21(4):663-714.
61. Su H, Xu Q, Chong J, Li H, Sita C, Pasupathi S. Eliminating micro-porous layer from gas diffusion electrode for use in high temperature polymer electrolyte membrane fuel cell. *Journal of Power Sources*. 2017;341:302-8.
62. Park S, Lee J-W, Popov BN. A review of gas diffusion layer in PEM fuel cells: Materials and designs. *International Journal of Hydrogen Energy*. 2012;37(7):5850-65.
63. El-Kharouf A, Mason TJ, Brett DJ, Pollet BG. Ex-situ characterisation of gas diffusion layers for proton exchange membrane fuel cells. *Journal of Power Sources*. 2012;218:393-404.

64. Niblett D, Niasar V, Holmes S. Enhancing the performance of fuel cell gas diffusion layers using ordered microstructural design. *Journal of The Electrochemical Society*. 2019;167(1):013520.
65. Wang C, Spendelow JS. Recent developments in Pt–Co catalysts for proton-exchange membrane fuel cells. *Current Opinion in Electrochemistry*. 2021;28(LA-UR-20-25517).
66. Qiao Z, Wang C, Li C, Zeng Y, Hwang S, Li B, et al. Atomically dispersed single iron sites for promoting Pt and Pt 3 Co fuel cell catalysts: performance and durability improvements. *Energy & Environmental Science*. 2021;14(9):4948-60.
67. Thompson ST, Papageorgopoulos D. Platinum group metal-free catalysts boost cost competitiveness of fuel cell vehicles. *Nature Catalysis*. 2019;2(7):558-61.
68. Kregar A, Kravos A, Kutrašnik T. Methodology for evaluation of contributions of Ostwald ripening and particle agglomeration to growth of catalyst particles in PEM fuel cells. *Fuel Cells*. 2020;20(4):487-98.
69. Dhanasekaran P, Shukla A, Selvaganesh SV, Mohan S, Bhat S. Silica-decorated carbon-Pt electrocatalyst synthesis via single-step polyol method for superior polymer electrolyte fuel cell performance, durability and stack operation under low relative humidity. *Journal of Power Sources*. 2019;438:226999.
70. Esfahani RAM, Easton EB. Exceptionally durable Pt/TOMS catalysts for fuel cells. *Applied Catalysis B: Environmental*. 2020;268:118743.
71. Su H, Pasupathi S, Bladergroen B, Linkov V, Pollet BG. Optimization of gas diffusion electrode for polybenzimidazole-based high temperature proton exchange membrane fuel cell: evaluation of polymer binders in catalyst layer. *International journal of hydrogen energy*. 2013;38(26):11370-8.
72. Xu X, Wang H, Lu S, Guo Z, Rao S, Xiu R, et al. A novel phosphoric acid doped poly (ethersulphone)-poly (vinyl pyrrolidone) blend membrane for high-temperature proton exchange membrane fuel cells. *Journal of Power Sources*. 2015;286:458-63.
73. Kim S, Myles TD, Kunz HR, Kwak D, Wang Y, Maric R. The effect of binder content on the performance of a high temperature polymer electrolyte membrane fuel cell produced with reactive spray deposition technology. *Electrochimica Acta*. 2015;177:190-200.
74. Lee WJ, Lee JS, Park H-Y, Park HS, Lee SY, Song KH, et al. Improvement of fuel cell performances through the enhanced dispersion of the PTFE binder in electrodes for use in high temperature polymer electrolyte membrane fuel cells. *International Journal of Hydrogen Energy*. 2020;45(57):32825-33.
75. Hogarth WH, Da Costa JD, Lu GM. Solid acid membranes for high temperature (> 140° C) proton exchange membrane fuel cells. *Journal of Power Sources*. 2005;142(1-2):223-37.
76. Dicks AL, Rand DA. *Fuel cell systems explained*: John Wiley & Sons; 2018.
77. Peighambardoust SJ, Rowshanzamir S, Amjadi M. Review of the proton exchange membranes for fuel cell applications. *International journal of hydrogen energy*. 2010;35(17):9349-84.
78. Jung H-Y, Kim JW. Role of the glass transition temperature of Nafion 117 membrane in the preparation of the membrane electrode assembly in a direct methanol fuel cell (DMFC). *International Journal of Hydrogen Energy*. 2012;37(17):12580-5.
79. Guo Z, Perez–Page M, Chen J, Ji Z, Holmes SM. Recent advances in phosphoric acid–based membranes for high–temperature proton exchange membrane fuel cells. *Journal of Energy Chemistry*. 2021.

80. Xing BZ, Savadogo O. The effect of acid doping on the conductivity of polybenzimidazole (PBI). *J New Mat Electr Sys*. 1999;2(2):95-101.
81. Wu X, Scott K. A H₂SO₄ Loaded Polybenzimidazole (PBI) Membrane for High Temperature PEMFC. *Fuel Cells*. 2012;12(4):583-8.
82. Vilčiauskas L, Tuckerman ME, Bester G, Paddison SJ, Kreuer K-D. The mechanism of proton conduction in phosphoric acid. *Nature chemistry*. 2012;4(6):461-6.
83. Ma YL, Wainright JS, Litt MH, Savinell RF. Conductivity of PBI membranes for high-temperature polymer electrolyte fuel cells. *J Electrochem Soc*. 2004;151(1):A8-A16.
84. Lang S, Kazdal TJ, Kühl F, Hampe MJ. Experimental investigation and numerical simulation of the electrolyte loss in a HT-PEM fuel cell. *International Journal of Hydrogen Energy*. 2015;40(2):1163-72.
85. Jeong YH, Oh K, Ahn S, Kim NY, Byeon A, Park H-Y, et al. Investigation of electrolyte leaching in the performance degradation of phosphoric acid-doped polybenzimidazole membrane-based high temperature fuel cells. *Journal of Power Sources*. 2017;363:365-74.
86. Mori T, Honji A, Kahara T, Hishinuma Y. Acid Absorbancy of an Electrode and Its Cell Performance History. *J Electrochem Soc*. 1988;135(5):1104-9.
87. Li QF, He RH, Berg RW, Hjuler HA, Bjerrum NJ. Water uptake and acid doping of polybenzimidazoles as electrolyte membranes for fuel cells. *Solid State Ionics*. 2004;168(1-2):177-85.
88. Yu S, Xiao L, Benicewicz B. Durability studies of PBI-based high temperature PEMFCs. *Fuel Cells*. 2008;8(3-4):165-74.
89. Lee KS, Spendelow JS, Choe YK, Fujimoto C, Kim YS. An operationally flexible fuel cell based on quaternary ammonium-biphosphate ion pairs. *Nat Energy*. 2016;1.
90. Lee AS, Choe YK, Matanovic I, Kim YS. The energetics of phosphoric acid interactions reveals a new acid loss mechanism. *J Mater Chem A*. 2019;7(16):9867-76.
91. Eberhardt SH, Toulec M, Marone F, Stampanoni M, Büchi F, Schmidt TJ. Dynamic operation of HT-PEFC: in-operando imaging of phosphoric acid profiles and (Re) distribution. *Journal of the Electrochemical Society*. 2015;162(3):F310.
92. Maity S, Singha S, Jana T. Low acid leaching PEM for fuel cell based on polybenzimidazole nanocomposites with protic ionic liquid modified silica. *Polymer*. 2015;66:76-85.
93. Oh HS, Cho Y, Lee WH, Kim H. Modification of electrodes using Al₂O₃ to reduce phosphoric acid loss and increase the performance of high-temperature proton exchange membrane fuel cells. *J Mater Chem A*. 2013;1(7):2578-81.
94. Sondergaard T, Cleemann LN, Becker H, Aili D, Steenberg T, Hjuler HA, et al. Long-term durability of HT-PEM fuel cells based on thermally cross-linked polybenzimidazole. *Journal of Power Sources*. 2017;342:570-8.
95. Kannan A, Li Q, Cleemann LN, Jensen JO. Acid Distribution and Durability of HT-PEM Fuel Cells with Different Electrode Supports. *Fuel Cells*. 2018;18(2):103-12.
96. Oono Y, Sounai A, Hori M. Long-term cell degradation mechanism in high-temperature proton exchange membrane fuel cells. *Journal of Power Sources*. 2012;210:366-73.

97. Halter J, Bevilacqua N, Zeis R, Schmidt T, Büchi F. The impact of the catalyst layer structure on phosphoric acid migration in HT-PEFC—An operando X-ray tomographic microscopy study. *Journal of Electroanalytical Chemistry*. 2020;859:113832.
98. Araya SS, Zhou F, Liso V, Sahlin SL, Vang JR, Thomas S, et al. A comprehensive review of PBI-based high temperature PEM fuel cells. *International Journal of Hydrogen Energy*. 2016;41(46):21310-44.
99. Liao JH, Li QF, Rudbeck HC, Jensen JO, Chromik A, Bjerrum NJ, et al. Oxidative Degradation of Polybenzimidazole Membranes as Electrolytes for High Temperature Proton Exchange Membrane Fuel Cells. *Fuel Cells*. 2011;11(6):745-55.
100. Inaba M, Kinumoto T, Kiriake M, Umebayashi R, Tasaka A, Ogumi Z. Gas crossover and membrane degradation in polymer electrolyte fuel cells. *Electrochimica Acta*. 2006;51(26):5746-53.
101. Wu JF, Yuan XZ, Martin JJ, Wang HJ, Zhang JJ, Shen J, et al. A review of PEM fuel cell durability: Degradation mechanisms and mitigation strategies. *Journal of Power Sources*. 2008;184(1):104-19.
102. Ghassemzadeh L, Kreuer K-D, Maier J, Müller K. Chemical degradation of Nafion membranes under mimic fuel cell conditions as investigated by solid-state NMR spectroscopy. *The Journal of Physical Chemistry C*. 2010;114(34):14635-45.
103. Mench MM, Kumbur EC, Veziroglu TN. *Polymer electrolyte fuel cell degradation*: Academic Press; 2011.
104. Prabhakaran V, Arges CG, Ramani V. Investigation of polymer electrolyte membrane chemical degradation and degradation mitigation using in situ fluorescence spectroscopy. *P Natl Acad Sci USA*. 2012;109(4):1029-34.
105. Ghassemzadeh L, Kreuer KD, Maier J, Muller K. Evaluating chemical degradation of proton conducting perfluorosulfonic acid ionomers in a Fenton test by solid-state F-19 NMR spectroscopy. *Journal of Power Sources*. 2011;196(5):2490-7.
106. Zaton M, Roziere J, Jones DJ. Current understanding of chemical degradation mechanisms of perfluorosulfonic acid membranes and their mitigation strategies: a review. *Sustain Energ Fuels*. 2017;1(3):409-38.
107. Yang JS, Li QF, Jensen JO, Pan C, Cleemann LN, Bjerrum NJ, et al. Phosphoric acid doped imidazolium polysulfone membranes for high temperature proton exchange membrane fuel cells. *Journal of Power Sources*. 2012;205:114-21.
108. Stevens MP. *Polymer chemistry : an introduction*. Oxford: Oxford University Press; 2009.
109. He RH, Li QF, Bach A, Jensen JO, Bjerrum NJ. Physicochemical properties of phosphoric acid doped polybenzimidazole membranes for fuel cells. *Journal of Membrane Science*. 2006;277(1-2):38-45.
110. Mauritz KA, Moore RB. State of understanding of Nafion. *Chem Rev*. 2004;104(10):4535-85.
111. Subianto S, Pica M, Casciola M, Cojocaru P, Merlo L, Hards G, et al. Physical and chemical modification routes leading to improved mechanical properties of perfluorosulfonic acid membranes for PEM fuel cells. *Journal of Power Sources*. 2013;233:216-30.
112. Vielstich W. *Handbook of fuel cells : fundamentals, technology, and applications*. 2010.
113. Kundu S, Simon LC, Fowler M, Grot S. Mechanical properties of Nafion electrolyte membranes under hydrated conditions. *Polymer*. 2005;46(25):11707-15.

114. Rodgers MP, Bonville LJ, Kunz HR, Slattery DK, Fenton JM. Fuel cell perfluorinated sulfonic acid membrane degradation correlating accelerated stress testing and lifetime. *Chem Rev.* 2012;112(11):6075-103.
115. Chen X, Qian G, Molle MA, Benicewicz BC, Ploehn HJ. High temperature creep behavior of phosphoric acid-polybenzimidazole gel membranes. *Journal of Polymer Science Part B: Polymer Physics.* 2015;53(21):1527-38.
116. Liao J, Li Q, Rudbeck H, Jensen JO, Chromik A, Bjerrum N, et al. Oxidative degradation of polybenzimidazole membranes as electrolytes for high temperature proton exchange membrane fuel cells. *Fuel Cells.* 2011;11(6):745-55.
117. Villa DC, Angioni S, Dal Barco S, Mustarelli P, Quartarone E. Polysulfonated Fluoro-oxyPBI Membranes for PEMFCs: An Efficient Strategy to Achieve Good Fuel Cell Performances with Low H₃PO₄ Doping Levels. *Advanced Energy Materials.* 2014;4(11).
118. Lu CL, Chang CP, Guo YH, Yeh TK, Su YC, Wang PC, et al. High-performance and low-leakage phosphoric acid fuel cell with synergic composite membrane stacking of micro glass microfiber and nano PTFE. *Renew Energ.* 2019;134:982-8.
119. Jang J, Kim DH, Ahn MK, Min CM, Lee SB, Byun J, et al. Phosphoric acid doped triazole-containing cross-linked polymer electrolytes with enhanced stability for high-temperature proton exchange membrane fuel cells. *Journal of Membrane Science.* 2020;595.
120. Tang QW, Qian GQ, Huang K. H₃PO₄-imbibed three-dimensional polyacrylamide/polyacrylamide hydrogel as a high-temperature proton exchange membrane with excellent acid retention. *Rsc Adv.* 2012;2(27):10238-44.
121. Tang QW, Huang K, Qian GQ, Benicewicz BC. Phosphoric acid-imbibed three-dimensional polyacrylamide/poly(vinyl alcohol) hydrogel as a new class of high-temperature proton exchange membrane. *Journal of Power Sources.* 2013;229:36-41.
122. Tang QW, Yuan SS, Cai HY. High-temperature proton exchange membranes from microporous polyacrylamide caged phosphoric acid. *J Mater Chem A.* 2013;1(3):630-6.
123. Pu HT, Wang L, Pan HY, Wan DC. Synthesis and Characterization of Fluorine-Containing Polybenzimidazole for Proton Conducting Membranes in Fuel Cells. *J Polym Sci Pol Chem.* 2010;48(10):2115-22.
124. Sana B, Jana T. Polybenzimidazole composite with acidic surfactant like molecules: A unique approach to develop PEM for fuel cell. *Eur Polym J.* 2016;84:421-34.
125. Hooshyari K, Javanbakht M, Shabanikia A, Enhessari M. Fabrication BaZrO₃/PBI-based nanocomposite as a new proton conducting membrane for high temperature proton exchange membrane fuel cells. *Journal of Power Sources.* 2015;276:62-72.
126. Ooi YX, Ya KZ, Maegawa K, Tan WK, Kawamura G, Muto H, et al. Incorporation of titanium pyrophosphate in polybenzimidazole membrane for medium temperature dry PEFC application. *Solid State Ionics.* 2020;344.
127. Lobato J, Canizares P, Rodrigo MA, Ubada D, Pinar FJ. Promising TiOSO₄ Composite Polybenzimidazole-Based Membranes for High Temperature PEMFCs. *Chemsuschem.* 2011;4(10):1489-97.
128. Pinar FJ, Canizares P, Rodrigo MA, Ubada D, Lobato J. Long-term testing of a high-temperature proton exchange membrane fuel cell short stack operated with improved polybenzimidazole-based composite membranes. *Journal of Power Sources.* 2015;274:177-85.
129. Pu HT, Liu L, Chang ZH, Yuan JJ. Organic/inorganic composite membranes based on polybenzimidazole and nano-SiO₂. *Electrochimica Acta.* 2009;54(28):7536-41.

130. Li XB, Ma HW, Wang P, Liu ZC, Peng JW, Hu W, et al. Construction of High-Performance, High-Temperature Proton Exchange Membranes through Incorporating SiO₂ Nanoparticles into Novel Cross-linked Polybenzimidazole Networks. *Acs Appl Mater Inter*. 2019;11(34):30735-46.
131. Chu FQ, Lin BC, Qiu B, Si ZH, Qiu LH, Gu ZZ, et al. Polybenzimidazole/zwitterion-coated silica nanoparticle hybrid proton conducting membranes for anhydrous proton exchange membrane application. *J Mater Chem*. 2012;22(35):18411-7.
132. Cheng Y, Zhang J, Lu S, Kuang H, Bradley J, De Marco R, et al. High CO tolerance of new SiO₂ doped phosphoric acid/polybenzimidazole polymer electrolyte membrane fuel cells at high temperatures of 200–250° C. *International Journal of Hydrogen Energy*. 2018;43(49):22487-99.
133. Cheng Y, Zhang J, Lu S. Significantly enhanced performance of direct methanol fuel cells at elevated temperatures. *Journal of Power Sources*. 2020;450:227620.
134. Qiu X, Ueda M, Hu HY, Sui YG, Zhang X, Wang LJ. Poly(2,5-benzimidazole)-Grafted Graphene Oxide as an Effective Proton Conductor for Construction of Nanocomposite Proton Exchange Membrane. *Acs Appl Mater Inter*. 2017;9(38):33049-58.
135. Singha S, Jana T. Influence of interfacial interactions on the properties of polybenzimidazole/clay nanocomposite electrolyte membrane. *Polymer*. 2016;98:20-31.
136. Guo Z, Chen J, Byun JJ, Cai R, Perez–Page M, Sahoo M, et al. High–performance polymer electrolyte membranes incorporated with 2D silica nanosheets in high–temperature proton exchange membrane fuel cells. *J Energy Chem*. 2021;64:323-34.
137. Lobato J, Canizares P, Rodrigo MA, Ubada D, Pinar FJ. Enhancement of the fuel cell performance of a high temperature proton exchange membrane fuel cell running with titanium composite polybenzimidazole-based membranes. *Journal of Power Sources*. 2011;196(20):8265-71.
138. Pinar FJ, Canizares P, Rodrigo MA, Ubada D, Lobato J. Titanium composite PBI-based membranes for high temperature polymer electrolyte membrane fuel cells. Effect on titanium dioxide amount. *Rsc Adv*. 2012;2(4):1547-56.
139. Mustarelli P, Quartarone E, Grandi S, Carollo A, Magistris A. Polybenzimidazole-Based Membranes as a Real Alternative to Nafion for Fuel Cells Operating at Low Temperature. *Adv Mater*. 2008;20(7):1339-43.
140. Uregen N, Pehlivanoglu K, Ozdemir Y, Devrim Y. Development of polybenzimidazole/graphene oxide composite membranes for high temperature PEM fuel cells. *International Journal of Hydrogen Energy*. 2017;42(4):2636-47.
141. Si ZH, Gu FL, Guo JN, Yan F. Phosphoric Acid-Doped Imidazolium Ionomers with Enhanced Stability for Anhydrous Proton-Exchange Membrane Applications. *J Polym Sci Pol Phys*. 2013;51(17):1311-7.
142. Hu M, Li T, Neelakandan S, Wang L, Chen Y. Cross-linked polybenzimidazoles containing hyperbranched cross-linkers and quaternary ammoniums as high-temperature proton exchange membranes: Enhanced stability and conductivity. *Journal of Membrane Science*. 2020;593:117435.
143. Liu FX, Wang S, Chen H, Li JS, Tian X, Wang X, et al. Cross-Linkable Polymeric Ionic Liquid Improve Phosphoric Acid Retention and Long-Term Conductivity Stability in Polybenzimidazole Based PEMs. *Acs Sustain Chem Eng*. 2018;6(12):16352-62.
144. Li JS, Wang S, Liu FX, Tian X, Wang X, Chen H, et al. HT-PEMs based on nitrogen-heterocycle decorated poly (arylene ether ketone) with enhanced proton conductivity and excellent stability. *International Journal of Hydrogen Energy*. 2018;43(33):16248-57.

145. Venugopalan G, Chang K, Nijoka J, Livingston S, Geise GM, Arges CG. Stable and Highly Conductive Polycation-Polybenzimidazole Membrane Blends for Intermediate Temperature Polymer Electrolyte Membrane Fuel Cells. *Acs Appl Energ Mater*. 2020;3(1):573-85.
146. Berber MR, Fujigaya T, Sasaki K, Nakashima N. Remarkably Durable High Temperature Polymer Electrolyte Fuel Cell Based on Poly(vinylphosphonic acid)-doped Polybenzimidazole. *Sci Rep-Uk*. 2013;3.
147. Berber MR, Fujigaya T, Nakashima N. High-Temperature Polymer Electrolyte Fuel Cell Using Poly(vinylphosphonic acid) as an Electrolyte Shows a Remarkable Durability. *Chemcatchem*. 2014;6(2):567-71.
148. Wang D, Wang S, Tian X, Li JS, Liu FX, Wang X, et al. Ethyl phosphoric acid grafted amino-modified polybenzimidazole with improved long-term stability for high-temperature proton exchange membrane applications. *International Journal of Hydrogen Energy*. 2020;45(4):3176-85.
149. Krueger RA, Vilciauskas L, Melchior JP, Bester G, Kreuer KD. Mechanism of Efficient Proton Conduction in Diphosphoric Acid Elucidated via First-Principles Simulation and NMR. *J Phys Chem B*. 2015;119(52):15866-75.
150. Collier A, Wang HJ, Yuan XZ, Zhang JJ, Wilkinson DP. Degradation of polymer electrolyte membranes. *International Journal of Hydrogen Energy*. 2006;31(13):1838-54.
151. Xie HX, Tao D, Ni JP, Xiang XZ, Gao CM, Wang L. Synthesis and properties of highly branched star-shaped sulfonated block polymers with sulfoalkyl pendant groups for use as proton exchange membranes. *Journal of Membrane Science*. 2016;497:55-66.
152. Gittleman CS, Coms FD, Lai Y-H. Membrane durability: physical and chemical degradation. *Polymer electrolyte fuel cell degradation*. 2012:15-88.
153. Li QF, Rudbeck HC, Chromik A, Jensen JO, Pan C, Steenberg T, et al. Properties, degradation and high temperature fuel cell test of different types of PBI and PBI blend membranes. *Journal of Membrane Science*. 2010;347(1-2):260-70.
154. Yang JS, Li QF, Cleemann LN, Xu CX, Jensen JO, Pan C, et al. Synthesis and properties of poly(aryl sulfone benzimidazole) and its copolymers for high temperature membrane electrolytes for fuel cells. *J Mater Chem*. 2012;22(22):11185-95.
155. Wang YY, Xu JM, Zang H, Wang Z. Synthesis and properties of sulfonated poly(arylene ether ketone sulfone) containing amino groups/functional titania inorganic particles hybrid membranes for fuel cells. *International Journal of Hydrogen Energy*. 2019;44(12):6136-47.
156. Gao CM, Hu MS, Wang L, Wang L. Synthesis and Properties of Phosphoric-Acid-Doped Polybenzimidazole with Hyperbranched Cross-Linkers Decorated with Imidazolium Groups as High-Temperature Proton Exchange Membranes. *Polymers-Basel*. 2020;12(3).
157. Shen CH, Jheng LC, Hsu SLC, Wang JTW. Phosphoric acid-doped cross-linked porous polybenzimidazole membranes for proton exchange membrane fuel cells. *J Mater Chem*. 2011;21(39):15660-5.
158. Wang J, Zheng JF, Zhao Z, Zhang SB. Synthesis and characterization of a novel poly(arylene ether sulfone) containing pendent imidazole groups for high temperature proton exchange membranes. *J Mater Chem*. 2012;22(42):22706-12.
159. Li Q, Liu L, Liang SE, Li QB, Jin BK, Bai RK. A novel poly(2,6-dimethyl-1,4-phenylene oxide) with pendant imidazolium groups for high-temperature proton exchange membrane. *Polym Chem-Uk*. 2014;5(7):2425-32.

160. Jiang JJ, Zhu XY, Qian HD, Xu JF, Yue ZY, Zou ZQ, et al. Cross-linked sulfonated poly(ether ether ketone) electrolytes bearing pendent imidazole groups for high temperature proton exchange membrane fuel cells. *Sustain Energy Fuels*. 2019;3(9):2426-34.
161. Pan HY, Chen SX, Zhang YY, Jin M, Chang ZH, Pu HT. Preparation and properties of the cross-linked sulfonated polyimide containing benzimidazole as electrolyte membranes in fuel cells. *Journal of Membrane Science*. 2015;476:87-94.
162. Wang S, Zhang G, Han MM, Li HT, Zhang Y, Ni J, et al. Novel epoxy-based cross-linked polybenzimidazole for high temperature proton exchange membrane fuel cells. *International Journal of Hydrogen Energy*. 2011;36(14):8412-21.
163. Han MM, Zhang G, Liu ZG, Wang SA, Li MY, Zhu J, et al. Cross-linked polybenzimidazole with enhanced stability for high temperature proton exchange membrane fuel cells. *J Mater Chem*. 2011;21(7):2187-93.
164. Yang JS, Xu YX, Liu PP, Gao LP, Che QT, He RH. Epoxides cross-linked hexafluoropropylidene polybenzimidazole membranes for application as high temperature proton exchange membranes. *Electrochimica Acta*. 2015;160:281-7.
165. Yang JS, Aili D, Li QF, Cleemann LN, Jensen JO, Bjerrum NJ, et al. Covalently Cross-Linked Sulfone Polybenzimidazole Membranes with Poly(Vinylbenzyl Chloride) for Fuel Cell Applications. *Chemsuschem*. 2013;6(2):275-82.
166. Wang S, Zhao CJ, Ma WJ, Zhang N, Liu ZG, Zhang G, et al. Macromolecular cross-linked polybenzimidazole based on bromomethylated poly (aryl ether ketone) with enhanced stability for high temperature fuel cell applications. *Journal of Power Sources*. 2013;243:102-9.
167. Zhang N, Zhao CJ, Ma WJ, Wang S, Wang BL, Zhang G, et al. Macromolecular covalently cross-linked quaternary ammonium poly(ether ether ketone) with polybenzimidazole for anhydrous high temperature proton exchange membranes. *Polym Chem-Uk*. 2014;5(17):4939-47.
168. Yue ZY, Cai YB, Xu SA. Phosphoric acid-doped cross-linked sulfonated poly (imide-benzimidazole) for proton exchange membrane fuel cell applications. *Journal of Membrane Science*. 2016;501:220-7.
169. Shen CH, Hsu SLC. Synthesis of novel cross-linked polybenzimidazole membranes for high temperature proton exchange membrane fuel cells. *Journal of Membrane Science*. 2013;443:138-43.
170. Zhang N, Wang BL, Zhao CJ, Zhang YR, Bu FZ, Cui Y, et al. Dual cross-linked organic-inorganic hybrid polymer electrolyte membranes based on quaternized poly(ether ether ketone) and (3-aminopropyl)triethoxysilane. *Journal of Power Sources*. 2015;275:815-22.
171. Wang S, Zhao CJ, Ma WJ, Zhang N, Zhang YR, Zhang G, et al. Silane-cross-linked polybenzimidazole with improved conductivity for high temperature proton exchange membrane fuel cells. *J Mater Chem A*. 2013;1(3):621-9.
172. Yue ZY, Cai YB, Xu SA. Phosphoric acid-doped organic-inorganic cross-linked sulfonated poly(imide-benzimidazole) for high temperature proton exchange membrane fuel cells. *International Journal of Hydrogen Energy*. 2016;41(24):10421-9.
173. Wang S, Zhao CJ, Ma WJ, Zhang G, Liu ZG, Ni J, et al. Preparation and properties of epoxy-cross-linked porous polybenzimidazole for high temperature proton exchange membrane fuel cells. *Journal of Membrane Science*. 2012;411:54-63.
174. Ni JP, Hu MS, Liu D, Xie HX, Xiang XZ, Wang L. Synthesis and properties of highly branched polybenzimidazoles as proton exchange membranes for high-temperature fuel cells. *J Mater Chem C*. 2016;4(21):4814-21.

175. Wang L, Ni JP, Liu D, Gong CL, Wang L. Effects of branching structures on the properties of phosphoric acid-doped polybenzimidazole as a membrane material for high-temperature proton exchange membrane fuel cells. *International Journal of Hydrogen Energy*. 2018;43(34):16694-703.
176. Wang L, Wu YN, Fang ML, Chen JL, Liu XT, Yin BB, et al. Synthesis and preparation of branched block polybenzimidazole membranes with high proton conductivity and single-cell performance for use in high temperature proton exchange membrane fuel cells. *Journal of Membrane Science*. 2020;602.
177. Wang L, Liu ZR, Liu Y, Wang L. Crosslinked polybenzimidazole containing branching structure with no sacrifice of effective N-H sites: Towards high-performance high-temperature proton exchange membranes for fuel cells. *Journal of Membrane Science*. 2019;583:110-7.
178. Ooi YX, Ya KZ, Maegawa K, Tan WK, Kawamura G, Muto H, et al. CHS-WSiA doped hexafluoropropylidene-containing polybenzimidazole composite membranes for medium temperature dry fuel cells. *International Journal of Hydrogen Energy*. 2019;44(60):32201-9.
179. Hazarika M, Jana T. Novel proton exchange membrane for fuel cell developed from blends of polybenzimidazole with fluorinated polymer. *Eur Polym J*. 2013;49(6):1564-76.
180. Chen JC, Chen PY, Lee SW, Liou GL, Chen CJ, Lan YH, et al. Synthesis of soluble polybenzimidazoles for high-temperature proton exchange membrane fuel cell (PEMFC) applications. *React Funct Polym*. 2016;108:122-9.
181. Chen JC, Chen PY, Liu YC, Chen KH. Polybenzimidazoles containing bulky substituents and ether linkages for high-temperature proton exchange membrane fuel cell applications. *Journal of Membrane Science*. 2016;513:270-9.
182. Li X, Qian G, Chen X, Benicewicz BC. Synthesis and Characterization of a New Fluorine-Containing Polybenzimidazole (PBI) for Proton-Conducting Membranes in Fuel Cells. *Fuel Cells*. 2013;13(5):832-42.
183. Mack F, Aniol K, Ellwein C, Kerres J, Zeis R. Novel phosphoric acid-doped PBI-blends as membranes for high-temperature PEM fuel cells. *J Mater Chem A*. 2015;3(20):10864-74.
184. Muthuraja P, Prakash S, Shanmugam VM, Manisankar P. Stable nanofibrous poly(aryl sulfone ether benzimidazole) membrane with high conductivity for high temperature PEM fuel cells. *Solid State Ionics*. 2018;317:201-9.
185. Lee SY, Kang NR, Shin DW, Lee CH, Lee KS, Guiver MD, et al. Morphological transformation during cross-linking of a highly sulfonated poly(phenylene sulfide nitrile) random copolymer. *Energ Environ Sci*. 2012;5(12):9795-802.
186. Yuan Q, Sun GH, Han KF, Yu JH, Zhu H, Wang ZM. Copolymerization of 4-(3,4-diaminophenoxy)-benzoic acid and 3,4-diaminobenzoic acid towards H₃PO₄-doped PBI membranes for proton conductor with better processability. *Eur Polym J*. 2016;85:175-86.
187. Singha S, Jana T. Effect of composition on the properties of PEM based on polybenzimidazole and poly(vinylidene fluoride) blends. *Polymer*. 2014;55(2):594-601.
188. Angioni S, Villa DC, Dal Barco S, Quartarone E, Righetti PP, Tomasi C, et al. Polysulfonation of PBI-based membranes for HT-PEMFCs: a possible way to maintain high proton transport at a low H₃PO₄ doping level. *J Mater Chem A*. 2014;2(3):663-71.
189. Wu YZ, Zhu WH. Organic sensitizers from D-pi-A to D-A-pi-A: effect of the internal electron-withdrawing units on molecular absorption, energy levels and photovoltaic performances. *Chemical Society Reviews*. 2013;42(5):2039-58.

190. Muthuraja P, Prakash S, Shanmugam VM, Radhakrishnan S, Manisankar P. Novel perovskite structured calcium titanate-PBI composite membranes for high-temperature PEM fuel cells: Synthesis and characterizations. *International Journal of Hydrogen Energy*. 2018;43(9):4763-72.
191. Qian W, Shang YM, Wang SB, Xie XF, Mao ZQ. Phosphoric acid doped composite membranes from poly (2,5-benzimidazole) (ABPBI) and Cs₂H₃-xPW₁₂O₄₀/CeO₂ for the high temperature PEMFC. *International Journal of Hydrogen Energy*. 2013;38(25):11053-9.
192. Tian X, Wang S, Li JS, Liu FX, Wang X, Chen H, et al. Composite membranes based on polybenzimidazole and ionic liquid functional Si-O-Si network for HT-PEMFC applications. *International Journal of Hydrogen Energy*. 2017;42(34):21913-21.
193. Liu F, Wang S, Li J, Tian X, Wang X, Chen H, et al. Polybenzimidazole/ionic-liquid-functional silica composite membranes with improved proton conductivity for high temperature proton exchange membrane fuel cells. *Journal of Membrane Science*. 2017;541:492-9.
194. Hao J, Jiang Y, Gao X, Xie F, Shao Z, Yi B. Degradation reduction of polybenzimidazole membrane blended with CeO₂ as a regenerative free radical scavenger. *Journal of Membrane Science*. 2017;522:23-30.
195. Tartaglione G, Tabuani D, Camino G. Thermal and morphological characterisation of organically modified sepiolite. *Micropor Mesopor Mat*. 2008;107(1-2):161-8.
196. Beauger C, Laine G, Burr A, Taguet A, Otazaghine B, Rigacci A. Nafion (R)-sepiolite composite membranes for improved proton exchange membrane fuel cell performance. *Journal of Membrane Science*. 2013;430:167-79.
197. Çalı A, Şahin A, Ar İ. Incorporating sepiolite and kaolinite to improve the performance of SPEEK composite membranes for proton exchange membrane fuel cells. *The Canadian Journal of Chemical Engineering*. 2020;98(4):892-904.
198. Babu S, Velez A, Wozniak K, Szydłowska J, Seal S. Electron paramagnetic study on radical scavenging properties of ceria nanoparticles. *Chem Phys Lett*. 2007;442(4-6):405-8.
199. Kerres J, Atanasov V. Cross-linked PBI-based high-temperature membranes: Stability, conductivity and fuel cell performance. *International Journal of Hydrogen Energy*. 2015;40(42):14723-35.
200. Subianto S. Recent advances in polybenzimidazole/phosphoric acid membranes for high-temperature fuel cells. *Polym Int*. 2014;63(7):1134-44.
201. Yang JS, Gao LP, Wang J, Xu YX, Liu C, He RH. Strengthening Phosphoric Acid Doped Polybenzimidazole Membranes with Siloxane Networks for Using as High Temperature Proton Exchange Membranes. *Macromol Chem Phys*. 2017;218(10).
202. Tian X, Wang S, Li JS, Liu FX, Wang X, Chen H, et al. Benzimidazole grafted polybenzimidazole cross-linked membranes with excellent PA stability for high-temperature proton exchange membrane applications. *Appl Surf Sci*. 2019;465:332-9.
203. Li XB, Ma HW, Wang P, Liu ZC, Peng JW, Hu W, et al. Highly Conductive and Mechanically Stable Imidazole-Rich Cross-Linked Networks for High-Temperature Proton Exchange Membrane Fuel Cells. *Chemistry of Materials*. 2020;32(3):1182-91.
204. Wang J, Jiang HX, Xu YX, Yang JS, He RH. Quaternized poly(aromatic ether sulfone) with siloxane crosslinking networks as high temperature proton exchange membranes. *Appl Surf Sci*. 2018;452:473-80.
205. Sithambaranathan P, Nasef MM, Ahmad A, Ripin A. Crosslinked composite membrane by radiation grafting of 4-vinylpyridine/triallyl-cyanurate mixtures onto poly(ethylene-co-

- tetrafluoroethylene) and phosphoric acid doping. *International Journal of Hydrogen Energy*. 2017;42(14):9333-41.
206. Luo HC, Pu HT, Chang ZH, Wan DC, Pan HY. Crosslinked polybenzimidazole via a Diels-Alder reaction for proton conducting membranes. *J Mater Chem*. 2012;22(38):20696-705.
207. Tu CH, Hsu SLC, Bulycheva E, Belomoina N. Novel crosslinked AB-type polyphenylquinoxaline membranes for high-temperature proton exchange membrane fuel cells. *Polym Eng Sci*. 2019;59(10):2169-73.
208. Aili D, Cleemann LN, Li QF, Jensen JO, Christensen E, Bjerrum NJ. Thermal curing of PBI membranes for high temperature PEM fuel cells. *J Mater Chem*. 2012;22(12):5444-53.
209. Ma WJ, Zhao CJ, Yang JS, Ni J, Wang S, Zhang N, et al. Cross-linked aromatic cationic polymer electrolytes with enhanced stability for high temperature fuel cell applications. *Energ Environ Sci*. 2012;5(6):7617-25.
210. Lai S, Park J, Cho S, Tsai M, Lim H, Chen K. Mechanical property enhancement of ultra-thin PBI membrane by electron beam irradiation for PEM fuel cell. *International Journal of Hydrogen Energy*. 2016;41(22):9556-62.
211. Zhang N, Wang B, Zhao C, Wang S, Zhang Y, Bu F, et al. Quaternized poly (ether ether ketone) s doped with phosphoric acid for high-temperature polymer electrolyte membrane fuel cells. *J Mater Chem A*. 2014;2(34):13996-4003.
212. Yang JS, Wang YH, Yang GH, Zhan SF. New anhydrous proton exchange membranes based on fluoropolymers blend imidazolium poly (aromatic ether ketone)s for high temperature polymer electrolyte fuel cells. *International Journal of Hydrogen Energy*. 2018;43(17):8464-73.
213. Ren X, Li H, Liu K, Lu H, Yang J, He R. Preparation and investigation of reinforced PVP blend membranes for high temperature polymer electrolyte membranes. *Fiber Polym*. 2018;19(12):2449-57.
214. Li MQ, Scott K. A polymer electrolyte membrane for high temperature fuel cells to fit vehicle applications. *Electrochimica Acta*. 2010;55(6):2123-8.
215. Lu S, Xiu R, Xu X, Liang D, Wang H, Xiang Y. Polytetrafluoroethylene (PTFE) reinforced poly (ethersulphone)-poly (vinyl pyrrolidone) composite membrane for high temperature proton exchange membrane fuel cells. *Journal of Membrane Science*. 2014;464:1-7.
216. Cao YC, Xu CX, Zou LL, Scott K, Liu JY. A polytetrafluoroethylene porous membrane and dimethylhexadecylamine quaternized poly (vinyl benzyl chloride) composite membrane for intermediate temperature fuel cells. *Journal of Power Sources*. 2015;294:691-5.
217. Koyilapu R, Singha S, Sana B, Jana T. Proton exchange membrane prepared by blending polybenzimidazole with poly (aminophosphonate ester). *Polym Test*. 2020;85.
218. Lu SF, Xiu RJ, Xu X, Liang DW, Wang HN, Xiang Y. Polytetrafluoroethylene (PTFE) reinforced poly(ethersulphone)-poly(vinyl pyrrolidone) composite membrane for high temperature proton exchange membrane fuel cells. *Journal of Membrane Science*. 2014;464:1-7.
219. Tao P, Dai Y, Chen S, Wang J, He R. Hyperbranched polyamidoamine modified high temperature proton exchange membranes based on PTFE reinforced blended polymers. *Journal of Membrane Science*. 2020;604:118004.
220. Sana B, Koyilapu R, Dineshkumar S, Muthusamy A, Jana T. High temperature PEMs developed from the blends of Polybenzimidazole and poly(azomethine-ether). *J Polym Res*. 2019;26(2).

221. Devrim Y, Devrim H, Eroglu I. Polybenzimidazole/SiO₂ hybrid membranes for high temperature proton exchange membrane fuel cells. *international journal of hydrogen energy*. 2016;41(23):10044-52.
222. Suryani, Chang YN, Lai JY, Liu YL. Polybenzimidazole (PBI)-functionalized silica nanoparticles modified PBI nanocomposite membranes for proton exchange membranes fuel cells. *Journal of Membrane Science*. 2012;403:1-7.
223. Linlin M, Mishra AK, Kim NH, Lee JH. Poly (2, 5-benzimidazole)–silica nanocomposite membranes for high temperature proton exchange membrane fuel cell. *Journal of membrane science*. 2012;411:91-8.
224. Rajabi Z, Javanbakht M, Hooshyari K, Badiei A, Adibi M. High temperature composite membranes based on polybenzimidazole and dendrimer amine functionalized SBA-15 mesoporous silica for fuel cells. *New J Chem*. 2020;44(13):5001-18.
225. Cai YB, Yue ZY, Jiang QL, Xu SA. Modified silicon carbide whisker reinforced polybenzimidazole used for high temperature proton exchange membrane. *J Energy Chem*. 2018;27(3):820-5.
226. Bao XJ, Zhang F, Liu QT. Sulfonated poly(2,5-benzimidazole) (ABPBI)/MMT/ionic liquids composite membranes for high temperature PEM applications. *International Journal of Hydrogen Energy*. 2015;40(46):16767-74.
227. Cai YB, Yue ZY, Teng X, Xu SA. Phosphoric Acid Doped Crosslinked Polybenzimidazole/Modified Graphene Oxide Composite Membranes for High Temperature Proton Exchange Membrane Applications. *J Electrochem Soc*. 2018;165(11):F914-F20.
228. Cai YB, Yue ZY, Xu SA. A novel polybenzimidazole composite modified by sulfonated graphene oxide for high temperature proton exchange membrane fuel cells in anhydrous atmosphere. *J Appl Polym Sci*. 2017;134(25).
229. Abouzari-Lotf E, Zakeri M, Nasef MM, Miyake M, Mozarmnia P, Bazilah NA, et al. Highly durable polybenzimidazole composite membranes with phosphonated graphene oxide for high temperature polymer electrolyte membrane fuel cells. *Journal of Power Sources*. 2019;412:238-45.
230. Yang JS, Liu C, Gao LP, Wang J, Xu YX, He RH. Novel composite membranes of triazole modified graphene oxide and polybenzimidazole for high temperature polymer electrolyte membrane fuel cell applications. *Rsc Adv*. 2015;5(122):101049-54.
231. Zou GW, Wu W, Cong CB, Meng XY, Zhao K, Zhou Q. Improved performance of poly(vinyl pyrrolidone)/phosphonated poly(2,6-dimethyl-1,4-phenylene oxide)/graphitic carbon nitride nanocomposite membranes for high temperature proton exchange membrane fuel cells. *Rsc Adv*. 2016;6(108):106237-47.
232. Bai HJ, Wang HN, Zhang J, Wu CX, Zhang JJ, Xiang Y, et al. Simultaneously enhancing ionic conduction and mechanical strength of poly (ether sulfones)-poly(vinyl pyrrolidone) membrane by introducing graphitic carbon nitride nanosheets for high temperature proton exchange membrane fuel cell application. *Journal of Membrane Science*. 2018;558:26-33.
233. Fei MM, Lin RZ, Deng YM, Xian HX, Bian RJ, Zhang XL, et al. Polybenzimidazole/Mxene composite membranes for intermediate temperature polymer electrolyte membrane fuel cells. *Nanotechnology*. 2018;29(3).
234. Zheng HT, Mathe M. Enhanced conductivity and stability of composite membranes based on poly (2,5-benzimidazole) and zirconium oxide nanoparticles for fuel cells. *Journal of Power Sources*. 2011;196(3):894-8.

235. Esmailzade B, Esmailzadeh S, Ahmadizadegan H. Ultrasonic irradiation to modify the functionalized bionanocomposite in sulfonated polybenzimidazole membrane for fuel cells applications and antibacterial activity. *Ultrason Sonochem.* 2018;42:260-70.
236. Nguyen VT, Ziolo JT, Yang Y, Diercks D, Alfaro SM, Hjuler HA, et al. 12-Silicotungstic Acid Doped Phosphoric Acid Imbibed Polybenzimidazole for Enhanced Protonic Conductivity for High Temperature Fuel Cell Applications. *J Electrochem Soc.* 2017;164(6):F504-F13.
237. Dai LM. Functionalization of Graphene for Efficient Energy Conversion and Storage. *Accounts Chem Res.* 2013;46(1):31-42.
238. Karim MR, Hatakeyama K, Matsui T, Takehira H, Taniguchi T, Koinuma M, et al. Graphene Oxide Nanosheet with High Proton Conductivity. *Journal of the American Chemical Society.* 2013;135(22):8097-100.
239. Ghidui M, Lukatskaya MR, Zhao MQ, Gogotsi Y, Barsoum MW. Conductive two-dimensional titanium carbide 'clay' with high volumetric capacitance. *Nature.* 2014;516(7529):78-U171.
240. Hope MA, Forse AC, Griffith KJ, Lukatskaya MR, Ghidui M, Gogotsi Y, et al. NMR reveals the surface functionalisation of Ti₃C₂ MXene. *Phys Chem Chem Phys.* 2016;18(7):5099-102.
241. Cronin L, Muller A. From serendipity to design of polyoxometalates at the nanoscale, aesthetic beauty and applications. *Chemical Society Reviews.* 2012;41(22):7333-4.
242. Kourasi M, Wills RGA, Shah AA, Walsh FC. Heteropolyacids for fuel cell applications. *Electrochimica Acta.* 2014;127:454-66.
243. Sunarso J, Hashim SS, Zhu N, Zhou W. Perovskite oxides applications in high temperature oxygen separation, solid oxide fuel cell and membrane reactor: A review. *Prog Energ Combust.* 2017;61:57-77.
244. Bai HJ, Wang HN, Zhang J, Zhang JJ, Lu SF, Xiang Y. High temperature polymer electrolyte membrane achieved by grafting poly (1-vinylimidazole) on polysulfone for fuel cells application. *Journal of Membrane Science.* 2019;592.
245. Li XB, Wang P, Liu ZC, Peng JW, Shi CY, Hu W, et al. Arylether-type polybenzimidazoles bearing benzimidazolyl pendants for high-temperature proton exchange membrane fuel cells. *Journal of Power Sources.* 2018;393:99-107.
246. Yang T, Huang N, Meng LY. Chitosan modified by nitrogen-containing heterocycle and its excellent performance for anhydrous proton conduction. *Rsc Adv.* 2013;3(13):4341-9.
247. Zhang JJ, Zhang J, Bai HJ, Tan QL, Wang HN, He BS, et al. A new high temperature polymer electrolyte membrane based on trifunctional group grafted polysulfone for fuel cell application. *Journal of Membrane Science.* 2019;572:496-503.
248. Hong LH, Wang BL, Zhao CJ. Phosphoric acid doped high temperature proton exchange membranes based on comb-shaped polymers with quaternized graft architectures. *Appl Surf Sci.* 2019;483:785-92.
249. Lin HL, Hu CR, Lai SW, Yu TL. Polybenzimidazole and butylsulfonate grafted polybenzimidazole blends for proton exchange membrane fuel cells. *Journal of Membrane Science.* 2012;389:399-406.
250. Yang JS, Cleemann LN, Steenberg T, Terkelsen C, Li QF, Jensen JO, et al. High Molecular Weight Polybenzimidazole Membranes for High Temperature PEMFC. *Fuel Cells.* 2014;14(1):7-15.

251. Cai YB, Yue ZY, Teng X, Xu SA. Radiation grafting graphene oxide reinforced polybenzimidazole membrane with a sandwich structure for high temperature proton exchange membrane fuel cells in anhydrous atmosphere. *Eur Polym J.* 2018;103:207-13.
252. Deng YM, Wang G, Fei MM, Huang X, Cheng JG, Liu XT, et al. A polybenzimidazole/graphite oxide based three layer membrane for intermediate temperature polymer electrolyte membrane fuel cells. *Rsc Adv.* 2016;6(76):72224-9.
253. Yu JM, Cheng SC, Che QT. Preparation and characterization of layer-by-layer self-assembly membrane based on sulfonated polyetheretherketone and polyurethane for high-temperature proton exchange membrane. *J Polym Sci Pol Chem.* 2017;55(20):3446-54.
254. Park J, Wang L, Advani SG, Prasad AK. Mechanical Stability of H₃PO₄-Doped PBI/Hydrophilic-Pretreated PTFE Membranes for High Temperature PEMFCs. *Electrochimica Acta.* 2014;120:30-8.
255. Iwakura Y, Imai Y, Uno K. Polyphenylenebenzimidazoles. *J Polym Sci Part A.* 1964;2(6pa):2605-&.
256. Kim TH, Lim TW, Lee JC. High-temperature fuel cell membranes based on mechanically stable para-ordered polybenzimidazole prepared by direct casting. *Journal of Power Sources.* 2007;172(1):172-9.
257. Molle MA, Chen X, Ploehn HJ, Benicewicz BC. High Polymer Content 2,5-Pyridine-Polybenzimidazole Copolymer Membranes with Improved Compressive Properties. *Fuel Cells.* 2015;15(1):150-9.
258. Yao D, Jao T-C, Zhang W, Xu L, Xing L, Ma Q, et al. In-situ diagnosis on performance degradation of high temperature polymer electrolyte membrane fuel cell by examining its electrochemical properties under operation. *international journal of hydrogen energy.* 2018;43(45):21006-16.
259. Chen H, Song Z, Zhao X, Zhang T, Pei P, Liang C. A review of durability test protocols of the proton exchange membrane fuel cells for vehicle. *Appl Energ.* 2018;224:289-99.
260. Yang J, Jiang H, Wang J, Xu Y, Pan C, Li Q, et al. Dual cross-linked polymer electrolyte membranes based on poly (aryl ether ketone) and poly (styrene-vinylimidazole-divinylbenzene) for high temperature proton exchange membrane fuel cells. *Journal of Power Sources.* 2020;480:228859.
261. Liu R, Dai Y, Li J, Chen X, Pan C, Yang J, et al. 1-(3-Aminopropyl) imidazole functionalized poly (vinyl chloride) for high temperature proton exchange membrane fuel cell applications. *Journal of Membrane Science.* 2020:118873.
262. Wu Y, Liu X, Yang F, Zhou LL, Yin B, Wang P, et al. Achieving high power density and excellent durability for high temperature proton exchange membrane fuel cells based on crosslinked branched polybenzimidazole and metal-organic frameworks. *Journal of Membrane Science.* 2021;630:119288.
263. Mogg L, Hao G-P, Zhang S, Bacaksiz C, Zou Y-C, Haigh S, et al. Atomically thin micas as proton-conducting membranes. *Nature nanotechnology.* 2019;14(10):962-6.
264. Hatakeyama K, Karim MR, Ogata C, Tateishi H, Funatsu A, Taniguchi T, et al. Proton conductivities of graphene oxide nanosheets: single, multilayer, and modified nanosheets. *Angewandte Chemie.* 2014;126(27):7117-20.
265. Achtyl JL, Unocic RR, Xu L, Cai Y, Raju M, Zhang W, et al. Aqueous proton transfer across single-layer graphene. *Nature communications.* 2015;6(1):1-7.

266. Aili D, Yang J, Jankova K, Henkensmeier D, Li Q. From polybenzimidazoles to polybenzimidazoliums and polybenzimidazolides. *Journal of Materials Chemistry A*. 2020;8(26):12854-86.
267. Zhang C, Zhang L, Zhou W, Wang Y, Chan SH. Investigation of water transport and its effect on performance of high-temperature PEM fuel cells. *Electrochimica Acta*. 2014;149:271-7.
268. Zhang C, Zhou W, Zhang L, Chan SH, Wang Y. An experimental study on anode water management in high temperature PEM fuel cell. *international journal of hydrogen energy*. 2015;40(13):4666-72.
269. Zhang C, Liu Z, Zhou W, Chan SH, Wang Y. Dynamic performance of a high-temperature PEM fuel cell—An experimental study. *Energy*. 2015;90:1949-55.
270. Zhang C, Zhou W, Ehteshami MM, Wang Y, Chan SH. Determination of the optimal operating temperature range for high temperature PEM fuel cell considering its performance, CO tolerance and degradation. *Energy conversion and management*. 2015;105:433-41.
271. Zhang C, Yu T, Yi J, Liu Z, Raj KAR, Xia L, et al. Investigation of heating and cooling in a stand-alone high temperature PEM fuel cell system. *Energy Conversion and Management*. 2016;129:36-42.
272. Wang J, Dai Y, Wan R, Wei W, Xu S, Zhai F, et al. Grafting free radical scavengers onto polyarylethersulfone backbones for superior chemical stability of high temperature polymer membrane electrolytes. *Chem Eng J*. 2021;413:127541.
273. Ren J, Zhang S, Liu Y, Wang Y, Pang J, Wang Q, et al. A novel crosslinking organic–inorganic hybrid proton exchange membrane based on sulfonated poly (arylene ether sulfone) with 4-amino-phenyl pendant group for fuel cell application. *Journal of membrane science*. 2013;434:161-70.
274. Liu D, Yates M. Electric field processing to control the structure of poly (vinylidene fluoride) composite proton conducting membranes. *Journal of Membrane Science*. 2009;326(2):539-48.
275. Zhao S, Ren J, Wang Y, Zhang J. Electric field processing to control the structure of titanium oxide/sulfonated poly (ether ether ketone) hybrid proton exchange membranes. *Journal of membrane science*. 2013;437:65-71.
276. Liu X, Li Y, Xue J, Zhu W, Zhang J, Yin Y, et al. Magnetic field alignment of stable proton-conducting channels in an electrolyte membrane. *Nature communications*. 2019;10(1):1-13.
277. Wang X, Zhai H, Qie B, Cheng Q, Li A, Borovilas J, et al. Rechargeable solid-state lithium metal batteries with vertically aligned ceramic nanoparticle/polymer composite electrolyte. *Nano Energy*. 2019;60:205-12.
278. Yang J, Yang W, Chen W, Tao X. An elegant coupling: Freeze-casting and versatile polymer composites. *Progress in Polymer Science*. 2020:101289.
279. Tripathi BP, Shahi VK. Organic–inorganic nanocomposite polymer electrolyte membranes for fuel cell applications. *Progress in Polymer Science*. 2011;36(7):945-79.
280. Yoonoo C, Dawson CP, Roberts EP, Holmes SM. Nafion®/mordenite composite membranes for improved direct methanol fuel cell performance. *Journal of membrane science*. 2011;369(1-2):367-74.
281. Al-Batty S, Dawson C, Shanmukham S, Roberts E, Holmes S. Improvement of direct methanol fuel cell performance using a novel mordenite barrier layer. *J Mater Chem A*. 2016;4(28):10850-7.

282. Nicotera I, Enotiadis A, Angjeli K, Coppola L, Gournis D. Evaluation of smectite clays as nanofillers for the synthesis of nanocomposite polymer electrolytes for fuel cell applications. *international journal of hydrogen energy*. 2012;37(7):6236-45.
283. Choudalakis G, Gotsis A. Permeability of polymer/clay nanocomposites: a review. *European polymer journal*. 2009;45(4):967-84.
284. Choi YS, Kim TK, Kim EA, Joo SH, Pak C, Lee YH, et al. Exfoliated sulfonated poly (arylene ether sulfone)–clay nanocomposites. *Advanced Materials*. 2008;20(12):2341-4.
285. Sasikala S, Meenakshi S, Bhat S, Sahu A. Functionalized Bentonite clay-sPEEK based composite membranes for direct methanol fuel cells. *Electrochimica Acta*. 2014;135:232-41.
286. Xu F, Mu S, Pan M. Mineral nanofibre reinforced composite polymer electrolyte membranes with enhanced water retention capability in PEM fuel cells. *Journal of membrane science*. 2011;377(1-2):134-40.
287. Li X, Roberts EP, Holmes SM, Zholobenko V. Functionalized zeolite A–nafion composite membranes for direct methanol fuel cells. *Solid State Ionics*. 2007;178(19-20):1248-55.
288. Brigatti MF, Galan E, Theng B. Structures and mineralogy of clay minerals. *Developments in clay science*. 2006;1:19-86.
289. Ma Q, Sun X, Liu P, Xia Y, Liu X, Luo J. Bio-Inspired Stable Lithium-Metal Anodes by Co-depositing Lithium with a 2D Vermiculite Shuttle. *Angewandte Chemie International Edition*. 2019;58(19):6200-6.
290. Tang W, Tang S, Guan X, Zhang X, Xiang Q, Luo J. High-performance solid polymer electrolytes filled with vertically aligned 2D materials. *Advanced Functional Materials*. 2019;29(16):1900648.
291. Gogoi RK, Raidongia K. Intercalating cation specific self-repairing of vermiculite nanofluidic membrane. *J Mater Chem A*. 2018;6(44):21990-8.
292. Huang K, Rowe P, Chi C, Sreepal V, Bohn T, Zhou K-G, et al. Cation-controlled wetting properties of vermiculite membranes and its promise for fouling resistant oil–water separation. *Nature communications*. 2020;11(1):1-10.
293. Liu D, Deng S, Vakili M, Du R, Tao L, Sun J, et al. Fast and high adsorption of Ni (II) on vermiculite-based nanoscale hydrated zirconium oxides. *Chem Eng J*. 2019;360:1150-7.
294. Yen M, Bitla Y, Chu Y-H. van der Waals heteroepitaxy on muscovite. *Materials Chemistry and Physics*. 2019;234:185-95.
295. Abukhadra MR, Mostafa M. Effective decontamination of phosphate and ammonium utilizing novel muscovite/phillipsite composite; equilibrium investigation and realistic application. *Science of the Total Environment*. 2019;667:101-11.
296. Bao T, Damtie MM, Hosseinzadeh A, Frost RL, Yu ZM, Jin J, et al. Catalytic degradation of P-chlorophenol by muscovite-supported nano zero valent iron composite: Synthesis, characterization, and mechanism studies. *Applied Clay Science*. 2020;195:105735.
297. Le V-Q, Do T-H, Retamal JRD, Shao P-W, Lai Y-H, Wu W-W, et al. Van der Waals heteroepitaxial AZO/NiO/AZO/muscovite (ANA/muscovite) transparent flexible memristor. *Nano Energy*. 2019;56:322-9.
298. Yu X. The preparation and characterization of cetyltrimethylammonium intercalated muscovite. *Microporous and mesoporous materials*. 2007;98(1-3):70-9.

299. Radoslovich E. The structure of muscovite, $\text{KA}12 (\text{Si}3\text{Al}) \text{O}10 (\text{OH}) 2$. *Acta Crystallographica*. 1960;13(11):919-32.
300. Huang W-Y, Li D, Liu Z-Q, Tao Q, Zhu Y, Yang J, et al. Kinetics, isotherm, thermodynamic, and adsorption mechanism studies of $\text{La} (\text{OH}) 3$ -modified exfoliated vermiculites as highly efficient phosphate adsorbents. *Chemical Engineering Journal*. 2014;236:191-201.
301. Wang L, Zang L, Zhao J, Wang C. Green synthesis of shape-defined anatase $\text{TiO} 2$ nanocrystals wholly exposed with {001} and {100} facets. *Chem Commun*. 2012;48(96):11736-8.
302. Coleman JN, Lotya M, O'Neill A, Bergin SD, King PJ, Khan U, et al. Two-dimensional nanosheets produced by liquid exfoliation of layered materials. *Science*. 2011;331(6017):568-71.
303. Wang M, Zhang F, Wang Z, Xu X. Liquid-phase exfoliated silicon nanosheets: saturable absorber for solid-state lasers. *Materials*. 2019;12(2):201.
304. Prapainainar C, Kanjanapaisit S, Kongkachuichay P, Holmes SM, Prapainainar P. Surface modification of mordenite in Nafion composite membrane for direct ethanol fuel cell and its characterizations: Effect of types of silane coupling agent. *Journal of environmental chemical engineering*. 2016;4(3):2637-46.
305. Zhang J, Lu S, Zhu H, Chen K, Xiang Y, Liu J, et al. Amino-functionalized mesoporous silica based polyethersulfone–polyvinylpyrrolidone composite membranes for elevated temperature proton exchange membrane fuel cells. *RSC advances*. 2016;6(89):86575-85.
306. Du M, Yang L, Luo X, Wang K, Chang G. Novel phosphoric acid (PA)-poly (ether ketone sulfone) with flexible benzotriazole side chains for high-temperature proton exchange membranes. *Polymer Journal*. 2019;51(1):69-75.
307. Guo Z, Xu X, Xiang Y, Lu S. New anhydrous proton exchange membranes for high-temperature fuel cells based on PVDF–PVP blended polymers. *Journal of Materials Chemistry A*. 2015;3(1):148-55.
308. Guo Z, Xiu R, Lu S, Xu X, Yang S, Xiang Y. Submicro-pore containing poly (ether sulfones)/polyvinylpyrrolidone membranes for high-temperature fuel cell applications. *Journal of Materials Chemistry A*. 2015;3(16):8847-54.
309. Yuan S, Tang Q, He B. Three-dimensional hydrogel frameworks for high-temperature proton exchange membrane fuel cells. *Journal of Materials Science*. 2014;49(15):5481-91.
310. Souquet-Grumey J, Perrin R, Cellier J, Bigarré J, Buvat P. Synthesis and fuel cell performance of phosphonated hybrid membranes for PEMFC applications. *Journal of membrane science*. 2014;466:200-10.
311. Anahidzade N, Abdolmaleki A, Dinari M, Tadavani KF, Zhiani M. Metal-organic framework anchored sulfonated poly (ether sulfone) as a high temperature proton exchange membrane for fuel cells. *Journal of Membrane Science*. 2018;565:281-92.
312. Yang JS, Wang J, Liu C, Gao LP, Xu YX, Che QT, et al. Influences of the structure of imidazolium pendants on the properties of polysulfone-based high temperature proton conducting membranes. *Journal of Membrane Science*. 2015;493:80-7.
313. Bai H, Li Y, Zhang H, Chen H, Wu W, Wang J, et al. Anhydrous proton exchange membranes comprising of chitosan and phosphorylated graphene oxide for elevated temperature fuel cells. *Journal of Membrane Science*. 2015;495:48-60.

314. Jeong G, Kim M, Han J, Kim H-J, Shul Y-G, Cho E. High-performance membrane-electrode assembly with an optimal polytetrafluoroethylene content for high-temperature polymer electrolyte membrane fuel cells. *Journal of Power Sources*. 2016;323:142-6.
315. Liu S, Wippermann K, Lehnert W. Mechanism of action of polytetrafluoroethylene binder on the performance and durability of high-temperature polymer electrolyte fuel cells. *international journal of hydrogen energy*. 2021;46(27):14687-98.
316. Galbiati S, Baricci A, Casalegno A, Carcassola G, Marchesi R. On the activation of polybenzimidazole-based membrane electrode assemblies doped with phosphoric acid. *International Journal of Hydrogen Energy*. 2012;37(19):14475-81.
317. Prokop M, Bystron T, Belsky P, Tucek O, Kodym R, Paidar M, et al. Degradation kinetics of Pt during high-temperature PEM fuel cell operation Part III: Voltage-dependent Pt degradation rate in single-cell experiments. *Electrochimica Acta*. 2020;363:137165.
318. Halter J, Thomas S, Kær SK, Schmidt TJ, Büchi FN. The influence of phosphoric acid migration on the performance of high temperature polymer electrolyte fuel cells. *Journal of Power Sources*. 2018;399:151-6.
319. Gamry.com. Use of Transmission Lines for Electrochemical Impedance Spectroscopy 2014 [Available from: <https://www.gamry.com/assets/Uploads/Use-of-Transmission-Lines-for-EIS.pdf>].
320. Netzsch-thermal-analysis.com. Simultaneous Thermal Analysis (STA) [Available from: <https://www.netzsch-thermal-analysis.com/en/contract-testing/methods/simultaneous-thermal-analysis-sta/>].
321. Mohamed MA, Jaafar J, Ismail A, Othman M, Rahman M. Fourier transform infrared (FTIR) spectroscopy. *Membrane Characterization: Elsevier*; 2017. p. 3-29.
322. Bunaciu AA, Udriștioiu EG, Aboul-Enein HY. X-ray diffraction: instrumentation and applications. *Critical reviews in analytical chemistry*. 2015;45(4):289-99.
323. Epp J. X-ray diffraction (XRD) techniques for materials characterization. *Materials characterization using nondestructive evaluation (NDE) methods: Elsevier*; 2016. p. 81-124.
324. Sowinska M. In-operando hard X-ray photoelectron spectroscopy study on the resistive switching physics of HfO₂-based RRAM. 2014.
325. McKeen L. Introduction to the Mechanical, Thermal, and Permeation Properties of Plastics and Elastomer Films, *Film Properties of Plastics and Elastomers*, 2017, *Plastics Design Library*. William Andrew Publishers.
326. Bardestani R, Patience GS, Kaliaguine S. Experimental methods in chemical engineering: specific surface area and pore size distribution measurements—BET, BJH, and DFT. *The Canadian Journal of Chemical Engineering*. 2019;97(11):2781-91.
327. micromeritics.com. Accelerated Surface Area and Porosimetry System [Available from: https://www.micromeritics.com/Repository/Files/ASAP_2020_Brochure_3.pdf].
328. Inkson B. Scanning electron microscopy (SEM) and transmission electron microscopy (TEM) for materials characterization. *Materials characterization using nondestructive evaluation (NDE) methods: Elsevier*; 2016. p. 17-43.
329. Chandan A, Hattenberger M, El-Kharouf A, Du S, Dhir A, Self V, et al. High temperature (HT) polymer electrolyte membrane fuel cells (PEMFC)—A review. *Journal of Power Sources*. 2013;231:264-78.
330. Büsselmann J, Rastedt M, Klicpera T, Reinwald K, Schmies H, Dyck A, et al. Analysis of HT-PEM MEAs' Long-Term Stabilities. *Energies*. 2020;13(3):567.

331. Pinar FJ, Pilinski N, Rastedt M, Wagner P. Performance of a high-temperature PEM fuel cell operated with oxygen enriched cathode air and hydrogen from synthetic reformat. *international journal of hydrogen energy*. 2015;40(15):5432-8.
332. Moura FC, Lago RM. Catalytic growth of carbon nanotubes and nanofibers on vermiculite to produce floatable hydrophobic “nanosponges” for oil spill remediation. *Applied Catalysis B: Environmental*. 2009;90(3-4):436-40.
333. Wang L, Wang X, Yin J, Wang C. Insights into the physicochemical characteristics from vermiculite to silica nanosheets. *Applied Clay Science*. 2016;132:17-23.
334. Ishii R, Nakatsuji M, Ooi K. Preparation of highly porous silica nanocomposites from clay mineral: a new approach using pillaring method combined with selective leaching. *Micropor Mesopor Mat*. 2005;79(1-3):111-9.
335. Ghosh S, Maity S, Jana T. Polybenzimidazole/silica nanocomposites: Organic-inorganic hybrid membranes for PEM fuel cell. *J Mater Chem*. 2011;21(38):14897-906.
336. Santos S, Silva H, De Souza A, Alves A, da Silva Filho E, Fonseca M. Acid-leached mixed vermiculites obtained by treatment with nitric acid. *Applied Clay Science*. 2015;104:286-94.
337. Wang L, Wang X, Cui S, Fan X, Zu B, Wang C. TiO₂ supported on silica nanolayers derived from vermiculite for efficient photocatalysis. *Catalysis today*. 2013;216:95-103.
338. Wu H, Zheng B, Zheng X, Wang J, Yuan W, Jiang Z. Surface-modified Y zeolite-filled chitosan membrane for direct methanol fuel cell. *Journal of power sources*. 2007;173(2):842-52.
339. Yan Z, Fu L, Zuo X, Yang H. Green assembly of stable and uniform silver nanoparticles on 2D silica nanosheets for catalytic reduction of 4-nitrophenol. *Applied Catalysis B: Environmental*. 2018;226:23-30.
340. Mosa J, Durán A, Aparicio M. Sulfonic acid-functionalized hybrid organic–inorganic proton exchange membranes synthesized by sol–gel using 3-mercaptopropyl trimethoxysilane (MPTMS). *Journal of Power Sources*. 2015;297:208-16.
341. Zhao L, Li Y, Zhang H, Wu W, Liu J, Wang J. Constructing proton-conductive highways within an ionomer membrane by embedding sulfonated polymer brush modified graphene oxide. *Journal of Power Sources*. 2015;286:445-57.
342. Liu Y, Zhang J, Zhang X, Li Y, Wang J. Ti₃C₂T_x Filler Effect on the Proton Conduction Property of Polymer Electrolyte Membrane. *Acs Appl Mater Inter*. 2016;8(31):20352-63.
343. Zhang J, Liu J, Lu S, Zhu H, Aili D, De Marco R, et al. Ion-exchange-induced selective etching for the synthesis of amino-functionalized hollow mesoporous silica for elevated-high-temperature fuel cells. *ACS applied materials & interfaces*. 2017;9(37):31922-30.
344. Seo K, Seo J, Nam KH, Han H. Polybenzimidazole/inorganic composite membrane with advanced performance for high temperature polymer electrolyte membrane fuel cells. *Polymer Composites*. 2017;38(1):87-95.
345. Kim D, Lee Y, Seo J, Han H, Khan SB. Preparation and properties of poly (urethane acrylate)(PUA) and tetrapod ZnO whisker (TZnO - W) composite films. *Polym Int*. 2013;62(2):257-65.
346. McKeen JC, Yan YS, Davis ME. Proton conductivity in sulfonic acid-functionalized zeolite beta: effect of hydroxyl group. *Chemistry of materials*. 2008;20(12):3791-3.
347. Vilekar SA, Datta R. The effect of hydrogen crossover on open-circuit voltage in polymer electrolyte membrane fuel cells. *Journal of Power Sources*. 2010;195(8):2241-7.

348. Gang M, He G, Li Z, Cao K, Li Z, Yin Y, et al. Graphitic carbon nitride nanosheets/sulfonated poly (ether ether ketone) nanocomposite membrane for direct methanol fuel cell application. *Journal of Membrane Science*. 2016;507:1-11.
349. Marani D, D'Epifanio A, Traversa E, Miyayama M, Licoccia S. Titania nanosheets (TNS)/sulfonated poly ether ether ketone (SPEEK) nanocomposite proton exchange membranes for fuel cells. *Chemistry of Materials*. 2010;22(3):1126-33.
350. Seo K, Nam K-H, Han H. proton transport in Aluminum-Substituted Mesoporous Silica channel-embedded High-temperature Anhydrous proton-exchange Membrane fuel cells. *Sci Rep-Uk*. 2020;10(1):1-9.
351. Chen C-Y, Lai W-H. Effects of temperature and humidity on the cell performance and resistance of a phosphoric acid doped polybenzimidazole fuel cell. *Journal of Power Sources*. 2010;195(21):7152-9.
352. Aili D, Zhang J, Jakobsen MTD, Zhu H, Yang T, Liu J, et al. Exceptional durability enhancement of PA/PBI based polymer electrolyte membrane fuel cells for high temperature operation at 200° C. *J Mater Chem A*. 2016;4(11):4019-24.
353. Chang W, Hwang J, Weng F, Chan S. Effect of clamping pressure on the performance of a PEM fuel cell. *Journal of Power Sources*. 2007;166(1):149-54.
354. Liu G, Zhang H, Hu J, Zhai Y, Xu D, Shao Z-g. Studies of performance degradation of a high temperature PEMFC based on H3PO4-doped PBI. *Journal of Power Sources*. 2006;162(1):547-52.
355. Galbiati S, Baricci A, Casalegno A, Marchesi R. Degradation in phosphoric acid doped polymer fuel cells: A 6000 h parametric investigation. *International Journal of Hydrogen Energy*. 2013;38(15):6469-80.
356. Jia F, Su J, Song S. Can natural muscovite be expanded? *Colloids and Surfaces A: Physicochemical and Engineering Aspects*. 2015;471:19-25.
357. Ilić B, Radonjanin V, Malešev M, Zdujić M, Mitrović A. Effects of mechanical and thermal activation on pozzolanic activity of kaolin containing mica. *Applied Clay Science*. 2016;123:173-81.
358. Hamzaoui R, Bouchenafa O, Maaouia OB, Guessasma S. Introduction of milled kaolinite obtained by mechanosynthesis to cement mixture for the production of mortar: Study of mechanical performance of modified mortar. *Powder Technology*. 2019;355:340-8.
359. Panda AK, Mishra BG, Mishra DK, Singh RK. Effect of sulphuric acid treatment on the physico-chemical characteristics of kaolin clay. *Colloids and surfaces A: Physicochemical and engineering aspects*. 2010;363(1-3):98-104.
360. Hamzaoui R, Muslim F, Guessasma S, Bennabi A, Guillin J. Structural and thermal behavior of proclay kaolinite using high energy ball milling process. *Powder Technology*. 2015;271:228-37.
361. Selim AQ, Mohamed EA, Seliem MK, Zayed AM. Synthesis of sole cancrinite phase from raw muscovite: Characterization and optimization. *Journal of Alloys and Compounds*. 2018;762:653-67.
362. Huo J, Min X, Wang Y. Zirconium-modified natural clays for phosphate removal: Effect of clay minerals. *Environmental Research*. 2021;194:110685.
363. Ossianer T, Heinzl C, Gleich S, Schönberger F, Völk P, Welsch M, et al. Influence of the size and shape of silica nanoparticles on the properties and degradation of a PBI-based high temperature polymer electrolyte membrane. *Journal of Membrane Science*. 2014;454:12-9.

364. Krishnan NN, Lee S, Ghorpade RV, Konovalova A, Jang JH, Kim H-J, et al. Polybenzimidazole (PBI-OO) based composite membranes using sulfophenylated TiO₂ as both filler and crosslinker, and their use in the HT-PEM fuel cell. *Journal of Membrane Science*. 2018;560:11-20.
365. Eberhardt SH, Marone F, Stampanoni M, Büchi FN, Schmidt TJ. Operando X-ray tomographic microscopy imaging of HT-PEFC: a comparative study of phosphoric acid electrolyte migration. *Journal of the Electrochemical Society*. 2016;163(8):F842.
366. Wang FF. *Treatise on materials Science and Technology*. vol. 1976;9:79-81.
367. Nawn G, Pace G, Lavina S, Vezzù K, Negro E, Bertasi F, et al. Nanocomposite membranes based on polybenzimidazole and ZrO₂ for high-temperature proton exchange membrane fuel cells. *ChemSusChem*. 2015;8(8):1381-93.
368. Sadeghi M, Semsarzadeh MA, Moadel H. Enhancement of the gas separation properties of polybenzimidazole (PBI) membrane by incorporation of silica nano particles. *Journal of Membrane Science*. 2009;331(1-2):21-30.
369. Akhtar FH, Kumar M, Villalobos LF, Vovusha H, Shevate R, Schwingenschlögl U, et al. Polybenzimidazole-based mixed membranes with exceptionally high water vapor permeability and selectivity. *Journal of Materials Chemistry A*. 2017;5(41):21807-19.
370. Nawn G, Pace G, Lavina S, Vezzu K, Negro E, Bertasi F, et al. Interplay between composition, structure, and properties of new H₃PO₄-doped PBI₄N–HfO₂ nanocomposite membranes for high-temperature proton exchange membrane fuel cells. *Macromolecules*. 2015;48(1):15-27.
371. Asensio JA, Borrós S, Gómez-Romero P. Polymer electrolyte fuel cells based on phosphoric acid-impregnated poly (2, 5-benzimidazole) membranes. *J Electrochem Soc*. 2004;151(2):A304.
372. Giffin GA, Conti F, Lavina S, Majerus A, Pace G, Korte C, et al. A vibrational spectroscopic and modeling study of poly (2, 5-benzimidazole)(ABPBI)–Phosphoric acid interactions in high temperature PEFC membranes. *international journal of hydrogen energy*. 2014;39(6):2776-84.
373. Nawn G, Vezzù K, Bertasi F, Pagot G, Pace G, Conti F, et al. Electric response and conductivity mechanism reciprocity in H₃PO₄-doped Polybenzimidazole-4N–ZrO₂ nanocomposite membranes. *Solid State Ionics*. 2018;320:172-6.
374. Rathod D, Vijay M, Islam N, Kannan R, Kharul U, Kurungot S, et al. Design of an “all solid-state” supercapacitor based on phosphoric acid doped polybenzimidazole (PBI) electrolyte. *Journal of applied electrochemistry*. 2009;39(7):1097-103.
375. Bu F, Zhang Y, Hong L, Zhao W, Li D, Li J, et al. 1, 2, 4-Triazole functionalized poly (arylene ether ketone) for high temperature proton exchange membrane with enhanced oxidative stability. *Journal of Membrane Science*. 2018;545:167-75.
376. Nawn G, Vezzù K, Bertasi F, Pagot G, Pace G, Conti F, et al. Electric Response and Conductivity Mechanism in H₃PO₄-Doped Polybenzimidazole-4N– HfO₂ Nanocomposite Membranes for High Temperature Fuel Cells. *Electrochimica Acta*. 2017;228:562-74.
377. Yusoff YN, Loh KS, Wong WY, Daud WRW, Lee TK. Sulfonated graphene oxide as an inorganic filler in promoting the properties of a polybenzimidazole membrane as a high temperature proton exchange membrane. *International Journal of Hydrogen Energy*. 2020;45(51):27510-26.

References

378. Ramani V, Kunz HR, Fenton JM. The polymer electrolyte fuel cell. *Interface*. 2004;13(3):17-9.
379. Li J, Yang L, Wang Z, Sun H, Sun G. Degradation study of high temperature proton exchange membrane fuel cell under start/stop and load cycling conditions. *International Journal of Hydrogen Energy*. 2021;46(47):24353-65.
380. Zhang X, Yang Y, Guo L, Liu H. Effects of carbon corrosion on mass transfer losses in proton exchange membrane fuel cells. *International Journal of Hydrogen Energy*. 2017;42(7):4699-705.
381. Parnian MJ, Rowshanzamir S, Prasad AK, Advani SG. High durability sulfonated poly (ether ether ketone)-ceria nanocomposite membranes for proton exchange membrane fuel cell applications. *Journal of Membrane Science*. 2018;556:12-22.
382. Dotelli G, Ferrero R, Stampino PG, Latorrata S. Analysis and compensation of PEM fuel cell instabilities in low-frequency EIS measurements. *IEEE Transactions on Instrumentation and Measurement*. 2014;63(7):1693-700.
383. Shao Y, Yin G, Gao Y. Understanding and approaches for the durability issues of Pt-based catalysts for PEM fuel cell. *Journal of Power Sources*. 2007;171(2):558-66.
384. S ndergaard T, Cleemann LN, Becker H, Steenberg T, Hjuler HA, Seerup L, et al. Long-term durability of PBI-based HT-PEM fuel cells: effect of operating parameters. *J Electrochem Soc*. 2018;165(6):F3053.

Appendix A: Publications

1. **Zunmin Guo**, Jianuo Chen, Jae Jong Byun, Rongsheng Cai, María Pérez-Page, Madhumita Sahoo, Zhaoqi Ji, Sarah J. Haigh, Stuart M. Holmes*. High-performance polymer electrolyte membranes incorporated with 2D silica nanosheets in high-temperature proton exchange membrane fuel cells (HT-PEMFCs). **Journal of Energy Chemistry**. 2021. 64: 323-334.
2. **Zunmin Guo**, Jianuo Chen, Jae Jong Byun, Maria Perez-Page, Zhaoqi Ji, Ziyu Zhao, Stuart M. Holmes*. Insights into the performance and degradation of polybenzimidazole/muscovite composite membranes in high-temperature proton exchange membrane fuel cells. **Journal of Membrane Science**. 2021. 119868.
3. **Zunmin Guo***, Maria Perez Page, Jianuo Chen, Stuart Holmes*. Recent advances in phosphoric acid-based membranes for high-temperature proton exchange membrane fuel cells. **Journal of Energy Chemistry**. 2021. 63:393-429.
4. **Zunmin Guo**, Ziyu Zhao, Jianuo Chen, Zhaoqi Ji, Stuart M. Holmes*. A structured catalyst support combining silica nanosheets and carbon black for enhanced performance and durability in high-temperature proton exchange membrane fuel cells. (Ready to submit)
5. Sajjad Mohsenpour, **Zunmin Guo***, Stuart M. Holmes, Patricia Gorgojo*. Incorporating 2D silica nanosheets in PIM-1 membrane to enhance CO₂ capture and slow physical aging. **Journal of Membrane Science**. (Ready to submit)
6. Daniel Niblett^{1*}, **Zunmin Guo**¹, Stuart Holmes, Vahid Niasar, Robert Prosser. Utilisation of 3D printed carbon gas diffusion layers in polymer electrolyte membrane fuel cells. **International Journal of Hydrogen Energy**. (Accepted)
7. Jianuo Chen, **Zunmin Guo**, María Pérez-Page, Zhaoqi Ji, Zhe Zhang, Stuart M. Holmes*. Synthesis of Phosphonated Graphene Oxide by Electrochemical Exfoliation to Enhance the Performance and Durability of High-temperature Proton Exchange Membrane Fuel cells. (Ready to submit)
8. Zhaoqi Ji, Jianuo Chen, **Zunmin Guo**, María Pérez-Page*, Stuart M. Holmes*. Graphene/carbon structured catalyst layer to mitigate phosphoric acid loss and catalyst degradation in the high-temperature PEMFCs. **Journal of Energy Chemistry**. (Under revision)
9. Zhaoqi Ji, Jianuo Chen, María Pérez-Page*, **Zunmin Guo**, Ziyu Zhao, Rongsheng Cai, Maxwell T. P. Rigby, Sarah J. Haigh, Stuart M. Holmes*. Doped graphene/carbon black

- hybrid catalyst giving enhanced oxygen reduction reaction activity with high resistance to corrosion in proton exchange membrane fuel cells. **Journal of Energy Chemistry**. 2022. 68:143-153.
10. Jianuo Chen, Josh J. Bailey, Liam Britnell, Maria Perez-Page, Madhumita Sahoo, Zhe Zhang, Andrew Strudwick, Jennifer Hack, **Zunmin Guo**, Zhaoqi Ji, Philip Martin, Dan J.L. Brett, Paul R. Shearing, and Stuart M. Holmes*. Single-layer Graphene Enhances the Performance and Durability of High-temperature Proton Exchange Membrane Fuel Cells. **Nano Energy**. 2021 Dec 11:106829.
 11. Jianuo Chen, María Pérez-Page*, Zhaoqi Ji, Zhe Zhang, **Zunmin Guo**, Stuart M. Holmes*. One Step Electrochemical Exfoliation of Natural Graphite Flakes into Graphene Oxide for Polybenzimidazole Composite Membranes Giving Enhanced Performance in High Temperature Fuel Cells. **Journal of Power Sources**. 2021.491: 229550.
 12. Boya Qiu, Monica Alberto, Sajjad Mohsenpour, Andrew Foster, **Zunmin Guo**, Shengzhe Ding, Peter Budd, Patricia Gorgojo*, Xiaolei Fan. ZIF-8/GO/PIM-1 thin film nanocomposite membrane for enhanced organophilic separations by pervaporation. **Journal of Membrane Science**. (under revision)

Appendix B: Conferences

1. **Zunmin Guo**, Stuart Holmes*, High-performance polymer electrolyte membranes incorporated with 2D silica nanosheets in high-temperature proton exchange membrane fuel cells. **15th International conference on materials chemistry (MC15)**, 2021, poster.
2. **Zunmin Guo**, Stuart Holmes*, Improvement of Performance and Lifetime of Polybenzimidazole Membranes in High Temperature Fuel Cells by Incorporation of muscovite. **240th ECS Meeting**, 2021, oral presentation.
3. **Zunmin Guo**, Stuart Holmes*, Durable silica nanosheets/carbon black supported catalyst for proton exchange membrane fuel cells. **241th ECS Meeting**, 2022, oral presentation.